



THE HONG KONG
POLYTECHNIC UNIVERSITY

香港理工大學

Pao Yue-kong Library

包玉剛圖書館

Copyright Undertaking

This thesis is protected by copyright, with all rights reserved.

By reading and using the thesis, the reader understands and agrees to the following terms:

1. The reader will abide by the rules and legal ordinances governing copyright regarding the use of the thesis.
2. The reader will use the thesis for the purpose of research or private study only and not for distribution or further reproduction or any other purpose.
3. The reader agrees to indemnify and hold the University harmless from and against any loss, damage, cost, liability or expenses arising from copyright infringement or unauthorized usage.

If you have reasons to believe that any materials in this thesis are deemed not suitable to be distributed in this form, or a copyright owner having difficulty with the material being included in our database, please contact lbsys@polyu.edu.hk providing details. The Library will look into your claim and consider taking remedial action upon receipt of the written requests.

THE HONG KONG POLYTECHNIC UNIVERSITY

THE DEPARTMENT OF APPLIED PHYSICS

SYNTHESIS AND CHARACTERIZATION OF

MAGNETIC NANOPARTICLES AND

NANO-COMPOSITES

SIN WAI LUN

A THESIS SUBMITTED IN PARTIAL FULFILMENT OF

THE REQUIREMENTS FOR THE DEGREE OF

DOCTOR OF PHILOSOPHY

July 2007

CERTIFICATE OF ORIGINALITY

I hereby declare that this thesis is my own work and that, to the best of my knowledge and belief, it reproduces no material previously published or written, nor material which has been accepted for the award of any other degree or diploma, except where due acknowledgement has been made in the text.

_____(Signed)

SIN WAI LUN (Name of student)



Abstract

Abstract of thesis entitled ‘Synthesis and Characterization of Magnetic Nanoparticles and Nano-composites’ submitted by Sin Wai Lun for the degree of PhD at The Hong Kong Polytechnic University in August, 2007.

The design, synthesis, and characterization of particles with nanometer dimensions have attracted intense interests in recent years. The novel electronic, optical, magnetic, and other properties that arise from the quantum size effect and large surface-to-volume ratio can have immense application value. Magnetic nanoparticles are important examples of how a reduction in size changes the properties of a ferromagnetic material. It is a big challenge to understand and control the interfacial magnetism for developing novel devices with strong correlated electron oxides. Indeed spin-polarized ferromagnetic $\text{La}_x\text{Sr}_{1-x}\text{MnO}_3$ (LSMO) has been identified as a good candidate for stable room temperature spintronic applications.

This project involves a modified hydrothermal method for synthesizing magnetic nanoparticles with controllable chemical, composition and particle morphology. We have demonstrated that nanoscale manganite particles formed from a metal chloride precursor in water under mild hydrothermal conditions yields high crystalline, thermally stable and pure phase particles, whose sizes and morphology can also be tuned through adjustment of reaction temperature, precursor concentration, concentration of mineralizers and the presence of surfactants.



Indeed our work represents the first experimental investigation and synthesis of LSMO nanoparticles using cationic surfactant assisted hydrothermal process. Characterization of the nanocrystals was done by Transmission Electron Microscope (TEM), Scanning Electron Microscope (SEM), X-ray Powder Diffraction (XRD) and Vibrating Sample Magnetometer (VSM).

Generally, stoichiometric $\text{La}_x\text{Sr}_{1-x}\text{MnO}_3$ (LSMO) nanoparticles were obtained at low process temperature of 240 °C under the hydrothermal condition. Structural characterization by XRD showed that the particles started to crystallize at 210 °C. Crystalline LSMO particles with grain size as small as 20 nm and confined to a narrow size distribution have been obtained. Progressively improved crystalline structure and orientation were seen at higher processing temperature. The nucleation and crystal growth processes mediated by macromolecule (CTAB) finally results in more uniform and controllable products.

Based on these magnetic nano-sized perovskite manganites, we have systematically studied their magnetic hysteresis, magnetic anisotropy and exchange coupling. Several magnetometry techniques such as Zero Field-Cooled (ZFC)/Field-Cooled (FC) measurements, magnetic hysteresis curve above and below the blocking temperature have been employed in these studies.

Since LSMO is in a family of large bandwidth and exhibits a colossal magneto-resistivity, a systematic study of the temperature dependence and the magnetic effects on electrical conductivity in LSMO nanoparticle has been made.



The experimental results were explained satisfactory by several scattering and hopping models.

The effects of exchange coupling between the manganite nanoparticles with antiferromagnetic phase in core-shell structured were also investigated. The composite consists of ferromagnetic $\text{La}_{0.67}\text{Sr}_{0.33}\text{MnO}_3$ core and antiferromagnetic LaMnO_3 shell. Formation of this manganites core-shell structure has been done by a two-step hydrothermal process, which involves the use of two precursor solutions in succession. To ensure the homogeneous overcoat the shell layer, cationic surfactant CTAB has been used to modify the surface of core particle. Structural properties of the core-shell arrangement are confirmed by TEM and XRD experiment. We are able to show that a 5 nm thin layer is clearly coated on LSMO particles to form the desired core-shell architecture. The effects on the magnetic properties such as the coercive field enhancement are also discussed.

Finally, LSMO/Poly(vinyl alcohol) (PVA) composites have been prepared by simple ultrasonic mixing of as-prepared nanoparticles and polymer solution. Then, films of LSMO/PVA composites have been fabricated on insulating substrate by traditional spin coating method. The microstructure, magnetic and magnetoresistivity properties of these films have been studied also. The experimental resistivity data of the present investigation are fitted to a simple empirical equation in order to reveal conduction mechanism in these composites.



List of Publications

1. W. L. Sin, K. H. Wong and P. Li, “Surfactant effect on synthesis of nanocrystalline $\text{La}_x\text{Sr}_{1-x}\text{MnO}_3$ by hydrothermal method”, ACTA Physica Polonica A, 111(2007) P.165
2. W. L. Sin, K. H. Wong and P. Li, “Synthesis and magnetic properties of $\text{La}_x\text{Sr}_{1-x}\text{MnO}_3$ rod like particles”, Abstract in International Conference on Materials for Advanced Technologies, M-4-PO34 (2007) P.57
3. W. L. Sin, K. H. Wong and P. Li, “Synthesis and magnetic properties of $\text{La}_x\text{Sr}_{1-x}\text{MnO}_3$ rod like particles”, Synthesis and Reactivity in Inorganic, Metal-Organic, and Nano-Metal Chemistry, 38 (2008) P.260 -263



ACKNOWLEDGEMENTS

This thesis is based on the experimental work carried out in the Department of Applied Physics, The Hong Kong Polytechnic University, during the years of 2004 – 2007.

I wish to express my deep gratitude to my supervisor Dr. K. H. Wong for his support, encouragement and advice throughout these years. I also thank my co-supervisor Dr. P. Lei for introducing me to the chemical technique to the nanoparticles synthesize.

I am also very grateful for the help of, present and past, members of the laser group in our department. Particularly I would like to express my thanks to my research colleagues: Mr. C. H. Lau, Mr. W. F. Cheng, Mr. H. Y. Kong and Mr. M. H. Wong, for their contributions in magnetic nanoparticles preparations and analyses as well as useful comments. I also wish to acknowledge Dr. Y. W. Wong, Dr. K. H. Pang, Dr. C. W. Tai, Dr. X. H. Zhang, Dr. K. M. Ho, Mr. M. N. Yeung and Mr. K. W. Ho for their advice and generous assistance in the TEM, SEM experiments and sample preparation.

During this work, I had the pleasure of working with many skillful scientists, without whom the comprehensive characterization of the nanoparticles would not



have been possible. Very special thanks go to Ms. Yoyo Yeung for the VSM measurement and also for her support and discussion on my research work. I am grateful to Mr. S. W. Cheung and Mr. W. F. Wong for their useful suggestions.

I own a great deal of my accomplishment to the immeasurable love and the never-ending support of my parents. They are the ones who always believe that my efforts will be rewards. I am heartfelt grateful to Ms. P. Y. Chu for her encouragement and kindness.

Last, but certainly not least, tons of thanks are extended to my close friends for their encouragement and support. Specially thanks to my friends, Ben, Laputa, Sing, Patrick, Terry, Eva, Kin, Pie, Will, Sandy, Michael, Kobe, Kee, Lam Two, Bessie, Li Heng, Kiff, Water, Fred, Albert, Vicky, Argus, Sun, Winnie, Eddy, Bong, Annie, Frances, Lilian, Hilda, Phoebe, Candy, Victor, Rodney, Ray, Yee, Andy, Yao, Janet, Zhuang Lin, Helios, Irene, Edward, for their friendship and encouragement.

This study was supported by the Research Grant Council of Hong Kong (Project codes: A-PE96, 5-ZH42 and RP97). I am grateful for the award of a research studentship by the Hong Kong Polytechnic University.



TABLE OF CONTENTS

ABSTRACT	i
LIST OF PUBLICATIONS	iv
ACKNOWLEDGEMENTS	v
TABLE OF CONTENTS	vii
LIST OF FIGURES	xvi
LIST OF TABLES	xxvii
LIST OF ABBREVIATIONS	xxviii

**CHAPTER 1**

Introduction to Magnetic Nanoparticles	1-1
1.1 Background on magnetic nanoparticles	1-1
1.2 Fundamentals of magnetism	1-4
1.2.1 <i>Classification of magnetic behavior</i>	<i>1-7</i>
1.2.2 <i>Multidomain against single domain</i>	<i>1-11</i>
1.3 Superparamagnetism of magnetic nanomaterials	1-12
1.3.1 <i>Exchange interaction</i>	<i>1-12</i>
1.3.2 <i>Magnetic anisotropy</i>	<i>1-13</i>
1.3.3 <i>Single domain theory and superparamagnetism</i>	<i>1-18</i>
1.4 Manganite materials	1-21
1.4.1 <i>Perovskite structure of manganite materials</i>	<i>1-24</i>
1.4.2 <i>Half-metal nature of manganite</i>	<i>1-26</i>
1.4.3 <i>Nanosized manganite</i>	<i>1-29</i>
1.5 Outline of thesis	1-31



CHAPTER 2

Nanoparticle Formation and Hydrothermal Technique	2-1
2.1 Introduction	2-1
2.1.1 <i>Top-down and bottom-up approaches</i>	2-4
2.1.2 <i>Chemical approach of synthesis process</i>	2-6
2.1.3 <i>Nucleation and crystal growth</i>	2-7
2.2 Hydrothermal process	2-9
2.2.1 <i>Background</i>	2-9
2.2.2 <i>Mechanism of hydrothermal process</i>	2-12
2.2.3 <i>Role of supercritical water</i>	2-14
2.2.4 <i>Apparatus for hydrothermal process</i>	2-15
2.2.5 <i>Hydrothermal reaction</i>	2-16
2.3 Control of particle size and morphology	2-18
2.3.1 <i>Approach of soft-template and hard template</i>	2-19
2.3.2 <i>Surfactants</i>	2-20
2.3.3 <i>Particle aggregation</i>	2-25
2.4 Reported work in hydrothermal derived manganite	2-26
2.5 Experimental details of our hydrothermal process	2-27



3.3	Magnetic properties measurement	3-20
3.3.1	<i>Vibrating sample magnetometer (VSM)</i>	3-20
3.3.2	<i>Operation of vibrating sample magnetometer</i>	3-22
3.3.3	<i>Magnetic hysteresis loop</i>	3-23
3.3.4	<i>Technique of magnetization measurement</i>	3-25
3.4	Electrical measurement	3-28
3.4.1	<i>Temperature dependent resistivity measurement</i>	3-28
3.4.2	<i>Two-point probe method</i>	3-29
3.4.3	<i>Four-point against two-point</i>	3-30

**CHAPTER 4**

Synthesis of Magnetic Manganite Nanoparticles	4-1
4.1 Introduction	4-1
4.2 Experimental	4-7
4.2.1 <i>Chemistry of hydrothermal synthesis of LSMO nanoparticles</i>	4-7
4.2.2 <i>Synthesis of reference sample</i>	4-11
4.2.3 <i>Characterization methods</i>	4-11
4.3 Effect of hydrothermal condition on LSMO particles formation	4-12
4.3.1 <i>Cationic surfactant modified hydrothermal process</i>	4-12
4.3.2 <i>Effect of processing temperature</i>	4-31
4.3.3 <i>Influence of aging process on LSMO particles</i>	4-37
4.3.4 <i>Influence of concentration of mineralizer</i>	4-49



4.4	Composition studies	4-56
4.5	Size induced change of magnetic properties of LSMO nanoparticles	4-66
4.6	Electrical transport measurement	4-68
4.7	Magnetoresistance	4-70
4.8	Synthesis of $\text{La}_x\text{Ba}_{1-x}\text{MnO}_3$ (LBMO) particles	4-72
4.9	Summary	4-81

**CHAPTER 5****Synthesis and Characterization of Nano-Manganite**

Particles with Core-Shell Architecture	5-1
5.1 Introduction	5-1
5.1.1 <i>Magnetic coupling interaction</i>	5-6
5.1.2 <i>Epitaxial approach</i>	5-8
5.2 Experimental details	5-10
5.2.1 <i>Preparation of LSMO nanoparticles</i>	5-10
5.2.2 <i>Hydrothermal process for LaMnO₃ (LMO)</i> <i>shell layer on LSMO particles</i>	5-11
5.2.3 <i>Characterization of core-shell particles</i>	5-13
5.3 Results and discussion	5-14
5.3.1 <i>Structural characterization</i>	5-14
5.3.2 <i>Magnetization characterization</i>	5-18
5.4 Summary	5-22

**CHAPTER 6**

Dispersion of Magnetic Nano-Manganite in Polymer Matrix	6-1
6.1 Introduction	6-1
6.1.1 <i>Magnetoresistance (MR) of polycrystalline manganite</i>	6-4
6.1.2 <i>Extrinsic effect in polycrystals sample</i>	6-5
6.2 Nanoparticle/ polymer composite processing	6-6
6.2.1 <i>Polymer matrix of Poly(vinyl alcohol) – PVA</i>	6-9
6.2.2 <i>Mixing of LSMO nanoparticles in PVA polymer matrix</i>	6-11
6.3 Experimental Details	6-12
6.3.1 <i>Synthesis of LSMO/PVA composite</i>	6-12
6.3.2 <i>Characterization of LSMO/PVA composite</i>	6-13
6.4 Results and Discussion	6-15
6.5 Summary	6-29

CHAPTER 7

Conclusion	7-1
REFERENCES	R-1



List of Figures

Chapter 1. Introduction

Figure 1.1	Dipole moment produced from the electron movement.	1-5
Figure 1.2	Magnetic ordering of diamagnetic materials.	1-7
Figure 1.3	Magnetic ordering of paramagnetic materials.	1-8
Figure 1.4	Magnetic ordering of ferromagnetic materials.	1-9
Figure 1.5	Magnetic ordering of antiferromagnetic materials.	1-10
Figure 1.6	Schematic of magnetic domain configuration for (a) multi-domain and (b) single domain ferromagnets.	1-11
Figure 1.7	The relationships between spin, orbit and lattice coupling.	1-14
Figure 1.8	Shape anisotropy induces in prolate spheroid.	1-16
Figure 1.9	Double potential well as a model of superparamagnetism (SPM).	1-19
Figure 1.10	Coercive fields as a function of particle size.	1-20
Figure 1.11	Phase diagram of perovskite $\text{La}_x\text{Sr}_{1-x}\text{MnO}_3$ bulk sample.	1-22
Figure 1.12	Unit cell of a typical manganite with perovskite structure.	1-25
Figure 1.13	Electron band structures of different materials.	1-27



Chapter 2. Nanoparticle formation and hydrothermal process

- Figure 2.1** The La Mer diagram. Producing a mono-disperse sol by confining the formation of nuclei to a short period (τ) and allowing growth to occur only on those nuclei already formed. 2-7
- Figure 2.2** Flow chart of typical hydrothermal process. 2-10
- Figure 2.3** Hydrothermal dissolution/precipitation and in-situ transformation process 2-12
- Figure 2.4** Arrangement of the apparatus for the growth of nanoparticles by a hydrothermal method. 2-16
- Figure 2.5** Schematic of cationic surface of CTAB: (a) chemical formula, (b) ball model structure and (c) some physical parameters of CTAB. 2-22
- Figure 2.6** Schematic phase diagram for CTAB in water. 2-24



Chapter 3. Characterization method

Figure 3.1	Schematic diagram of different electron interactions.	3-4
Figure 3.2	Schematic diagram of the ray path of electron beam in TEM (a) image mode and (b) diffraction mode.	3-8
Figure 3.3	Bragg diffraction of X-rays from successive planes of atoms. Constructive interference occurs for ABC equal to an integral number of wavelengths.	3-14
Figure 3.4	The schematic diagram shows the operation of XRD ω -scan.	3-16
Figure 3.5	Sub unit of crystal lattice.	3-17
Figure 3.6	Schematic diagram of vibrating sample magnetometer (VSM) set-up.	3-21
Figure 3.7	Typical hysteresis loop of ferromagnetic materials.	3-24
Figure 3.8	Typical ZFC and FC curve for magnetic nanoparticles with blocking temperature (T_B).	3-25
Figure 3.9	Sketch of the sample for DC conduction measurement.	3-28
Figure 3.10	(a) Two point probe method and (b) Four point probe method for measuring transport properties.	3-32



Chapter 4. Synthesis of magnetic manganite nanoparticles

- Figure 4.1** X-ray powder diffraction pattern of LSMO nanoparticles produced in the presence of CTAB with different quantity: (a) 0 g; (b) 0.05 g; (c) 0.10 g and (d) 0.20 g. (●: LSMO phase; □: Impurities phase) 4-14
- Figure 4.2** Lattice parameters for LSMO particles prepared with different CTAB content. 4-15
- Figure 4.3** Particles size of LSMO particles formed with different CTAB content. 4-15
- Figure 4.4** TEM images of LSMO particle prepared by hydrothermal method with (a) 0 g, (b) 0.05 g, (c) 0.10 g and (d) 0.20 g CTAB. The small inset image is the respective electronic diffraction pattern. 4-17
- Figure 4.5** (a) High resolution TEM images of individual LSMO nanoparticles. The lattice fringes correspond to the (110) plane. (b) shows the fast Fourier transform pattern of this plane. 4-18
- Figure 4.6** Histogram of particle size distribution of LSMO particle grown by hydrothermal process with (a) 0.05 g CTAB surfactant and (b) 0.2 g CTAB surfactant. 4-20
- Figure 4.7** The room-temperature magnetization curve of LSMO powders obtained with (a) no CTAB, (b) 0.05 g CTAB, (c) 0.1 g CTAB and (d) 0.2 g CTAB. 4-22
- Figure 4.8** Magnetic hysteresis loop for nanoparticles of LSMO prepared by cationic surfactant assisted hydrothermal method. 4-24
- Figure 4.9** Saturation magnetization of as-prepared LSMO particles as a function of measurement temperature. 4-25
- Figure 4.10** Coercive field of as-prepared as-synthesized LSMO particles as a function of measurement temperature. 4-25



Figure 4.11	Fitting of magnetization curve of (M/M_s) against (H/T) for the sample at different temperatures.	4-28
Figure 4.12	The ZFC/FC curve shows a typical behavior of magnetic nanoparticles.	4-29
Figure 4.13	The XRD patterns of LSMO nanoparticles prepared from surfactant assisted hydrothermal method at various processing temperatures.	4-33
Figure 4.14	Lattice parameter (d_{110}) of LSMO particles as a function of processing temperatures.	4-34
Figure 4.15	Particle size of as-synthesized LSMO particles as a function of processing temperatures.	4-34
Figure 4.16	TEM images of LSMO particles prepared by hydrothermal process at 220°C.	4-36
Figure 4.17	Electron diffraction pattern of LSMO particles prepared by hydrothermal process at 220°C.	4-36
Figure 4.18	TEM images of LSMO particles prepared by hydrothermal process at 240°C.	4-37
Figure 4.19	Electron diffraction pattern of LSMO particles prepared by hydrothermal process at 240°C.	4-37
Figure 4.20	XRD patterns of LSMO nanoparticles prepared with an ageing process at (a) 30 °C, (b) 50 °C, (c) 60 °C and (d) 70 °C for 5 hours.	4-40
Figure 4.21	Lattice constant of LSMO nanoparticles prepared with an aging process at different aging temperatures.	4-41
Figure 4.22	Peak broadening and average crystallite size of LSMO nanoparticles prepared with at different aging temperatures.	4-41



- Figure 4.23** TEM images of LSMO nanoparticles prepared with an aging process at (a) 30 °C, (b) 50 °C, (c) 60 °C and (d) 70 °C for 5 hours. The inset images shows the coressponding SAD. 4-44
- Figure 4.24** (a) HRTEM image and (b) FFT image of the tip of LSMO rod like particle prepared with aging process at 30°C. 4-45
- Figure 4.25** Size distributions of LSMO nanoparticles prepared by hydrothermal method with aging temperature of 70°C. 4-46
- Figure 4.26** Field dependent magnetization curves of sample prepared at different aging temperatures: (a) 70 °C, (b) 50 °C and (c) 30 °C, respectively. 4-48
- Figure 4.27** Temperature dependence of saturation magnetization of LSMO particles prepared at different T_{aging} . 4-49
- Figure 4.28** Temperature dependence of coercive field of LSMO particles prepared at different T_{aging} . 4-50
- Figure 4.29** XRD diffractions of LSMO samples synthesized at 240°C with different initial KOH concentration: (a) 1.5 M, (b) 2.5 M, (c) 4.5 M, (d) 7.5 M and (e) 10.5 M, respectively. 4-53
- Figure 4.30** Lattice parameters of LSMO particles prepared at different initial [KOH]. 4-54
- Figure 4.31** TEM images of LSMO particles synthesized at 240°C with different KOH concentration: (a) 2 M, (b) 3 M, (c) 5 M, (d) 8 M, (e) 10 M and (f) 12 M, respectively. 4-55
- Figure 4.32** XRD patterns of $\text{La}_x\text{Sr}_{1-x}\text{MnO}_3$ particles prepared by hydrothermal process with composition of (a) $x = 0.5$, (b) $x = 0.67$ and (c) $x = 0.7$. 4-59
- Figure 4.33** The diffraction peaks of d_{110} of as-synthesized LSMO nanoparticles with different composition (x). 4-59
- Figure 4.34** (a) TEM image and (b) SAD image of hydrothermal $\text{La}_x\text{Sr}_{1-x}\text{MnO}_3$ nanoparticles ($x = 0.5$). 4-61



- Figure 4.35** Magnetization curves of $\text{La}_{0.5}\text{Sr}_{0.5}\text{MnO}_3$ nanoparticles. 4-63
- Figure 4.36** Temperature dependence of saturation magnetization of hydrothermal $\text{La}_{0.5}\text{Sr}_{0.5}\text{MnO}_3$ nanoparticles. 4-63
- Figure 4.37** Temperature dependence of coercive field of $\text{La}_{0.5}\text{Sr}_{0.5}\text{MnO}_3$ nanoparticles. 4-65
- Figure 4.38** Graph of $H_c^{1/2}$ against $T^{2/3}$ for $\text{La}_{0.5}\text{Sr}_{0.5}\text{MnO}_3$ nanoparticles. 4-65
- Figure 4.39** A graph of M/M_s against H/T for $\text{La}_{0.5}\text{Sr}_{0.5}\text{MnO}_3$ nanoparticles. 4-67
- Figure 4.40** Saturation magnetization (M_s) of the LSMO particles with different particle dimensions. 4-68
- Figure 4.41** Effect of particle size on the saturation magnetization (M_s) at 20 K temperature. 4-70
- Figure 4.42** Interface thickness against the particle size of LSMO samples. 4-70
- Figure 4.43** The temperature dependence of the resistance of nanocrystalline $\text{La}_x\text{Sr}_{1-x}\text{MnO}_3$ ($x = 0.67$) pellets with initial crystal size of (a) 2000 nm, (b) 40 nm and (c) 20 nm. 4-72
- Figure 4.44** Low-field magnetoresistance (MR) of sintered LSMO pellet as a function of temperature. 4-71
- Figure 4.45** A graph of R against T^2 for LSMO sample with 40 nm grains. 4-76
- Figure 4.46** A graph of $\ln(\rho)$ against $T^{-1/4}$ for LSMO sample with 40 nm grains 4-76
- Figure 4.47** A graph of $\ln(\rho)$ against $T^{-1/4}$ for LSMO sample with 20 nm grain size 4-77



- Figure 4.48** Magnetoresistance (MR) of sintered LSMO pellet as a function of an applied magnetic field at different temperatures. 4-80
- Figure 4.49** Low-field magnetoresistance (MR) of sintered LSMO pellet as a function of temperature. 4-80
- Figure 4.50** XRD patterns of LBMO samples synthesized at 240 °C at different initial KOH concentration: (a) 3.2 M, (b) 8.0 M and (c) 12.0 M. 4-83
- Figure 4.51** TEM images of LBMO particles prepared by cationic surfactant hydrothermal process with (a) [KOH] = 3 M and (b) [KOH] = 12 M. 4-85
- Figure 4.52** Field dependent magnetization curves of the hydrothermal $\text{La}_{0.67}\text{Ba}_{0.33}\text{MnO}_3$ particles at 20 K and 300 K, respectively. 4-86
- Figure 4.53** Temperature dependence of the saturation magnetization (M_s) of the hydrothermal LBMO particles. 4-87
- Figure 4.54** Temperature dependence of the coercive field (H_c) of the hydrothermal LBMO particles. 4-87
- Figure 4.55** A graph of $H_c^{1/2}$ against $T^{2/3}$ of the hydrothermal LBMO particles. 4-88
- Figure 4.56** The temperature dependence of resistivity of LBMO pellet. 4-89
- Figure 4.57** A graph of R against T^2 for the sintered LBMO sample. 4-90
- Figure 4.58** A graph of R against $T^{2.5}$ for the sintered LBMO sample. 4-90



Chapter 5. Synthesis and characterization of nano manganites particles with core shell architecture

Figure 5.1	Schematic diagram of core shell architecture	5-4
Figure 5.2	Magnetic ordering for the Mn ion in the perovskite lattice of (a) antiferromagnetic LaMnO_3 and (b) ferromagnetic $\text{La}_x\text{Sr}_{1-x}\text{MnO}_3$.	5-5
Figure 5.3	Hysteresis loops for the material (a) with and (b) without magnetic coupling.	5-7
Figure 5.4	XRD patterns of (a) as-prepared LSMO particles and (b) LSMO particles with shell layer.	5-15
Figure 5.5	Typical TEM images showing the morphology of LSMO (a-b) without LMO shell layer and (c-d) with LMO shell layer.	5-17
Figure 5.6	Temperature dependence of saturation magnetization of (a) as-synthesized LSMO nanoparticles and (b) LMO/LSMO core shell particles.	5-20
Figure 5.7	Temperature dependence of coercive field of (a) as-synthesized LSMO nanoparticles and (b) LMO/LSMO core shell particles.	5-20
Figure 5.8	Hysteresis loop of LSMO/LMO core-shell architecture at 20K.	5-21



Chapter 6. Dispersion of magnetic nano-manganite in polymer matrix

- Figure 6.1** Grains of the polycrystalline samples. (a) at zero magnetic field $H = 0$, (b) under magnetic field $H > 0$. Small arrows indicate the orientations of the magnetization for each grain. 6-5
- Figure 6.2** Repeating unit of Poly(vinyl alcohol) polymer. 6-10
- Figure 6.3** Procedures for synthesizing LSMO/PVA magnetic composites. 6-11
- Figure 6.4** XRD pattern of as-synthesized LSMO particles. 6-15
- Figure 6.5** (a) TEM image and (b) electron diffraction of as-synthesized LSMO nanoparticles. 6-17
- Figure 6.6** SEM images of the LSMO nanoparticles inside the PVA matrix. The bright dots are LSMO nanoparticles and the ridges are associated with the polymer surface. 6-19
- Figure 6.7** Magnetic hysteresis loop for nanocomposite of LSMO/PVA prepared by cationic surfactant assisted hydrothermal method at 20 K and 300 K, respectively. 6-21
- Figure 6.8** Saturation magnetization of LSMO/PVA nanocomposite as a function of temperature. 6-21
- Figure 6.9** Temperature dependence of coercive field of as-synthesized LSMO/PVA nanocomposites. 6-22
- Figure 6.10** Temperature dependence of resistance of the LSMO-PVA composite. 6-24



- Figure 6.11** A graph of $\ln(\rho)$ against $1/T$. 6-25
- Figure 6.12** A graph of $\ln(p)$ versus $1/T^4$. 6-25
- Figure 6.13** Magnetoresistance ratio of LSMO/PVA composite at different temperatures. 6-26
- Figure 6.14** Temperature dependence of MR ratio for the LSMO/PVA composite under different applied fields. 6-28



List of Tables

Table 2.1	Oxide powder synthesis route comparison.	2-11
Table 2.2	Role of different minerals in the precursor solution.	2-13
Table 2.3	Some commonly surfactants of each type.	2-21
Table 3.1	The seven crystal systems and the restrictions placed on the lattice parameters of the unit cell	3-18
Table 3.2	Specification of vibration sample magnetometer (VSM).	3-24
Table 4.1	Specifications of the raw materials used in hydrothermal synthesis of $A_xB_{1-x}MnO_3$.	4-9
Table 4.2	Composition of LSMO nanoparticles formed by hydrothermal process with different cationic surfactant concentration.	4-21
Table 4.3	Remanence magnetization and coercive fields of LSMO prepared by hydrothermal process with different CTAB content.	4-23
Table 4.4	Composition measurement (EDX) of LSMO particle compared with expected value.	4-62
Table 5.1	Summary of chemicals and processing conditions for preparing core-shell architecture.	5-12



List of Abbreviations

CTAB	Cetyltrimethylammonium bromide (cationic surfactant)
LSMO	Lanthanum Strontium Manganite
LBMO	Lanthanum Barium Manganite
LCMO	Lanthanum Calcium Manganite
LMO	Lanthanum Manganite
TEM	Transmission electron microscope
HRTEM	High resolution transmission electron microscope
EDX	Energy dispersive X-ray spectroscopy
XRD	X-ray Diffraction
PTFE	Teflon (Polytetrafluoroethylene)
HRTEM	High resolution transmission electron microscope
ZFC	Zero field-cooled
FC	Field-cooled
SAD	Selected area diffraction
BF	Bright field image
DF	Dark field image
M_S	Saturation magnetization
M_R	Remanent magnetization
H	Magnetic field strength
H_c	Coercivity
M	Mass magnetization
θ_c (T_c)	Curie temperature
θ_N	Néel temperature
T_B	Blocking temperature
T_p	Metal-insulator transition temperature
T_N	Néel temperature
σ_R	Specific remanent magnetization
σ_S	Specific saturation magnetization
AFM	Antiferromagnetic
KOH	Potassium hydroxide
VSM	Vibrating sample magnetometer
SPM	Superparamagnetic



MR	Magnetoresistance
CMR	Colossal Magnetoresistance
LFMR	Low field magnetoresistance
K	Magneto-anisotropy
χ	Magnetic susceptibility
D_c	Critical size
SEM	Scanning electron microscope
R-T	Temperature-resistivity measurement
FWHM	Full width at half maximum
2-theta	X-ray diffraction angle
CCD	Charge coupled device
λ	Wavelength
FM	Ferromagnetic-metal
FI	Ferromagnetic insulator
CO	Charge ordering
CAF	Canted antiferromagnetic phases
DE	Double exchange
Γ	Tolerance factor
a.u.	Arbitrary Units
μ	Permeability
μ_r	Relative permeability
I	Electrical current
ρ	Resistivity
B	Magnetic flux density
[KOH]	Concentration of potassium hydroxide
SPT	Spin polarized tunneling
P	Spin polarization

Physical constants:

Symbol	Quantity	Value	Units
E	Electron charge	1.60218×10^{-19}	C
k_B	Boltzmann's constant	1.3807×10^{-23}	JK ⁻¹
μ_0	Vacuum permeability	$4\pi \times 10^{-7}$	NA ⁻²



CHAPTER 1

Introduction to magnetic nanoparticles

1.1 Background on magnetic nanoparticles

The history of utilization of magnetic materials by mankind can plausibly be traced back to more than five thousand years ago in ancient China, where our ancestors used a natural mineral magnetite (Fe_3O_4) as a navigational compass [1]. Today, magnetic materials are indispensable and widely used in our everyday life. Examples of modern technologies and devices that exploit the magnetic properties of materials are numerous. Three areas in which magnetic materials have played fundamental roles are (i) data storage and processing, (ii) electric power generation and (iii) telecommunication [2].

On the other hand, nanotechnology, which involves the manipulation of matter at nanometer length scales to produce new structures and devices, has been shown to revolutionize the industry of today [3]. Owing to the many significant advances made in materials processing and characterization technique in recent years, it is now easier for us to design and manufacture devices with nanometer dimensions. The development of new “nano-” products leading to improved properties and performance is truly encouraging.



Nowadays, magnetic materials are being ubiquitously used in our daily life. Nanostructured magnetic materials (or termed as nanomagnetism), have generated continuous interest since the late 1940s. The investigation of their properties turned out to be challenging from both scientific and technological points of view [4]. Nanomagnetism and spintronics are highly creative research fields with a strong potential for future expansion. Nanomagnetism comprises the concerns of magnetic properties of materials at the nanoscale. Together with spintronics, which utilize the spin degree of freedom of electrons in conventional charge-based electronics, it offers great opportunities for developing a new generation of electronic devices [5].

At nanoscale, the size limitation introduces quantum confinement. Other physical and chemical properties of the nanomaterials will be primarily dominated by atoms located on the surface. Indeed, magnetic nanoparticles show a variety of unusual magnetic behaviors, mostly due to surface/interface effects [6]. Examples include symmetry breaking, electronic environment/charge transfer, and superparamagnetic interactions. Since nano-phase particles can possess as much as 50 % surface material, the new magnetic properties that may develop could have high practical value [7]. This is especially true for the room temperature superparamagnetism that results from thermally activated crossing of the anisotropy energy barrier by the magnetic moment of the magnetic nanoparticles [8].



To date, the unusual magnetic properties of magnetic nanoparticles have been demonstrated and utilized in many new and traditional uses, such as ultrahigh density magnetic data storage [9], giant magnetoresistance sensor [10], magnetocaloric refrigerator [11], magnetic resonance imaging contrast enhancement agents, magnetically guided target-specific drug delivery systems, cells/ DNAs/ genes sorting [12] and ferrofluids [13].



1.2 Fundamentals of magnetism

Before studying the magnetism of nanosized material, an overview of the fundamentals in magnetism is presented. It is followed by discussions of some important issues on nanomagnetism such as single domain theory, superparamagnetism (SPM) and magnetic anisotropy mechanism.

The origins of the physical phenomenon known as magnetism lie in the motion of electrons orbiting the nucleus in an atom. The atoms that make up all matter contain moving electrons whose motions produce tiny magnetic fields in the space around them. When an electron travels with a uniform angular speed around a circle of radius r , the period of the motion is $2\pi/\omega$. So the current is $e\omega/2\pi$ and the magnitude of the dipole moment is $\mu = (e\omega/2\pi) \pi r^2 = \frac{1}{2} e\omega r^2$ [14]. The direction of the moment is shown in Fig. 1.1. The particle also possesses an intrinsic spin (s), which can be thought of as a rotation about its own axis [15]. This produces an associated, intrinsic magnetic moment. In most materials these individual currents are randomly oriented and there is no net, magnetic effect. But, in some materials, a field exerted by an external source can cause the microscopic magnets to align along the external field direction. The result is a net addition to the external field and the material is then described as being magnetized.

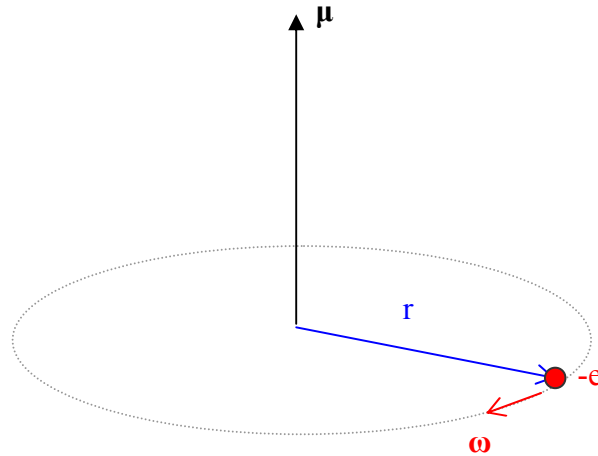


Figure 1.1 Dipole moment produced from the electron movement.

Magnetic materials can be classified according to the difference between their internal and external flux and the variation of the magnetization (M) or magnetic induction (B) when a magnetic field (H) is applied [16]. There are two quantities that relate M and B to H : the susceptibility χ and the permeability μ . A universal equation relating these magnetic quantities is as follows.

$$B = \mu_0(H + M) = \mu H$$

From this equation, one can see that $\mu_0 H$ is the magnetic induction generated by the field alone and $\mu_0 M$ is the additional magnetic induction contributed by a material.



The magnetic susceptibility (χ) is defined as the ratio of magnetization (M) to applied magnetic field (H):

$$\chi = \frac{M}{H}$$

Therefore, from the above equations, the permeability of a material is correlated with respect to each other by:

$$\mu = \mu_0(1 + \chi)$$

The susceptibility is a measure of the increase in magnetic moment caused by an applied field, whereas permeability represents the relative increase in flux caused by the presence of the magnetic material. It is a major parameter in characterization of magnetic properties of a material. The magnitude of the susceptibility and its temperature and field dependencies provide a measure of magnetic behavior of different types of magnetic materials.



1.2.1 Classification of magnetic behavior

Generally, according to the alignment of magnetic moments at absolute zero, the various magnetic behaviors of materials are classified into diamagnetism, paramagnetism, ferromagnetism and antiferromagnetism.

1.2.1.1 Diamagnetism (DM)

Diamagnetism is an inherent result of the orbital motion of the electrons in a magnetic field. It is present when the atom has zero net magnetic moment. In this case the orbital motion generates a field opposite to the applied field. The magnetic ordering of diamagnetic materials was schematically predicted in Fig. 1.2. Most materials are diamagnetic, including Cu, B, S and most organic compounds [17]. Materials that are said to be diamagnetic are those which are usually considered as "non-magnetic". The temperature independence is the characteristic of diamagnetic materials.

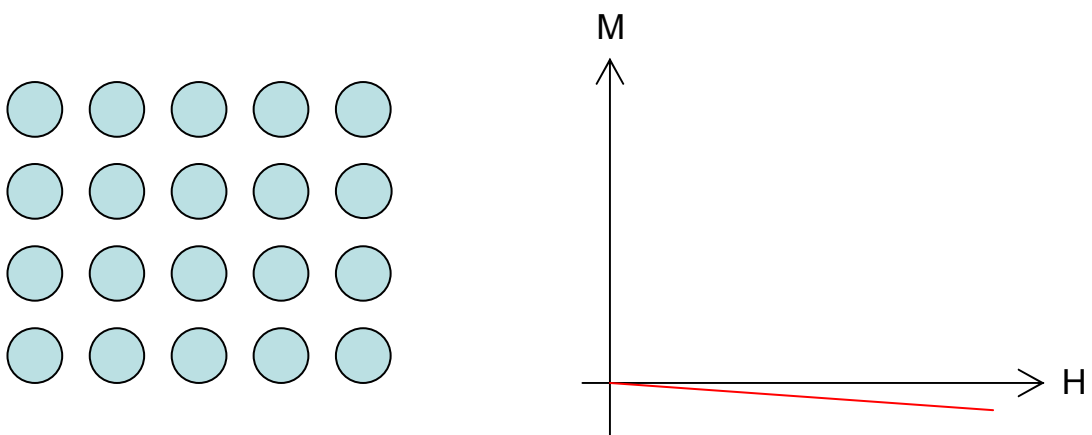


Figure 1.2 Magnetic ordering of diamagnetic materials.



1.2.1.2 Paramagnetism (PM)

In a paramagnetic material each individual electron spin is unaffected by its neighbors. Normally, the dipoles are randomly orientated, resulting a zero net magnetic moment. The spins of a paramagnetic material can easily be aligned by an applied magnetic field. Indeed this alignment is weak, and upon removal of the magnetic field the system relaxes back to a random distribution of magnetic moments. So, these materials have a small positive susceptibility with the order of 10^{-5} to 10^{-3} . The susceptibility of a paramagnetic material is inversely dependent on temperature which is known as Curie Law. The magnetic ordering of paramagnetic materials was schematically predicted in Fig. 1.3. Common examples of materials with paramagnetic ordering include Sr, Cr, Ba, Mg and Ca [18].

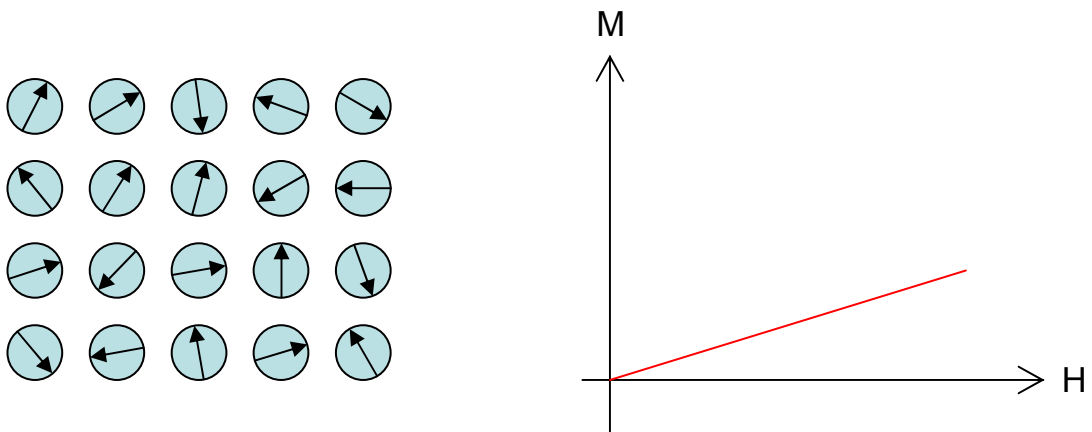


Figure 1.3 Magnetic ordering of paramagnetic materials.



1.2.1.3 Ferromagnetism (FM)

Ferromagnetism (FM) is characterized by parallel alignment of adjacent magnetic spins that results in a large net magnetic moment. Ferromagnetic alignment of adjacent magnetic spins is rare since it can only be achieved if there is zero quantum mechanical overlap between the spin orbital. In this case alignment of the spins, which correlates their motions and minimizes electron-electron repulsions, is the most stable state. Unlike paramagnets, ferromagnets exhibit a net moment in the absence of an applied magnetic field. Also the magnetic susceptibility (χ) of a ferromagnetic material follows the Curie-Weiss law [19]:

$$\chi = C/(T - T_w)$$

where C is a constant and T_w is Weiss constant and T is temperature. For ferromagnetic materials, the Weiss constant is almost identical to the Curie temperature. At temperature below Curie temperature, the magnetic moments are ordered, whereas above T_c , material loses magnetic ordering and shows paramagnetic character. The magnetic ordering of ferromagnetic materials was schematically predicted in Fig. 1.4. Examples are Fe, Co, Ni and Fe_2O_3 [20].

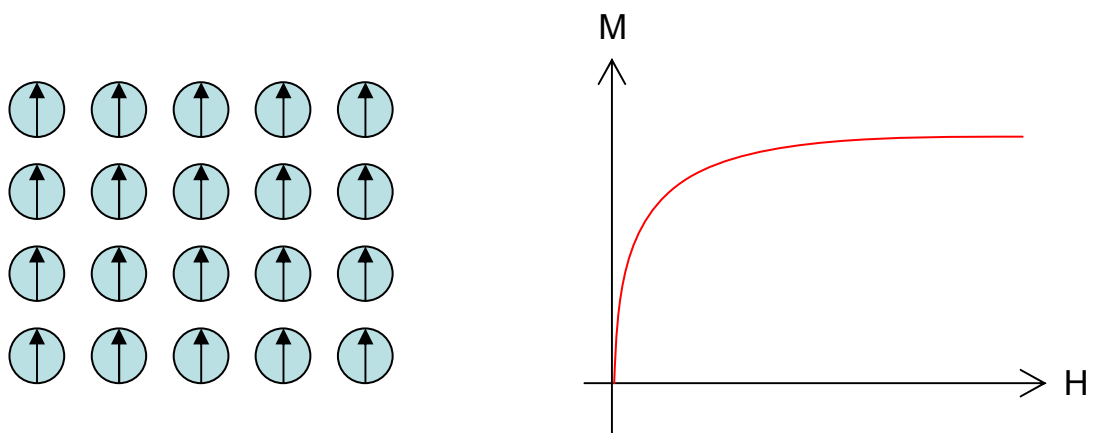


Figure 1.4 Magnetic ordering of ferromagnetic materials.

1.2.1.4 Antiferromagnetism (AFM)

In an AFM material, magnetic spins are aligned antiparallel, which results in a material with no net magnetic moment. The antiferromagnetic susceptibility is followed the Curie-Weiss law with a negative T_w as in the equation shown before. As shown in Fig. 1.5, antiferromagnetic materials exhibit antiferromagnetism at a low temperature, and become paramagnetic above Neél temperature (T_N) [21]. Antiferromagnetic materials are relative uncommon. Materials with antiferromagnetic ordering include transition metal monoxide such as CoO, MnO and NiO [22]. These materials can couple to ferromagnetic materials through a mechanism known as exchange anisotropy, in which the ferromagnetic film is either grown upon the antiferromagnet or annealed in an aligning magnetic field, causing the surface atoms of the ferromagnet to align with the surface atoms of the antiferromagnet. This provides the ability to "pin" the orientation of a ferromagnetic film, which in turn provides one of the main uses in so-called spin valves, which are the basis of magnetic sensors including modern hard drive read heads [23].

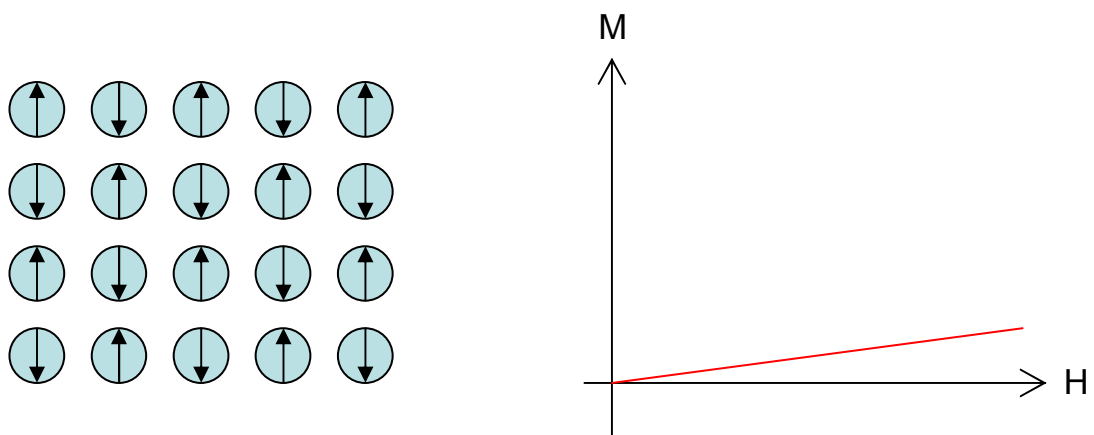


Figure 1.5 Magnetic ordering of antiferromagnetic materials.

1.2.2 Multidomain against single domain

Generally, for a bulk magnetic material, it consists of a large number of magnetic domains that formed and aligned in such a way as to minimize the magnetostatic energy [24]. A schematic of simplified domain configuration is shown in Fig. 1.6(a). For this reason the microstructure of bulk magnetic material plays a major role in determining the magnetic properties. As the particle size is reduced down to nano scale, the particle size and the exchange length converge, allowing for single domain states to stabilize, such as shown the picture in Fig. 1.6(b). The magnetism and hence the magnetic properties of nanoparticles are predominantly dictated by the intrinsic properties of a material such as the anisotropy and saturation magnetization [25].

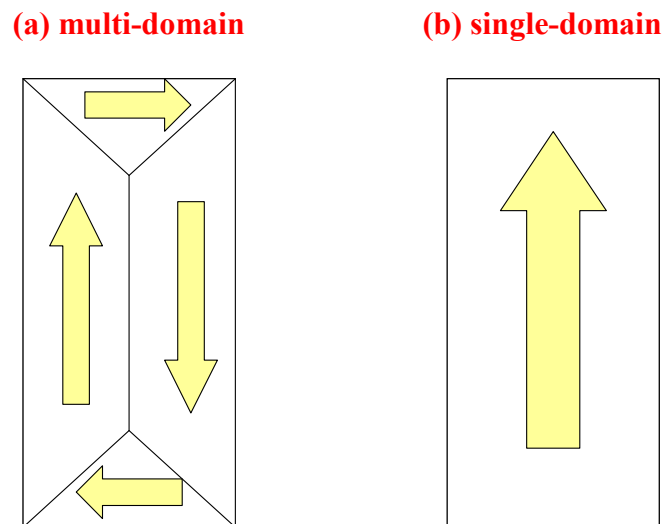


Figure 1.6 Schematic of magnetic domain configuration for (a) multi-domain and (b) single domain ferromagnets.



1.3 Superparamagnetism of magnetic nanoparticles

As the size of a magnetic particle is reduced down to nanoscale, the physical dimension is comparable to those that mediate the properties of the material. In such case the size effects induced anisotropy and superparamagnetism become important.

1.3.1 Exchange interaction

The fundamental basis for the magnetic behavior of magnetic materials relies on two mechanisms, exchange interaction and anisotropy [26]. The quantum origin of exchange interaction derives from the combination of electrostatic coupling between electron orbitals and the necessity to satisfy the Pauli Exclusion Principle, leading to spin - spin interactions that favor long range spin ordering. The energy of the exchange interaction in a ferromagnet between two spins S_i and S_j is typically modeled using the basic Heisenberg Hamiltonian [27] as:

$$H_{exch} = -\sum_{i,j} J_{ij} S_i S_j$$

where S_i is the spin angular momentum located at i^{th} site of a particular lattice, and the exchange integral J_{ij} represents the strength of the exchange coupling between the spin angular momentum i and j . If J_{ij} is positive, the parallel spin configuration will minimize the system total energy and all spins aligned to each other is the ground state. Therefore, a magnetic material is ferromagnetic. On the other hand, a negative J_{ij} favors the anti-parallel alignment of spins and consequently gives rise to antiferromagnetic ordering [28].



The exchange interactions are isotropic relative to any externally fixed spatial direction. In reality, the exchange spherical symmetry is always broken, because the electron orbitals interact with the potential created by the hosting crystal lattice. As a result of the potential symmetry is characterized in the symmetry of the lattice, spin orientation along certain spatial direction becomes energetically favorable [29]. The macroscopic magnetic behavior will eventually depend on the spatial direction in which it is measured. Such a phenomenon is called magnetic anisotropy.

1.3.2 Magnetic anisotropy

All materials exhibit varying degree of anisotropy due to their crystal structure, shape and surface. In the case of magnetic nanomaterials, surface anisotropy can be of important. A brief description of three major magnetic anisotropies responsible for the magnetic properties of magnetic nanomaterials is outlined here:

1. Magnetocrystalline anisotropy
2. Shape anisotropy
3. Surface anisotropy



1.3.2.1 Magnetocrystalline anisotropy

An intrinsic anisotropy of a magnetic crystal is the magnetocrystalline anisotropy [30]. Magnetocrystalline anisotropy depends on spin – orbital coupling and shows various symmetries [31]. In a crystal, orbital electrons are tightly bound to the lattice because of the crystal field, or the electric field from the surrounding sites on the lattice. Spins, by comparison, are only loosely bound to the orbits. Therefore, when a magnetic field is applied, spins are relatively free to respond while the orbital moments are pinned. Because the orbital moments are not free to respond, they are said to be quenched and act as though they were not there. Given this, the spins are then the primary source of the magnetization of a sample. The relationship between the spin, orbit and lattice contributions is shown in Fig. 1.7.

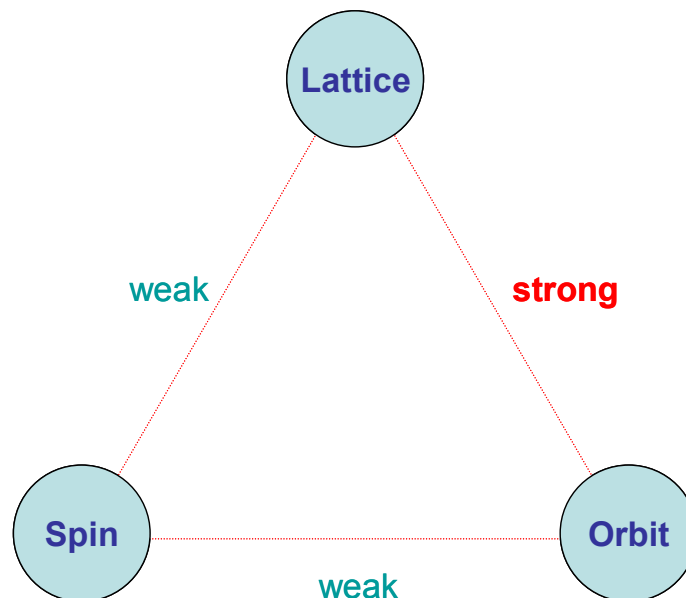


Figure 1.7 The relationships between spin, orbit and lattice coupling.



The two most common cases are uniaxial and cubic forms [32]:

(A) For uniaxial symmetry, the magnetocrystalline anisotropy constant (K_u) is:

$$K_u = K_0 + K_1 \sin^2 \theta + K_2 \sin^4 \theta + \dots$$

where K_0 , K_1 and K_2 are anisotropy constants, θ is the angle between the magnetization and the easy axis.

(B) While for cubic symmetry, the magnetocrystalline anisotropy constant (K_c) is

$$K_c = K_0 + [K_1 \sin 2\theta + K_2 \sin^4 \theta + \dots]/4 + (K_2 \sin^2 2\theta \sin^2 \varphi)/16 + \dots$$

The magnetocrystalline anisotropy is intrinsic and its magnitude determines the magnetization in response of the magnetic field. Large magnetocrystalline anisotropy energy of a magnetic material is called hard magnetic material and shows a large coercivity in hysteresis measurement. A magnetic material with small magnetocrystalline anisotropy energy is referred to soft magnetic material and has a small value of coercivity.

1.3.2.2 Shape anisotropy

Shape anisotropy is induced from magnetostatic energy and is an extrinsic property. It comes from the anisotropy of the demagnetizing field (H_D) arising from long range dipolar interaction in the particles. When a body is being magnetized, it will produce magnetic charges or poles at the surface. This surface charge distribution is another source of a magnetic field. It plays a significant role when the magnetic materials that has a high aspect ratio (length/width), such as shown in Fig. 1.8.

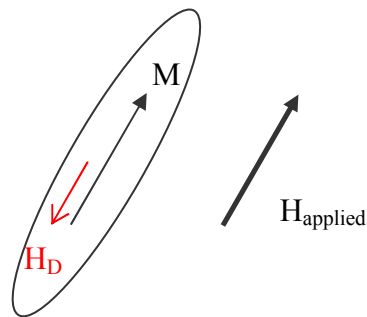


Figure 1.8 Shape anisotropy induces in prolate spheroid.

For a prolate spheroid with major axis greater than the other two and equal axes length a , the shape anisotropy constant (K_s) is

$$K_s = M_s^2 (N_a - N_c) / 2$$

where M_s is the saturation magnetization, N_a and N_c are demagnetization factors [33].

For non-spherical magnetic materials such as a long rod, the sharp anisotropy can be very predominant.



1.3.2.3 Surface anisotropy

Surface anisotropy is caused by the existence of a surface that represents a discontinuity for magnetic interactions. Such surface effects become more significant as the size of magnetic nanomaterials decrease, because the increasing numbers of atoms are on the surface layer of a particle [34]. In order to take into account surface effect, Néel first proposed the surface anisotropy. Recently theoretical studies indicated that spins at surface are dictated by the local crystal field, a lower coordination number and a broken magnetic exchange bond. Thus, surface spins are often canted and disordered [35].

Considering the surface effect which is dependent on the size and often correlated to the nanoparticle size effect, an effective anisotropy constant (K_{eff}), which includes the surface anisotropy constant, is used to describe surface effect. For a spherical particle, K_{eff} is given by

$$K_{eff} = K_u + (6/d)K_s,$$

where K_s is the surface anisotropy constant, K_u is magnetocrystalline anisotropy constant, and d is the diameter of the particle [36]. Generally, surface anisotropy leads the surface to be magnetically harder than the core of the particle [37].



1.3.3 Single domain theory and superparamagnetism (SPM)

In bulk magnetic materials, domains of magnetic order may be up to hundreds of nanometers in size. In a particle with dimensions of tens of nanometers or smaller, it is simply not large enough for multiple domains formation and a nanoparticle will exhibit magnetic behavior different to that seen on larger scales. The single domain particle will have a single large magnetic moment with thousands of Bohr magnetons [38]. Because of the large separation between particles, the exchange interaction can be neglected. The magnetic properties are determined mostly by dipole field energy, thermal energy and magnetic anisotropy energies. At finite temperatures, these particles usually exhibit superparamagnetic relaxation dependent on the particle size and temperature [39].

Superparamagnetism (SPM) of magnetic nanoparticles refers to the influence of thermal energy on the ferromagnetic properties of the particles. In the superparamagnetic size regime the moments of the nanoparticles fluctuate due to thermal energy. This fluctuation tends to randomize the moments of the nanoparticles unless a magnetic field is applied [40]. The basis of superparamagnetism can be summarized by a double potential well as shown in the following Fig. 1.9.

As seen in the schematic diagram of Fig. 1.9, the two states of magnetization of a uniaxial magnetic particle are separated by an energy barrier, $K_u V$ where K_u is the anisotropy energy density and V is the particle volume. If the thermal energy becomes comparable to the barrier height there is an increased probability of the magnetization reversing.

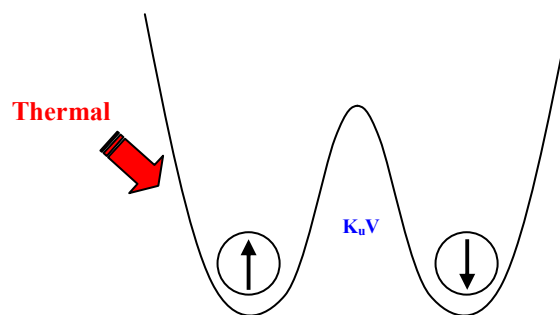


Figure 1.9 Double potential well as a model of superparamagnetism (SPM).

Superparamagnetism (SPM) is a phenomenon by which magnetic materials may exhibit a behavior similar to paramagnetism. At high enough temperature, thermal energy is sufficient to overcome the magnetic interaction between the magnetic domains, causing the atomic magnetic moments to fluctuate randomly [41]. Therefore, a material in superparamagnetic state exhibits no hysteresis and has zero coercivity. The critical size (D_c) for single domain formation has been determined by Kittle [42], which depends on spontaneous magnetization (M_s), the anisotropy constant (K), and the exchange energy density or constant (A) as given in equation:

$$D_c = 36(KA)^{\frac{1}{2}} / \mu_o M_s^2$$

The critical size (D_c) for typical magnetic materials is in the range of 10 – 100 nm. A magnetic particle smaller than the critical size prefers to be uniformly magnetized along one of its anisotropy easy axes, is accompanied by a strong enhancement in coercive field (H_c). The strength of magnetic-magnetic interaction between particles becomes so low as to be comparable to or even lower than the thermal energy. The transition from multi-domain to single domain becomes very apparent when one considers the coercivity as a function of particle size shown in Fig. 1.10:

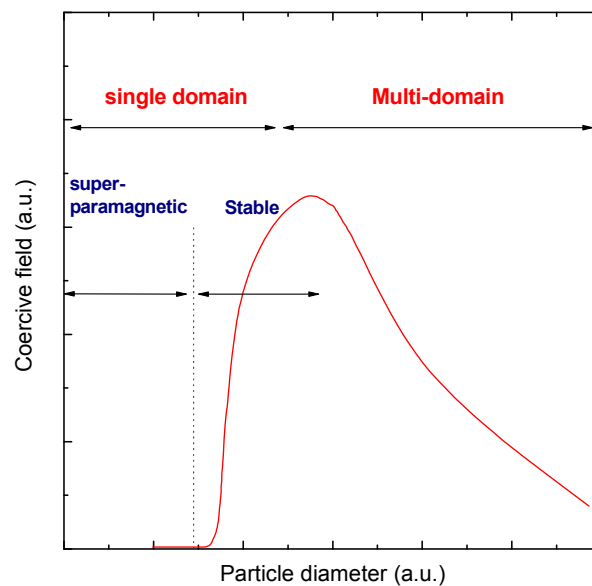


Figure 1.10 Coercive field as a function of particle size [43].

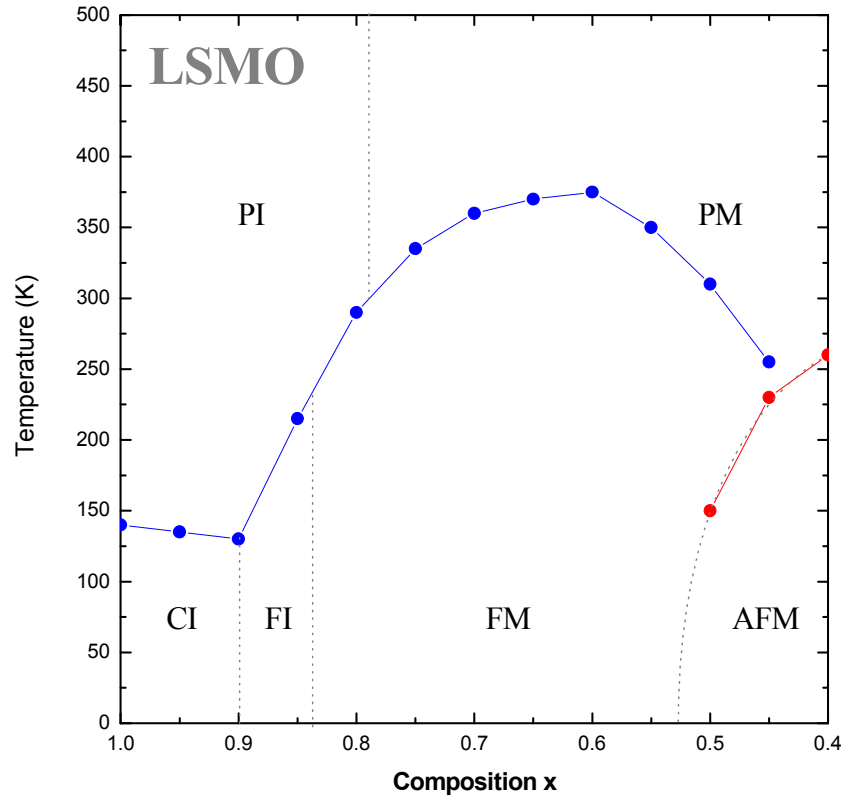
Indeed, in magnetic studies of nanoparticles the most interesting property is the H_c because of the following reasons: (1) in order to use these fine particles in a permanent magnets application, the H_c must be high (larger than few hundred Oe), and (2) the H_c is a quantity which comes quite naturally out of theoretical calculations of the hysteresis loop.



1.4 Manganite materials

Magnetic nanoparticles systems receiving the most attention are those based on iron oxides such as magnetite (Fe_3O_4) and maghemite ($\gamma\text{-Fe}_2\text{O}_4$). This is owing to their ease of preparation and oxidative stability, not to mention their biocompatibility [44]. Other systems that have been under intense general investigation are ground state transition metals of iron, cobalt and nickel [45]. Although they have quite large magnetic susceptibilities compared with the iron oxides, the naked metals readily oxidize leading to a decline in their magnetic properties. Alloys of transition metals such as FeCo, FePt, CoPt, FeCoNi etc. have also been studied [46].

Among the magnetic materials, the hole-doped manganite compounds with perovskite structure are probably best known for exhibiting colossal magnetoresistance (CMR) [47]. Amazing magnetic and electrical properties of these hole-doped manganites became a subject of numerous experimental and theoretical investigations. Lanthanum strontium manganite in a chemical formula of $\text{La}_x\text{Sr}_{1-x}\text{MnO}_3$ (LSMO) is a typical example. It belongs to the family of magnetic manganite ceramics. In Fig. 1.11, it shows the magnetic characteristics of LSMO with different compositions. It also exhibits a variety of stable phases, with unusual spin, charge, lattice, and orbital order [48]. The fascinating physics of the perovskite manganites is governed by electrons which hop among or are localized on the Mn^{3+} and Mn^{4+} ions [49]. A large number of experiments on polycrystals [50], single crystals [51] and thin films [52] have been carried out to study the physics involved and to explore possible applications of the CMR effect.



- Remarks:
- PM : paramagnetic metal
 - PI : paramagnetic insulator
 - FM : ferromagnetic metal
 - FI : ferromagnetic insulator
 - CI : spin-canted insulator
 - AFM : antiferromagnetic

Figure 1.11 Phase diagram of perovskite $\text{La}_x\text{Sr}_{1-x}\text{MnO}_3$ bulk sample [53].



The properties of manganite compounds with a $\text{Mn}^{3+}/\text{Mn}^{4+}$ mixed valence keep attracting much attention from both experimentalists and theorists. The sophisticated phase diagram with entangled insulating, metallic, ferromagnetic (FM), antiferromagnetic (AFM) and paramagnetic (PM) phases, reveals a strong coupling between the lattice, spin, and electronic degrees of freedom. The so-called double-exchange (DE) mechanism assuming the oxygen mediated electron exchange between neighboring $\text{Mn}^{3+}/\text{Mn}^{4+}$ sites is only a starting point for modeling [54]. The mobility of the conduction electrons between heterovalent $\text{Mn}^{3+}/\text{Mn}^{4+}$ pairs is greatly enhanced when the magnetic moments on adjacent Mn ions are aligned. The mixed valence also leads to the formation of small polarons, arising from $\text{Mn}^{3+}/\text{Mn}^{4+}$ valence changes and to Jahn-Teller distortions involving Mn that leads to incoherent hopping and high resistivity in the insulating phase [55]. The $\text{Mn}^{3+}\text{-O-Mn}^{4+}$ bond lengths and angles play a crucial role in determining the magnetotransport in manganites [56]. Moreover, an applied magnetic field enhances the FM order, thus reduces the spin scattering and produces a negative so-called colossal magnetoresistance (CMR) peak.



1.4.1 Perovskite structure of manganite materials

Oxide nanoparticles are more widely studied due to its characteristic physical properties and potential applications, which including electro-optic, luminescent, magneto-optic, sono-optics, ferroelectric, piezoelectric, electromagnetic absorption, photoelectric, photo or electro-chromic properties [57]. These properties are the basis of many modern electronics. Transition metal oxide such as titanates, niobates and manganite are the typical substance showing the above physical properties.

The manganese oxide with perovskite structure, known as manganites, is probably best known for exhibiting colossal magnetoresistance (CMR). Typically, the physical properties of perovskite manganites are determined by two main parameters: the doping level, $x = \text{Mn}^{4+} / (\text{Mn}^{3+} + \text{Mn}^{4+})$ and the average size of the cation A $\langle r_A \rangle$ [58].

Often, the ideal perovskite structure is distorted by the cation sizes mismatch. One of the parameters that can be used to describe the degree of distortion of the structure is the tolerance factor Γ [59], which is represented by:

$$\Gamma = \frac{(r_A + r_o)}{\sqrt{2}(r_B + r_o)}$$

where r_A is the size of cation in A-site, r_B is size of the cation in B-site and r_o is the size of oxygen ion. For ideally sized ions the tolerance factor is unity, and the structure is cubic. Typical perovskite structure is shown in Fig. 1.12.

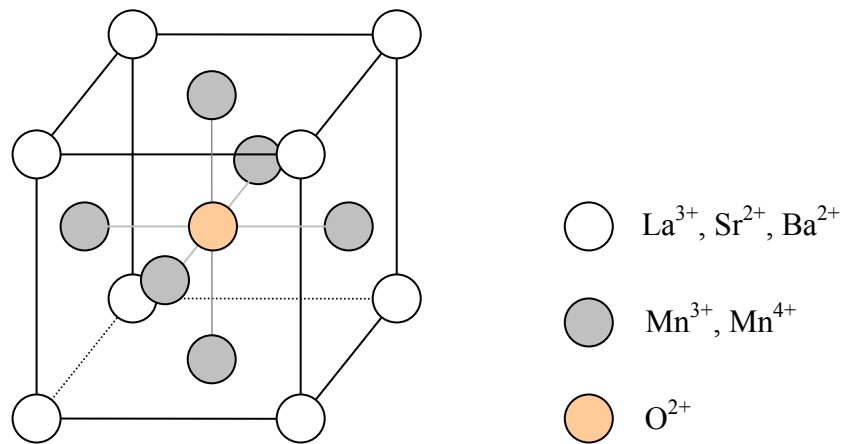


Figure 1.12 Unit cell of a typical manganite with perovskite structure.

The materials mentioned in this thesis such as LSMO and LBMO are interesting magnetic oxides with a perovskite structure. The perovskite is one of the most common structures among all complex oxides. The ideal perovskite structure, ABO_3 can be regarded as a cubic, close packed array of O^{2-} atoms and large A cations, with small B cations in the octahedral interstitial sites. Typically, A-site is an alkaline, alkaline-earth or rare-earth cation, while B-site is occupied by a transition metal cation [60]. Nevertheless, most of the metallic ions can be accommodated into the perovskite structure. From geometrical considerations, A-cations must be large in order to be able to pack efficiently with large oxygen anions. At the same time B cations must be small enough to fit into the octahedral interstice. For stoichiometry, the total charge of A and B cations must be $6+$ [61]. These requirements limit the type and amount of element that can be fitted into the structure.



1.4.2 Half-metal nature of manganite

The manganites itself have a high degree of spin polarization, and can in some cases be regarded as half-metals [62]. Half-metals are unusual ferromagnets that have electrons at the Fermi level in a single spin state, either spin up and spin down [63]. Schematic band structures for half-metallic LSMO are illustrated in the Fig. 1.13.

One of the important parameter for classifying the material is the spin polarization (P). Spin polarization is the degree by which the spin, i.e. the intrinsic angular momentum of elementary particles, is aligned to a given direction. The spin polarization is defined by the density of spin up (N_{\uparrow}) and spin down (N_{\downarrow}) at the Fermi level as follows [64]:

$$P = \frac{[N_{\uparrow}(E_F) - N_{\downarrow}(E_F)]}{[N_{\uparrow}(E_F) + N_{\downarrow}(E_F)]}$$

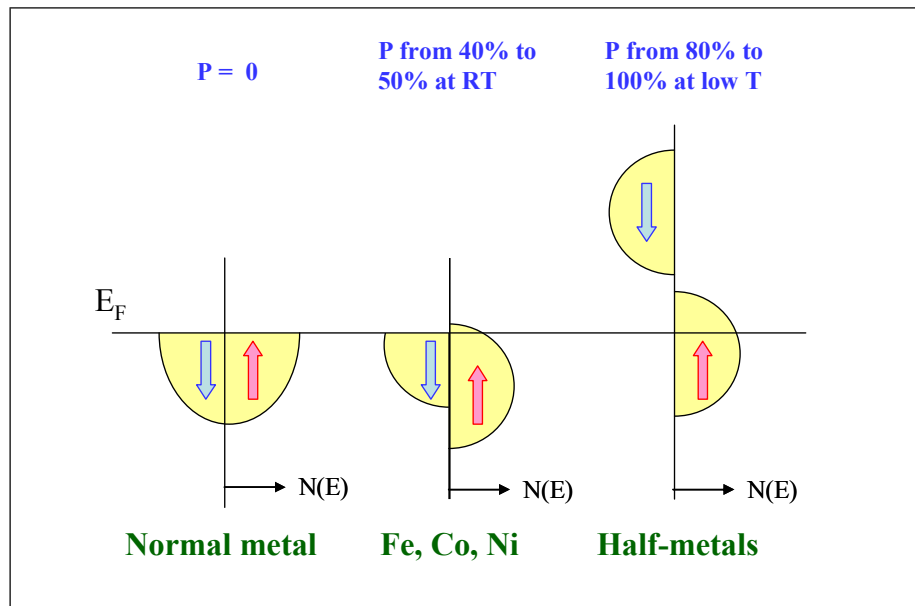


Figure 1.13 Electron band structures of different materials [65].

Since the density of states of up-spin and down-spin electrons are equal in non-magnetic materials, $P = 0$ for non-magnetic materials such as Cu and Au. For materials such as Fe, Co and Ni, P is known to be around 50%. A few compounds have been predicted to be half-metallic, such as CrO_2 , Fe_3O_4 , mixed-valence manganites, or some Heusler alloys [66]. In the particular case of manganites such as $\text{La}_{0.67}\text{Sr}_{0.33}\text{MnO}_3$ (LSMO) and $\text{La}_{0.67}\text{Ca}_{0.33}\text{MnO}_3$ (LCMO), there is a lot of controversy regarding their properties of half-metal. The half-metallic properties of materials such as LSMO are of great important for applications in spintronic. For example, the tunnel magnetoresistance junction (MTJ) of LSMO/STO/LSMO heterostructures shows magnetoresistance (MR) in excess of 1800% at 4K [67]. Indeed, the performance of spintronic device such as spin valve can be enhanced by using high spin polarized materials [68].



The half-metallic nature of the ferromagnetic phase of LSMO can be demonstrated by spin-resolved photoemission measurement. Some experiments have shown that the polarization can be up to 90 % [69]. The half-metallic property is attractive for applications, especially in spintronic devices utilizing tunneling magnetoresistance. Materials with higher polarization can dramatically enhance device performance and may be necessary for new generation of three terminal devices such as spin transistors. Such applications can be divided into two catalogs:

- (i) the CMR phenomenon of the manganite can be exploited in devices for computers, using it as a reading head to obtain information
- (ii) manganites can be made part of artificially prepared structure, such as spin valves

However, the intrinsic CMR effect in the perovskite manganites is only triggered within a narrow temperature range around the ferromagnetic transition at high magnetic fields of several T, which restrains its use for practical applications [70].



1.4.3 Nanosized manganite

The close interplay between spin, charge, orbital and lattice degrees of freedom are the source of the complex behavior found in manganites. The competing interactions/orders inherent in the manganites, such as double-exchange ferromagnetism versus super-exchange antiferromagnetism and charge-orbital order as metallic states, tend to produce the multi-critical state where external stimuli occasionally cause a dramatic phase conversion. The properties of manganite are expected to depend on material size [71]. Previous investigations on thin film manganite samples have shown that their properties depend sensitively on the film thickness, leading to surface-induced phase separation and strain-dependent metal-insulator transitions [72].

Nowadays, intensive attentions have been paid towards nano-granular perovskite manganites. Mahesh [73] has investigated the effects of particle size on electron transport and magnetic properties of $\text{La}_{0.7}\text{Ca}_{0.3}\text{MnO}_3$ (LCMO). They found that the Curie temperature (T_c) and metal-insulator transition temperature (T_p) decrease with the particle size. It is known that ferromagnetic particles with diameter smaller than a critical size (D_c) become single domain. According to Sanchez [74], the critical size for manganites is around 80 nm. Spin-glass behaviors have been observed in ultra fine LSMO and LCMO nanostructured material [75].



Indeed magnetic nanostructures can be produced in a variety of geometries, such as nanoparticles, nanowires, dots, particulate thin films, nanotubes, nano-junctions and nano-rings. Artificial nanostructuring is a way of creating completely new technologies such as spin electronics.

Although advances have been made in the preparation of nanoscale manganite in the laboratory, detailed physical investigations have not been possible due to the lack of reliable methods to prepare manganite nanocrystals with controllable chemical doping. Additionally, issues pertaining to nanoparticle size, monodispersity, biocompatibility, magnetization and stability have not been studied in detail. Practically, an efficient, economic and scalable synthesis of ultra fine magnetic particles is highly desirable for potential applications and fundamental research.

**Outline of thesis**

This thesis describes the experimental investigation of magnetic perovskite manganite nanoparticles synthesized by cationic surfactant assisted hydrothermal route. The objectives of this research can be divided into three main parts:

(1) The development of the hydrothermal system for producing high quality manganite nanoparticles such as hole-doped LSMO and LBMO. Particular attention will be paid to control the morphology and crystal structure of the nanocrystallites. This includes experimental investigation of the fundamental properties and phenomena of the preparation process in order to understand the behavior of the particles formation under different hydrothermal conditions. As a result, optimized processing parameters such as concentration of surfactant, processing temperature, concentration of mineralizer, aging temperature etc. can be identified and used to fabricate high quality manganite nanoparticle. We also aimed at exploring the possible modification of sample microstructure by varying the chemical composition and various thermal and magnetic treatments.

(2) The aim is to gain understanding of the inter-relation between their electric/magnetic characteristics and their structural properties. Comprehensive investigations of manganite based materials by structural, magnetic, magneto-transport and other complementary characterization techniques have been carried out. Attempts to correlate the physical properties of the materials with their grains size ranging from nanometer to micrometer are also presented.



(3) We seek to develop a simple method for preparing magnetic composite system such as magnetic polymer-nanocomposite and magnetic core-shell architecture. The mechanism of low-field magnetoresistance and magnetic coupling effect of these hybrid-structures are discussed.

In Chapter 2, a brief description on the fundamental mechanism of hydrothermal is presented. The advantages and disadvantages of the hydrothermal processing technique are also explicitly described. Topics on crystal growth mode from a metal-salt precursor are also reviewed. The hydrothermal system used is presented in the second half of this chapter.

The particle characterization techniques in the present studies are addressed in Chapter 3. The working principles of major characterization equipments such as X-ray Diffractometry (XRD), Transmission Electron Microscope (TEM) and Vibrating Sample Magnetometer (VSM) etc. are discussed. Techniques of SEM, magneto-transport measurement, temperature dependent resistivity measurement are also explained.

In Chapter 4, we report the fabrication and characterization of LSMO manganite nanoparticles. An emphasis is placed on the correlation between the particle morphology and the process conditions. An examination and discussion of the development of particle morphology during synthesis based on surfactant, mineralizer, processing temperature and aging process is presented. The physical properties of nanosized manganite particles are compared to those of bulk sample.



In Chapter 5, results of antiferromagnetic LMO thin shell layer with ferromagnetic LSMO core nano structure are given. Structural properties of the core-shell arrangement will be examined in detailed. The temperature dependent magnetic properties are also presented. The magnetic coupling in these systems are characterized and compared.

Chapter 6 deals with the fabrication and characterization of magnetic manganite-polymer nanocomposites. The microstructure, magnetic and magnetoresistive properties are studied also. A comparison between experimental resistivity data of the present investigation and some theoretical formulisms are also given.

Conclusions of this thesis with a summary of the important results and achievements attained in the present investigation are given in Chapter 7. In view of the successes of hydrothermal synthesis of magnetic manganite nanoparticles, as demonstrated in our work, suggestions for further studies in the future, on LSMO in particular, and on all other magnetic compound in general, are given at the end of this closing chapter.



CHAPTER 2

Nanoparticle formation and hydrothermal technique

2.1 Introduction

The term “nano”, which is derived from the Greek word “nanos” (dwarf), designates a milliardth (10^{-9}) fraction of a unit [1]. The science of nanostructures and nanomaterials manages objects in condensed matter physics on a size scale of 1 to 100 nm. Such materials can be designed to exhibit novel and significantly improvement in physical, chemical and biological properties. Recent publications in scientific literature demonstrate a fast growing interest in new method of synthesizing nanoparticles, nanocrystals and nanocomposites, driven primarily by an every increasing awareness of the unique properties and technological importance of nanostructured materials.



In short, there are several important aspects of modern nanoparticle research

[2]:

- (i) the preparation of nanoparticles,
- (ii) the manipulation and study of individual nanospheres or nanoparticles,
- (iii) the assembly of two- or three- dimensional materials and structures with controllable arrangement of nanoparticle
- (iv) fabrication of nanostructures
- (v) miniaturization of device

The synthesis of nanoparticles has been intensively studied not only for their fundamental scientific interest but also for many technological applications. Nanoparticles with controlled particle size and morphology are of key importance because the electrical, optical, and magnetic properties of these nanoparticles depend strongly on their size. In order to realize the tremendous potential of nanomaterials, the important and immediate challenges lie in exploiting new synthesis methods for regulating and assembling materials at the atomic scale.



Indeed, the physical and chemical properties of nanocrystals are greatly influenced by the synthesis route [3]. This is the reason why various approaches are being adopted to produce nanomaterials to realize the desired properties. In the past, research has been focused towards obtaining the required material along with other favorable physical properties. Synthetic control over the nanocrystals phase is therefore an additional degree of freedom for yielding new properties of the materials.

In this chapter we summarize and discuss data from open literature concerning the nanoparticle preparations. Topics on crystal growth of nanoparticles are also reviewed. The hydrothermal system used in the present studies is presented in the second half of this chapter. The advantages and disadvantages of hydrothermal are also explicitly described.



2.1.1 Top-down and bottom-up approaches

A variety of techniques have been developed to synthesize mixed-oxide ceramic materials. Some techniques have become available for both laboratory trials and industrial production. For example, multi-component ceramics have been prepared by standard solid state reaction methods, which involve mechanical mixing and high temperature calcination. Typical and successful examples such as the high temperature superconductor of $\text{YBa}_2\text{Cu}_3\text{O}_7$ (YBCO) [4] and ferroelectric $\text{Pb}_x\text{Zr}_{1-x}\text{TiO}_3$ (PZT) [5] can be produced by this method. Due to the slow diffusion of elements in the bulk material, the processing time is often long and the ceramic product suffers from non-stoichiometry.

When we consider preparing the ceramic material in nano-scale, the formation mechanism may be totally different. Generally, the synthesis of nanomaterials has been classified into “top-down” and “bottom-up” approaches [6]. In fact we may view these two approaches as different forms of microstructural engineering.

For the “top-down” approach, a typical example is the fine powder obtained by mechanical grinding of bulk materials. This approach is inherently simpler and relies either on the removal or division of bulk material. However, the prepared samples have a broad size distribution, varied particle shape and geometry and different defects. In addition the prepared particles may contain large fraction of different impurities.



In the “bottom-up” approach, atoms, molecules and even nanoparticles themselves can be used as the building blocks for the creation of complex nanostructures; the useful size of the building blocks depends on the properties to be engineered [7]. By altering the size of the building blocks, controlling their surface and internal chemistry, and then controlling their organization and assembly, it is possible to engineer properties and functionalities of the overall nanostructured solid or system. These processes are essentially highly controlled complex chemical syntheses. The implementation of this “bottom-up” approach often relies on the wet chemical reduction of metal salts or, alternatively, the controlled decomposition of metastable organometallic compounds such as metal acetate [8]. A large variety of organic compounds such as donor ligands and polymers are used to control the growth of initially formed nanoparticles and to prevent them from agglomeration. It has become one of the most common and powerful synthesis methods in this field.



2.1.2 Chemical approach of synthesis process

Different techniques have been used for production of nanoparticles: gas evaporation [9], sputtering [10], sol-gel method [11], hydrothermal [12], microemulsion [13], laser pyrolysis [14], sonochemical synthesis [15] and chemical coprecipitation [16]. Over the last few decades, chemical techniques were extensively used to synthesize nanoparticles with a proper morphology. In principle, chemical synthesis of mixed-oxide powders can promote the chemical homogeneity of the fine particles produced because the mixing of starting materials is in the solution state. The hydrothermal synthesis method has been often used in the direct preparation of crystalline ceramic oxide materials. The process has the advantage of being an environmentally friendly, one step process, with low reaction temperatures and inexpensive starting materials. However, in order to obtain pure phase materials, optimal process conditions in pH value, temperature, pressure and initial precursors need to be identified and maintained.

2.1.3 Nucleation and crystal growth

In order to appreciate the merits of the hydrothermal method, it is necessary to understand some physics of crystal growth. As mentioned before, the chemical methods have been widely used to produce nanostructured materials due to their straight forward nature and their potential for mass production of the final product. The particle size and morphology control during synthesis can be achieved by utilizing the direct competition between crystal nucleation and crystal growth processes [17].

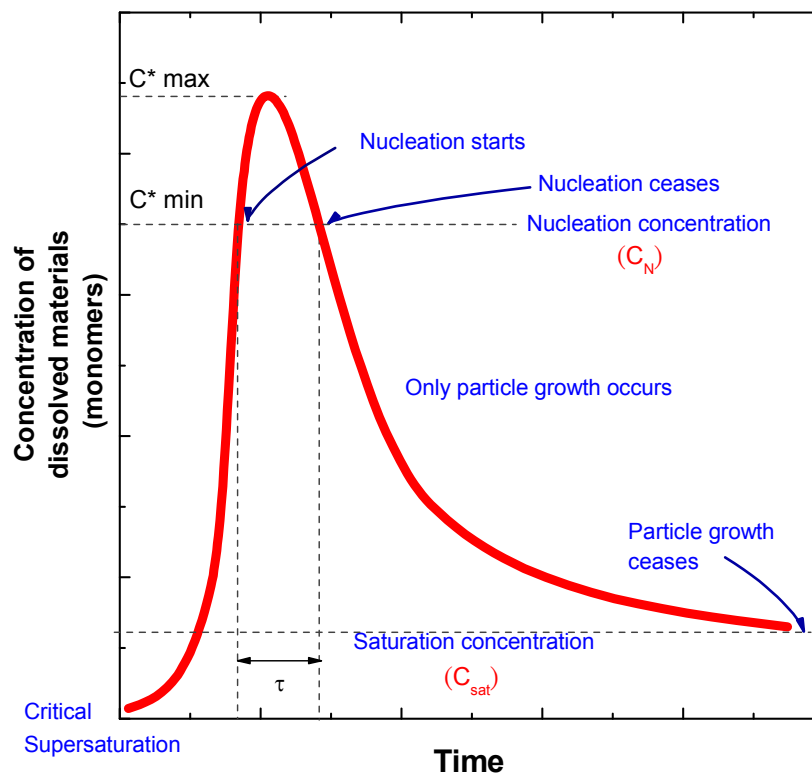


Figure 2.1 The La Mer diagram. Producing a monodisperse sol by confining the formation of nuclei to a short period (τ) and allowing growth to occur only on those nuclei already formed [18].



Generally, there are synthetic procedures for synthesizing monodispersed nanoparticles. It is well known that a short burst of nucleation followed by slow controlled growth is critical to produce monodispersed particles. The principle involved in the formation of monodispersed systems is illustrated in Fig. 2.1.

Some means must be found to produce a gradual increase in the concentration of the required material in solution. Precipitation usually does not occur immediately after the concentration reaches the saturation value because the molecules or ions have no existing crystal structure on which to build. When the concentration reaches a certain degree of supersaturation, the driving force for formation of the solid is sufficient to induce the formation of tiny nuclei which will ultimately grow into the final particles [19]. We call this critical concentration the nucleation concentration (C_N).

Formation of the nuclei reduces the solution concentration and, from that point on, the aim is to maintain the solution concentration between nucleation and the saturation concentration (C_{sat}). If that can be done there will be no new nuclei formed and all subsequent growth occurs on those formed in the first burst of nucleation [20].



2.2 Hydrothermal process

2.2.1 Background

Now we go back to our synthesis method for producing magnetic nanoparticles – hydrothermal process. The term “hydrothermal” came from the earth sciences, where it implies a regime of high temperatures and water pressure [21]. As one kind of solution-based chemical processes, the hydrothermal process has been widely used for the synthesis of a wide range of solid-state compounds such as oxides, sulfides, halides, zeolites and other microporous phases since the pioneering work from the 1960s to 1980s [22].

In recently years, this approach has been extended to the synthesis of various kinds of nanosized functional oxides and non-oxide materials with specific shape and size. Some examples such as complex oxide ceramic, magnetic materials, luminescence phosphors, electronically conducting solids, superionic conductor and microporous crystals have been successfully fabricated [23]. The main advantages of the hydrothermal process come from the extremely low crystallization temperature in this single step process.



Usually, the technique starts from the preparation of a precursor solution, in which the ions are well mixed on a molecular scale. Sequential procedures of a typical hydrothermal process are shown as flowchart in Fig. 2.2. The precursors may be amorphous or crystalline. By use of proper ratio of different precursors in the hydrothermal reaction, the desired multi-component oxide phase can be prepared.

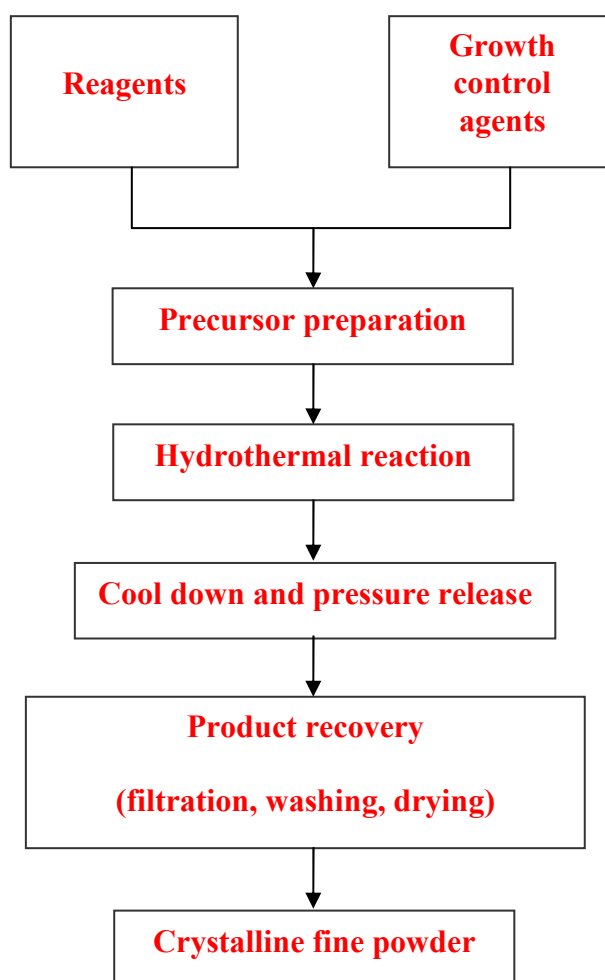


Figure 2.2 Flow chart of typical hydrothermal process.



The nature of the multi-component oxide nanoparticles, and in particular, their morphology will be critically depended on the entire synthesis route. A general comparison of the hydrothermal synthesis routes with other chemical techniques for oxide ceramic powders is listed in Table 2.1 below:

Table 2.1 Oxide powder synthesis route comparison. [24]

Synthesis method	Solid state reaction	Co-precipitation	Sol-gel	Spray/Freeze Drying	Spray Pyrolysis	Emulsion Synthesis	Hydrothermal synthesis
State of development	Commercial	Commercial	R & D	Demonstration	R & D	Demonstration	Demonstration
Compositional control	Poor	Good	Excellent	Excellent	Excellent	Excellent	Excellent
Morphology control	Poor	Moderate	Moderate	Moderate	Excellent	Excellent	Good
Powder reactivity	Poor	Good	Good	Good	Good	Good	Good
Particle size (nm)	> 1000	>10	>10	>10	>10	>100	>10
Purity (%)	<99.5	>99.5	>99.9	>99.9	>99.9	>99.9	>99.5
Agglomeration	Moderate	High	Moderate	Low	Low	Low	Low
Calcination step	Yes	Yes	Yes	Yes	No	Yes	No
Milling Step	Yes	Yes	Yes	Yes	No	Yes	No
Costs	Low – Moderate	Moderate	Moderate – high	Moderate – high	High	Moderate	Moderate

2.2.2 Mechanism of hydrothermal process

The basic mechanism for the hydrothermal formation of ceramic oxide particles is described by a “dissolution/precipitation process” and “in-situ transformation process” [25]. As shown in Fig. 2.3, the dissolution/precipitation process involves dissolving the suspended reactant particles, normally oxides and hydroxides, into solution, supersaturating the solution phase, and eventually precipitating out the product particles. The driving force in these reactions is the difference in solubility between the oxide phase and the least soluble precursor or intermediate. However, in many cases that the suspended solids have a too low solubility in aqueous solution, either mineralizer such as potassium hydroxide has to be added, or ceramic particles are formed via another in-situ transformation. In some cases, both mechanisms might occur simultaneously depending on the synthesis conditions.

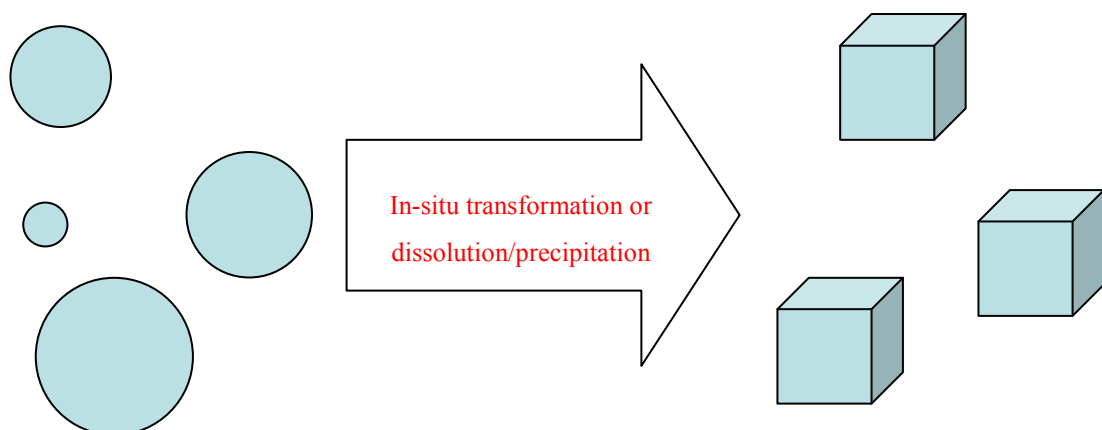


Figure 2.3 Hydrothermal dissolution/ precipitation and in-situ transformation process.



The actual hydrothermal process utilizes single or heterogeneous phase reaction in aqueous media at elevated temperature and high vapor pressure to crystallize ceramic materials directly from solutions. Different minerals in the precursor solution are acting in different role, they are shown in Table. 2.2.

Table 2.2 Role of different minerals in the precursor solution. [26]

Classification	Action	Application
1. Transfer Medium	Transfer of kinetic energy, Heat and pressure forming	Erosion, Machining, Abrasion
2. Adsorbate	Adsorption/ desorption at the surface	Dispersion, Surface Diffusion, Catalyst, Crystallization, Sintering, Ion Exchange
3. Solvent	Dissolution/ Precipitation	Synthesis, Growth, Purification, Extraction, Modification, Degradation, Etching, Corrosion
4. Reactant	Reaction	Formation, Decomposition, Corrosion



2.2.3 Role of supercritical water

Water is an important constituent of any hydrothermal system. It exhibits unique properties, especially under supercritical condition. Indeed, it is an environmentally safe material and cheaper than any other solvents. It acts as a catalyst for transformation of the desired materials by providing a homogeneous high pressure environment.

Basically, the mechanism of hydrothermal reaction follows a liquid nucleation, which depends on detail balance of the chemical equilibrium, chemical kinetics and thermodynamic properties of aqueous systems under hydrothermal conditions. However, little data in the supercritical region of water are available at present, except those for pure water and simple salt-water solutions. Thus the present studies are both challenging and interesting.

Actually, most hydrothermal crystal growth experiments are carried out under a temperature gradient in standard autoclaves. The growth of a single crystal from seed can be carried out in two ways [27]:

- (i) Recrystallization of the solid substance, including its dissolution in the liquid phase, convective mass transfer of the dissolved part of the substance to the growth zone or seed.
- (ii) Dissolution of the mixture of the nutrient components with the help of their convective mass transport into the growth zone and interaction of the dissolved components on the seed surface.



2.2.4 Apparatus for hydrothermal process

The crystal growth was performed in an apparatus consisting of a steel pressure vessel called autoclave as shown in Fig. 2.4. When selecting a suitable autoclave, the first and foremost parameter to be considered is the experimental temperature and pressure used. The corrosive resistance of the chamber in the pressure-temperature range of interest has also been decisive. In most hydrothermal experiments, the reactant used is highly corrosive and it can attack the metallic vessel, which is detrimental to obtain high purity crystals. For this reason, the autoclave requires a suitable lining for the inner wall. Polymer of Teflon (PTFE) with exceptionally good resistance to high temperatures, chemical reaction, corrosion, and stress cracking are often used [28]. Similarly for special studies pertaining to reaction kinetics, solubility and materials processing under mild hydrothermal conditions or pressure temperature conditions below 250 bars and 250 °C, Teflon is the most popularly lining material. As the temperature rises during the hydrothermal process, the Teflon expands and hermetic sealing can be obtained.

There are some precaution should be taken. For example, the Teflon liner should exactly fit inside the autoclave without leaving any gap, otherwise the liner will be deformed and the reactant will leak during the hydrothermal process. Since Teflon is a thermal insulator, the actual temperature inside the liner is difficult to measure. Moreover, the Teflon cannot be used at too high temperature since it will dissociate at beyond 300 °C [29]. The operation procedure of autoclave is simple, but the rational design of the reaction requires multidisciplinary and interdisciplinary knowledge.

Autoclave with about 11 ml in volume

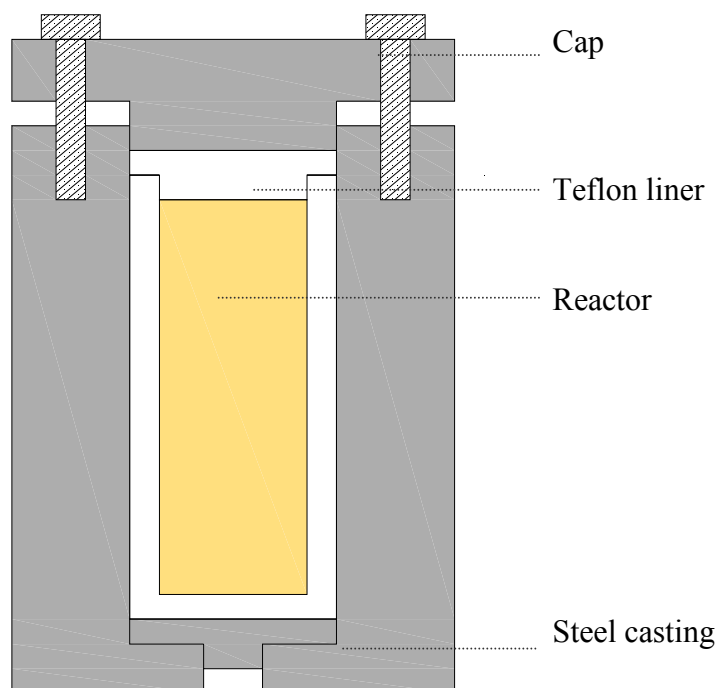


Figure 2.4 Arrangement of the apparatus for the growth of nanoparticles by a hydrothermal method.

2.2.5 Hydrothermal reaction

For a conventional hydrothermal reaction, the process involves heating the metal salts, oxides or hydroxides either as a solution or as a suspension in a liquid. Typically the temperature in a hydrothermal process falls between the boiling point of water and the critical temperature ($T_c \sim 374 \text{ }^\circ\text{C}$). The evaporating solvent generates a pressure inside the sealed vessel at this temperature; this pressure, due exclusively to the refluxing solvent, is known as “autogenous” pressure.



The temperature required for crystallization under hydrothermal conditions depends on the material. Typical reaction temperatures reported in the literature range from 150 °C to 350 °C, significantly below the temperatures needed for crystallization by calcinations. Also, the hydrothermal reaction times are often as short as 2 hours and are rarely longer than 1 – 2 days.

Actually, in the hydrothermal growth of crystals, the pressure-volume-temperature (PVT) diagram of water is very important [30]. In most hydrothermal experiments, the pressure prevailing under the working conditions is determined by the degree of filling and the temperature. When concentrated solutions are used, the critical temperature (T_c) can be several hundred degrees above that of pure water. The as-synthesized product is washed by de-ionized water to get rid of ions in the solvent and other impurities. After drying in air, fairly well dispersed ceramic nanoparticles are obtained.

Hydrothermal technique has found a niche in synthesizing electroceramic powders. It has been employed in industrial-scale production. One typical example is the preparation of aluminosilicate zeolites [31]. This synthesis offers a low temperature, direct route to oxide powders with a narrow size distribution, avoiding the high temperature calcinations step on its way. Additional merits of this technology can attribute to the low costs for instrumentation, energy and precursors. In the past years, numerous ceramic powders synthesized by hydrothermal technique have been reported.



2.3 Control of particle size and particle morphology

One of the most active trends in modern materials chemistry is the development of synthetic methods to obtain size- and shape- controlled inorganic nanocrystals. The size and shape of inorganic nanocrystals often produce novel physical and chemical properties. A reliable and practical synthesizing scheme can thus promise great technological impact.

In general, the particle size is dependent on a set of reaction parameters such as temperature, duration and precursor concentration. The longer the reaction time and the higher the reaction temperature typically results in the formation of larger particles. The size is also strongly influenced by some other parameters including the type of solvent and the characteristic of surfactants such as strong or weak binding capability and the steric hindrance. For example, a stronger binding or a bulky surfactant can retard the rate of precursor addition to the nanocrystals, leading to a smaller particle size. Finally, size-selective precipitation or size sorting has become a practical procedure and is frequently used to further narrow the size distribution of as-synthesized particles.



A variety of shapes of nanoparticles have been reported. Tubes, hexapods and platelets, all in the nanoscale, have been produced by hydrothermal synthesis [32]. By inhibiting or enhancing the growth in a specific direction an anisotropic morphology is achieved. Crystal chemistry and the presence of specific adsorbents often favor anisotropic crystal growth. For example, the perovskite BaTiO_3 have been reported that the stable crystal habit in hydrothermal reaction change from the {111} plane to the {100}, {110} and {211} planes with the addition of polymeric additives [33].

2.3.1 Approach of soft-template and hard template

There has been an extensive research on synthesis of nanosized oxide material by soft and hard template methods [34]. In a hard template method, it uses liquid crystal phases in high concentration of surfactant solution. It has been proven to be a simple and feasible method. Because the template is usually a thin membrane, this method is difficult to scale-up for large quantity production, although efforts in that direction are still in progress.

On the other hand, nano oxide material formed by the soft template method uses low concentration of surfactant. The cooperative self-assembly of surfactant with the inorganic species complexing with charged surfactant or hydrophilic nonionic surfactant moiety. An important advantage of the soft template method is that it can be scaled up to produce quantities of nanowires, especially when the synthesise process is done in chemically in solution.



2.3.2 Surfactants

“Surfactant” is a contraction of “surface active agent” [35]. The term surfactant originated by Antara Products in 1950. Surfactants are molecules which have a chemical structure that makes it particularly favorable for them to reside at interfaces. Surfactant compounds are made up of one hydrophilic part, referred to as the head group, which is covalently bonded to one hydrophobic part, generally a single or double alkyl chain also called the tail. The head group may be nonionic, ionic or Zwitterionic [36]. The alkyl chain may be a hydrocarbon, a perfluorocarbon, or a mixed hydrocarbon/perfluorocarbon group. Some common examples of surfactant are listed in Table 2.3.

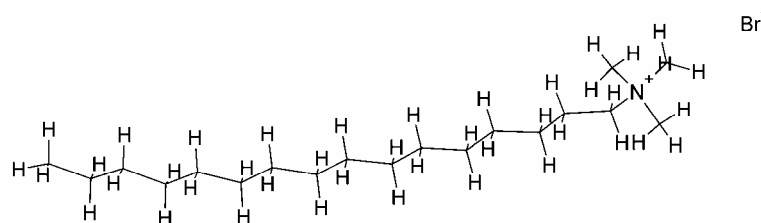
The surfactant we have applied in our particle synthesis process is hexadecyltrimethylammonium bromide (CTAB). It consists of a straight 16- carbon aliphatic chain with the quaternary ammonium group (NR_4^+) as the terminal group at one end [37]. The ionic terminal group carries a positive charge and is strongly solvated so that the long aliphatic chain is carried into solution in water. An aliphatic chain is not very soluble in water and there is strong adsorption at the water-vapor interface. As a result, they reduce the interfacial tension between oil and water by adsorbing at the liquid-liquid interface. In some chemical reactions, the CTAB also acts as a phase transfer catalyst to facilitate the migration of a particular chemical component in one phase into another phase in a heterogeneous system. The chemical component is soluble in one phase but insoluble in the other unless a phase transfer catalyst is present.

**Table 2.3 Some commonly surfactants of each type [38].**

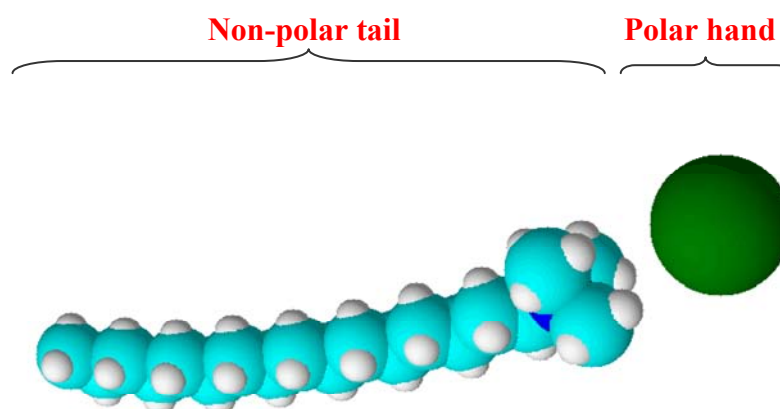
TYPE		SURFACTANT NAME	
Ionic	Anionic	Sodium dodecyl sulfate (SDS)	
		Sodium laureth sulfate (SLES)	
		Alkyl benzene sulfonate	
	Cationic	Cetyltrimethylammonium bromide (CTAB)	
		Cetylpyridinium chloride (CPC)	
		Polyethoxylated tallow amine (POEA)	
		Benzalkonium chloride (BAC)	
	Zwitterionic (amphoteric)	Dodecyl betaine	
		Dodecyl dimethylamine oxide	
		Cocamidopropyl betaine	
		Coco ampho glycinate	
Nonionic	Alkyl poly(ethylene oxide)		
	Copolymers		
	Alkyl polyglucosides		
	Fatty alcohols		

Schematic of Hexadecyltrimethylammonium bromide (CTAB)

(a) **Chemical formula**



(b) **Ball model**



(c) **Physical properties**

Chemical formula: $C_{19}H_{42}BrN$

Molecular mass: 364.48 g

Melting point: 243 °C

Typical CMC at 30 °C: 400

Figure 2.5 Schematic of cationic surface of CTAB: (a) chemical formula, (b) ball model structure and (c) some physical parameters of CTAB.



Indeed, the concentration of surfactant is a very important parameter in the reaction processes. As shown in Fig. 2.6, surfactant forms true solution at low concentration. Some molecules, however, will adhere to the wall of the containing vessel and the air/solution interface. This is because, in such way, it is possible for the two distinct parts of the molecule to find a more favorable environment. As the concentration rises, molecules begin to interact laterally with one another through the mutual attraction of their hydrocarbon chains. The surfaces then become covered with a monolayer of surfactant.

At about this stage, further dissolution in the normal way ceases and a new process becomes possible. The molecules in the solution begin to aggregate into what are called micelles, containing some 50 - 100 individuals. This process is a cooperative one and it occurs at a fairly precisely defined concentration, called the critical micellar concentration (CMC) which can be identified from the fact that the equilibrium and transport properties of the solution are affected by the aggregation process [40].

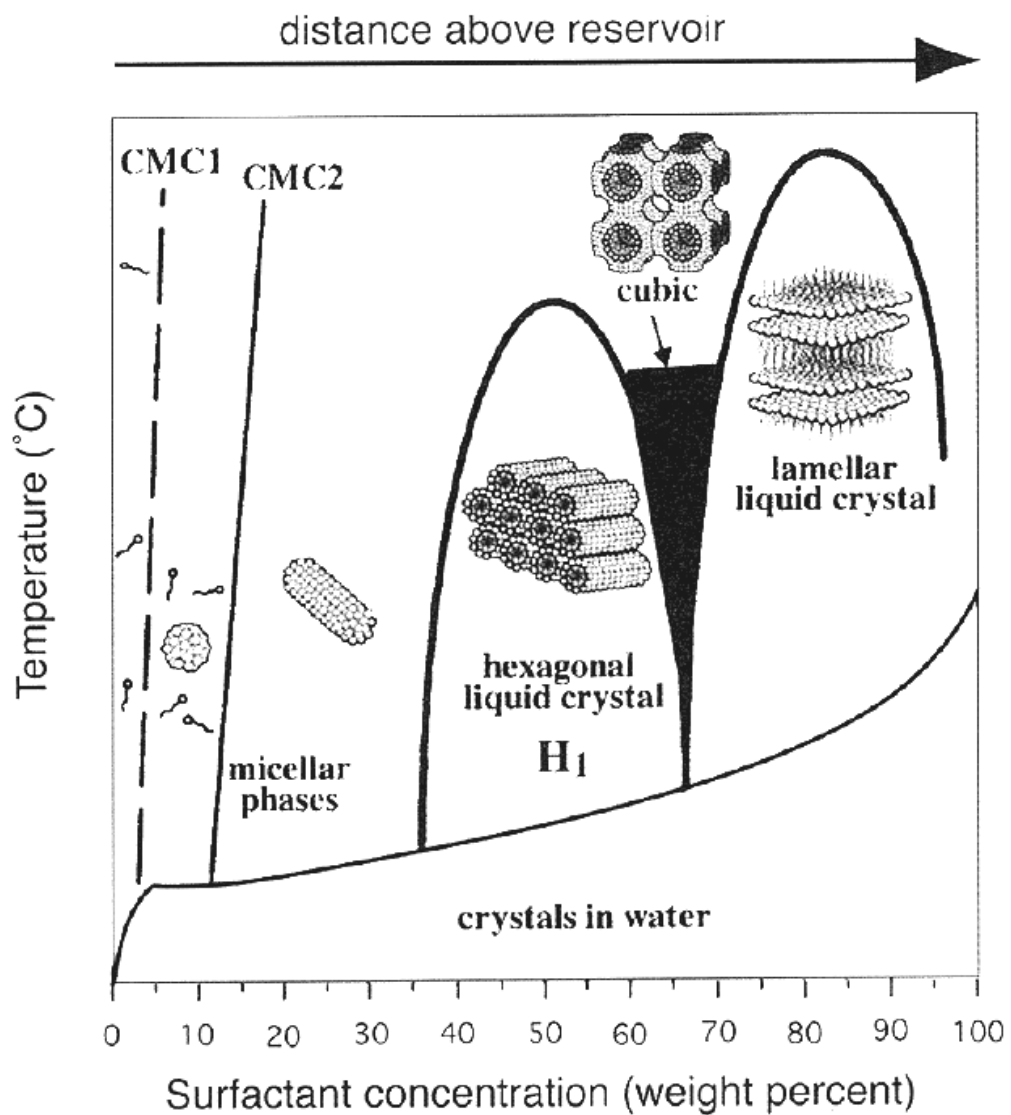


Figure 2.6 Schematic phase diagram for CTAB in water [39].



2.3.3 Particle aggregation

Aggregation, a common yet complex phenomenon for small particles, is problematic in the production and usage of many chemical and pharmaceutical products. Aggregation makes it especially difficult to explore the properties and applications of nanostructured materials. For magnetic material, agglomeration can increase the magnetic interaction between particles, and therefore may influence the magnetic properties or even leads to lost of superparamagnetism (SPM).

In many synthetic processes for making particles, especially surfactant-free chemical reactions, aggregation occurs immediately as the particles are generated. In conventional studies, aggregation has been simply ascribed to the direct mutual attraction between particles via Van der Waals force or chemical bonding. Strategies for preventing aggregation mainly come from conventional colloid science in which particles are coated with foreign capping agents and/or the surface charges that are tailored to separate them through electrostatic repulsions.



2.4 Reported work in hydrothermal derived manganite

In the search of a novel route for the synthesis of manganite nanoparticles, hydrothermal method has also been proposed in some reports. Bernard et al. have prepared $\text{La}_{1-x}\text{Sr}_x\text{MnO}_3$ (LSMO) by using nitrate and acetate precursors in hydrothermal conditions, adding citric acid as complexing agent, and adjusting the pH value with ammonia or tetramethyl ammonium hydroxide [41]. Zhu et al. have prepared $\text{La}_{0.5}\text{Sr}_{0.5}\text{MnO}_3$ and $\text{La}_{0.5}\text{Ba}_{0.5}\text{MnO}_3$ nanowires by adding potassium permanganate in alkaline medium to the metallic precursor [42]. Urban et al. have improved the synthetic conditions of the last procedure and were able to prepare $\text{La}_{0.5}\text{Ba}_{0.5}\text{MnO}_3$ single crystalline nanocubes [43]. However, the quality of the nanoparticles in terms of size control, size distribution is not good. In many cases, a very broad size distribution and even the loss of size control were reported. Also, in some reports, the preparation of crystalline manganite from acetate precursors in hydrothermal media requires further high temperature annealing [44]. Otherwise, the reaction may not be completed and the stoichiometric ratio of the final product altered.



2.5 Experimental details of our hydrothermal process

In order to establish the correlation of size and shape of the nanoparticles with magnetic properties, it is useful to develop a general synthetic method that can control the crystal growth process. In the current hydrothermal process used in this work the crystal growth control is accomplished via selection of raw chemicals, mineralizer, processing temperature, surfactant, etc. The most commonly used precursors for the hydrothermal synthesis of LSMO (manganite) powders are nitrate, chlorides, acetates, and hydroxide. To synthesize the mixed valence manganites with adjustable doping levels, one important control parameter is the average oxidation state of the Mn ion. The procedure of control over the Mn oxidation state is achieved by changing the ratio of two Mn precursors, namely potassium permanganate (KMnO_4) and manganese chloride (MnCl_2). These two precursors contain Mn ions with distinct initial oxidation states.

The use of mineralizer for LSMO powder synthesis is necessary too as it increases the solubility of the starting precursors. The most common mineralizer is the strong alkalis hydroxide such as KOH or NaOH. During the reaction process, hydroxides not only act as solvent but also as a reactant for decreasing the reaction temperature.



CHAPTER 3

Characterization method

3.1 Introduction

Nanoparticle is one of the most studied nano-systems in modern materials science. To characterize nanoparticles, important features such as the degree of aggregation, particle size and morphology need to be measured quantitatively. It has been realized that the properties of the nanoparticles are extremely sensitive to their structural features. One of the main tasks in materials science is to establish the inter-relationships between structure and properties. Therefore, in this chapter we review methods used in this project for characterizing the physical properties of nanostructures.

In this study, we have used several techniques to yield information on the physical properties of nanomaterials. The crystalline structures of the particles were examined by X-ray diffractometer (XRD) using CuK_α radiation. Surface morphology of the particles was studied by scanning electron microscopy (SEM). The transmission electron microscope (TEM) was used to visualize the internal structure by bright and dark field imaging. Orientation and identification of the crystalline structure were performed by selected area electron diffractions (SAD). The elemental and chemical information can be simultaneously derived from data of the energy dispersive x-ray spectroscopy.



For magnetic nanoparticles, the magnetization measurement was achieved using a vibrating sample magnetometer (VSM). The temperature dependent resistivity measurements of the LSMO samples were carried out in temperatures down to 20 K, which was obtained by a close cycle helium cryostat. Two-probe and four-probe techniques were used for the DC electrical transport measurement. For the magnetotransport evaluation, an electromagnet providing a maximum magnetic field of 0.5 T was used. The details of the experimental setups and the characterization techniques are discussed in the following sections.



3.2 Structural characterization

The particle size is one of the most important parameters that govern the characteristic properties of the nanomaterials. Investigations of materials with nano-sized grains show that there is a critical crystallite size below which a dramatic change value of magnetic properties occurs. Physical parameters such as the size of magnetic domains, the mean-free-path of the electron, the de-Broglie wavelength, the coherence length in superconductors, the wavelength of elastic oscillations, and the size of the excitons in semiconductors have all been used to evaluate the threshold transition to the nanocrystalline state [1].

The most widely used and direct method to determine sub-micrometer sized particles is the electron microscopy. It is a powerful method that also yields easily the morphological and structural information of the nanoparticles. By use of advanced electron microscopy, structural characteristics of specimens under investigation may be examined down to the atomic scale in resolution.

3.2.1 Scanning electron microscopy (SEM)

Scanning electron microscopy (SEM) is one of the most versatile and well proven analytical techniques. Compared to conventional microscopy, an electron microscope offers many advantages including high magnification, large depth of focus, better resolution, and simplicity for sample preparation and observation.

In SEM, a focused high-energy electrons beam is scanned over the surface of the specimen. The electrons are accelerated over a voltage of a few 100 eV to 30 keV. The electron beam interacts with the material giving out a variety of signals. As shown in Fig. 3.1, they include secondary electrons, backscattered electrons, characteristic x-ray etc., each of which may be used to characterize a material with respect to some specific properties.

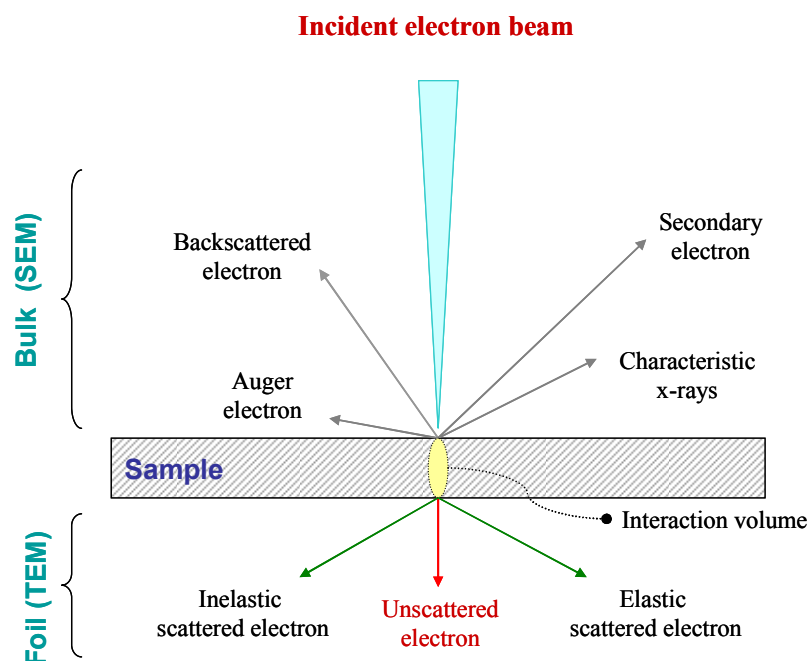


Figure 3.1 Schematic diagram of different electron interactions.



During the SEM examination, high-energy incident electrons interact with some loosely bound conduction band electrons in the sample. The amount of energy given to these secondary electrons as a result of the interactions is small. So only those secondary electrons that are produced within a very short distance from the surface can escape from the sample. This means that this detection mode provides high-resolution topographical images, making this the most widely used of the SEM modes.

On the other hand, when an electron from the beam encounters a nucleus in the sample, the Coulombic attraction results in the deflection of the electron. This is known as the Rutherford elastic scattering. A few of these electrons will be completely backscattered, re-emerging from the incident surface of the sample. Since the scattering angle is strongly dependent on the atomic number of the nucleus involved, the primary electrons arriving at a given detector position can be used to yield images containing both the topological and compositional information.

Indeed, not all specimens can be analyzed by SEM directly. One typical example is insulating material. For specimen with poor electrical conductivity, a negative charge builds up gradually from bombardment by the high-energy electron beam. An abnormal contrast and splitting of the image result from the uneven distribution of the negative charge on the sample. A simple solution is to coat a very thin (generally 10 - 20 nm thick) gold layer on the sample's surface. It can enhance the emission of secondary and backscattered electron, reduction of thermal damages as well as the elimination of charging effect.



In this study, a JEOL JSM-6335F field emission scanning electron microscope was used to obtain the images of nano-scale particles.

3.2.2 Energy Dispersive X-ray analysis (EDX)

In addition to secondary electrons imaging, energy dispersive X-ray (EDX) is a widely used tool for chemical analysis. A beam of electron can interact with an atom by ionization of the inner shell electron. The resultant vacancy is filled by an outer shell electron, which can release its energy either through an Auger electron or by emitting an X-ray. The characteristic X-rays emitted from the sample serve as fingerprints and give elemental information of the samples including semi-quantitative analysis, quantitative analysis, line profiling and spatial distribution of elements.



3.2.3 Transmission electron microscopy (TEM)

The transmission electron microscope (TEM) is a powerful instrument for structural, chemical and magnetic characterization at the nanoscale. Imaging, electron diffraction and microanalytical information can be combined with complementary micromagnetic information to provide a more thorough understanding of magnetic behavior. Routine low resolution TEM studies provide images of nanoparticle ensembles, thus permitting a statistical description of the size and shape of the nanoparticle in a given sample. TEM images are two dimensional, therefore, three dimensional structures of the nanoparticles should be considered with the contrast or fringes. On the other hand, high resolution TEM (HRTEM) observations provide understanding the crystallinity of the particles, especially for small nanoparticles. Even for very small nanoparticles, lattice fringes can be found in the images.

3.2.3.1 General operation of TEM

The design of a TEM is analogous to that of an optical microscope. In TEM, energetic electron (> 100 keV) are used instead of photons. Focusing and imaging is done by electromagnetic lenses instead of glass lenses. The ray path of the electrons is schematically represented in Fig. 3.2. The electron beam passes an electron-transparent sample and a magnified image is formed using a set of electromagnetic lenses. This image is projected onto a florescent screen, a CCD camera, or a photographic plate.

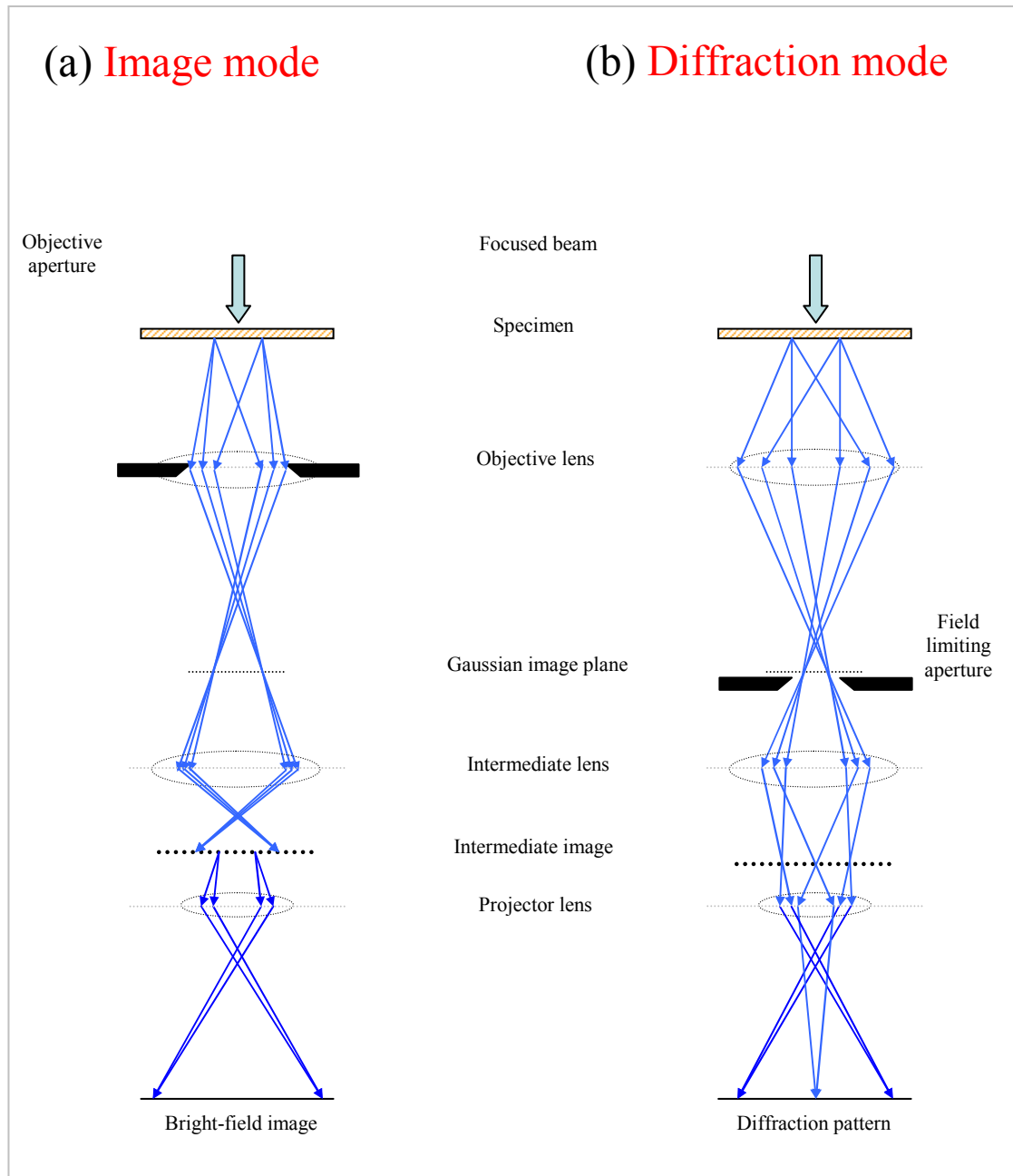


Figure 3.2 Schematic diagram of the ray path of electron beam in TEM (a) image mode and (b) diffraction mode [2].



A conventional electron microscope image, the so-called bright-field image, can be obtained by using the transmitted beam at the center of a diffraction pattern, i.e., by inserting a small aperture (objective aperture) that excludes the other spots at the back focal plane. In this observation mode, the contrast of the image is attributed to the change of the amplitude of the transmitted beam due to absorption and scattering in the specimen. Therefore, the image is called absorption-diffraction contrast or amplitude contrast. This conventional transmission electron microscope image clearly shows the internal structures of the specimens. For example, it reveals the presence of defects like twins, dislocations and subcrystals [3]. Selection of the diffracted beam produces a dark-field image. This observation mode is especially useful to see the distribution of a specific phase or structure in a specimen.

3.2.3.2 Sample preparation

For the preparation of TEM samples of nanoparticles, amorphous carbon coated TEM grids were used. Thinner carbon coats are required for high resolution observation. The preparation procedure is quite simple. A drop of the homogeneous dispersion of the particles is put onto a carbon coated copper microgrids. Since the excess stabilizing reagent will act as contamination which could fade the TEM image contrast of the nanoparticles, it should be removed before the sample preparation.



3.2.3.3 High resolution TEM

A high resolution electron microscope (HRTEM) image, by which the atomic arrangements can be observed, is formed by using more than two beams. Since the contrast in a HRTEM image arise from the difference of phase between the transmitted beam and diffracted beams, the image is called the phase contrast.

When the image conditions are properly optimized, phase contrast images can be directly interpreted in terms of the projected crystal potential. The resolution of a TEM is basically defined by the following equation:

$$d = 0.65K^{\frac{1}{4}}\lambda^{\frac{3}{4}}$$

where λ and K are the wavelength of incident electrons and the spherical aberration of the objective lens, respectively [5]. In some modern TEMs, the image resolution is usually better than 0.2 nm. Hence TEM becomes a powerful tool to probe the crystalline properties of the nanoparticles directly.



3.2.3.4 Electron diffraction

A crystal may be described in terms of periodic arrangement of scattering elements. The crystal lattice expresses this periodicity in three dimensions. Elastic scattering elements caused diffraction effects. A geometric formulation of the diffraction condition is given by the Bragg equation:

$$2d \sin \theta = n\lambda$$

which describes the diffraction of electrons of wavelength by a set of lattice planes of spacing d , n being the reflection order. As shown in Fig. 3.2(b), the electron beams transmitted through a specimen form a diffraction pattern at the back focal plane of the objective lens. This produces distinct spotty patterns for single crystals, or ring patterns for polycrystalline objects. Comparing with X-ray diffraction, the radius of the Edward sphere is much larger in electron diffraction due to the very small wavelength of electron beams. This allows the diffraction experiment to verify more of the two dimensional distribution of reciprocal lattice points.

Moreover, a single crystal grain or particle may be selected for the electron diffraction experiments in a TEM. This means that the diffraction experiments can be performed on single crystals of nanometer size, whereas other diffraction techniques would be limited to studying the diffraction from a polycrystalline or powder sample.



3.2.3.5 Drawback of TEM

Although TEM is superior in image magnification, there are a number of drawbacks to the TEM technique. For example, many materials require extensive sample preparation to produce a sample thin enough to be electron transparent, which makes the TEM analysis a relatively time consuming process with a low throughput of samples. The structure of the sample may also be changed during the preparation process. There is potential that the sample may be damaged by the electron beam, particularly in the case of organic materials. With TEM observations, only metal cores can be observed, but organic coating layers usually cannot show enough contrast in the images. Also the field of view is relatively small, raising the possibility that the region analyzed may not reflect the characteristics of the whole sample.

3.2.3.6 General information of our TEM system

In our project, we used a JEOL JEM-2010 electron microscope to observe the crystal structure and morphology of particles. This transmission electron microscope operated at 200 kV accelerating voltage provides a maximum resolution of 0.24 nm.



3.2.4 X-ray diffractometry (XRD)

The texture can strongly affect the properties and behavior of materials. Tensor properties of the material such as magnetic susceptibility, magneto-anisotropy, elastic coefficients and electro-optic coefficient are especially dependent on texture. Indeed, bulk materials, thin film and even the powder used in electronic applications have been fabricated to carry preferred crystallographic orientation or texture. Various analytical methods have been used to fulfill the requirement for the accurate crystallographic characterization. Among them, X-ray diffraction (XRD) is a well-developed and widely used technique [6].

X-ray diffraction (XRD) is a standard structural characterization technique for bulk materials. A straight forward application of XRD technique is the determination of the crystalline phase of a material. This is done by comparing the diffraction spectrum peak positions and intensities with those in database. This is especially informative for nanocrystalline materials that may contain several crystallographic phases, including highly disordered or amorphous phases, and for nanocrystals whose crystal structure may be different from that of the corresponding bulk due to surface effects.

Conventional XRD methods (Bragg Brentano, grazing incidence) can provide information regarding crystallinity, phase identification and qualitative assessment of planar orientation. We have two XRD instruments: “Philips X’pert system” and “Bruker D8 Advance”. Both machines use K_{α} radiation of Cu at wavelength of 0.154 nm. The K_{β} emission was filtered out by Ni filter. The crystalline structures of our sample were characterized by XRD operating in four-circle mode.

3.2.4.1 General mechanism of X-ray diffraction

Now considering an X-ray beam incident on a single crystal, a small fraction of the incident beam will be scattered by the regular arrangement of atoms. To simplify the case, the crystal was treated as a pair of parallel planes, P1 and P2, separated by an interplanar spacing d .

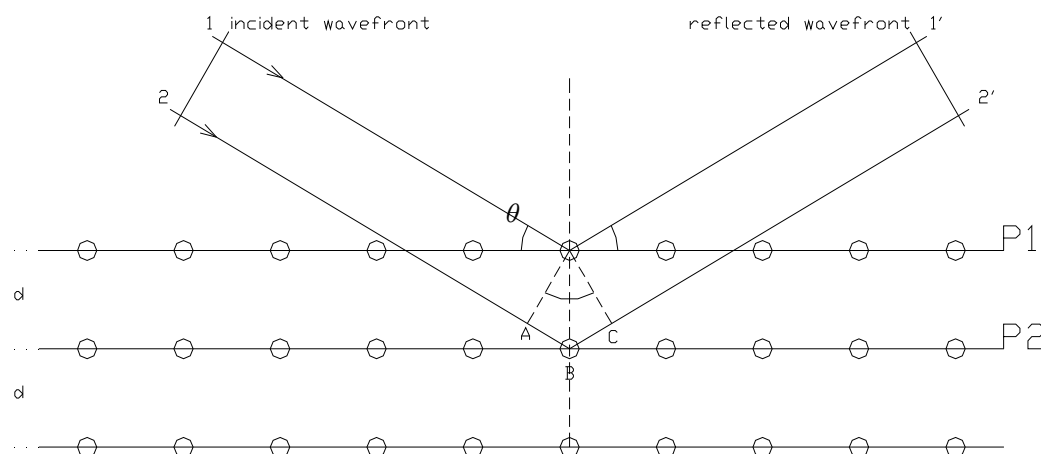


Figure 3.3 Bragg diffraction of X-rays from successive planes of atoms. Constructive interference occurs for ABC equal to an integral number of wavelengths.



In Fig. 3.3, the two parallel incident rays 1 and 2 make an angle θ with these planes. A reflected beam of maximum intensity will result if the waves represented by 1' and 2' are in phase. The path difference between 1 to 1' and 2 to 2' (AB+BC) must be an integral number of wavelengths λ to satisfy the constructive interference. Then we can express this relationship mathematically in Bragg's law:

$$AB + BC = 2 d \sin \theta = n \lambda, \quad \text{where } n = 1, 2, 3 \dots$$

The interplanar spacing d , the distance between adjacent planes in the set $(h k l)$ of a material with a cubic structure and lattice parameter a , can be obtained from the equation:

$$\frac{1}{d^2} = \frac{h^2 + k^2 + l^2}{a^2}$$

Combined these two equations, we can obtain:

$$\frac{1}{d^2} = \frac{h^2 + k^2 + l^2}{a^2} = \frac{4 \sin^2 \theta}{n^2 \lambda^2}$$

Hence, it can yield:

$$2d \sin \theta = \lambda$$

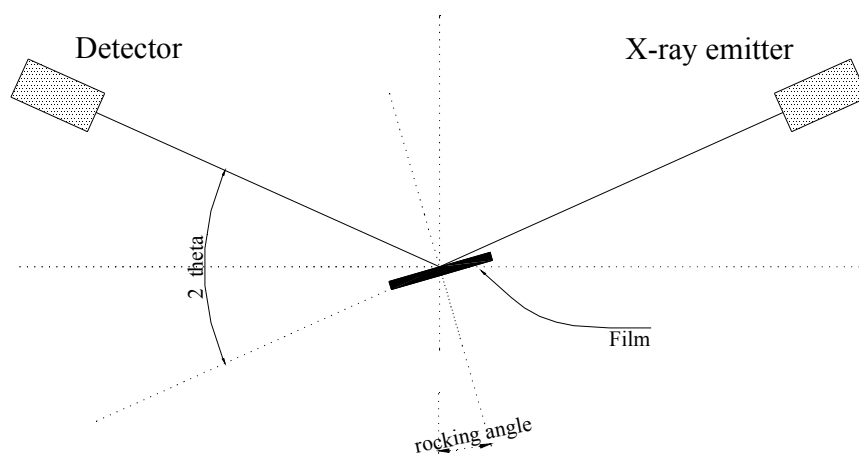


Figure 3.4 The schematic diagram shows the operation of XRD ω -scan.

Each crystalline material has a unique x-ray diffraction pattern. The number of observed peaks is related to the symmetry of the unit cell (higher symmetry generally means fewer peaks). The locations of observed peaks are related to the repeating distances between planes of atoms in the structure. And finally, the intensities of the peaks are related to what kinds of atoms are in the repeating planes. The scattering intensities for X-rays are directly related to the number of electrons in the atom. Hence, light atoms scatter X-rays weakly, while heavy atoms scatter X-rays more effectively. These three features of a diffraction pattern: the number of peaks, the positions of the peaks, and the intensities of the peaks, define a unique, fingerprint X-ray powder pattern for every crystalline material.



X-ray powder diffraction is a powerful tool for characterizing the products of a solid state synthesis reaction. At the simplest level, diffraction patterns can be analyzed for phase identification, it can determine what crystalline substances present in a given sample. More quantitatively, the peak positions can be used to refine the lattice parameters for a given unit cell. Unit cells in three-dimensional repeating structures have different shapes based upon the symmetry of the structure. In all cases, the unit cells are parallelepipeds, but the different shapes arise depending on restrictions placed on the lengths of the three edges (a , b , and c) and the values of the three angles (α , β , and γ) as showed in Fig 3.5. The seven different unit cell shapes or the so-called seven crystal systems that result from these restrictions are listed below in Table 3.1.

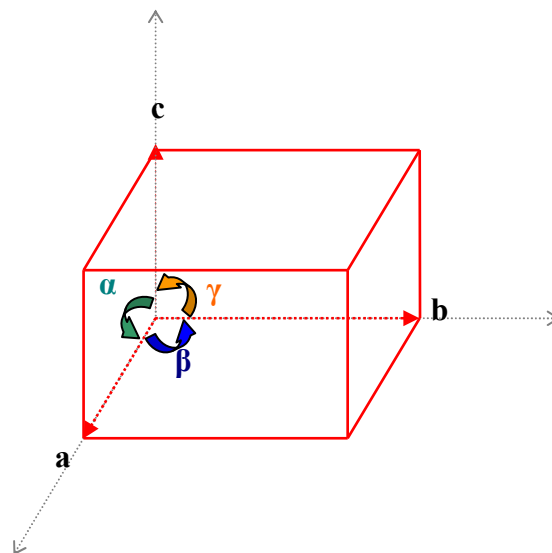


Figure 3.5 Sub unit of crystal lattice.



Table 3.1 The seven crystal systems and the restrictions placed on the lattice parameters of the unit cell [7].

CRYSTAL SYSTEM	LATTICE PARAMETER RESTRICTIONS	INTERPLANAR SPACING
Cubic	$a = b = c$ $\alpha = \beta = \gamma = 90^\circ$	$d_{hkl} = \frac{a_o}{(h^2 + k^2 + l^2)^{1/2}}$
Tetragonal	$a = b \neq c$ $\alpha = \beta = \gamma = 90^\circ$	$\frac{1}{d_{hkl}^2} = \frac{h^2 + k^2}{a^2} + \frac{l^2}{c^2}$
Orthorhombic	$a \neq b \neq c$ $\alpha = \beta = \gamma = 90^\circ$	$\frac{1}{d_{hkl}^2} = \frac{h^2}{a^2} + \frac{k^2}{b^2} + \frac{l^2}{c^2}$
Monoclinic	$a \neq b \neq c$ $\alpha = \gamma = 90^\circ; \beta \neq 90^\circ$	$\frac{1}{d_{hkl}^2} = \frac{1}{\sin^2 \beta} \left(\frac{h^2}{a^2} + \frac{k^2 \sin^2 \beta}{b^2} + \frac{l^2}{c^2} - \frac{2hl \cos \beta}{ac} \right)$
Triclinic	$a \neq b \neq c$ $\alpha \neq \gamma \neq \beta \neq 90^\circ$	$\frac{1}{d_{hkl}^2} = \frac{a^2 b^2 c^2}{V^2} \left[\frac{h^2 \sin^2 \alpha}{a^2} + \frac{k^2 \sin^2 \beta}{b^2} + \frac{l^2 \sin^2 \gamma}{c^2} + \frac{2hk}{ab} (\cos \alpha \cos \beta - \cos \gamma) + \frac{2kl}{bc} (\cos \beta \cos \gamma - \cos \alpha) + \frac{2lh}{ac} (\cos \gamma \cos \alpha - \cos \beta) \right]$
Hexagonal	$a = b \neq c$ $\alpha = \beta = 90^\circ; \gamma = 120^\circ$	$\frac{1}{d_{hkl}^2} = \frac{4}{3} \left(\frac{h^2 + hk + k^2}{a^2} \right) + \frac{l^2}{c^2}$
Trigonal / Rhombohedral	$a = b \neq c$ $\alpha = \beta = 90^\circ; \gamma = 120^\circ$	$\frac{1}{d_{hkl}^2} = \frac{(h^2 + k^2 + l^2) \sin^2 \alpha + 2(hk + kl + hl)(\cos^2 \alpha - \cos \alpha)}{a^2(1 - 3 \cos^2 \alpha + 2 \cos^3 \alpha)}$



3.2.4.2 Determination of particle size from X-ray powder diffraction

One of the more frequent applications of XRD analysis is to determine the crystalline size and lattice strain in nanocrystalline materials. The peak broadening in X-ray powder diffraction patterns for nanomaterials is the results of the finite size effect. For a finite size nanocrystal, the number of x-ray radiation reflected from successive lattice planes that add up to produce constructive or destructive interference becomes finite and therefore they can reinforce or cancel out completely. Additionally, some other factors such as inhomogeneous lattice strains, variations in the lattice constants from one crystallite to another and structural faults can also yield the broadening of the diffraction peaks.

According to the Scherrer equation [8], which is normally applied to powder specimens, the crystalline dimension D is estimated by:

$$D = \frac{K\lambda}{\beta \cos \theta_B}$$

where K represents the correction factor to account for the shape of specimen, β the broadening of the diffraction line measured at full width at half maximum in radians, λ represents the wavelength of x-ray source and θ_B the Bragg angle of the reflection that is analyzed. This Scherrer equation can be used to obtain a rough estimate of the nanocrystalline size when there are no inhomogeneous strains and when the size distribution is narrow.



3.3 Magnetic characterization

3.3.1 Vibrating sample magnetometer

The vibrating sample magnetometer (VSM) is a basic instrument for characterizing magnetic materials. It can determine the magnetic properties in a variety of studies of the structure of paramagnetic, ferromagnetic, antiferromagnetic, diamagnetic materials and even the superparamagnetic in nano-materials. VSM have been used in such area as the study of amorphous and magnetic bubble domain materials, dilute magnetic semiconductors, inter-metallic components, etc.

VSMs are widely used since magnetic properties can be measured for a wide range of sample sizes and configurations such as powders, solids, single crystals, thin films and liquids. Also, they are particularly well suited to allow measurements at both low and high temperatures. In the development of rare-earth magnetic materials the VSM has been used extensively to measure saturation magnetization, coercive field, remanence, anisotropy fields and also temperature dependent parameters of interest, for example Curie temperatures (T_c).

Contemporary commercial VSMs feature virtually automated operation via data acquisition/ control and analysis software that runs on personal computer, making the VSM accessible to even non-specialists. This has dramatically increased the utility of this measurement technique in a broad range of measurement applications.

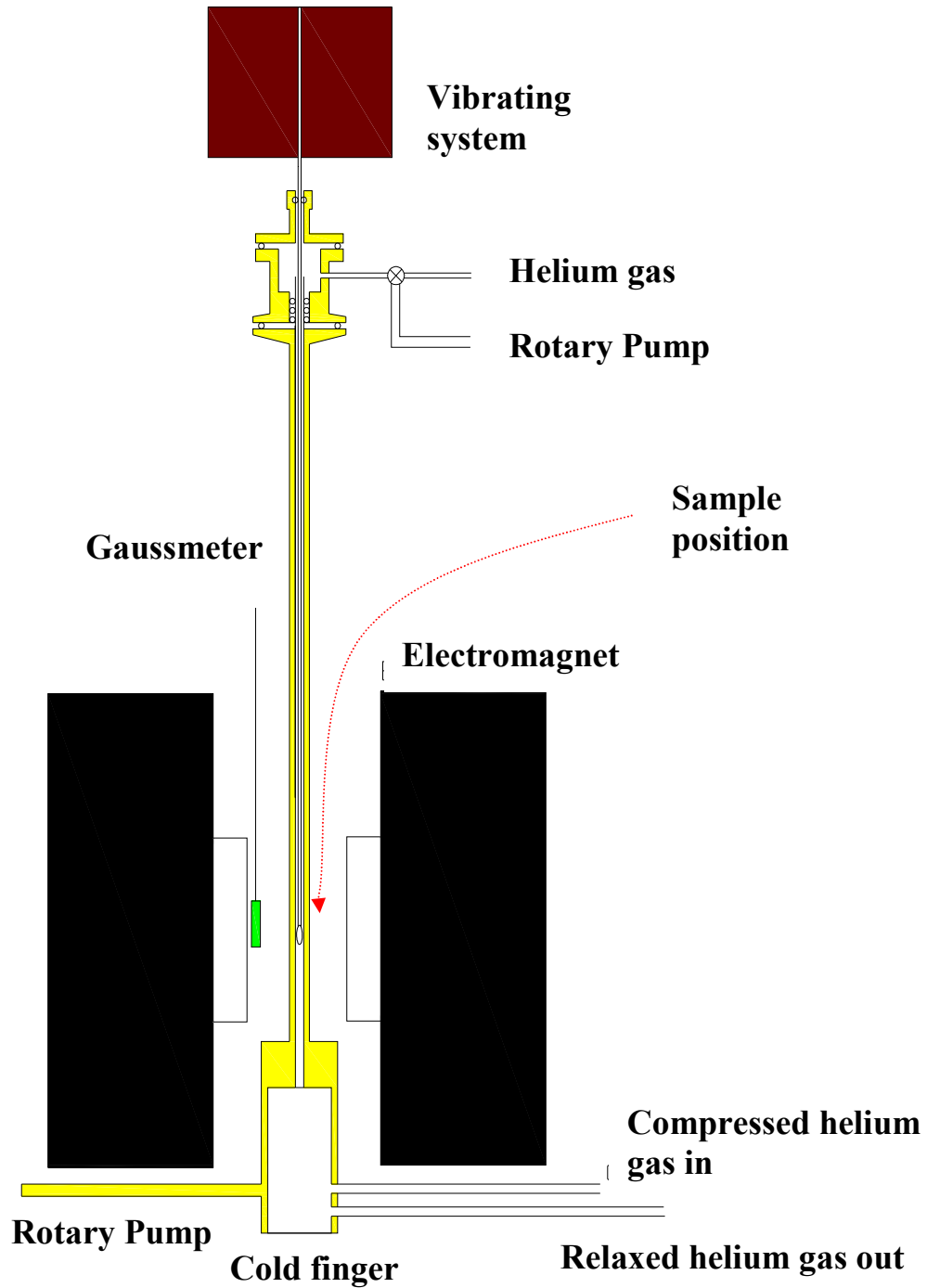


Figure 3.6 Schematic diagram of vibrating sample magnetometer (VSM) set-up.



3.3.2 Operation of a vibrating sample magnetometer (VSM)

The VSM shown schematically in the Fig. 3.6 employs an electromagnet which provides a horizontal magnetizing field (DC), a vibrating mechanism to vibrate the sample vertically in the magnetic field, and detection coils which generate the signal voltage due to the changing flux emanating from the vibrating sample. The output measurement displays the magnetic moment (m) as a function of the field (H).

VSM is able to take measurement at different temperatures. This is perhaps the most important and essential option. Special research application may require a liquid He cryostat and controller option in order to extend the temperature range down to the vicinity of 4 K. The handmade sample holders used with our VSM system are made of Teflon (PTFE). It offers good physical and mechanical properties, chemical resistance and near zero moisture absorption. The diamagnetic features of this material enjoy a negligible magnetic contribution in the magnetization measurement. Before the measurement, all sample holders are cleaned to remove any contaminants that may affect the background signal. Typically we use the ultrasonic etching in acidic solution and acetone, respectively.

In this research, the magnetic measurements are carried out on a LDJ 9500-vibrating sample magnetometer (VSM). The temperature ranges from 8 K to 325 K for temperature dependent magnetic studies. The magnetic field covers range of ± 6 kOe in the field dependent measurements. Some specifications of our VSM system are listed in Table 3.2



3.3.3 Magnetic hysteresis loop

In the case of a typical ferromagnetic material the hysteresis loop as shown in Fig. 3.7, it gives the relation between the magnetization (M) and the applied field (H). The parameters extracted from the hysteresis loop that are most often used to characterize the magnetic properties of magnetic media include: saturation magnetization (M_s), remanence (M_r), coercive field (H_c), susceptibility (χ) and Curie temperature (T_c).

The formal definition of the coercive field (H_c) is the field required to reduce the magnetization process. It is a complicated parameter for magnetic films and is related to reversal mechanisms, microstructure, sample shape, dimensions of the crystallites, nature of the boundaries, and also the surface and interfacial properties.

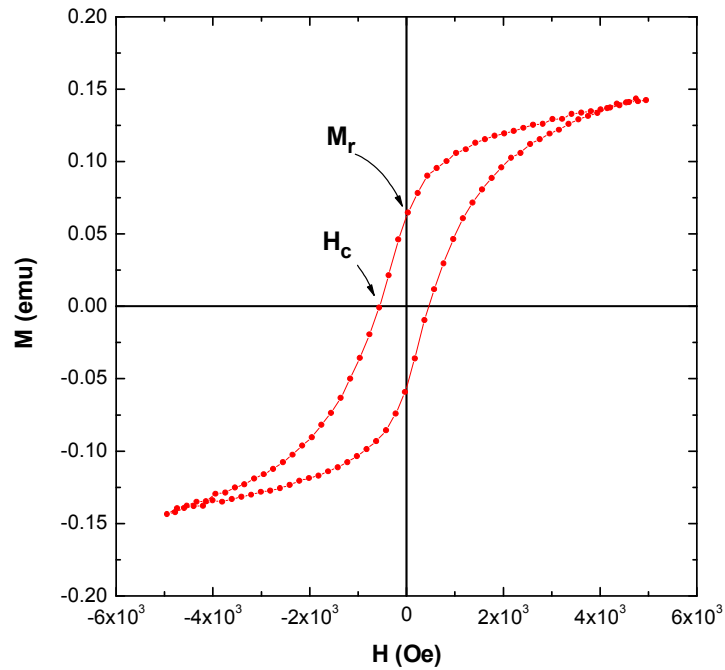


Figure 3.7 Typical hysteresis loop of ferromagnetic materials.

Table 3.2 Specification of vibration sample magnetometer (VSM).

Instrument Model: LDJ 9500
Electromagnet: uniform field strength up to: ± 10 kOe (1 T)
Magnetic moments in the range of 0.01 emu to 100 emu
Vibrating frequency: 85 Hz
Time constant setting: 0.3 s
Cryostat with temperature controller: (Lakeshore)
(Temperature range can provided: 8 K to 325 K)

3.3.4 Technique of magnetization measurement

In this section we focus on the discussion of experimental technique used for characterizing the magnetic nanoparticles and nanocomposites.

Zero-field cooled (ZFC) / Field-cooled curve (FC)

Zero field cooled (ZFC) experiments provide a means of investigating the effects of the various magnetic interactions [9]. For small magnetic particles, the curve of temperature dependence of magnetization has a typical shape as shown in Fig. 3.8.

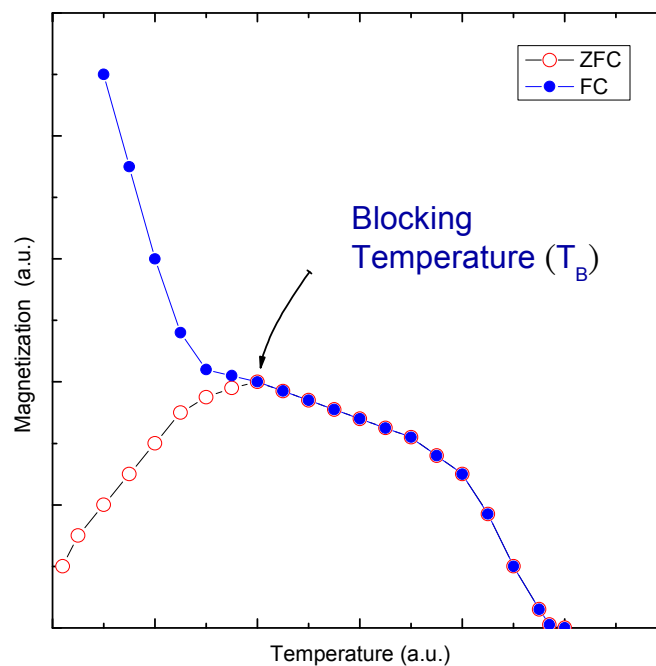


Figure 3.8 Typical ZFC and FC curve for magnetic nanoparticles with blocking temperature (T_B).



As the particles cool in zero applied magnetic fields, they tend to be magnetized along preferred crystal directions in the lattice, thus minimizing the magneto-crystalline energy. Since the orientation of each crystallite varies, the net moment of the system will be zero. Even when a small external field is applied, the moments will remain locked into the preferred crystal directions in the low temperature portion of the ZFC curve. As the temperature increases, more thermal energy is available to disturb the system. Therefore, more moments will align with the external field direction in order to minimize the Zeeman energy term. In other words, thermal vibration is providing the activation energy required for the Zeeman interaction. Eventually, the net moment of the system reaches a maximum where the greatest population of moments has aligned with the external field. The peak temperature is called the blocking temperature (T_B), which is dependent on the particle size. As temperature rises above T_B , thermal energy become strong enough to overcome the Zeeman interaction and then results of randomize the moments.

A field cooled (FC) measurement is proceed in a similar manner to zero-field cooled (ZFC) except that the constant applied field in both cooling and heating process. The net moment is usually measured while heating. However, the FC curve will diverge from the ZFC curve at a point near the blocking temperature as shown in Fig. 3.8. This divergence occurs because the spins from each particle will tend to align with the easy axis that is closest to the applied field direction, and remain frozen in that direction at low temperature.



The divergence of magnetization below T_B in the ZFC-FC curve is attributed to the existence of magnetic anisotropy barriers [10]. The derivation of the magnetization decay plot, $f(T)$ represents the distribution of anisotropy energy barriers:

$$f(T) = \frac{d}{dT} \left(\frac{M_{ZFC}}{M_{FC}} \right)$$

where M_{ZFC} denotes only the contribution of nanoparticles, the energy barriers of which are overcome by the thermal energy at the measurement, while M_{FC} represents the contribution from all nanoparticles.

For superparamagnetic particles, T_B can be determined from the following relation [11]:

$$T_B = K V / 25 k_B$$

where K denotes the magnetic anisotropy constant, k_B is the Boltzmann constant and V is the particle volume. Below the blocking temperature (T_B) the free magnetic moment $\mu = M_s V$ is blocked by the anisotropy, where M_s is the saturation magnetization. Above the blocking temperature (T_B), kT is large enough to offset magnetic interaction and the system appears to possess the superparamagnetic properties.

3.4 Electrical transport measurement

3.4.1 Temperature dependent resistivity measurement

The resistivity of magnetic manganite sample varies by several orders of magnitude over the temperature range from 20 K to 350 K. The measurement was taken by placing two to four electrodes (two-point probe method and four-point probe method) on the surface of the test sample. Potential difference was applied between the two electrodes and the resulting current was measured. In order to obtain an accurate value of resistivity, the samples were modified by a well defined active area as shown in Fig.3.9. The electrical lead was done by quick dry sliver paste.

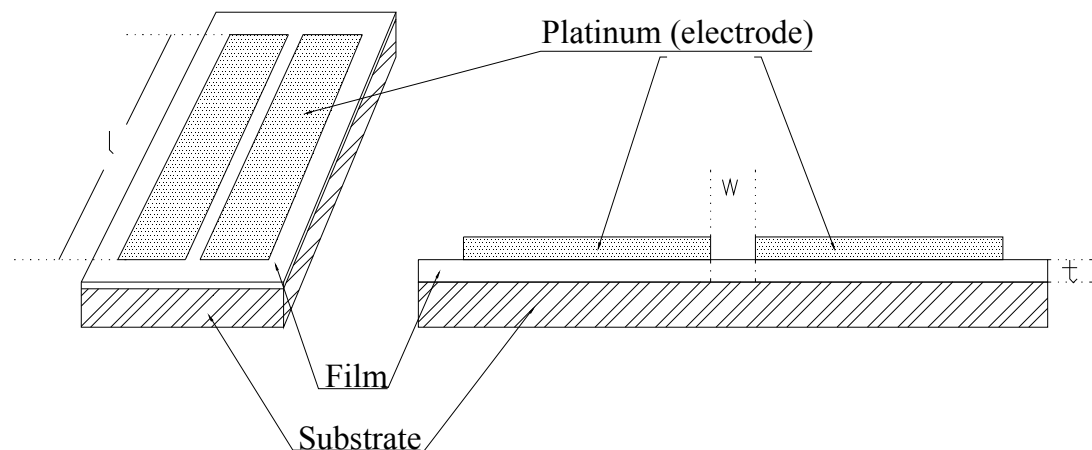


Figure 3.9 Sketch of the sample for DC conduction measurement.



3.4.2 Two-point probe method

The samples were mounted on a cold finger in a compressed helium cryostat. After cooling down the sample to 20 K, the sample temperature was programmed with a digital temperature controller. Resistance versus temperature data was taken on warming the sample to 350 K over a 5 hours period by an automated data acquisition system. The data was taken in steps of 0.5 °C. The measured resistance (R) is converted to resistivity (ρ) by knowing the sample dimension involved. The value of resistivity (ρ) in unit of Ω cm, was calculated by the relation:

$$\rho = \frac{Rlt}{w},$$

where l , t and w are as defined in Fig. 3.9.

A stable test environment is essential when making accurate resistivity measurements of a semiconductor. For example, humidity, temperature fluctuation and electromagnetic induction (EMI) can make the results erroneous. Some materials are excellent light detectors too. Consequently, the sample must be kept clean and free of contamination, and tested in a dark environment.



3.4.3 Four-point against two-point

Electrical transport measurement for sample in cryogenic environment is a big challenge [12]. When a current flowing through the wire leading to the sample, a large spurious voltage will be generated. In the two-point method as shown in Fig 3.10 (a), only one pair of electrodes were used. The I-V relationship is given by:

$$V = (I - \varepsilon)(R_{sample} + 2R_{contact} + 2R_{lead}) - \varepsilon(2r_{lead})$$

where I is the transport current supplied by the current source, ε is the current through the voltmeter, and the various resistance are define in Fig. 3.10 (a).

Usually, the resistance of the voltmeter is much larger than any of the other resistances in the circuit and thus $\varepsilon \ll I$, for which case the equations reduces to

$$V \approx I(R_{sample} + 2R_{contact} + 2R_{lead})$$

Thus, the voltage detected at the voltmeter is not only that from the sample resistance R_{sample} , but artificially enhanced by voltages across the contact resistances $R_{contact}$ and across the long instrumentation leads R_{lead} .



To avoid having these spurious voltages affecting the voltmeter reading, a separate pair of twisted leads were used to connect across the voltmeter, down the test probe, and attached directly to the central section of the sample. This so called four-point arrangement is show in Fig 3.10 (b).

In four-point probe case, the voltage measured by the voltmeter is given by

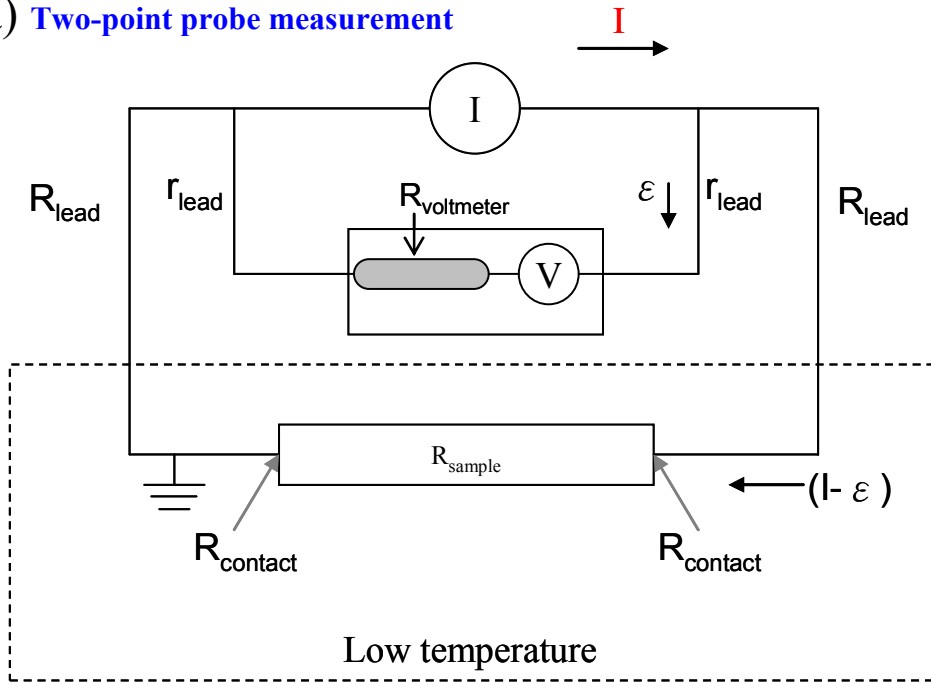
$$V = (I - \varepsilon)(R_{sample}) - \varepsilon(2r_{contact} + 2r_{lead})$$

where I , ε , and various resistance are defined by Fig 3.10 (b). Again, because $R_{voltmeter}$ is typically much larger than any of the other resistances in the circuit, $\varepsilon \ll I$ and the equation reduces to V

$$V \approx IR_{sample}$$

Electrical resistance contributed by the lead contacts can be eliminated completely. For this reason, almost without exception, a four-point probe method was used in electrical transport measurements for the sample with small resistance.

(a) Two-point probe measurement



(b) Four-point probe measurement

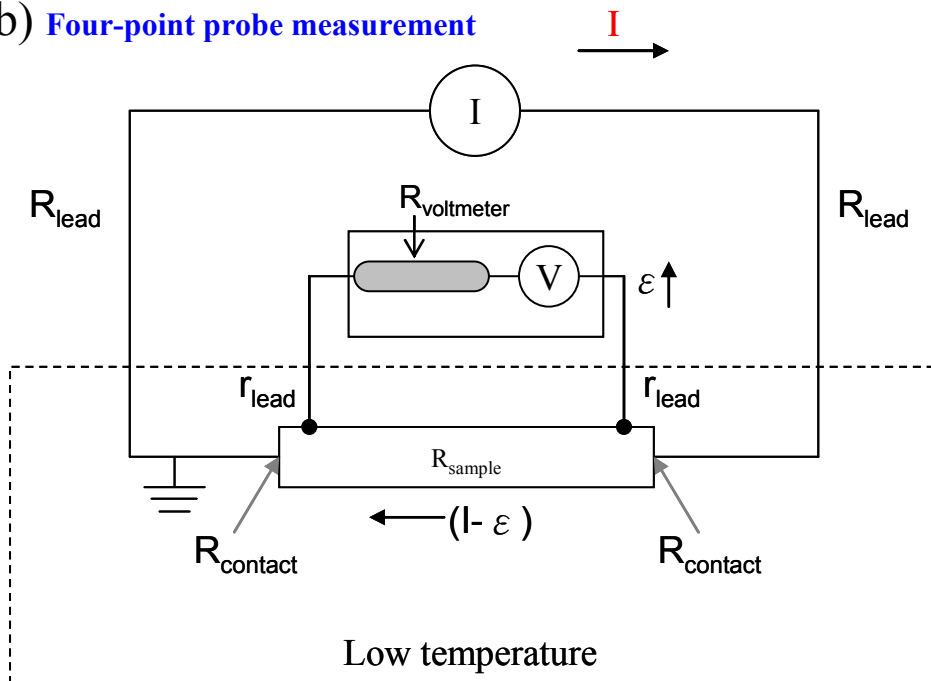


Figure 3.10 (a) Two point probe method and (b) Four point probe method for measuring transport properties.



CHAPTER 4

Synthesis of magnetic manganite nanoparticles

4.1 Introduction

Magnetic properties of materials have been investigated extensively for both fundamental interest and technology applications. As the size of magnetic material shrinks into nanoscale regime, each magnetic nanocrystal becomes a single magnetic domain because of the unfavorable energy compensation to form multiple domains. The magnetic behavior begins to exhibit the unique superparamagnetic (SPM) character as a consequence of the magnetic anisotropy energy that separates the two distinct stable states being comparable to the thermal energy. Moreover, some new phenomena such as high field irreversibility, high saturation field, extra anisotropy contributions or shifted loops after field cooling etc. that arisen from finite size and surface effects, dominate the magnetic behavior of individual nanoparticles.

Many different types of nanostructured magnetic materials are also of great interest for applications. For example, a sample may consist of granular or polycrystalline magnetic thin films, multilayer, complicated structures such as exchange-biased magnetic tunnel junctions or magnetic tunneling transistor, etc. Indeed magnetic nanomaterials and structures represent an unexploited area that offers numerous useful possibilities.



The preparation of the nano-structured materials represents one of the most important challenges in materials research. Techniques for determination of the particle size and shape, the size distribution, the surface chemistry of the particles and consequently the magnetic properties are some of the major concerns. Ferromagnetic materials such as Fe_3O_4 , $\text{SrFe}_{12}\text{O}_{19}$, FeC and some alloys like $\text{Nd}_2\text{Fe}_{14}\text{B}$, have irregular particle shape when obtained by grinding bulk materials, but have a spherical shape when prepared by wet chemistry, plasma atomization or from the aerosol and gas phase condensation [1]. Also, spherical particles obtained in solution can be amorphous or crystalline according to disorder or ordered aggregation, respectively. Many studies on nanoparticles have focused on the synthesis of uniform spherical forms and the control of their particle sizes [2]. Recently, the shape control of nanoparticles is also being recognized as a very important issue in the nanoparticles synthesis. In particular, anisotropic magnetic nanoparticles are exhibiting many interesting magnetic properties. The preparation method also determines, to a great extent, the degree of structural defects or impurities in the particles. The distribution of such defects within the particle significantly affects the magnetic behavior.

Among the various magnetic materials, mixed valence manganites are very attractive. Doping the parent compound with divalent alkaline earth cation such as Ca^{2+} , Ba^{2+} and Sr^{2+} will evoke the conversion of a proportional number of Mn^{3+} to Mn^{4+} [3]. The ground state of these compounds is ferromagnetic. At close to the Curie temperature (T_c), the doped manganites undergo a metal-insulator (IM) transition. The mixed valences of Mn ions play a major role in the double exchange



(DE) mechanism. It is believed that the DE interaction between Mn^{4+} and Mn^{3+} ion pairs is responsible for the metallic and ferromagnetic properties in these manganese oxides. The most interesting thing is that these compounds show colossal magnetoresistance (CMR) at near the metal-insulator transition. This unusual phenomenon has led to many useful technological development and applications. Over the past decades, magnetoresistive manganites have been extensively studied in bulk or in thin film forms.

However, the requirement of a large applied magnetic field to induce large magnetoresistance limits the practical applicability of these manganese perovskite. To achieve a low field magnetoresistance (LFMR), different extrinsic properties need to be explored. One of them is the reduction of grain size. In granular manganites, the low field magnetoresistance is enhanced. This is attributed to tunneling between neighboring grains through the boundaries.

Basically, fine grain of ferromagnetic manganite exhibits a low field negative magnetoresistance (LFMR) which increases with decreasing temperature and particle size [4]. The LFMR is clearly related to the alignment of the ferromagnetic domains in the typical field range 0 – 0.1 T. The relative MR can reach 50 % at low temperature have been reported [5]. This phenomenon, which differs from the intrinsic CMR, is reminiscent of the giant magnetoresistance (GMR) of granular alloys of ferromagnetic and noble metals.



In the polycrystalline sample the contribution to resistivity originates from two regions: grain and the grain boundary. Since the grain boundary is more chaotic than the core, the total resistivity in a polycrystalline sample therefore, always exceeds to that of the grain. Moreover, the energy level of the Mn ions at the surface is different from those deep inside the grain. Thus the electrons near the surface are likely to be localized. In general, the interfaces between grains are insulating. Hence, a sample with small grain size and large number of boundaries is of a ferromagnetic/insulating/ferromagnetic tunneling junction structure which can be described by the spin-polarized tunneling (SPT) model.

$\text{La}_{2/3}\text{Sr}_{1/3}\text{MnO}_3$ is one of the manganese oxide compounds that have received the most attention [6]. This material has a high Curie temperature (T_c) of 370 K [7]. It exhibits optimal metal-insulator phase transitions at this composition. Furthermore it also displays large magnetoresistance associated with the first order phase transition into ferromagnetic conducting state from paramagnetic insulating one at near Curie temperature (T_c). Additionally, using a photoemission technique, a 90 % spin polarization has been reported in thin film of $\text{La}_{0.7}\text{Sr}_{0.3}\text{MnO}_3$ [8]. Over the past decades, they have been extensively studied in bulk or in thin film forms. In-depth examinations on issues pertaining to the transition temperature and material composition have been reported.

Research on nanocrystallites of manganites is currently of great interest. Indeed, perovskite manganites powders can be prepared by a variety of methods, including the hydrothermal method, which utilizes aqueous solvents under pressure



and at temperatures above the normal boiling point of water in order to speed up the reaction. According to Jeroen [9], the manganite powder can be hydrothermally produced as pure phase polycrystalline in single step from solutions of metal salts at temperature of 240 °C. The basic mechanism for the hydrothermal formation of ceramic oxide particles involves dissolution/precipitation. As the precursors (such as hydroxides) of constituent oxides are heated, their solubility increases. Eventually, a sufficient concentration of the components exists in solution to initiate formation of the more stable oxide phase. The driving force in these reactions is the difference in solubility of the oxide phase from the least soluble precursor or intermediate.

Generally, the unique properties of nanocrystals are known to be closely related to their size, phase and shape. Therefore it would be very meaningful to prepare these materials with controllable characteristics. During the last decades, many researchers have devoted themselves to developing efficient synthetic routes to produce well-defined nanocrystals. Some experimental results found the growth parameters such as surface energy, growth rate, pH value, surfactant, reaction temperature and pressure are critical in determining the behavior of the ultimate nanocrystals [10].

In this chapter, we focus on the preparation of hole-doped manganite particles with composition $\text{La}_{0.67}\text{Sr}_{0.33}\text{MnO}_3$ by hydrothermal method. Our results clearly demonstrate the importance of controlling the particle size and the structure of the magnetic nanoparticles in order to produce the desired magnetic response. The effect of some processing parameters on the size and morphology of manganite



nanoparticles was investigated systematically. Finally, we try to apply the same preparation procedures and characterization technique to study other manganite systems. For example we wish to tune the composition of $\text{La}_x\text{Sr}_{1-x}\text{MnO}_3$ (LSMO) with $0.5 \leq x \leq 0.7$. We also want to replace Sr- with Ba- dopant to form $\text{La}_{0.67}\text{Ba}_{0.33}\text{MnO}_3$ (LBMO).



4.2 Experimental

4.2.1 Chemistry of hydrothermal synthesis of LSMO nanoparticles

According to Jeffrey et. al. [11], one important control parameter in the hydrothermal synthesis of mixed valence manganites with adjustable doping levels is the average oxidation state of the manganese ion. In order to make the desired manganite, the control over the oxidation state of Mn is achieved by changing the ratio of two Mn-precursors, KMnO_4 and MnCl_2 , which contain Mn ions with distinct different initial oxidation states. The details of the raw chemicals used in our particles synthesis, are shown in Table 4.1.

When we just consider the reaction between the two manganese compounds, the redox reaction can be written as follows:

A manganese (II) solution and manganese (VII) solution are mixed. Brown solid MnO_2 precipitates as manganese (IV). In this reaction manganese (IV) acts as oxidation agent for manganese (II):



The overall chemical reaction of the two manganese precursors can be written as:

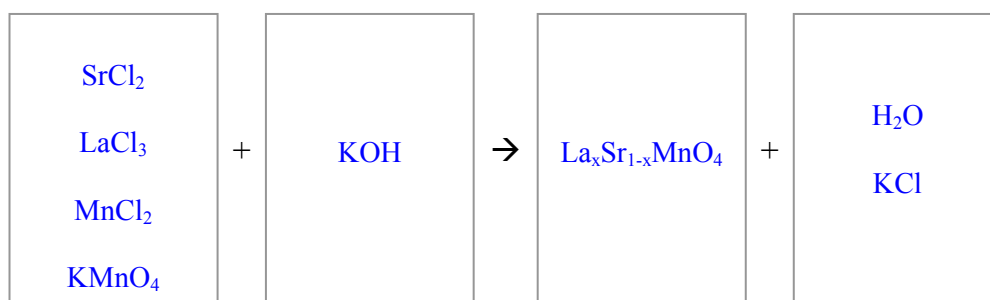


For the lanthanum chloride and strontium chloride in alkaline medium,





After obtaining the sub-products as shown in equations (i), (ii) and (iii), then the hydrothermal redox-reaction was proposed and simplified as follows:



In our approach, the synthesis process involves two steps. Firstly we mix the reagents in a vessel at a temperature (e.g. 20 °C) low enough to exclude any appreciable reactions. The solution temperature is then ramped up slowly to accelerate the chemical reaction and produce the requisite supersaturation, which is subsequently relieved by nucleation of primary particles. Secondly, as long as the temperature is adjusted so that the rate at which the reaction of reagents in the precursor is not faster than the rate at which materials condense on existing nuclei, the supersaturated state is never revisited and no new nuclei is formed. Then, the precursor solution will feed the crystal growth process only under such a hydrothermal condition.

**Table 4.1 Specifications of the raw materials used in hydrothermal synthesis of $A_xB_{1-x}MnO_3$.**

Components	Chemicals Name	Formula	Molecular	Purity	Provider
			Weight (g/mol)		
La precursor	Lanthanum chloride	$LaCl_3 \cdot 7H_2O$	345.27	$\geq 99.9\%$	Aldrich
Sr precursor	Strontium chloride	$SrCl_2 \cdot 6H_2O$	266.62	$\geq 99.5\%$	汕頭市光華化學廠
Mn precursor	Manganese chloride	$MnCl_2 \cdot 4H_2O$	197.91	$\geq 98\%$	International laboratory. USA
Mn precursor	Potassium Permanganate	$KMnO_4$	158.04	$\geq 99.5\%$	Panreac
Ba precursor	Barium chloride	$BaCl_2 \cdot 2H_2O$	244.26	$\geq 99.5\%$	台山化工廠
Calcium precursor	Calcium chloride anhydrous	$CaCl_2$	110.98	$\geq 98\%$	China national chemicals import & export corporation
Mineralizer	Potassium hydroxide	KOH	56.1	$\geq 85\%$	Advanced Technology
Surfactant	(CTAB)	$C_{19}H_{42}BrN$	364.48	$\geq 99\%$	Sigma
PVA	Poly(vinyl)-alcohol	$(CH_2CH-OH)_n$	15000	$\geq 98\%$	Sigma



4.2.2 Synthesis of reference sample

In order to obtain a polycrystalline reference pattern, ceramic samples of LSMO were prepared from high purity oxides (La_2O_3 , MnO_2 and SrCO_3) by conventional solid state reaction, i.e. sintering twice, each for 10 hours at 1300 °C in a static air atmosphere.

4.2.3 Characterization methods

Several techniques have been used to yield information on their structural and magnetic properties. The X-ray diffraction experiments were carried out by a Bruker D8 Advance X-ray diffractometer with CuK_α radiation. Transmission electron microscopy (TEM) was conducted on a JOEL 2100 operating at 200 kV. A vibrating sample magnetometer (VSM) was used for magnetic measurements with magnetic field up to 0.55 T (= 5500 Oe) and temperature ranging from 20 K to 320 K. All samples for magnetic measurements were prepared by pressing dry manganite powder in a handmade Teflon holder.



4.3 Effect of hydrothermal condition on LSMO particles formation

4.3.1 Cationic surfactant modified hydrothermal process

Several colloidal chemical preparation methods have been developed to produce mono-dispersed nanoparticles. Among them, hydrothermal method can provide an easy route to synthesize nano-scale oxide particle with controlled characteristic in a single step process and at a relatively low temperature using an aqueous medium. In some previous reports crystalline LSMO was mainly prepared from acetate precursor in hydrothermal media and required further high temperature annealing [12]. Otherwise, the reaction may not be completed and the final product deviates from the desired stoichiometric composition. To avoid the additional high temperature treatment, some modification should be made during the hydrothermal chemical reaction. One possible solution is to assist the reaction by introducing some additives in the precursor solution such as surfactant.

Surfactant can be classified into many families. Among them, cationic surfactants are often used for modification of solid surfaces, especially in the cases when surface charge is negative. Electrostatic adsorption of cations results in compensation of negative surface charge and producing a hydrophobic solid surface [13]. So the surface modification consists of enhancing both the electrostatic and hydrophobic properties. In this section the effect of the surfactant concentration on the particles are firstly described.



4.3.1.1 Experimental details

Analytical grade KMnO_4 , $\text{MnCl}_2 \cdot 4\text{H}_2\text{O}$, $\text{LaCl}_3 \cdot 7\text{H}_2\text{O}$ and $\text{SrCl}_2 \cdot 6\text{H}_2\text{O}$ were used as the starting materials. The reactions were performed in 10 ml Teflon-lined stainless steel autoclaves. KOH was added to maintain proper alkalinity. Then, the CTAB powder was mixed with the above solution containing metal ions and stirred vigorously to obtain a homogeneous black solution. As an additive, CTAB is a cationic surfactant with a critical micellar concentration (cmc) of 0.29 g/l in water at ambient conditions. After aging the reaction mixture at 60 °C for 5 hours, it was then placed in the autoclaves and heated at 240 °C under the autogenously pressure for 1 day.

The results was a black colored colloidal solution, which was then filtered off and washed with ethanol and deionized water in order to remove the residual CTAB and excess ions. The final product was then dried at 80 °C for 1 day to yield a small quantity of black powder.



4.3.1.2 Results

Fig. 4.1 shows the XRD pattern of LSMO nanoparticles. These LSMO samples were obtained by use of different content of CTAB cationic surfactant. It is clear that all the nanoparticles are well crystallized. The XRD patterns reveal characteristic peaks of LSMO. For sample prepared with 0.2 g CTAB (Fig. 4.1(d)), a single phase crystalline powder was obtained directly by the hydrothermal process. The cubic lattice parameter calculated from the scan of (110) reflection was found to be 0.387 nm, which matches well with the reported bulk value. For those made with lower content of CTAB, a trace amount of impurities phases were observed, although the formation of perovskite LSMO with good crystallinity is evident. The existence of impurities in the product indicates that the reaction has not been completed.

In order to compare the structural change in LSMO from the effect of surfactant content, the lattice parameters of the samples were summarized in Fig. 4.2(a)-(c). These figures clearly show that the lattice parameters were deviated from standard values for the sample without applying CTAB. Indeed a small distortion of the unit cell leads a drastically change in the electrical and magnetic properties of the LSMO materials.

On the other hand, the (110) lines of the diffraction patterns were used to calculate the particle size via Scherrer equation [14] ($B = 0.94 / L \cos \theta$). Fig. 4.3 shows the plot of particle size versus the content of cationic surfactant CTAB. The particle size decreases gradually from 54 nm (0 g) to 31 nm (0.2 g).

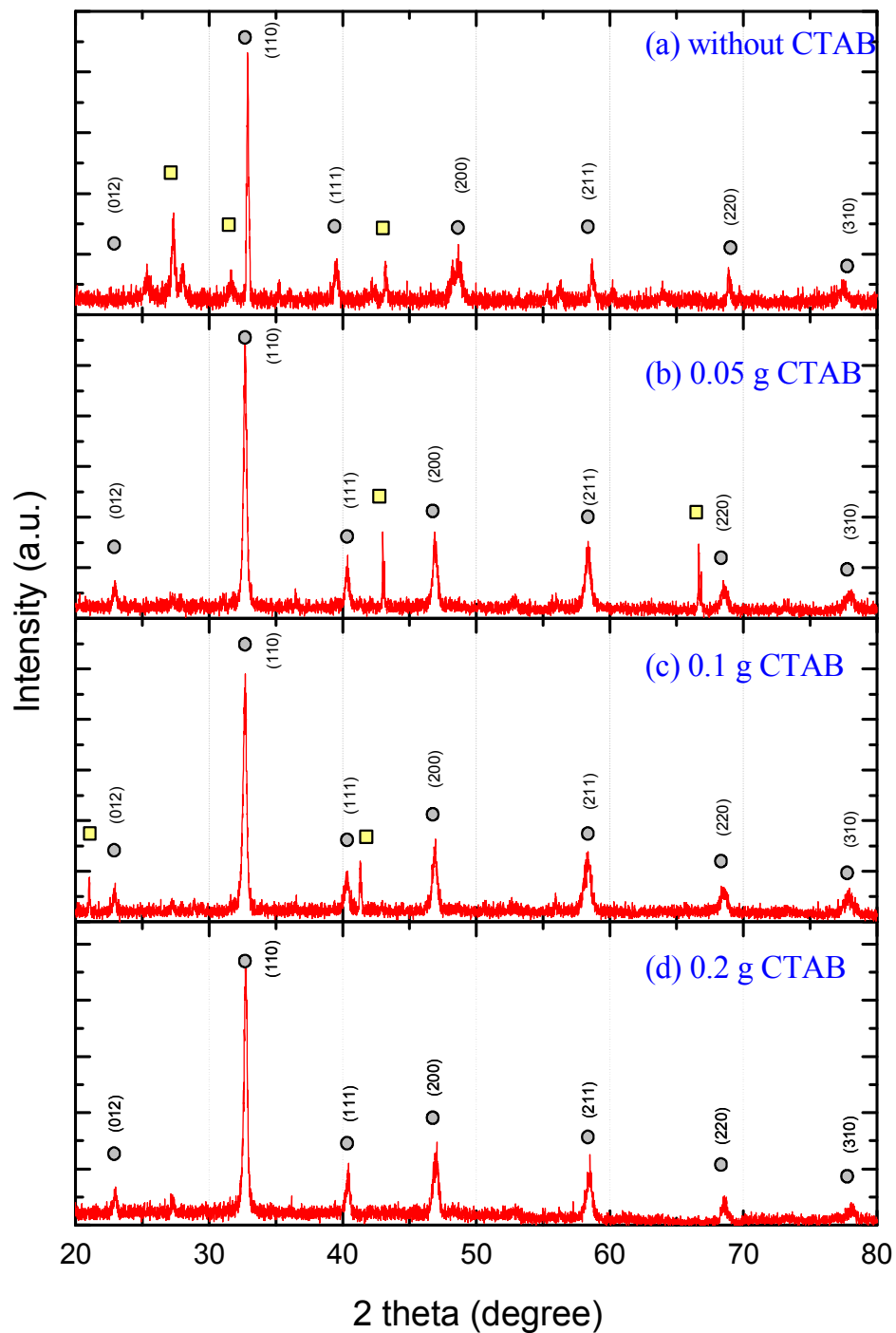


Figure 4.1 X-ray powder diffraction pattern of LSMO nanoparticles produced in the presence of CTAB with different quantity: (a) 0 g; (b) 0.05 g; (c) 0.10 g and (d) 0.20 g. (●: LSMO phase; □: Impurities phase)

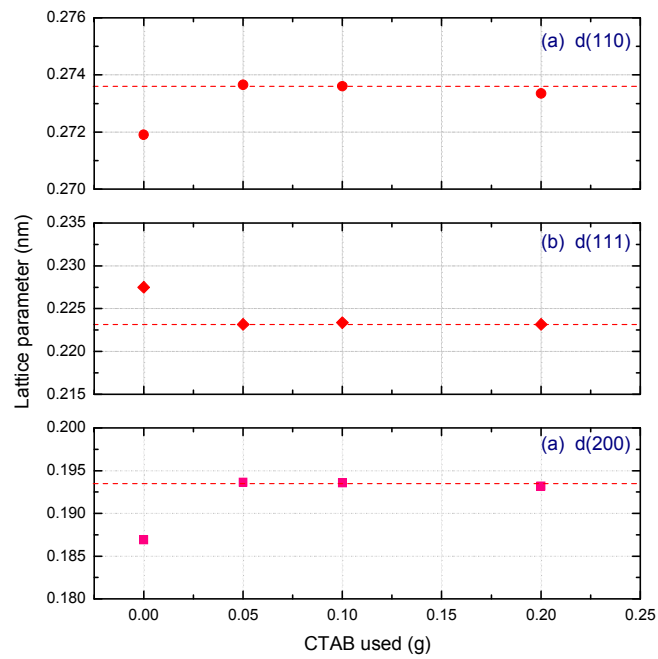


Figure 4.2 lattice parameters for LSMO particles prepared with different CTAB content.

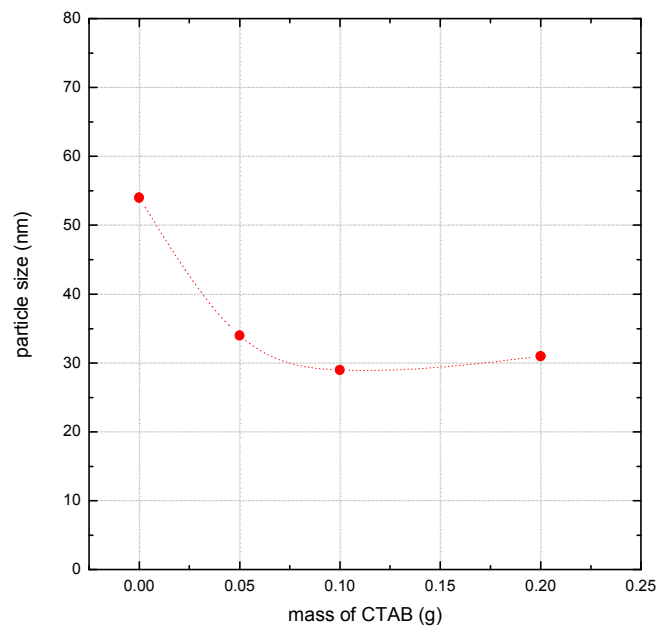


Figure 4.3 particles size of LSMO sample formed with different CTAB content.



In Fig. 4.4a, the transmission electron microscopy (TEM) studies of the hydrothermal sample without CTAB show that the product consists of a lump of nanoparticles and nanorods. Indeed the highly crystallized nanorods shown in the picture have been identified by SAD and EDX to be $\text{La}(\text{OH})_3$. The existence of impurities is in agreement with XRD results. It indicates that the application of CTAB is necessary to facilitate complete chemical reaction in our hydrothermal process. Fig. 4.4b and 4.4c reveal the formation of LSMO particles. The particles are relatively large and have a broad size distribution. In Fig. 4.4d, small particles with narrow size distribution are seen. This sample was obtained with 0.2 g CTAB treatment. The sharp SAD patterns indicate that all the as-prepared particles are of good crystalline structures. Although nanocrystallines were obtained by the hydrothermal method, the final product is nevertheless aggregated into big globular form.

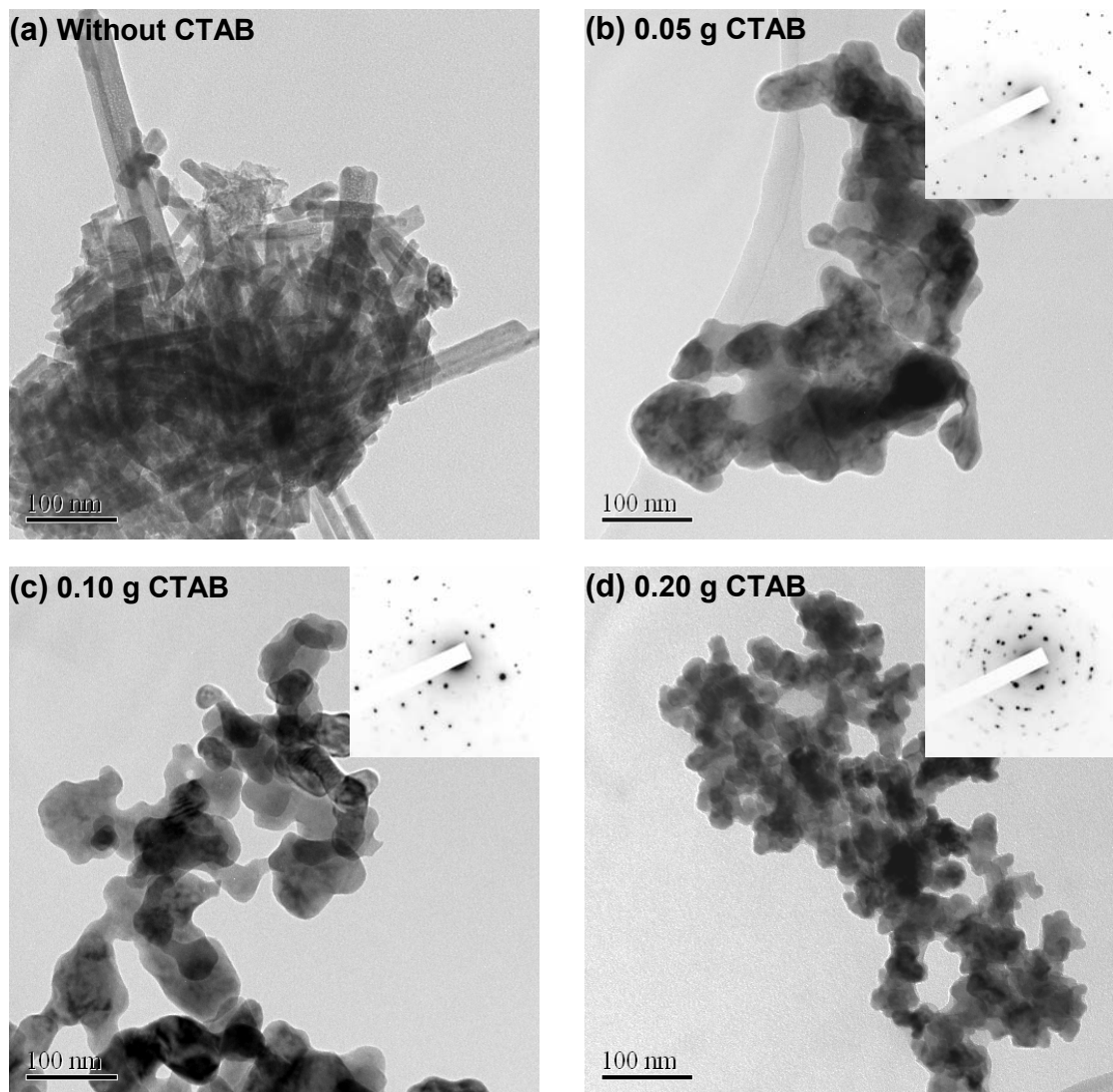


Figure 4.4 TEM images of LSMO particle prepared by hydrothermal method with (a) 0 g, (b) 0.05 g, (c) 0.10 g and (d) 0.20 g CTAB. The small inset image is the respective electron diffraction pattern.

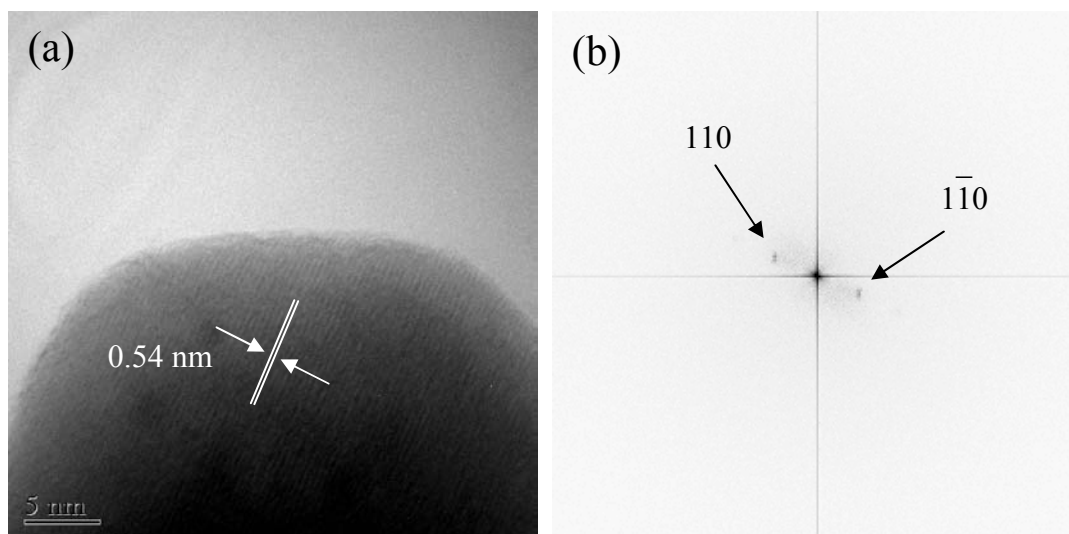


Figure 4.5 (a) High resolution TEM images of individual LSMO nanoparticles. The lattice fringes correspond to the (110) plane. (b) shows the fast Fourier transform pattern of this plane.

A typical lattice image of a nanocrystalline LSMO grain synthesized by the surfactant assisted hydrothermal process, with grains size of about 80 nm, is shown in Fig. 4.5a. Clear and uniform lattice fringes of the d_{110} plane suggest that it is a well crystallized LSMO nanocrystal. The surrounding edges of the particle are very smooth and no surface steps are observed. In Fig. 4.5b, a pair of dots clearly appears in the FFT image. It means that the particle is a single crystal.

The above results reveal that stoichiometric and well crystallized LSMO nanoparticles can be synthesized by this modified hydrothermal route. We have demonstrated that the surfactant helps to form spherical ultra fine particles. The reason may be that the cationic surfactant CTAB lowers the crystal surface energy during the crystal growth in hydrothermal condition. However, the nanoparticles tend to aggregate together because the reduction of energy associated with high surface area to volume ratio.



4.3.1.4 Particle distributions of LSMO particle with different surfactant content

By means of the software attached to the TEM – CCD and choosing an image of these nanoparticles, one can approximately estimate the diameter distribution of the LSMO nanocrystals with different CTAB content. Two typical particle size distribution histograms of the distribution are shown in Fig. 4.6(a) and Fig. 4.6(b). The analysis is obtained for studying 200 particles per sample. From these two figures, the average particle size of LSMO sample treated with 0.05 g and 0.2 g CTAB surfactant are 55 nm and 29 nm, respectively. The present results indicate that the application of surfactant not only improve the stoichiometry of the nanoparticles but also narrow the particle size distribution.

In fact, the polar head of the CTAB can adsorb onto the surfaces of the LSMO particles during the hydrothermal process, while the non-polar tail protects the particles from coagulation by steric stabilization of the colloids. This suggests that CTAB can control LSMO particle growth rate by preventing the nuclei from growing too fast and promoting the formation of particles of homogeneous size distribution. Therefore, the CTAB can influence crystal structure and particle size of LSMO in the experiment, resulting in its small particle size and relatively narrow particle size distribution. In aqueous solution without any CTAB, the nucleation and growth of LSMO crystals are spontaneous. When the nanoparticles are formed, they promptly coagulate and grow. Therefore, the nanoparticles cannot be obtained. The results indicate that the CTAB plays a significant role toward controlling the nucleation, growth and also aggregation of LSMO particles.

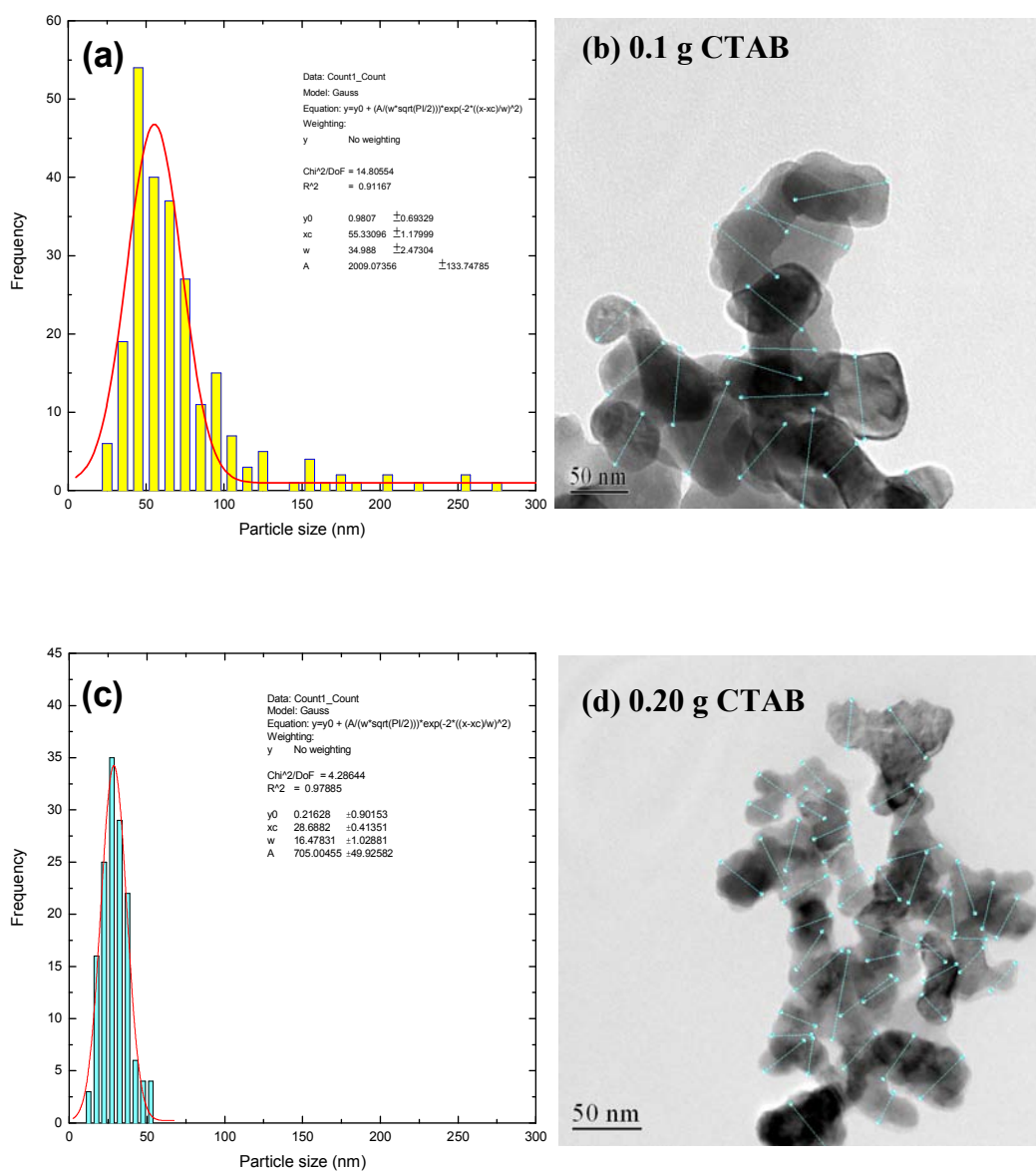


Figure 4.6 Histogram of particle size distribution of LSMO particle grown by hydrothermal process with (a) 0.1 g CTAB surfactant {typical TEM image in (b)} and (c) 0.2 g CTAB surfactant {typical TEM image in (d)}.



4.3.1.5 Composition of as-prepared LSMO particles

Table 4.2 Composition of LSMO nanoparticles formed by hydrothermal process with different cationic surfactant concentration.

	Composition (mole ratio)		
Content of CTAB (g)	La	Sr	Mn
Precursor	0.67	0.33	1.00
0	0.84	0.16	0.92
0.05	0.60	0.40	0.95
0.10	0.64	0.36	0.95
0.20	0.70	0.30	1.01

One important control parameter in the synthesis of mixed valence manganites with adjustable doping levels is the average oxidation state of the Mn ion [15]. The analysis of the LSMO powders by EDX shows the chemical composition. The data are listed in Table 4.2. For powder treated with a higher CTAB content, the La, Sr and Mn compositions are closer to the stoichiometric ratio. With 0.2 g CTAB added in the hydrothermal process, single phase $\text{La}_{0.7}\text{Sr}_{0.3}\text{MnO}_3$ nanoparticles are obtained. Since the XRD results indicate that unreacted $\text{La}(\text{OH})_3$ is the main impurities when the sample prepared without any surfactant, we believed that the off-stoichiometry is mainly induced by La deficiency. Evidently the usage of CTAB plays an important role in controlling the chemistry of hydrothermal process.

4.3.1.6 Magnetic properties measurement

It is recognized that the magnetization in the manganite perovskite phase is very sensitive to the stoichiometry, atomic defects, oxygen content, and the $\text{Mn}^{3+}/\text{Mn}^{4+}$ ratio. Notably, in Fig. 4.7a, the synthesized LSMO particles without CTAB modification show diamagnetic properties although they are of good crystallinity. The reason may due to the non-stoichiometric manganite. In our case, all the samples with surfactant CTAB exhibit clear ferromagnetic switching characteristics at room temperature (in Fig. 4.7b, 4.7c and 4.7d). The LSMO nanoparticles that we produced with surfactant are apparently smaller than the critical size of 80 nm and they can be regarded as being superparamagnetic at high enough temperature [24].

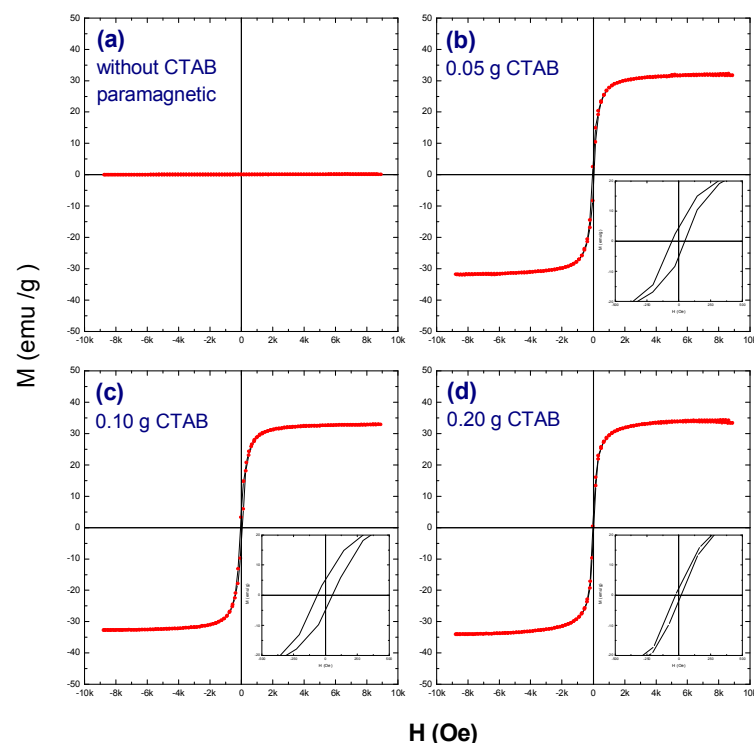


Figure 4.7 The room-temperature magnetization curves of LSMO powders obtained with (a) no CTAB, (b) 0.05 g CTAB, (c) 0.1 g CTAB and (d) 0.2 g CTAB. The insets show an enlargement of magnetization curves.



Table 4.3 Remanence magnetization and coercive fields of LSMO nanoparticles prepared by hydrothermal process with different CTAB content (measured at room temperature).

Content of CTAB (g)	Remanence magnetization (emu/g)		Coercive field (Oe)	
	M_R^+	M_R^-	H_C^+	H_C^-
0	--	--	--	--
0.05	4.46	-4.77	-56	49
0.10	5.18	-4.91	-66	54
0.20	3.03	-3.50	-30	30

The coercive fields of different samples are shown in Table. 4.3. As the content of cationic surfactant CTAB in the hydrothermal process is increased, the coercive field decreases. It should also be noted that the exchange bias (H_C^+ and H_C^-) in the present system is symmetric about the zero field axis.

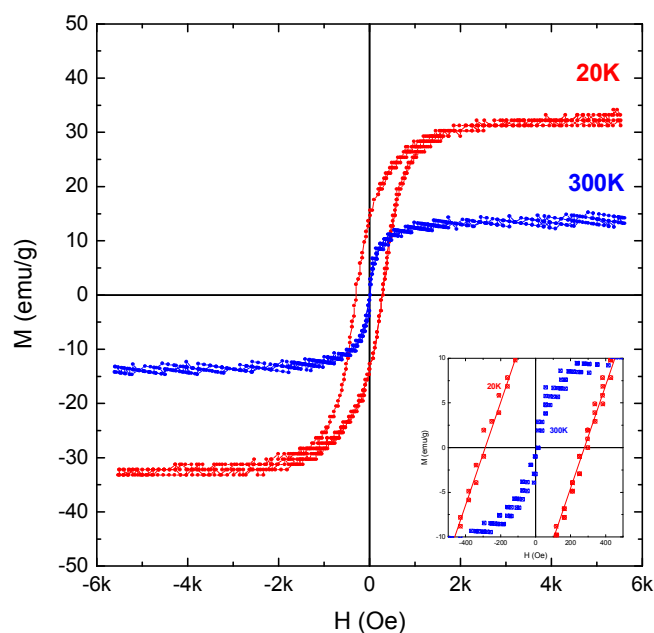


Figure 4.8 Magnetic hysteresis loop for nanoparticles of LSMO prepared by cationic surfactant assisted hydrothermal method (0.2g CTAB), the small inset shows an enlargement of the magnetization curves.

To study the magnetic nature of LSMO nanoparticles, a comparison of the magnetic hysteresis loops was made for the as-synthesized powder at different temperatures. As shown in Fig 4.8, it clearly illustrates that there is no hysteresis at room temperature. The magnetization at room temperature was relatively low and saturates at a low magnetic field of ~ 1 kOe. With decreasing temperature the magnetization increased. Ferromagnetic hysteresis is clearly discernible at 20 K with a coercive field of ~ 300 Oe. The large coercive field appeared at low temperature of the LSMO particles can be attributed to the particles with high anisotropy and also the magnetic domain wall pinning process. This behavior indicates that the LSMO nanoparticles are magnetically frozen below the blocking temperature and undergo a superparamagnetic-like to ferromagnetic transition.

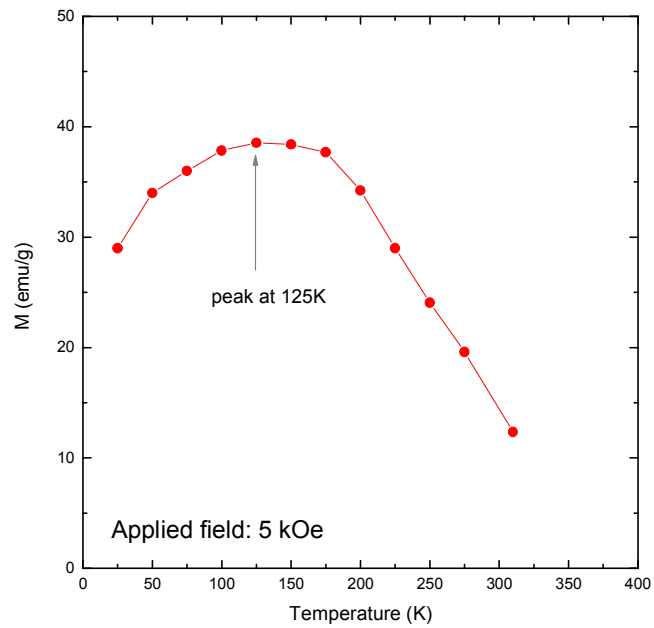


Figure 4.9 Magnetization of as-prepared LSMO particles as a function of measurement temperature.

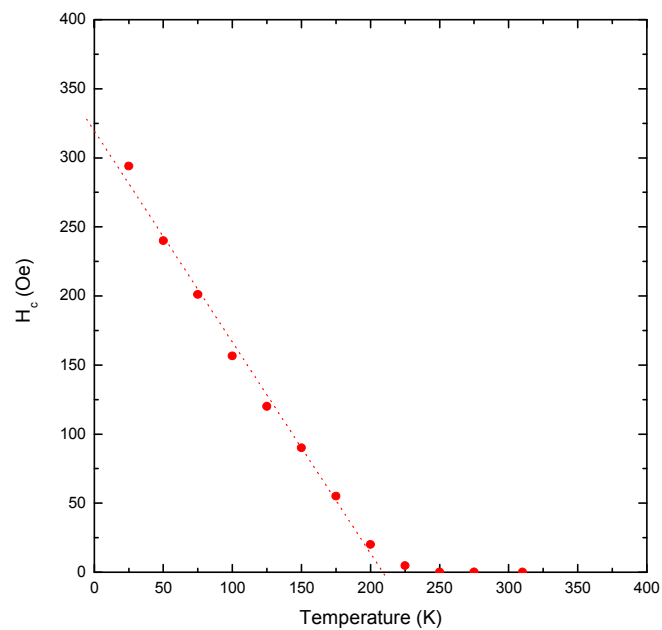


Figure 4.10 Coercive field of as-prepared LSMO particles as a function of measurement temperature.



The temperature dependent on magnetization of the as-prepared LSMO nanoparticles is shown in Fig. 4.9. It shows a value of 30 emu/g at 20 K which is much smaller than that of the corresponding bulk LSMO of 80 emu/g. It may be due to the small size and high surface disordering of the manganite particles. Apparently, a gentle drop in M of the as-prepared LSMO samples suggests that the particles have undergone a transition from ferromagnetic state to paramagnetic state. In fact, the broad transition can be interpreted by the existence of inhomogeneities and defect states in the particles. Although our cryostat only enables us to achieve a sample temperature of 300 K, the well defined magnetization at this temperature indicates that the Curie temperature (T_c) of these LSMO nanocrystallites is well above 300 K [16].

Since the sample was under zero-field cooled (ZFC) before the hysteresis loop measurement, the magnetization decreases with decreasing temperature from 150 K to 20 K infers a spin-freezing behavior. This magnetic feature has usually been observed in inhomogeneous system. The spin freezing behavior is explained by a frustration of the ferromagnetic domains which results from competitions between positive and negative exchange interactions. The competition is coming from the ferromagnetic interactions between spins and the RKKY or superexchange interaction [17]. As a result some ferromagnetic grains are frozen along a local easy direction below a certain temperature.

On the other hand, the coercive field (H_c) of the LSMO nanoparticle decreases with increasing temperature. The result shown in Fig. 4.10 gives a H_c of



296 Oe at 25 K but nearly 0 Oe at 225 K. Basically, for non-interacting magnetic nanoparticles below the blocking temperature (T_B), the coercive field (H_c) follows a relation to the temperature (T) as [18]:

$$\frac{H_c}{H_c(0)} = 1 - \left(\frac{T}{T_B} \right)^{1/2}$$

It should be noticed this expression only considers the magnetization reversal takes place coherently. Therefore, when we consider the sample is in a form of magnetic nanoparticles-compact, the dipole interaction between particles cannot be ignored. Because a fraction of magnetic particles are close to each other, they can be somehow magnetically coupled and a spurious ferromagnetism response could arise. Thus, the magnetic properties of these materials should be accounted for by the concept of domain wall pinning. According to Gaunt [19], the strength of a domain wall pinning is defined by the way in which a domain wall breaks free. If the domain wall bends prior to escape then the pinning is strong. If the wall moves in a planar manner and breaks away before bending then the pinning is weak. Based on the measurement of the temperature dependent coercive field, we may identify the mechanism responsible for it and to obtain insight into the properties of the pinning centers.

From Fig. 4.10, it verified that the temperature dependence of the coercive field follows a linear relation. This results show that the main domain-wall pinning mechanism present in manganite particles can be modeled as a weak domain wall pinning. In this model, the domain wall breaks away cooperatively from many



pinning sites in the coercive field. Thermal excitation leads to a linear decrease of the coercive field with temperature [20].

As mentioned before, the experimental criteria for superparamagnetism (SPM) include not only that the magnetization curve exhibits no hysteresis but also the magnetization curve at different temperatures should superimpose in a plot of normalized magnetization (M/M_s) against applied magnetic field/temperature (H/T). As shown in Fig. 4.11, data of (M/M_s) against (H/T) for the LSMO particles from 200 K to 310 K are superimposed perfectly. And also these curves have nearly zero remanence and coercive field. It can be therefore justifiably said that the particles are in superparamagnetic-like behavior at sufficient temperature.

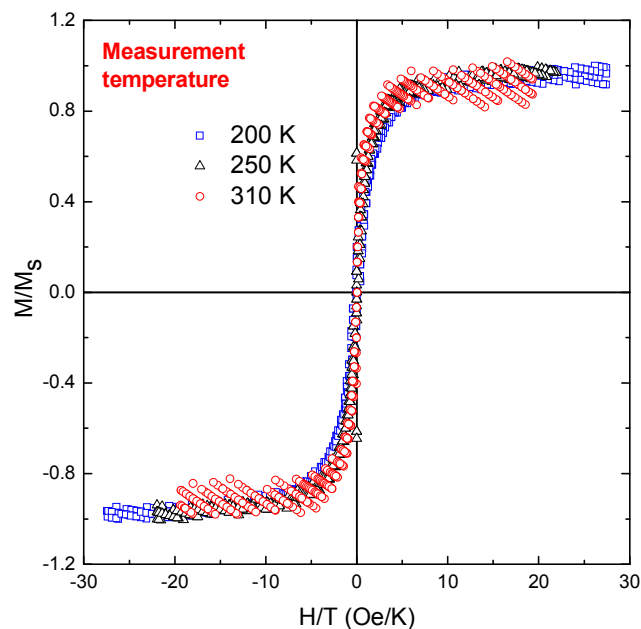


Figure 4.11 Fitting of magnetization curve of (M/M_s) against (H/T) for the sample at different temperatures.

Zero field-cooled and Field-cooled measurement

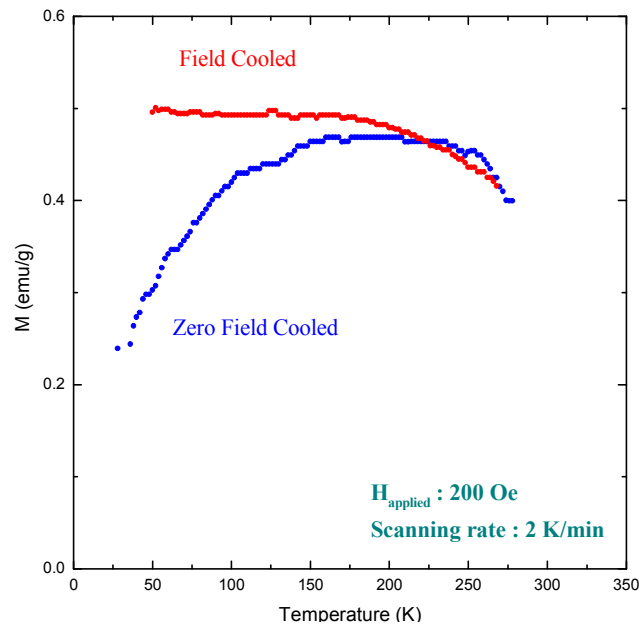


Figure 4.12 The ZFC/FC curves show a typical behavior of magnetic nanoparticles.

Zero field-cooled (ZFC) and field-cooled (FC) experiments provide a means of investigating the effects of the various magnetic interactions. A typical feature found in the magnetic nanoparticle is the reversible magnetic behavior below an irreversibility line or field dependent blocking temperature [21]. The ZFC and FC curves were obtained from sample of 50 nm sized $\text{La}_{0.67}\text{Sr}_{0.33}\text{MnO}_3$ particles. They are shown in the Fig 4.12. At 200 K, the FC magnetization begins to deviate from that of ZFC. This verifies a freezing behavior at low temperature. The particles have evolved into a disordered blocked state. Above this temperature, the magnetization is nearly reversible and symmetric. This discrepancy between ZFC and FC profiles is usually understood as a signature of spin-cluster glass state that has no simple long range ferromagnetic order. It is noted that the spin freezing behavior is often appeared in inhomogeneous magnetic system, such as oxygen deficient manganite



oxides and granular Co-Al₂O₃ films where fine ferromagnetic particles are embedded in a non-ferromagnetic background [22]. The origin of the irreversibility arises from the interplay between the thermal energy and energy barriers separating the different states. Also, the ZFC magnetization curve shows a broad maximum at about 200 K and this is the spin freezing temperature (T_f). The broadened maximum indicates a broad size distribution and relaxation times of the magnetic moments in the particles.

On the other hand, the FC magnetization curve remains almost constant below the freezing temperature. According to V. Sreeja, [23], in a system consisting of dense magnetic nanoparticles, the FC magnetization behaves in a fashion similar to that of spin-glass and this is because of the strong inter-particle interactions. For such interacting dense magnetic nanoparticles, the FC magnetization either decreases or remains constant below the blocking temperatures whereas for noninteracting nanoparticles, the FC curve increases below T_B . Therefore, the present results confirm the interacting nature with typical low-field magnetization behavior of a ferromagnet. Magnetic interactions between the particles should exist in these samples since the particles have not been isolated in a matrix or fluid. It is worthwhile to note that the freezing temperature obtained from the FC/ZFC measurements are in good agreement with the results of magnetic hysteresis measurements shown in Fig 4.10.



4.3.2 Effect of processing temperature in hydrothermal process

It is well known that the formation of oxide can be described by a typical hydrothermal ripening process. It means that the size and morphology of the particles are affected by the probabilities of crystal nucleation and crystal growth. If the probability of the crystal nucleation is higher than that the crystal growth, the crystal will be smaller; otherwise they will be larger. In this section, we examine the effect of processing temperature on the particle morphology.

Experiment details:

LSMO nanoparticles were prepared by the cationic surfactant assisted hydrothermal method. Apart from the processing temperature, all the other parameters were the same as mentioned in the previous section. The particles were prepared in this series of experiment at processing temperature varying from 210 °C to 250 °C.

Results:

LSMO nanoparticles were obtained by keeping the autoclaves in the oven at various processing temperatures for 1 day. They were characterized by XRD over 2-theta diffraction angles between 20° and 80°. The XRD profiles are shown in Fig. 4.13. Apart from the sample treated at 210 °C, all other samples are pure phase LSMO without any observable impurities. The diffraction patterns can be perfectly indexed to the pseudo-cubic perovskite structure. The sharp and strong peaks in the XRD pattern suggest that the products are well crystallized.



Lattice parameters were determined from the diffraction peaks of (110) plane in Fig. 4.13 and summarized in Fig. 4.14. For the sample prepared at 210 °C, the lattice parameter of d_{100} was found to be larger than bulk value for the same composition of LSMO. The main reason may due to the non-stoichiometric LSMO formed by the incomplete hydrothermal reaction. Hence we predict the critical temperature is about 220 °C for complete LSMO formation in our hydrothermal process. The average crystalline size (D) is determined by using the Scherrer's equation and the results are summarized in Fig. 4.15. From this figure, no obvious change in the average particle size with processing temperature. The average crystal size of the as-synthesized LSMO particles is found to be 23 – 27 nm, which is far below the critical size of 80 nm [24].

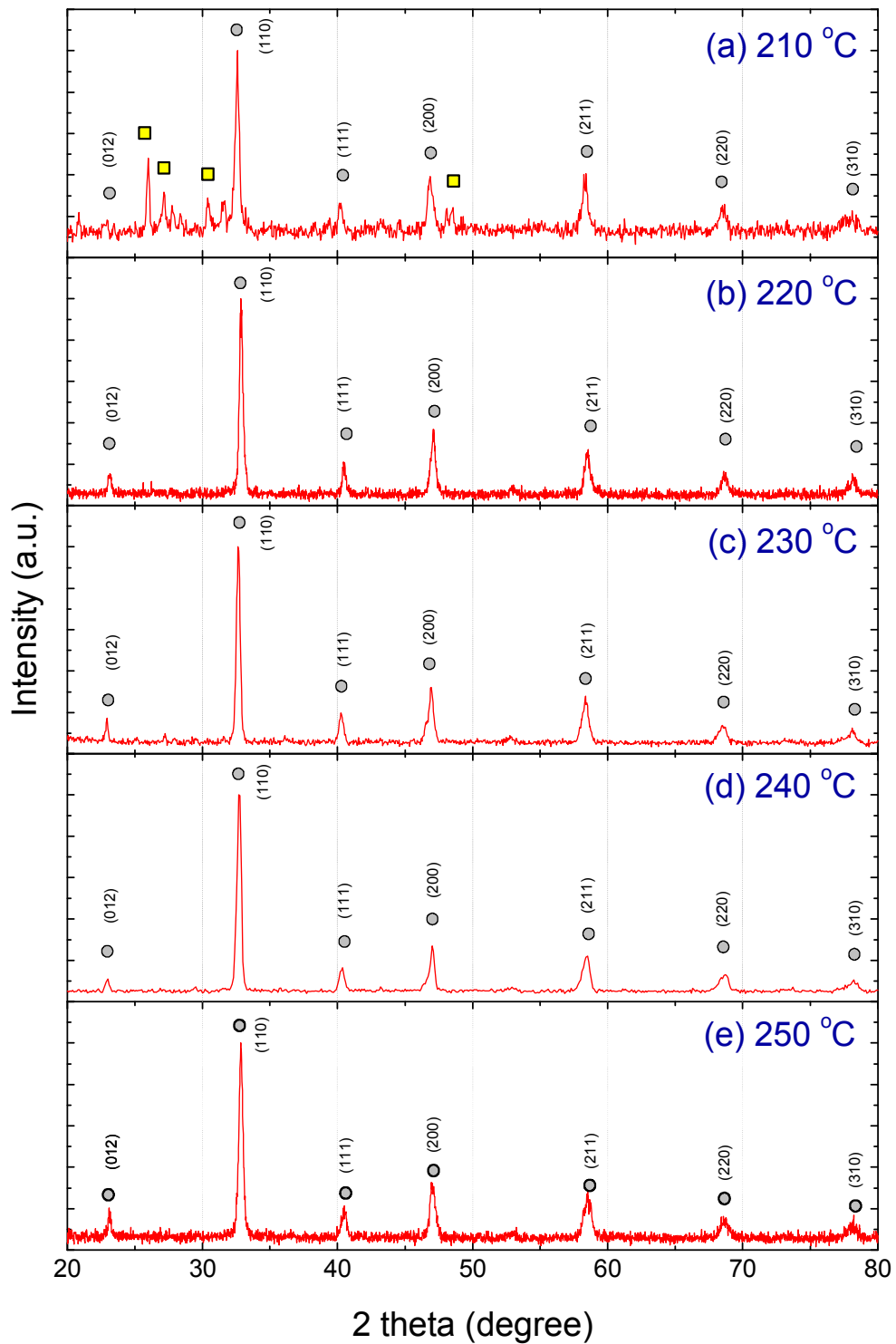


Figure 4.13 The XRD patterns of LSMO nanoparticles prepared from surfactant assisted hydrothermal method at various processing temperatures. (remark: \square —impurities, \circ —LSMO)

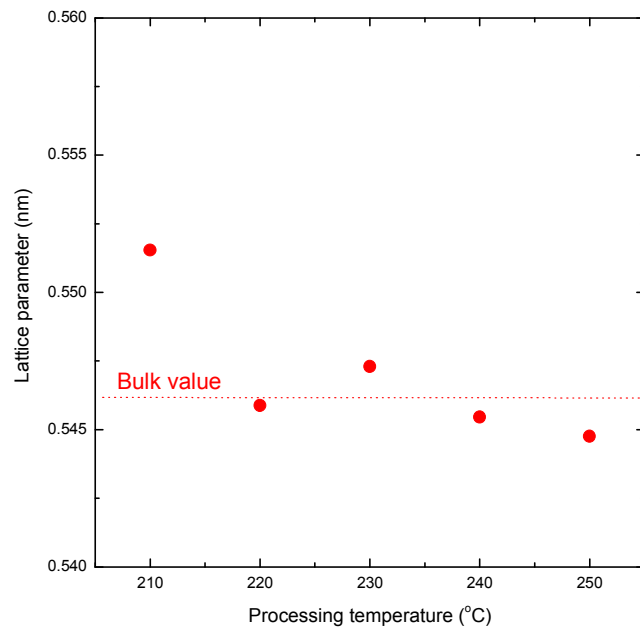


Figure 4.14 Lattice parameter (d_{110}) of LSMO particles as a function of processing temperatures.

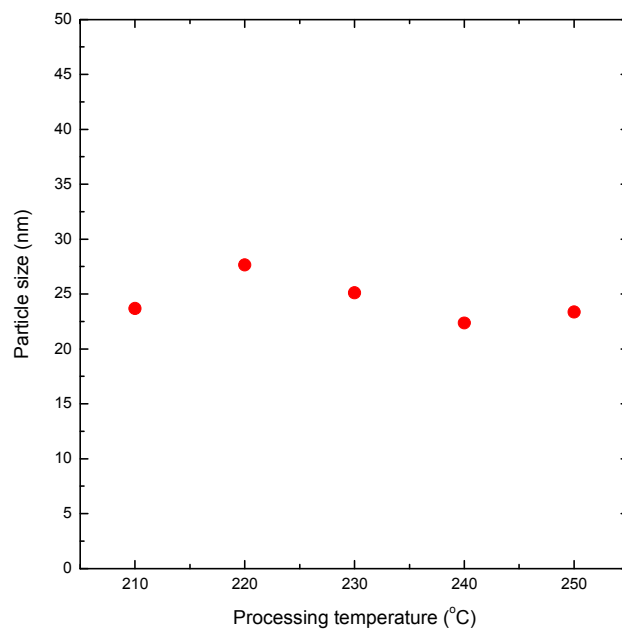


Figure 4.15 Particle size of as-synthesized LSMO particles as a function of processing temperatures.



Transmission electron micrograph (TEM) of the particles prepared at 220 °C and 240 °C along with the selected area diffraction (SAD) pattern are shown in Fig. 4.16- Fig. 4.19. The TEM images show that both samples consist of agglomerated and irregular shape particles. It also indicates that the particles prepared at these two temperatures have narrow size distribution. Most particles have size close to 25 nm. This is comparable to the average crystallite size obtained from the XRD analysis. On the other hand, the clear SAD diffraction spots on the ring of Debye cone of the samples clearly infer that the compound is fully crystallized.

In summary, when the processing temperature is over a critical temperature of 210 °C, especially in the range of 220 °C to 250 °C, good crystalline LSMO particle can be formed. Higher hydrothermal processing temperatures, however, appear to have little effect on altering the particle crystallinity, particle morphology and also particle size.

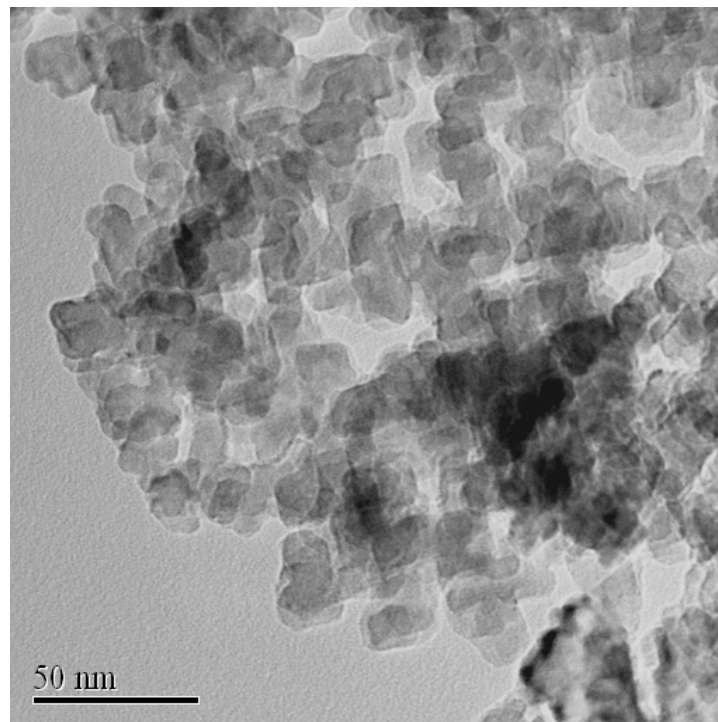


Figure 4.16 TEM image of LSMO particles prepared by hydrothermal process at 220°C.

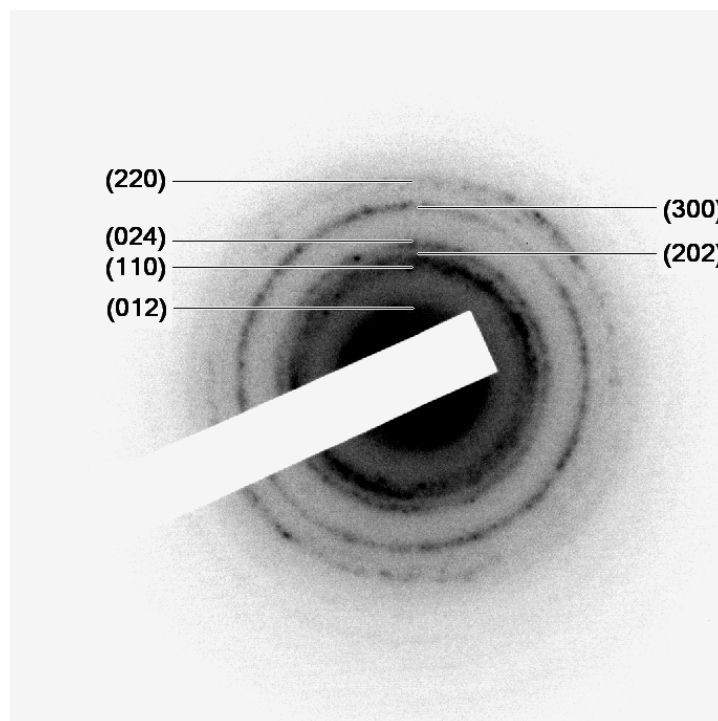


Figure 4.17 Electron diffraction pattern of LSMO particles prepared by hydrothermal process at 220°C.

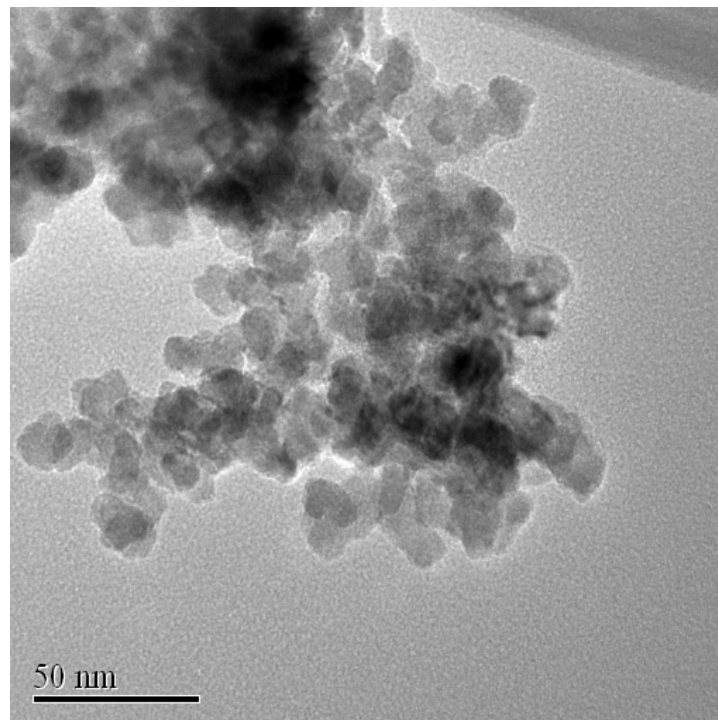


Figure 4.18 TEM image of LSMO particles prepared by hydrothermal process at 240°C.

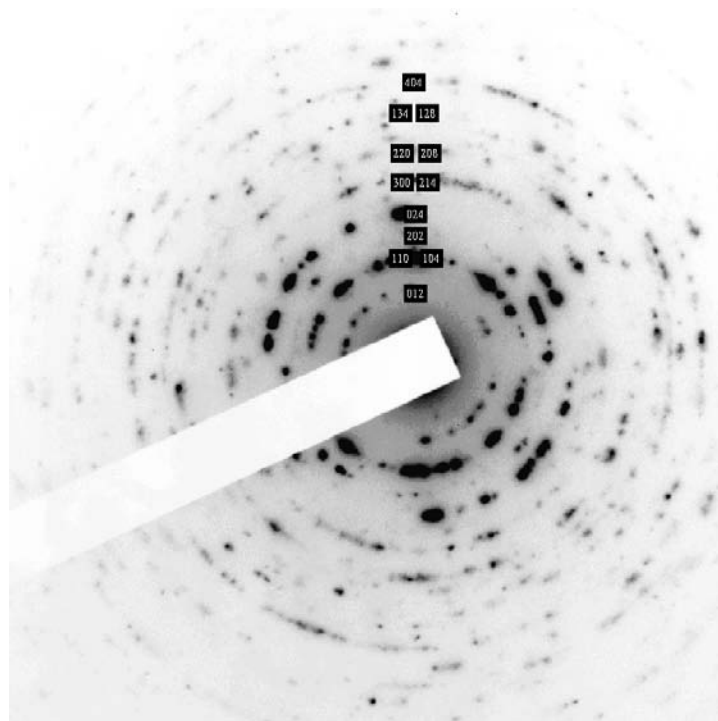


Figure 4.19 Electron diffraction pattern of LSMO particles prepared by hydrothermal process at 240°C.



4.3.3 Influence of aging process on LSMO particles

Since the particle formation is highly dependent on the initial state of the reactants, one of the critical factors that responsible for the final shape of the nanocrystals is the crystallographic phases of the initial seed during the nucleation processes. The seed can potentially have a variety of crystallographic phases. The most stable phase is highly dependent on their environments. For example, by adjusting the initial temperature during the nucleation processes, their crystalline phase can be controlled. Report by Andrzej [25] suggests that the aging of the precursor solution may lead to various modifications of the resultant precipitate such as change in particle size and morphology or even cause the crystallization of amorphous particles. In this section, the effect of the aging process on the particles size and morphology is explored.

Experimental:

From the foregoing discussion, the processing temperature of 240 °C was appropriately chosen to be our subsequent experimental condition. This set of experiment was performed with the presence of the cationic CTAB surfactant. The effects of aging can be observed by examining the particles obtained by using different aging temperature (T_{aging}). Apart from the T_{aging} , all other parameters were the same as mentioned in the pervious section. Therefore, the LSMO nanoparticles were prepared in this series of experiments with additional aging process before the hydrothermal reaction. The aging process was performed at temperature (T_{aging}) varying from 30 °C (RT) to 70 °C for 5 hours duration.



In order to verify the structural changes and the phase purity, the samples were characterized by XRD and TEM. The XRD profiles of the hydrothermal LSMO particles aged at different temperatures are shown in Fig. 4.20. From this figure, all the obtained diffraction patterns are best fitted to perovskite manganite structure, which suggests completed reaction in the LSMO synthesis. The small variation of the lattice constants of the as-prepared product due to the aging temperature is illustrated in Fig. 4.21. The values representing d_{110} are found to vary from 0.547 - 0.549 nm. Apparently the lattice constant does not show any obvious trend which could be associated with the stoichiometry of the particles form by the hydrothermal process. As such, the small variation in the lattice constant and good agreement with the same composition LSMO bulk sample implies stoichiometric LSMO particles with good crystallinity.

The relative intensity of the (110) peak is also found to decrease substantially when the aging temperature (T_{aging}) increased up to 70 °C. These observations reveal that the aging process also plays an important role in determining the anisotropic growth orientation of the crystal.

The average crystallite size is calculated from the XRD line broadening using the Scherrer's equation. The average crystallite size of LSMO is obtained as a function of T_{aging} and shown in Fig 4.22. It clearly indicates that the particle size decreases with increasing T_{aging} . It infers that the aging process promotes the formation of stable LSMO nuclei. As a result, the particle size and morphology can also be controlled through this thermal aging process.

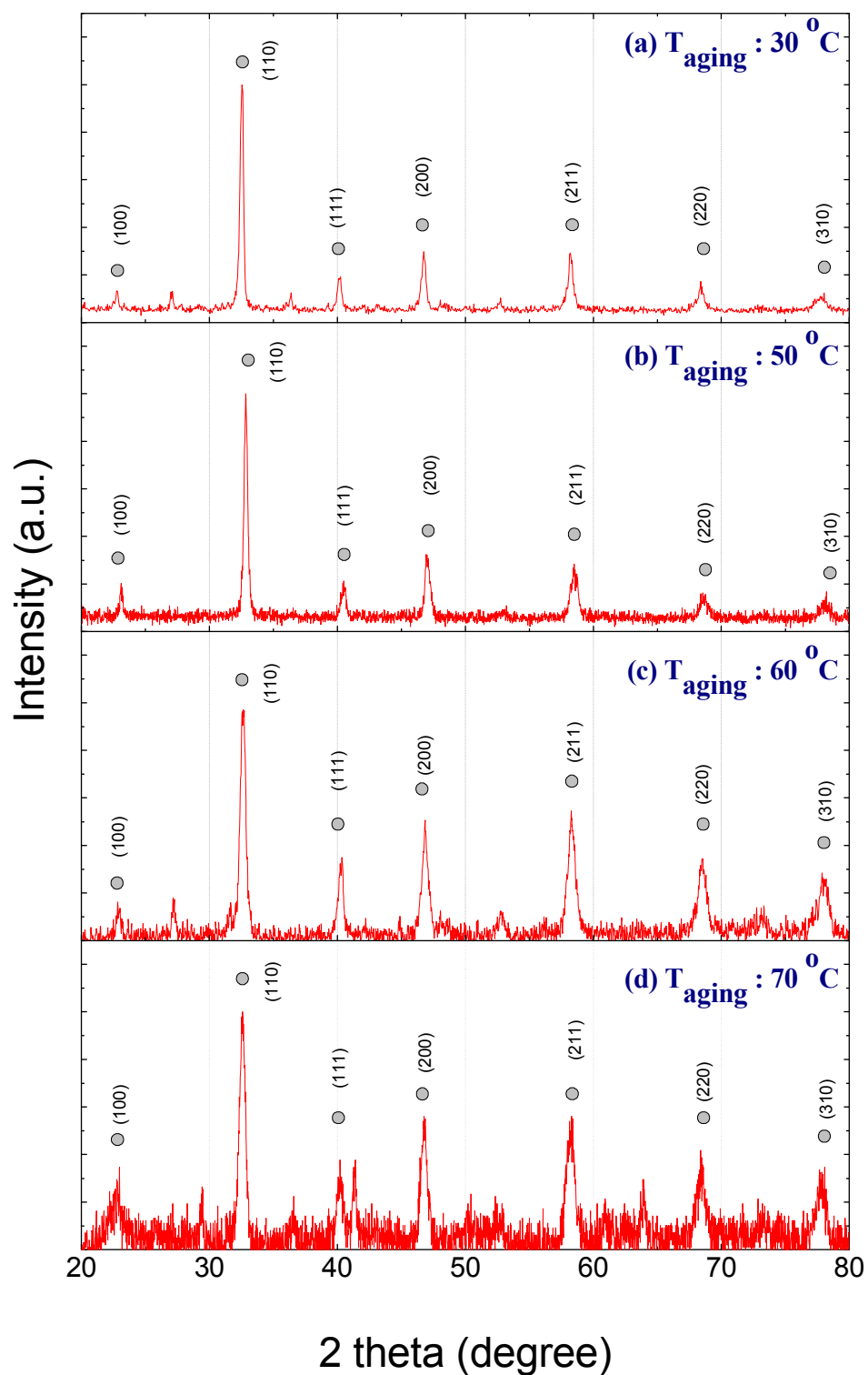


Figure 4.20 XRD patterns of LSMO nanoparticles prepared with an aging process at (a) 30 °C, (b) 50 °C, (c) 60 °C and (d) 70 °C for 5 hours.

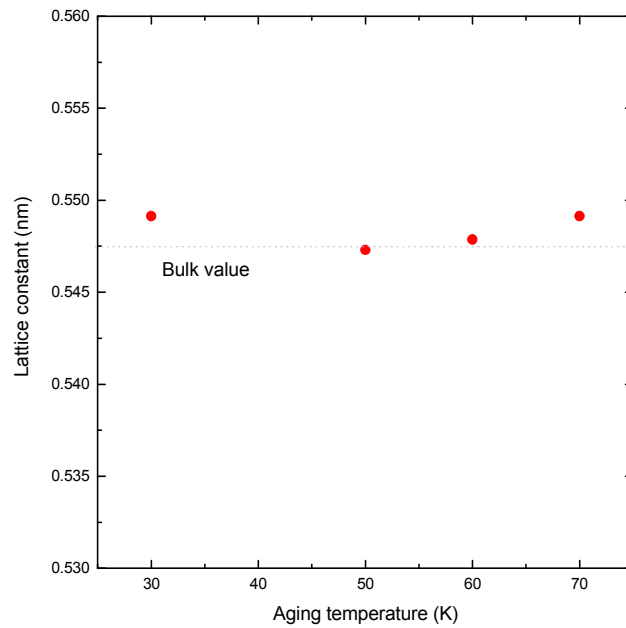


Figure 4.21 Lattice constant of LSMO nanoparticles prepared with an aging process at different aging temperatures.

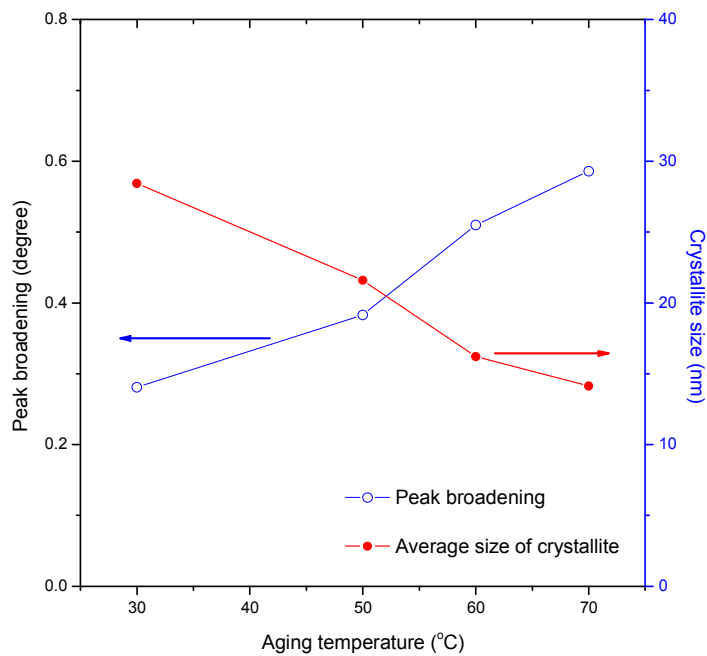


Figure 4.22 Peak broadening and average crystallite size of LSMO nanoparticles prepared at different aging temperatures.



TEM observation

The microstructure and growth orientation of the LSMO particles were further investigated by TEM. Fig 4.23 shows the nanocrystalline nature of the LSMO particle observed in TEM for different T_{aging} . Besides the surfactant, aging temperature (T_{aging}) also substantially affects the particle morphology. In this figure, all samples show various degrees of agglomeration. These agglomerates can increase the magnetic interaction between particles, and therefore may influence our measurements on the magnetic properties of the LSMO particles.

The representative patterns of the sample displayed in the figure show the particle morphology and particle size. Obviously they change according to different T_{aging} . As seen in Fig 4.23a, particles are formed in rod-like shape with some dendrites when the precursor aged at 30 °C. Typical dimensions of this particle are 100 nm thick with few microns in length. In fact, non-equilibrium growth and molecular anisotropy are the causes for the formation of dendrites structure [26]. The crystalline dendrites have a considerably increased surface energy in contrast to the equilibrium shape of the crystal, and therefore they are thermodynamically unstable.

According to Datta [27], the growth of dendrites particles can be explained by a mechanism of particle self-assembly. It suggests that certain amount of unstable nuclei will form after the precursor solution is aged at low temperature. In the early stage of hydrothermal process, random moving LSMO nuclei formed in precursor solution accumulate together to form kinetically roughened finger-like branches



under certain supersaturation conditions. Then the surface of these branches is smoothed by the CTAB films surrounding. Finally, the individual branches move randomly to give rise to the complex LSMO dendritic structures.

To show the growth direction of the dendrites particles, it is necessary to obtain high resolution TEM images (HRTEM) at the tips of the dendrites. Fig. 4.24 shows the HRTEM image recorded at near the tip of a LSMO dendrite that was aged at 30 °C. The regular fringe spacing is about 0.39 nm which is in agreement with the separation of (100) plane of LSMO particles. Considering the HRTEM images, we conclude that the nanoparticles preferentially grow along the (100) plane. Based on this result, the dendrites crystals are clearly connected by the co-ordination polyhedron growth unit along the fast growth direction of the corresponding crystals. Hence, the growth unit is put forward to construct the hierarchical LSMO crystals with secondary or tertiary branches parallel to the (100) plane.

On the other hand, when the T_{aging} is further increased, the particles are smaller and their shape becomes spherical. It can be explained by the formation of stable nuclei from precursor solution under a high temperature aging process. Since the particle grown individually from such stable nuclei and together with the surface modification by CTAB, spherical shaped and uniform size of LSMO particles were obtained finally.

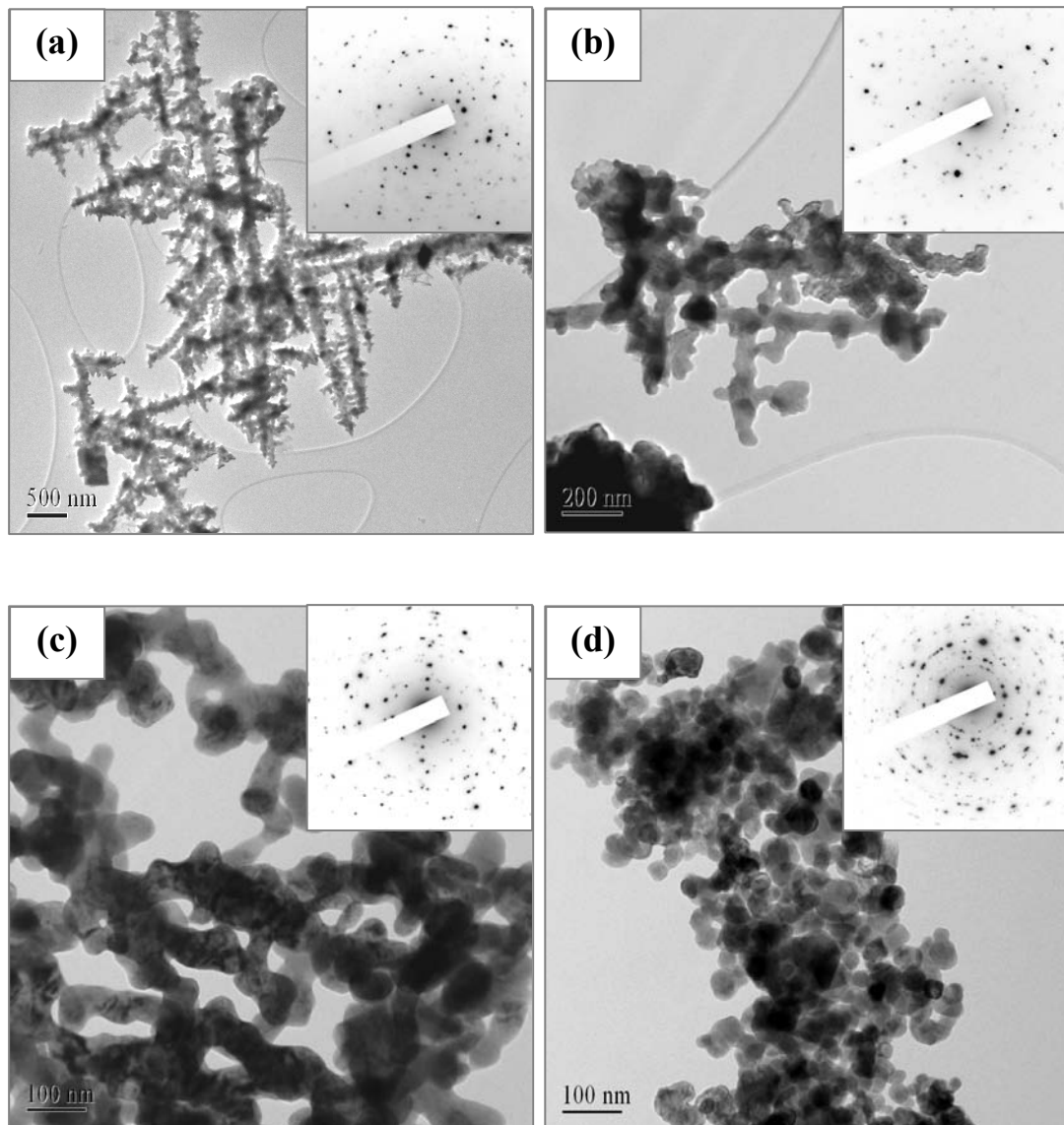


Figure 4.23 TEM images of LSMO nanoparticles prepared with an aging process at (a) 30 °C, (b) 50 °C, (c) 60 °C and (d) 70 °C for 5 hours. The inset images show the corresponding SAD.

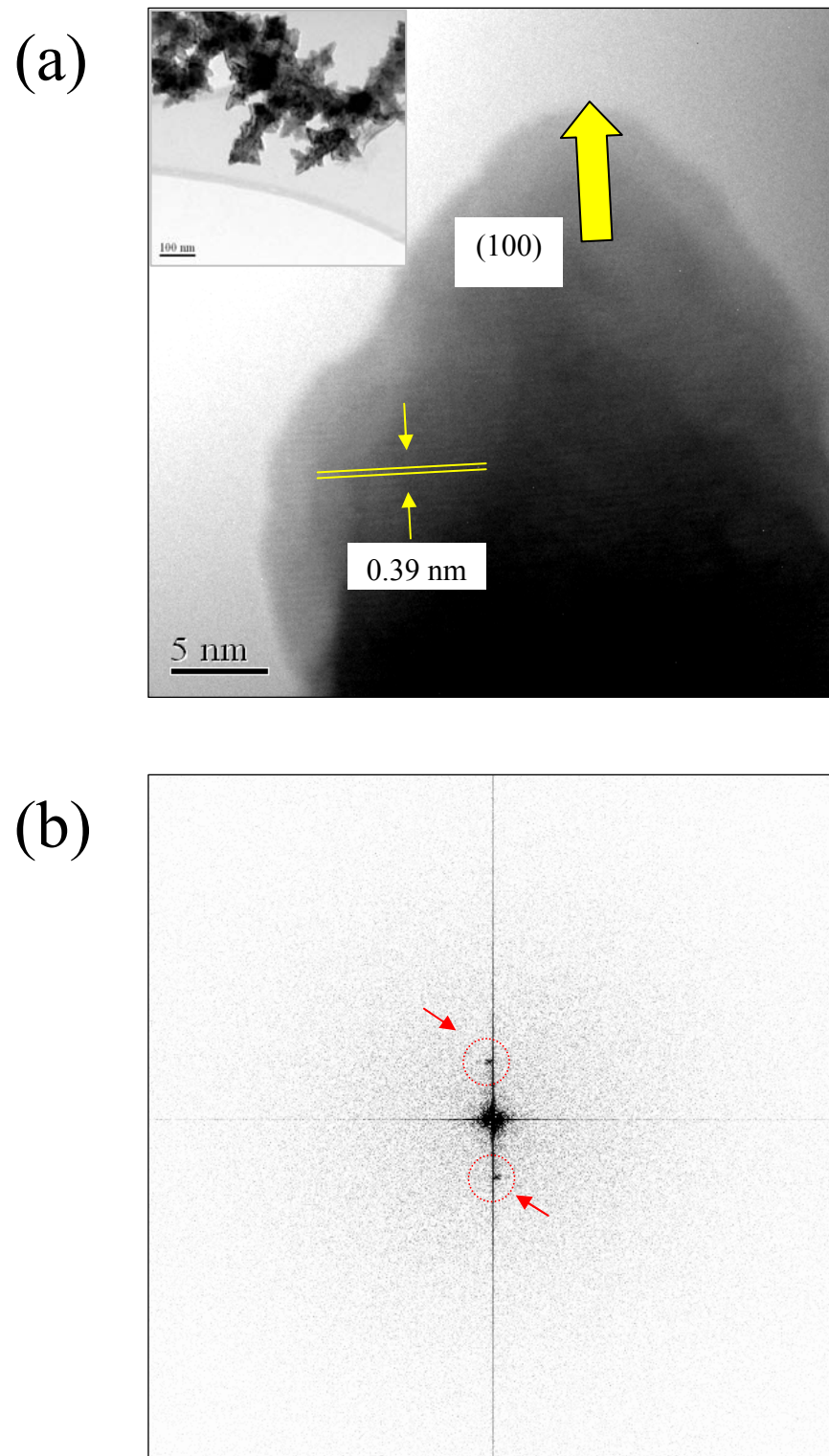


Figure 4.24 (a) HRTEM image (LRTEM image in smaller inset) and (b) FFT image of the tip of LSMO rod like particle prepared with aging process at 30°C.

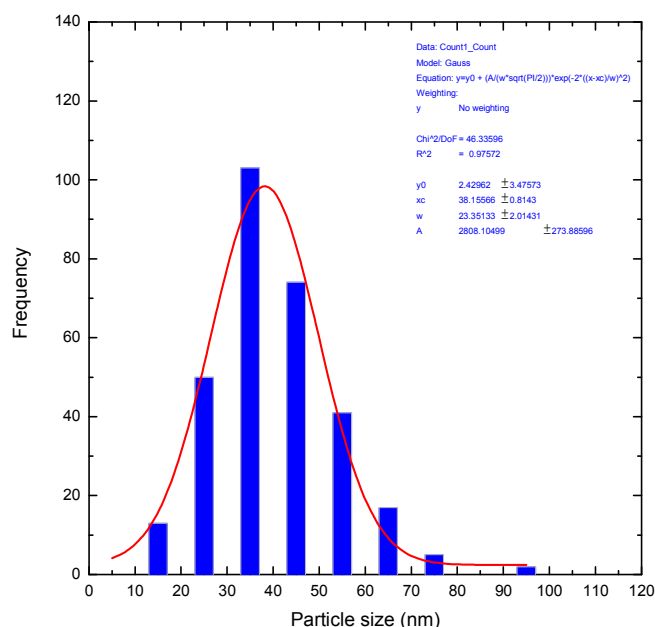
Particle size distribution for the sample prepared at $T_{\text{aging}} = 70\text{ }^{\circ}\text{C}$:

Figure 4.25 Size distribution of LSMO nanoparticles prepared by hydrothermal method with aging temperature of $70\text{ }^{\circ}\text{C}$.

Since only the LSMO particles prepared at aging temperature of $70\text{ }^{\circ}\text{C}$ show a well defined spherical structure, we can only determined the size distribution of this sample from the TEM images. The distribution of the nanoparticles is shown in Fig. 4.25. The particle size ranges from 15 nm to 95 nm and the size distributions matched very well with the Gaussian distribution. The geometric mean diameter of our LSMO particles obtained from the figure is 38 nm. As mentioned before, the critical size of perovskite manganite nanoparticles have been reported as 80 nm [24]. Our results imply that single magnetic domain occurs in this sample.

**Magnetic properties:**

As mentioned before, the magnetic properties are also highly dependent on the size and shape of the nanocrystals. For further understanding of the magnetic properties of LSMO particles with different morphology, we have performed field dependent magnetization measurements from 20 K to 300 K by a vibrating sample magnetometer (VSM).

In Fig 4.26, we plot the magnetic field dependence of the magnetization of LSMO particles formed from different aging temperatures. The figures clearly show that no magnetic hysteresis loops are obtained at 300 K for all samples. The magnetization at room temperature is low and saturates at a low magnetic field of 1 kOe. At low temperature of 20 K the magnetization is increased. The particles are obviously superparamagnetic (SPM) at 300 K, and ferromagnetic at 20 K. The large coercive field (H_c) of the particles at low temperature can be attributed to the high anisotropy and also the magnetic domain wall pinning process of particles. This behavior confirms that the LSMO nanoparticles are magnetically frozen below the blocking temperature (T_B) and undergo a superparamagnetic to ferromagnetic transition.

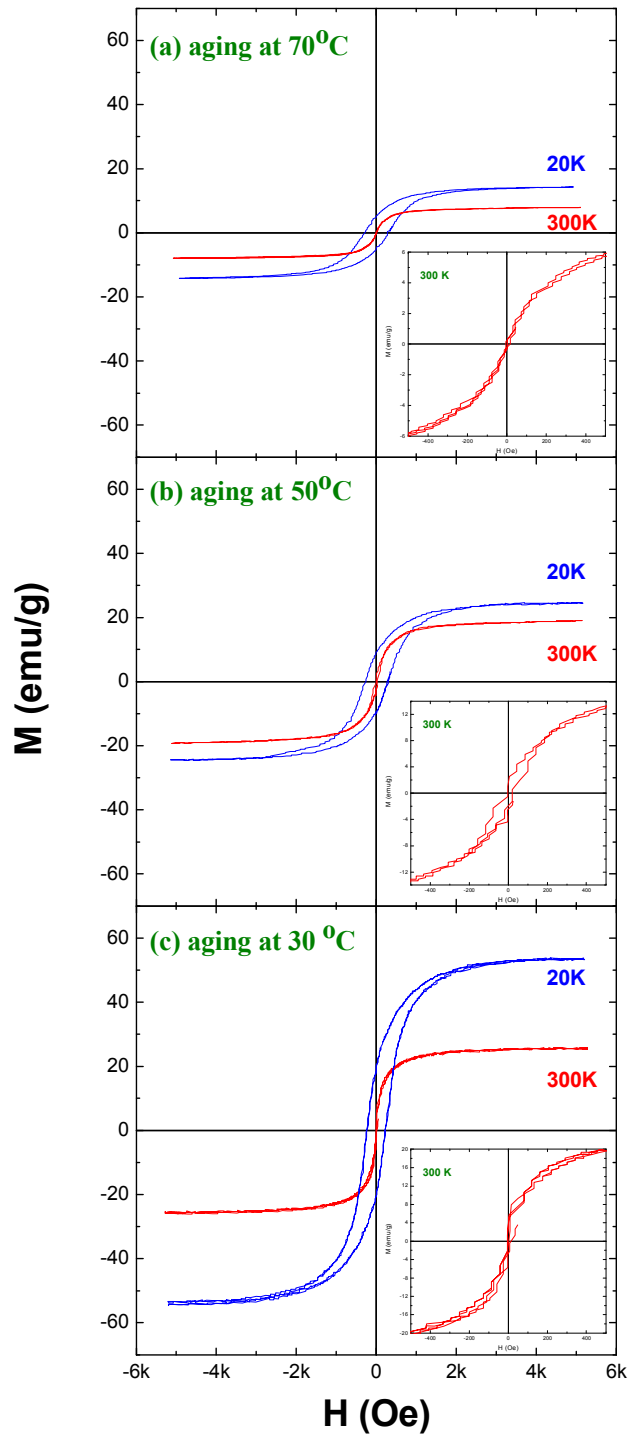


Figure 4.26 Field dependent magnetization curves of sample prepared at different aging temperatures: (a) 70 °C, (b) 50 °C and (c) 30 °C, respectively. (the small inset show M-H curve at 300 K in enlarged scale)

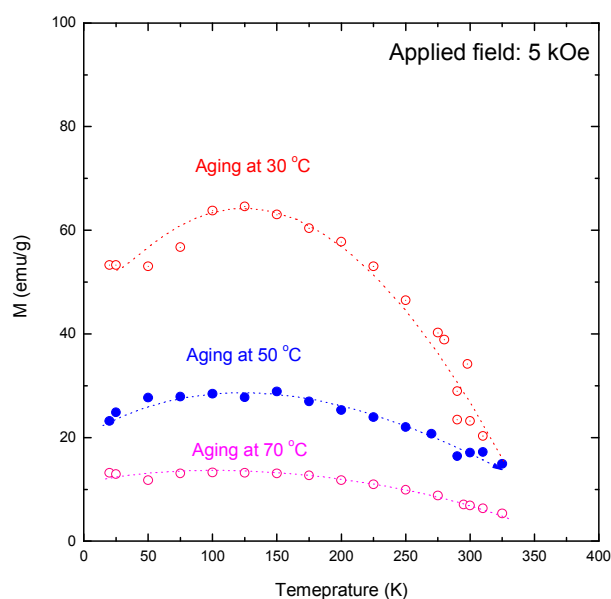


Figure 4.27 Temperature dependence of magnetization of LSMO particles prepared at different T_{aging}

The temperature dependence of magnetization (M) of the LSMO particles prepared at different aging temperatures (T_{aging}) is summarized in Fig. 4.27. As seen from our results, the M decreases with increasing T_{aging} . Although we cannot take the measurement at higher temperature, the presence of M_s at 300 K affirms that all samples have Curie temperature (T_c) well above room temperature. The decrease of M with increasing T_{aging} could also be explained by the combination of manganite crystallinity and surface effect of the nanostructured magnetic grain. In our previous XRD studies, it revealed that the best crystallinity was obtained for the sample treated at $T_{\text{aging}} = 30$ °C. TEM images on the other hand, indicate the particle size decreases with increasing aging temperature. Therefore, larger M could be obtained and the magnetic disorder could be suppressed by the reduction of surface area for sample treated at lower T_{aging} .

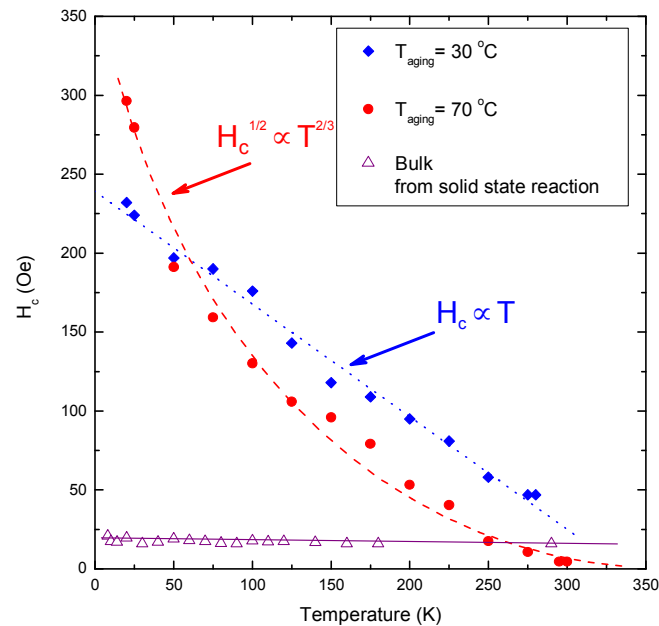


Figure 4.28 Temperature dependence of coercive field of LSMO particles prepared at different T_{aging} .

It is noted that the low temperature coercive field (H_c) has been enhanced remarkably for the LSMO particles prepared at higher aging temperature (T_{aging}) in comparison with bulk samples. The main reason is due to the reduction of particle size. Small particle size leads to a large number of broken bonds and enhanced surface stress, making the surface anisotropy term larger. Also, there is a strong interaction between the core and surface in LSMO nanoparticles. These cause an overall increase of anisotropy constant resulting in stronger coercive field.

In Fig. 4.28, it clearly illustrates the dependence of the H_c on the temperature for the sample treated at different T_{aging} . For the sample aged at $30\text{ }^\circ\text{C}$, the H_c decreases linearly with increasing temperature. This indicates a weak domain wall pinning feature. But for the sample aged at $70\text{ }^\circ\text{C}$, the coercive field only fits to a



relation of $H_c^{1/2}$ against $T^{2/3}$. In this case strong domain wall pinning dominates. In fact, it is well known that the surface morphology also play an important role for domain wall pinning. A rough surface causes formation of much more defects compared with a smooth surface. The surface defects easily act as domain wall pinning sites. Therefore a rich domain wall pinning sites in smaller sized particles provide an extra hindrance to the magnetization reversal. Correspondingly it induces an increase in coercive field.

4.3.4 Influence of concentration of mineralizer – potassium hydroxide (KOH) in hydrothermal process

The phase stability diagram under hydrothermal condition provides profound information about the optimal process requirements. However, the details of particle nucleation and coarsening mechanisms remain unknown. The particle morphology is not only important for application, but also provides insight into the mechanism in producing the magnetic nanoparticles. In this section, the influence of the concentration of mineralizer KOH in the starting precursor on the resulting morphology will be presented. A possible mechanism of morphological evolution under different initial KOH concentration is proposed to explain the observations.



Experiment:

Since the mineralizer plays a predominant role for precipitation of La, Sr and Mn, the addition of KOH in the precursor may be vital for the whole hydrothermal precipitation processing. In this section, aqueous KOH solution was added to adjust the pH to a required value. The KOH was added dropwise into the reagent solutions at a slow speed under magnetic stirring. Initial [KOH] of the precursors was varied from 1.5 M to 12 M in this experiment. Then the final precursor was subject to the hydrothermal treatment in an autoclave. The hydrothermal process was conducted at 240 °C for 24 hours.

Structural characterization

The x-ray powder diffraction patterns of the prepared $\text{La}_x\text{Sr}_{1-x}\text{MnO}_3$ powders are illustrated in Fig. 4.29. These samples correspond to the mixed solution of the reagents with different concentration of KOH mineralizer. These XRD patterns show the characteristic peaks of their perovskite structure. In addition to the peaks of manganite, extra peaks corresponding to impurities, mainly of $\text{La}(\text{OH})_3$, are observed for the samples prepared at low [KOH] at 1.5 M to 4.5 M. Also the relative intensity of diffraction peaks from this $\text{La}(\text{OH})_3$ impurity was substantially decreased with increasing the [KOH]. Hence, it indicates that the $\text{La}(\text{OH})_3$ is partially precipitated at low [KOH], meaning that the hydrothermal reaction is incomplete. When the concentration of KOH is increased to higher than 4.5 M, the diffraction peaks of the impurities are completely removed and LSMO is concurrently formed. It suggests that the minimum [KOH] required for the LSMO particle formation via our hydrothermal condition is $\sim 5\text{M}$.

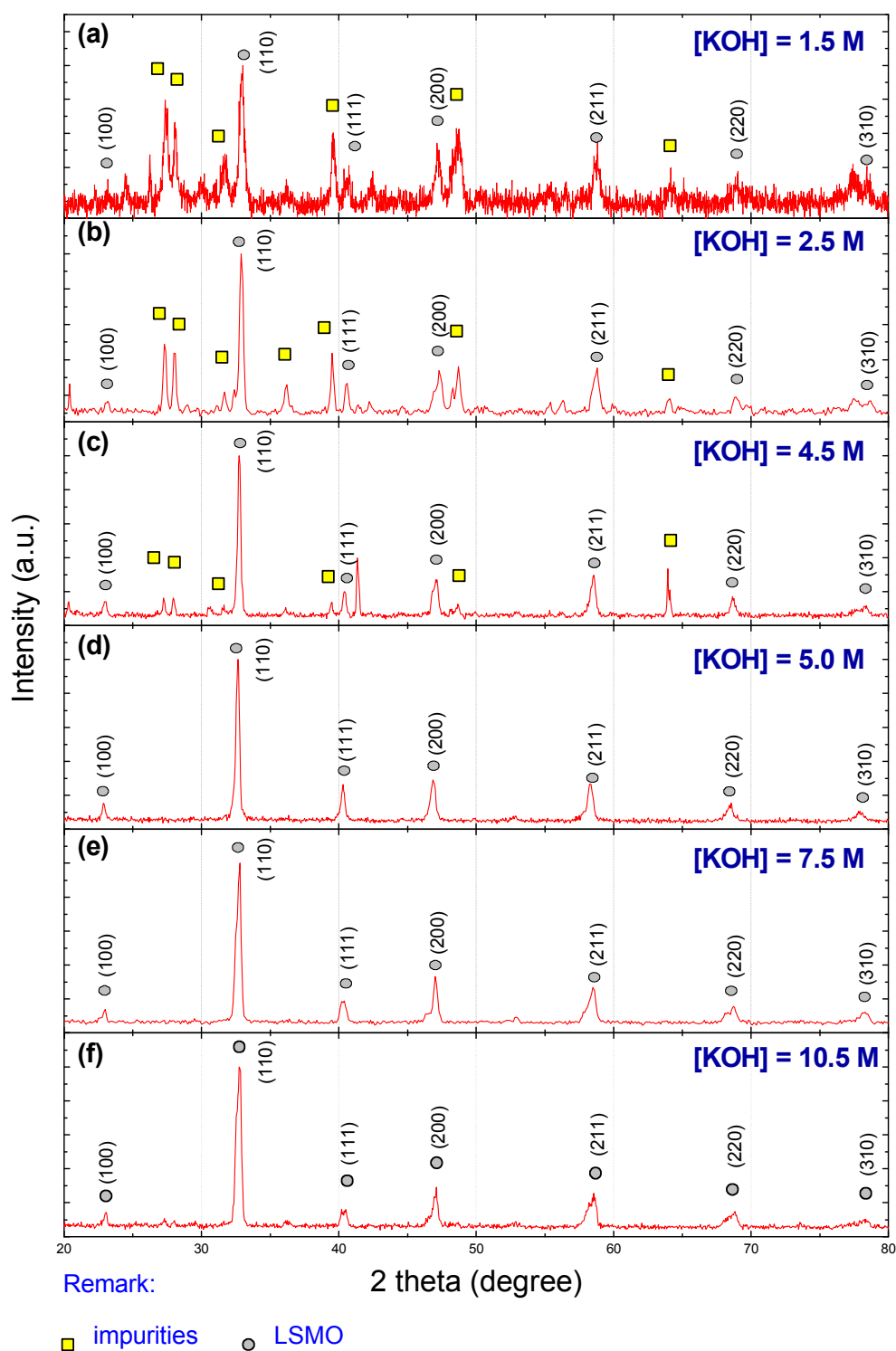


Figure 4.29 XRD diffractions of LSMO samples synthesized at 240°C with different initial KOH concentration: (a) 1.5 M, (b) 2.5 M, (c) 4.5 M, (d) 5.0 M, (e) 7.5 M and (f) 10.5 M, respectively.

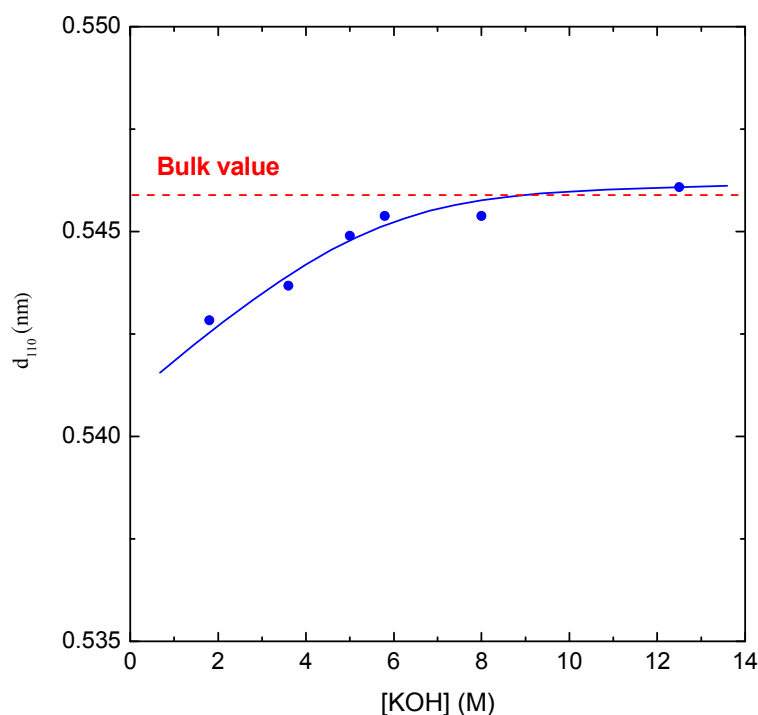


Figure 4.30 Lattice parameters of LSMO particles prepared at different initial [KOH].

Lattice parameters are obtained from the diffraction peaks of (110) plane in Fig. 4.29 and then summarized in Fig. 4.30. For the sample prepared in low [KOH], the lattice parameter of d_{100} is found to be smaller than the value for the LSMO bulk sample of the same composition. The main reason may be due to the non-stoichiometric LSMO formed by the incomplete hydrothermal reaction. When the amount of [KOH] is further increased, the lattice parameter of the LSMO particles becomes close to the bulk value. Phase pure LSMO are obtained when the initial [KOH] is over 4.5 M. It reveals that the KOH is playing an important role in the chemical reaction.

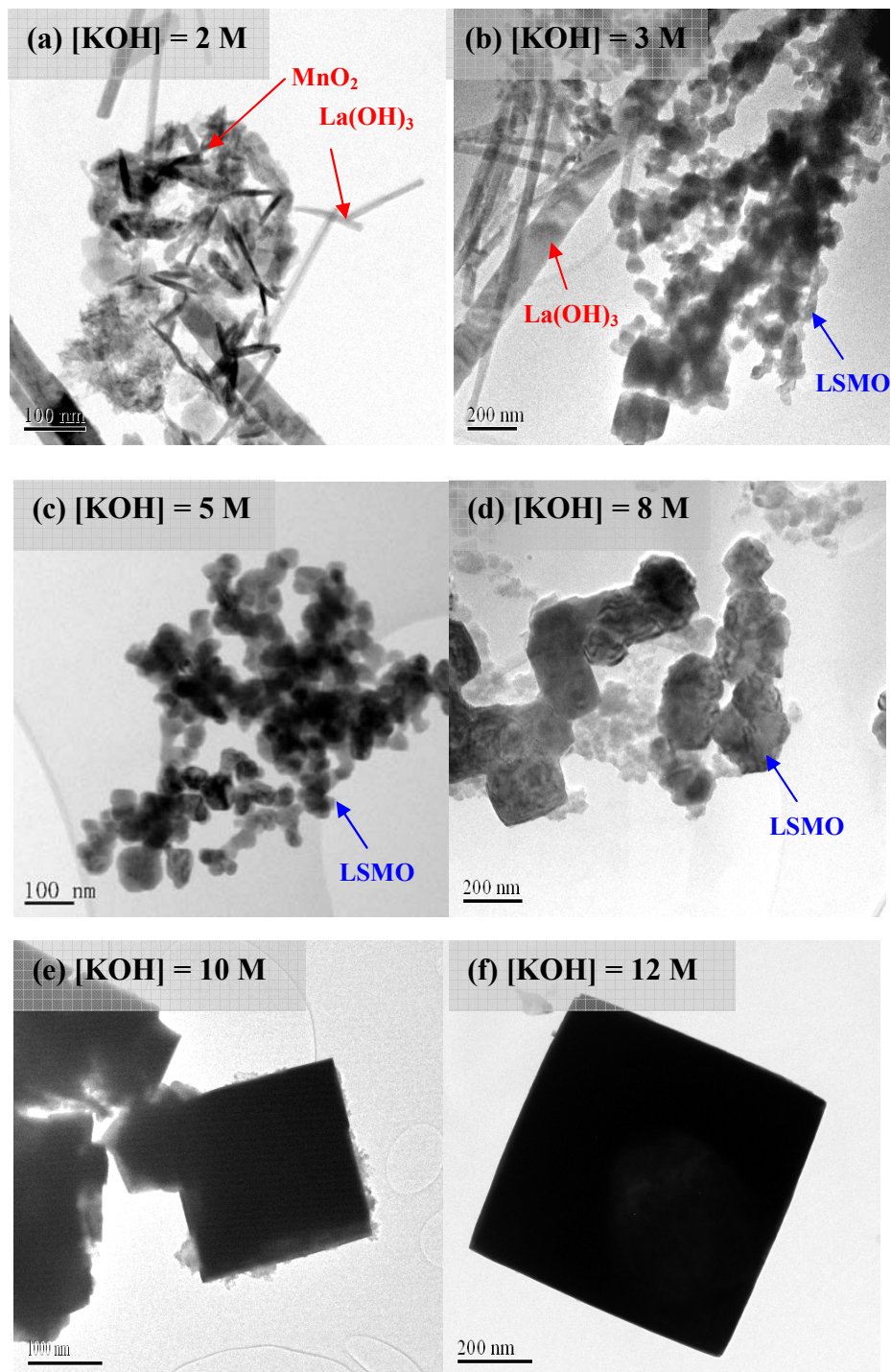


Figure 4.31 TEM images of LSMO particles synthesized at 240°C with different KOH concentration: (a) 2 M, (b) 3 M, (c) 5 M, (d) 8 M, (e) 10 M and (f) 12 M, respectively.



In order to investigate the effect of initial [KOH] on particles formation, transmission electron microscope (TEM) was used to study the as-synthesized LSMO particles. TEM observations have revealed that the initial [KOH] is more influential on the LSMO particle morphology than the processing temperature. The change of initial [KOH] not only affects the reaction rate, but also the crystal growth mechanism and anisotropy.

The TEM images as shown in Fig 4.31(a) and 4.31(b) are needle shaped MnO_2 and rod-like $\text{La}(\text{OH})_3$ nanoparticles. They are formed when the precursor is treated with 2 M to 3 M initial [KOH]. Evidently, manganese dioxide (MnO_2) and the lanthanum hydroxide ($\text{La}(\text{OH})_3$) are partially precipitated at lower initial [KOH]. The hydrothermal reaction (dissolution/precipitation) is incomplete. As a result, many unreacted species still exist in the product. This is consistent with the XRD observations, indicating that higher [KOH] will provide higher driving force to increase the reaction rate. As shown in Fig. 4.31(c), stoichiometric LSMO particles are formed in spherical shape with size less than 100 nm. Although there are some agglomerations, the nano-sized particles should be small enough to exhibit single domain features.

When the [KOH] is as high as 8M, particles of a few hundreds of nm in size with well defined edges and facets of cubic structure can be produced. They are represented by the TEM images shown in Fig 4.31(e) and 4.31(f). Therefore, the optimized initial [KOH] is about 5 M in order to produce good crystalline and small size LSMO nanoparticles from the hydrothermal process.



As mentioned before, the hydrothermal process is controlled by the dissolution-recrystallization mechanism. When the reactants are heated, hydrolyzation occurs. During this process, the precursors are dissolved in the aqueous solution to form anisotropic LSMO nuclei. It is believed that anisotropic growth occurs only when the chemical potential of several surfaces is much higher than others.

In fact, the influence of [KOH] on nucleation and grain growth in chemical synthesis of particle is quite different. At low initial [KOH], the concentration of reagents can hardly initiate the nucleation. The transformation of raw precursor to LSMO is dominated by continuous homogeneous nucleation inside the suspension. The majority of the precursor in the solution would be consumed in this stage. It therefore inhibits further nucleation. The higher solubility of LSMO at higher [KOH] could effectively prompt the dissolution-precipitation process, which might dominate the coarsening in this case. At intermediate [KOH], nucleation and grain growth can occur spontaneously, resulting in a high possibility of secondary nucleation and a broader size distribution. These observations reveal that [KOH] plays an important role in determining the anisotropic growth orientation of the crystal.



4.4 Composition study

The hole-doped perovskite manganites of composition $\text{La}_x\text{Sr}_{1-x}\text{MnO}_3$ exist over the whole range of x from 0 to 1. Especially in the range of x from 0.5 to 0.8, the material at low temperature is ferromagnetic and metallic-like [28]. In previous sections, we have mentioned that the modified hydrothermal method is a versatile method for the fabrication of $\text{La}_{0.67}\text{Sr}_{0.33}\text{MnO}_3$ with good stoichiometry. The present study is aimed at using the same method to synthesize LSMO particles with other composition. The structural and magnetic properties of these as-prepared particles are also presented.

As mentioned by Jeffrey [11] in the synthesis of mixed valence manganites with controllable doping levels by chemical approach, one of the important parameter is the average oxidation state of the Mn ion in the precursor. This control over the Mn oxidation state is achieved by changing the ratio of two Mn chemicals (MnCl_2 and KMnO_4), which contain Mn ions with two distinct initial oxidation states. Therefore, the flexibility of the chemical reaction enables us to synthesize other possible manganites by the same technique. In our experiments, LSMO precursors with different compositions (x from 0.5 to 0.7) were prepared accordingly to the stoichiometric amount of high purity LaCl_3 , SrCl_2 , MnCl_2 and KMnO_4 used. Hydrothermal reaction was performed at 240 °C for 24 hours duration.

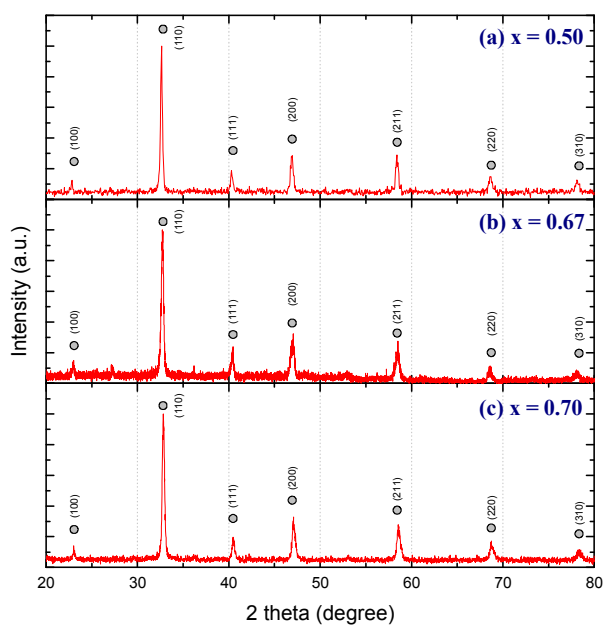


Figure 4.32 XRD patterns of $\text{La}_x\text{Sr}_{1-x}\text{MnO}_3$ particles prepared by hydrothermal process with composition of (a) $x = 0.5$, (b) $x = 0.67$ and (c) $x = 0.7$.

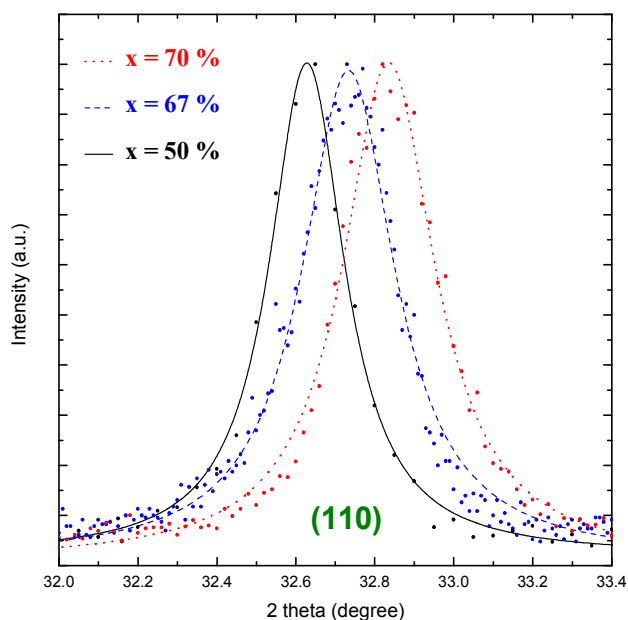


Figure 4.33 The diffraction peaks of d_{110} of as-synthesized LSMO nanoparticles with different composition (x).

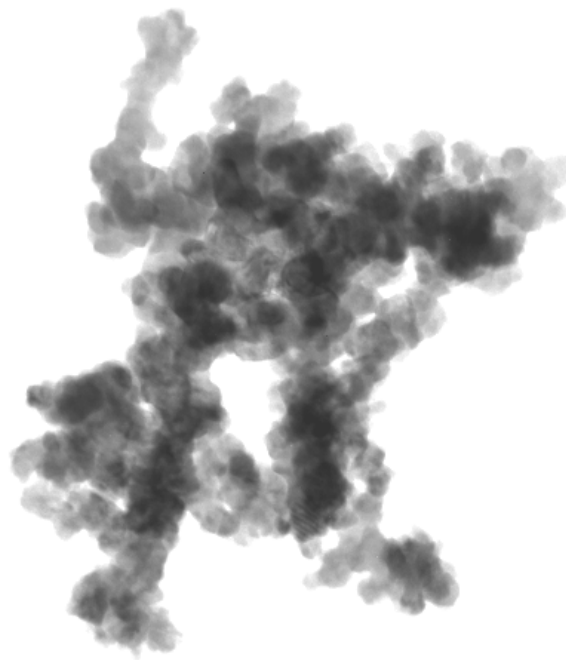


In order to evaluate the structural quality of the synthesized nanoparticles, X-ray diffraction patterns are obtained with a Philips X-ray diffractometer using CuK_α radiation with a nickel filter. Bragg equation and Scherrer's equation are used to determine the lattice parameter and the particle sizes, respectively. Fig. 4.32 shows the powder X-ray diffraction patterns of as-prepared LSMO particles with composition ranged of $0.5 \leq x \leq 0.7$, respectively. All the peaks in these figures can be indexed to the structure of perovskite manganite. The XRD patterns of the samples show good crystalline structure and without impurity phase.

In Fig 4.33, as the strontium content increases in $\text{La}_x\text{Sr}_{1-x}\text{MnO}_3$, the diffraction peaks of (110) slightly shift to smaller 2-theta values, indicating that the lattice-parameters increase with strontium doping content. This may be caused by the larger ionic radius of Sr^{2+} ion (0.127 nm) in comparison with La^{3+} ion (0.122 nm). This shift also confirms the accommodation of Sr^{2+} ion into the lattice structure. The lattice parameters of $\text{La}_x\text{Sr}_{1-x}\text{MnO}_3$ nanoparticles determined from the diffraction peaks are 0.388, 0.386 and 0.385 nm for $x = 0.5$, 0.67 and 0.7, respectively. The results are in agreement with the lattice parameters of bulk materials with the same doping level.

Crystalline sizes of the samples are calculated from broadening of the x-ray powder diffraction peaks using the Scherrer's equation. In the present work, the crystallite sizes of the manganite particles are all about 30 nm.

(a)



200 nm

(b)

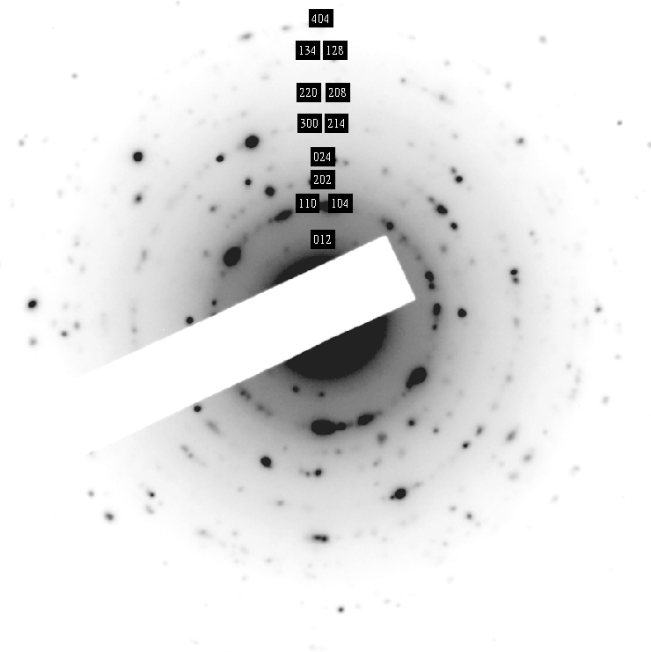


Figure 4.34 (a) TEM image and (b) SAD image of hydrothermal $\text{La}_x\text{Sr}_{1-x}\text{MnO}_3$ nanoparticles ($x = 0.5$).



The morphology of LSMO nanoparticles with composition $x = 0.5$ are investigated by TEM. The samples are seen to compose of LSMO nanoparticle aggregates. To access the stoichiometry of LSMO nanoparticle, energy dispersive x-ray spectrometry has also been performed on individual LSMO particles using a TEM. The composition of the as-synthesized LSMO particles from different precursor was determined by EDX and summarized in Table 4.4. The results have confirmed that La, Sr and Mn are present in the correct amount as the designed composition stoichiometry.

Table 4.4 Composition measurement (EDX) of LSMO particle compared with expected value.

Sample	Element:	La	Sr	Mn
1	Expected	0.5	0.5	1
	Experiment	0.48	0.52	0.90
2	Expected	0.67	0.33	1
	Experiment	0.64	0.36	0.95
3	Expected	0.7	0.3	1
	Experiment	0.72	0.28	0.95

In here, we have demonstrated that controllable composition of single crystalline LSMO can be produced by cationic surfactant hydrothermal methods. The technique therefore also enables us to investigate the size dependent evolution of nanoscale phase separation, magnetism and CMR in other mixed valence manganites.

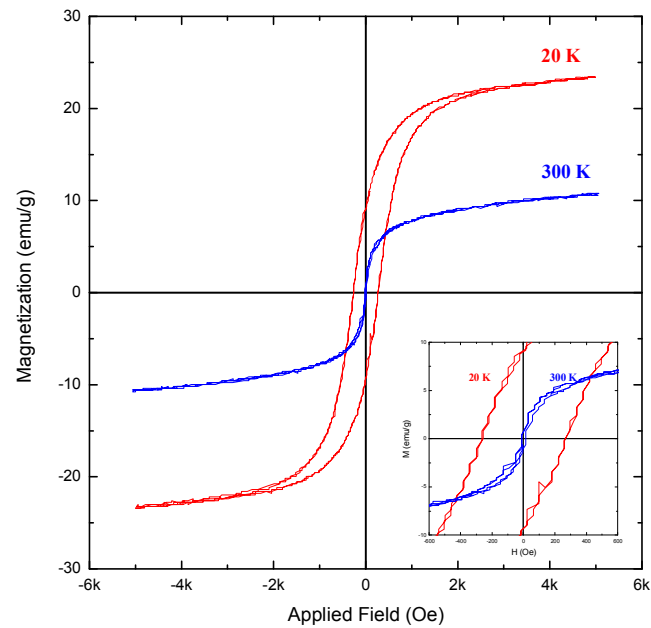


Figure 4.35 Magnetization curve of $\text{La}_{0.5}\text{Sr}_{0.5}\text{MnO}_3$ nanoparticles.

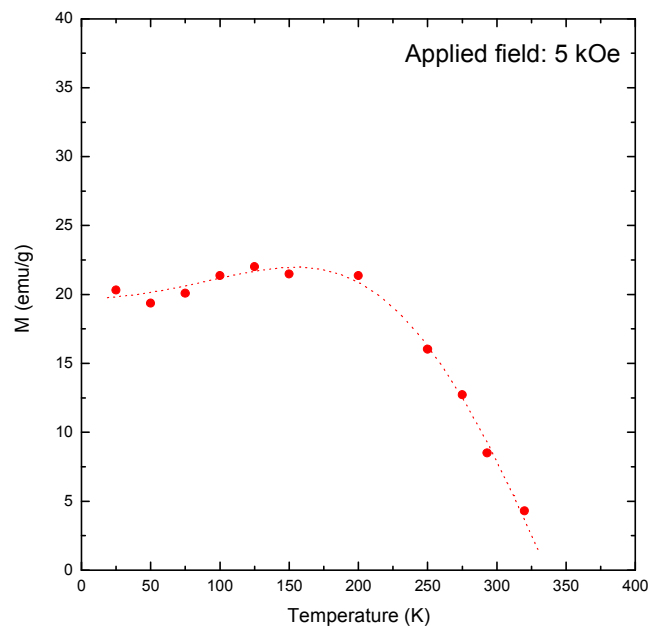


Figure 4.36 Temperature dependence of magnetization of hydrothermal $\text{La}_{0.5}\text{Sr}_{0.5}\text{MnO}_3$ nanoparticles.



Similar to measurements on $\text{La}_{0.67}\text{Sr}_{0.33}\text{MnO}_3$ as described in earlier sections, we focus on the magnetic characterization of $\text{La}_{0.5}\text{Sr}_{0.5}\text{MnO}_3$ in this section. Full magnetization measurements were performed as a function of temperature and applied field by vibrating sample magnetometer (VSM). During the measurement, the particles were compressed into a small pellet and mounted on the hand-made Teflon holder.

Fig 4.35 shows the magnetization curves of the sample measured at different temperatures. No magnetic hysteresis is observed at 300 K whereas a clear hysteresis loop with a large coercive field of 327 Oe is obtained at 20 K. This indicates that the $\text{La}_{0.5}\text{Sr}_{0.5}\text{MnO}_3$ nanoparticles are superparamagnetic at room temperature and the blocking temperature (T_B) is below room temperature.

The magnetization (M) of the sample is shown in Fig. 4.36. This figure shows a value of 20.5 emu/g at 20 K which is much smaller than that of the corresponding bulk $\text{La}_{0.5}\text{Sr}_{0.5}\text{MnO}_3$ of 80 emu/g. It may be due to the small particle size and high surface disordering of the manganite. In the low temperature range, the magnetization is more or less constant reflecting domain motion. Thus this sample shows a typical low field magnetization behavior of an ordinary ferromagnet. From this curve, the magnetization tends to zero at 337 K. This point should be the Curie temperature (T_C) of the $\text{La}_{0.5}\text{Sr}_{0.5}\text{MnO}_3$ particles. It is in good agreement with the bulk sample. Similarly, the transition is broad compared to the bulk samples. This suggests a possible existence of wide distribution of exchange interaction.

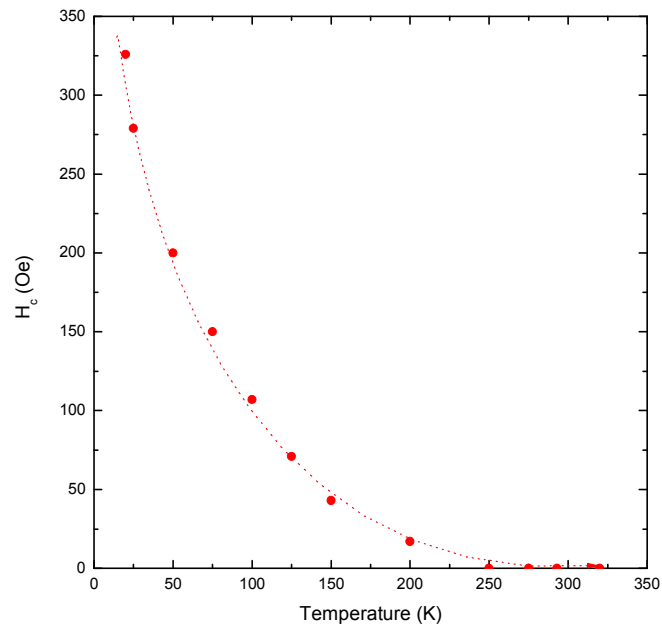


Figure 4.37 Temperature dependence of coercive field of $\text{La}_{0.5}\text{Sr}_{0.5}\text{MnO}_3$ nanoparticles.

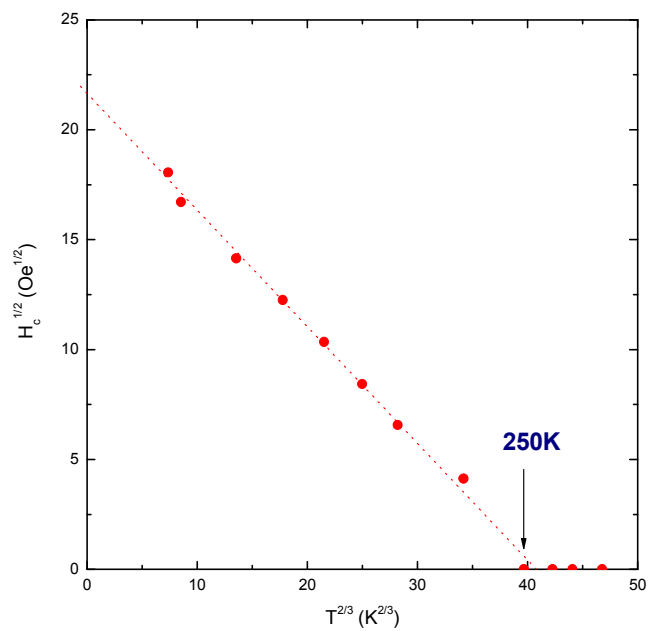


Figure 4.38 Graph of $H_c^{1/2}$ against $T^{2/3}$ for $\text{La}_{0.5}\text{Sr}_{0.5}\text{MnO}_3$ nanoparticles.



Fig. 4.37 shows the coercive field (H_c) dependence on temperature. Apparently the coercive field decreases with increase of measuring temperature. For example, H_c drops from 327 Oe at 20 K to about 0 Oe at 250 K for $\text{La}_{0.5}\text{Sr}_{0.5}\text{MnO}_3$. This may be caused by contributions of intrinsic temperature dependence of the anisotropy and magnetization, and thermal activation effects. Such result is similar to the sample of $\text{La}_{0.67}\text{Sr}_{0.33}\text{MnO}_3$. This figure also shows that the temperature dependence of the coercivity does not follow a linear law. We can then discard the existence of weak-domain wall pinning regime of random inhomogeneities. We have plotted another curve of $H_c^{1/2}$ against $T^{2/3}$ in Fig. 4.38. From this figure, the best fit was obtained using the strong domain wall pinning model in the temperature range from 20 to 250 K.

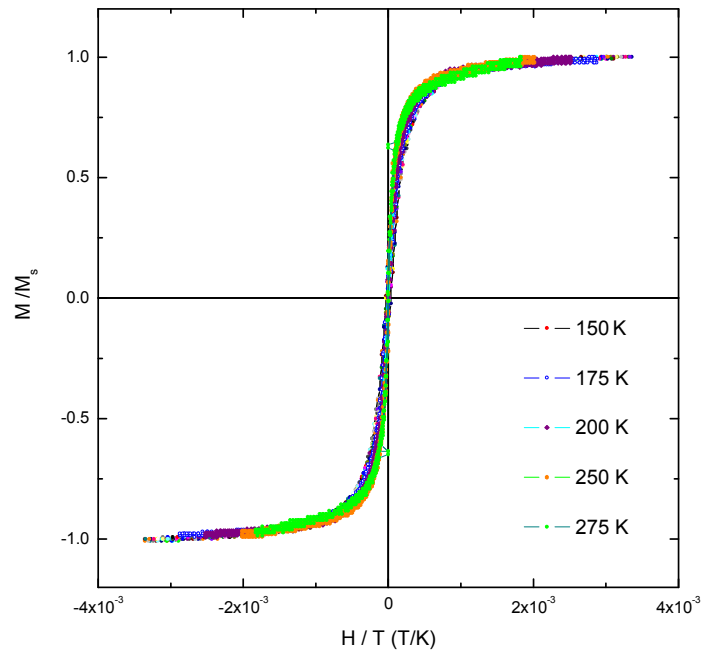


Figure 4.39 A graph of M/M_s against H/T for $\text{La}_{0.5}\text{Sr}_{0.5}\text{MnO}_3$ nanoparticles.

Moreover, the superparamagnetic behavior of this $\text{La}_{0.5}\text{Sr}_{0.5}\text{MnO}_3$ sample above T_B was confirmed by magnetization curves measured between 150 K to 275 K. Basically, the M/M_s curves plotted against H/T for the temperature above T_B should result in a universal curve in superparamagnetic particles. As shown in Fig. 4.39, the curves of (M/M_s) against (H/T) for the LSMO particles in this temperature range are superimposed perfectly. It can be said that the particles are in good agreement with the superparamagnetic state above the blocking temperature.



4.5 Size induced change of magnetic properties of LSMO nanoparticles

The effect of grain size on magnetic, transport and structural properties of manganites have been intensively investigated. General attributions are that the particle size and grain boundary effect play an important role in magnetic and electronic properties of these manganite materials. In this section, we study the magnetic properties of nanosized $\text{La}_{0.67}\text{Sr}_{0.33}\text{MnO}_3$ particles prepared by our cationic surfactant assisted hydrothermal method. The data obtained from the good crystalline high purity LSMO particles ($x = 0.67$) are compared with those for the bulk sample of the same composition in order to reveal the size induced changes from contribution of surface effects.

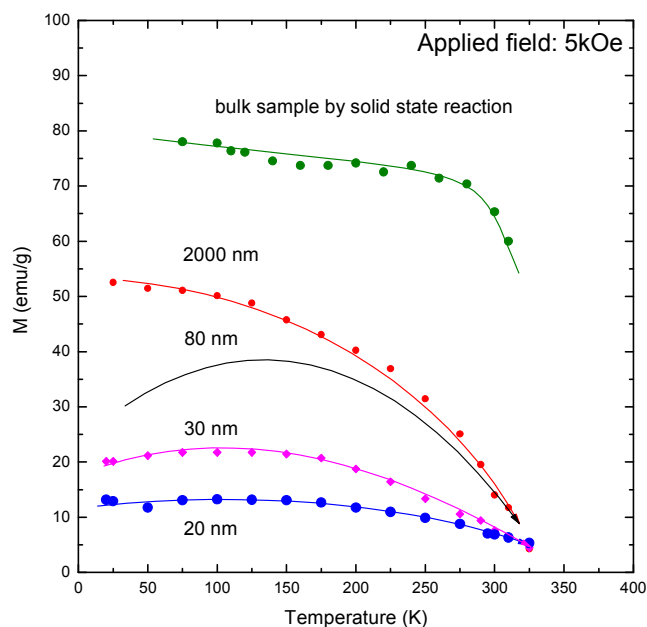


Figure 4.40 Magnetization (M) of the LSMO particles with different particle dimensions.



The temperature dependence of magnetization (M) of the LSMO nanoparticle exhibits a markedly different behavior than that of the bulk magnetization. In Fig. 4.40, the magnitude of the M for the bulk sample is close to the value for full ferromagnetic order of the constituent Mn^{3+} and Mn^{4+} ions. It shows the M of LSMO nanoparticles decrease with particle size. Although we cannot take the measurement at higher temperature, the presence of M at 300 °C verifies that both samples have Curie temperature (T_c) well above room temperature. Apparently, it can be observed that M of the LSMO samples with crystallite size of 80 nm was dropped gently at lower temperature. It may due to the spin freezing under a zero field-cooled (ZFC) process. Fig. 4.41 shows the variation of the M as a function of particle size measured at 20 K. The decrease of M with particle size could be explained by considering the formation of a non-magnetic surface layer of the particles, in which magnetic moments do not contribute to the magnetization in the applied field. It is well known that coupling among magnetic ions at the surface is much weaker than that in the core due to presence of a large number of dangling bonds and non-coordination of the atoms at the surface. The lattice structure on the surface is semi-amorphous and the magnetic configuration of such materials is very sensitive to the structure. According to Li [29], by assuming that the interface layers have zero magnetization, a lower limit of the layer thickness (t) can be determined by the equation: $t = (r/2)\{1 - (M_s / M_{so})^{1/3}\}$ where M_s and M_{so} represent the saturation magnetization of the particles and the conventional bulk sample, respectively. Results shown in Fig. 4.42 suggest the non-magnetic surface layer for the LSMO nanoparticles are around 5 - 8 nm.

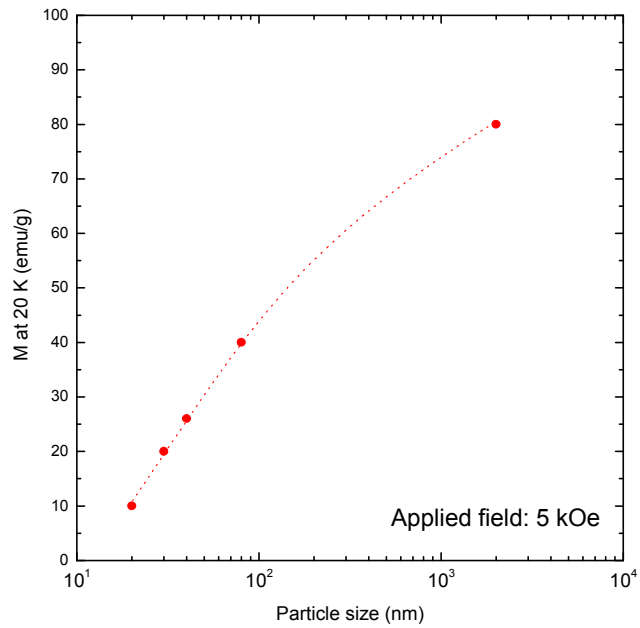


Figure 4.41 Effect of particle size on the magnetization (M_s) at 20 K temperature.

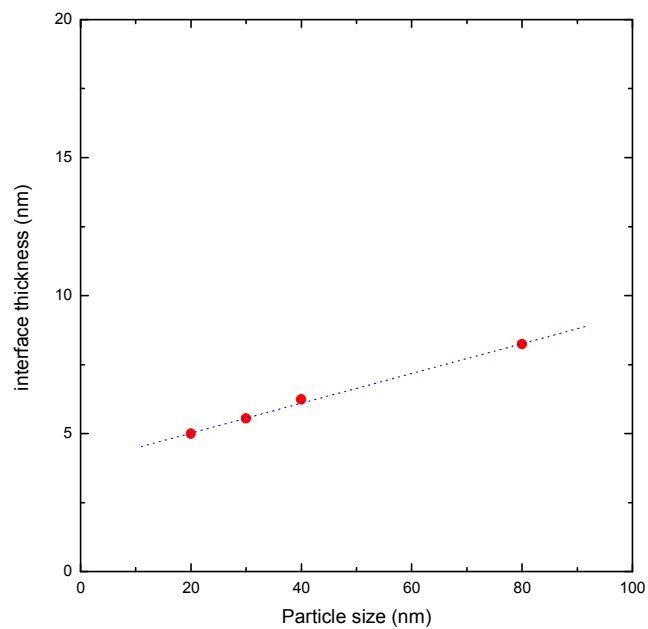


Figure 4.42 Interface thickness against the particle size of LSMO samples.



4.6 Electrical transport measurement

The electrical transport behavior of the LSMO particles was studied by measuring their resistivity as a function of temperature. Experiments used standard four-point probe method without applied magnetic field. Measurements were carried out using an electrometer with an applied current of 10 mA in the temperature range of 20 – 350 K at an interval of 0.2 K. The samples used in this experiment were 4 mm diameter pellets made from different sized initial LSMO particles. They were formed by compressing and then sintering at 800 °C for 10 hours in air.

The variation of zero field resistivity of LSMO ($x = 0.67$) pellets as a function of temperature down to 20 K is shown in Fig 4.43. These three samples have initial average particle size of 20 nm, 40 nm and 2000 nm, respectively. From the figure, we observe that the resistivity increases substantially as the particle size decreases. Also, it is found that the sample with initial particle sizes of 40 nm and 2000 nm sample show a metal-insulator (M-I) transition at T_p of 209.6 K and 309.7 K, respectively. For the 20 nm LSMO particles, no such transition is detected. It suggests that T_p decreases substantially with particle size. According to our previous experiments, all as-synthesized LSMO particles have a Curie temperature (T_c) well above room temperature. So, it implies that T_p is lower than its corresponding T_c when the LSMO particles size is reduced to nanoscale. The main reason may due to the insulating nature of the grain boundaries of manganites. This could increase the residual resistivity of the sample, which in turn decreases the density of ferromagnetic metallic region. Therefore, the T_p shifted to lower value and hence loss of long-range ferromagnetic order of the sample.

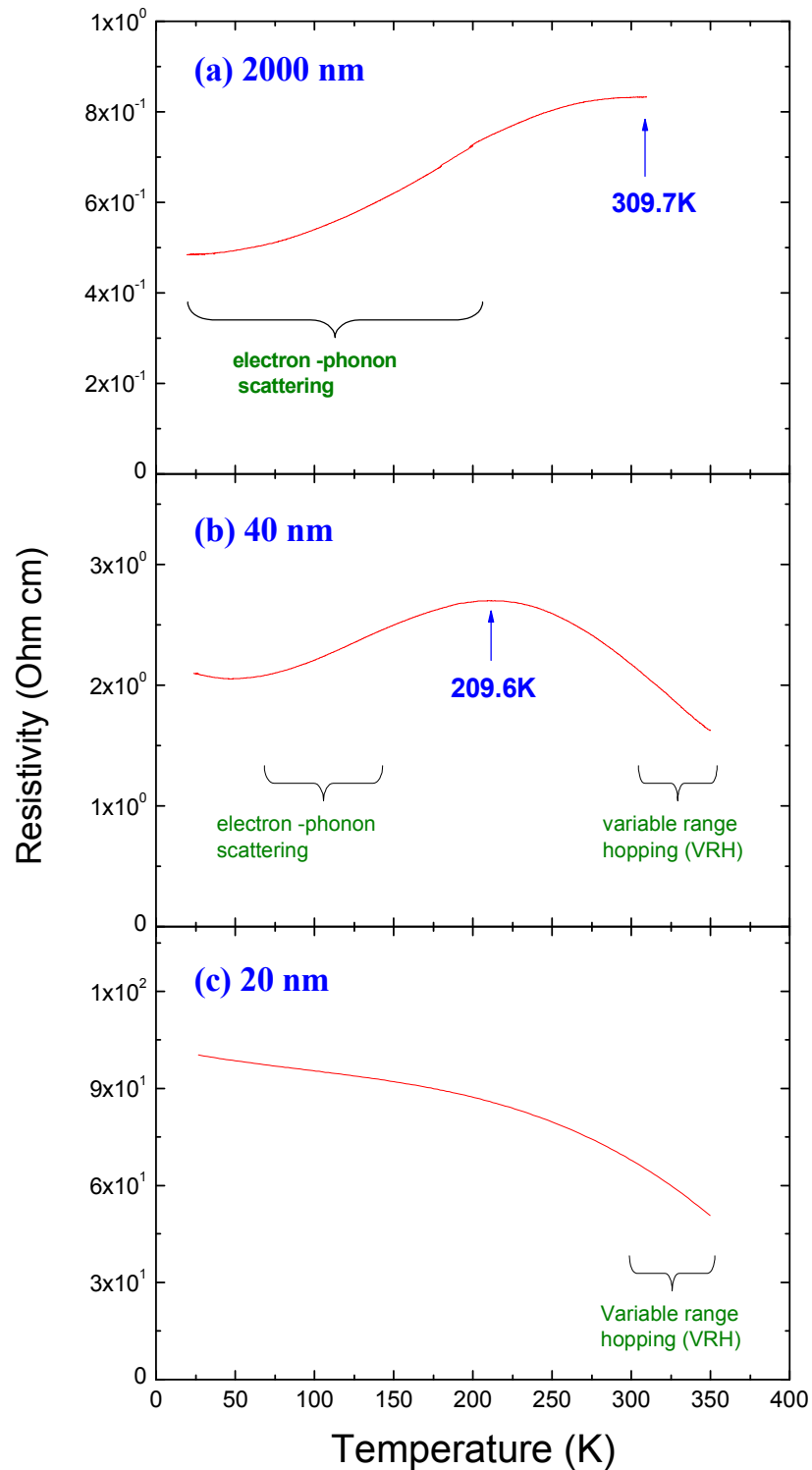


Figure 4.43 The temperature dependence of the resistance of nanocrystalline $\text{La}_x\text{Sr}_{1-x}\text{MnO}_3$ ($x = 0.67$) pellets with initial crystal size of (a) 2000 nm, (b) 40 nm and (c) 20 nm.



Electrical transport properties of LSMO with 2 μm grains

Now we only consider grains with size of 2000 nm. The positive slope of the ρ -T curve suggests a metallic like conduction in the temperature range from 20K to 300K. As mentioned by Nagabhushana [30], the electrical resistivity of divalent doped manganite such as $\text{La}_x\text{Sr}_{1-x}\text{MnO}_3$ can be fitted with an empirical equation in the low temperature regime: $\rho = \rho_1 + \rho_2 T^n$ where ρ_1 represents the resistivity due to grain boundary effect while T^n indicates resistivity due to scattering process. In our experiment, we can found that a best fit to the curve with $n = 2$ for the sample temperature between 20 K and 205 K as shown in Fig.4.44. Therefore, the above fit shows the electron-phonon scattering plays an important behavior of the sample.

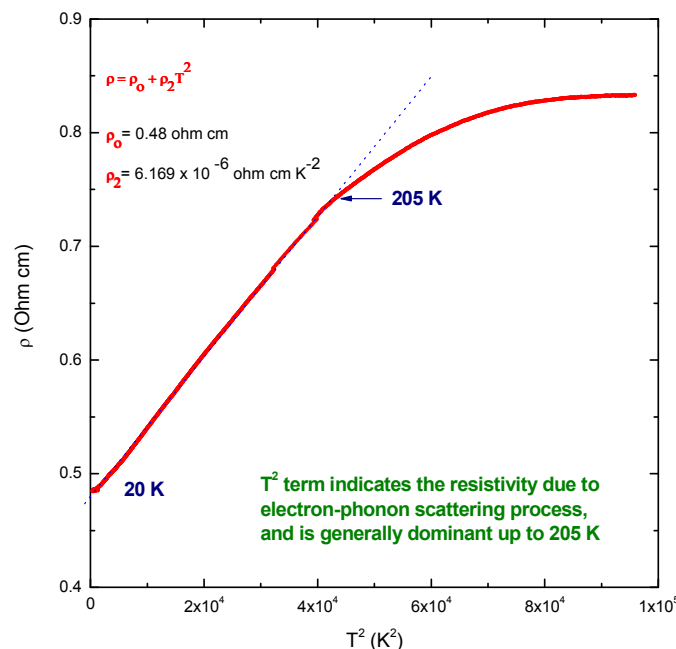


Figure 4.44 A graph of R against T^2 for LSMO particles with 2 micro grains.

**Electrical transport properties of LSMO with 40 nm grains**

For the sample with particle size of 40 nm, the electrical conductivity generally can be described by the same empirical equation below the metal-insulator transition temperature ($T_p = 209.6$ K). The experimental data of the present investigation were fitted to a simple equation of $\rho = \rho_1 + \rho_2 T^2$. Hence it indicates that the electron-phonon scattering process is the mechanism for the 40 nm LSMO in low temperature regime. Overall the results are similar to those of 2000 nm grain size LSMO sample.

But for the high temperature regime ($T > T_p$), the conduction mechanism of this sample is governed by the variable range hopping (VRH) model. This conducting behavior can be fitted by the follow equation:

$$\rho = \rho_o \exp\left(\frac{T_o}{T}\right)^{1/4}$$

where ρ is resistivity, ρ_o is pre-factor, T is temperature and T_o is the constant.

Indeed, variable range hopping is a model describing low temperature conduction in strongly disordered systems with localized states. T_o value for the sample was obtained from the slopes of $\ln(\rho)$ against $T^{1/4}$ plot as shown in Fig. 4.46. Finally, the density of states at the Fermi level for the sample was calculated by using the T_o values and the equation of:

$$T_o = \frac{16\alpha^3}{k_B N(E_F)}$$

where the inverse of the localization length (α) can be consider as 2.22 nm^{-1} [31].



Based on the present result, the density of states at the Fermi level for the LSMO (grain size = 20 nm) can be obtained as below:

$$T_0 = 1.677 \times 10^6 \text{ K}$$

$$\alpha = 2.22 \text{ nm}^{-1} = 2.22 \times 10^7 \text{ cm}^{-1}$$

$$k_B = 1.38 \times 10^{-23} \text{ JK}^{-1} = 8.617 \times 10^{-5} \text{ eV K}^{-1}$$

By substitution, the $N(E_F)$ was determined as $1.21 \times 10^{21} \text{ eV}^{-1} \text{ cm}^{-3}$.

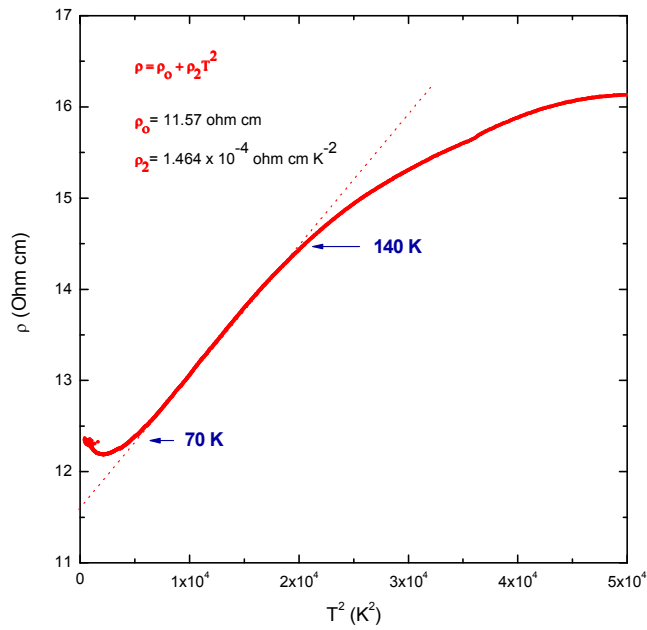


Figure 4.45 A graph of R against T^2 for LSMO sample with 40 nm grains.

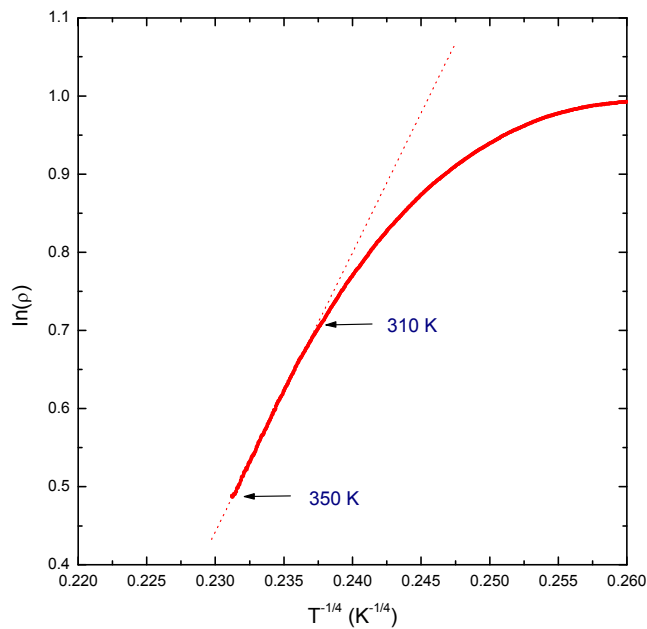


Figure 4.46 A graph of $\ln(\rho)$ against $T^{-1/4}$ for LSMO sample with 40 nm grains.

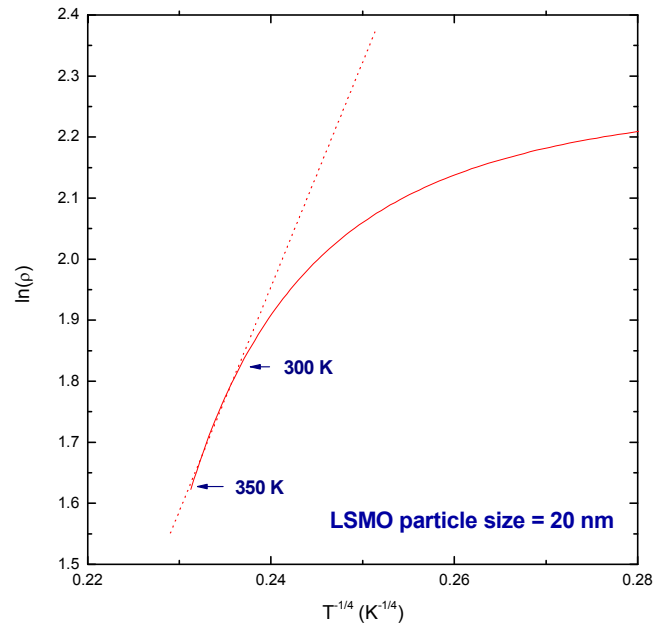
**Electrical transport properties of LSMO with 20 nm grains**

Figure 4.47 A graph of $\ln(\rho)$ against $T^{-1/4}$ for LSMO sample with 20 nm grain size.

For the LSMO sample with grain size of 20 nm, the temperature dependent resistivity in Fig. 4.47 shows a linear relation of ($\ln \rho$ against $T^{-1/4}$) in the temperature range from 300 to 350 K. Based on this result, the density of states at the Fermi level for the LSMO (grain size = 20 nm) can be obtained as below:

$$T_0 = 1.864 \times 10^6 \text{ K}$$

$$\alpha = 2.22 \text{ nm}^{-1} = 2.22 \times 10^7 \text{ cm}^{-1}$$

$$k_B = 1.38 \times 10^{-23} \text{ JK}^{-1} = 8.617 \times 10^{-5} \text{ eV K}^{-1}$$



By substitution, the $N(E_F)$ was determined as $1.09 \times 10^{21} \text{ eV}^{-1} \text{ cm}^{-3}$. T_0 is relatively higher than the reported value for bulk sample [32]. In fact, it is noticed that higher T_0 values indicate an increase in bending of Mn-O-Mn bond and hence it reflects the enhancement of carrier effective mass or the narrowing of the band width which in turn results in drastic change in the resistivity and sharpening the resistivity peak.

By comparing those results with the LSMO sample with 40 nm crystal grain, we obtain a higher $N(E_F)$ in 40 nm grains than in 20 nm grain. It verifies that more electrons are localized in smaller grains sample than in the larger one.



4.7 Magnetoresistance of sintered LSMO pellet

The manganites with relatively small grain sizes exhibit pronounced magnetoresistivity (MR) under a low applied magnetic field over a wide temperature range. The electronic and magnetic properties of nanocrystalline materials are modified due to the influence of structural and magnetic disorder at the interior and grain boundaries.

In order to explore the low-field MR (LFMR) in nano-sized grain of manganite, we have conducted a low temperature sintering (800 °C, 10 hours) of our as-prepared hydrothermal $\text{La}_{0.67}\text{Sr}_{0.33}\text{MnO}_3$ nanoparticles with a pre-treatment particle size of 20 nm. Fig. 4.48 shows the MR as a function of magnetic field up to 5 kOe. The MR loop of LSMO pellet at 20 K shows a butterfly feature at low-field region but quite linear at high fields region. It suggests that the sample is behaving like a typical granular ferromagnetic metal dispersed in non-magnetic matrix. This butterfly feature can be explained by the spin-polarized tunneling (SPT) mechanism [33]. The model predicts that the low-field MR (LFMR) is strongly dependent on temperature, i.e. the lower the temperature the higher the MR. Our data showed in Fig 4.49 is in broad agreement with this SPT model. Also, it is reported that the sharp increase of MR at low fields is due to the alignment of intergrain magnetic moment, and the almost linear increase of MR at high fields is due to the alignment of canted spins at intragrain [34]. As a result, it suggests that the SPT may be the dominant transport mechanism in our nano-sized grain manganite samples.

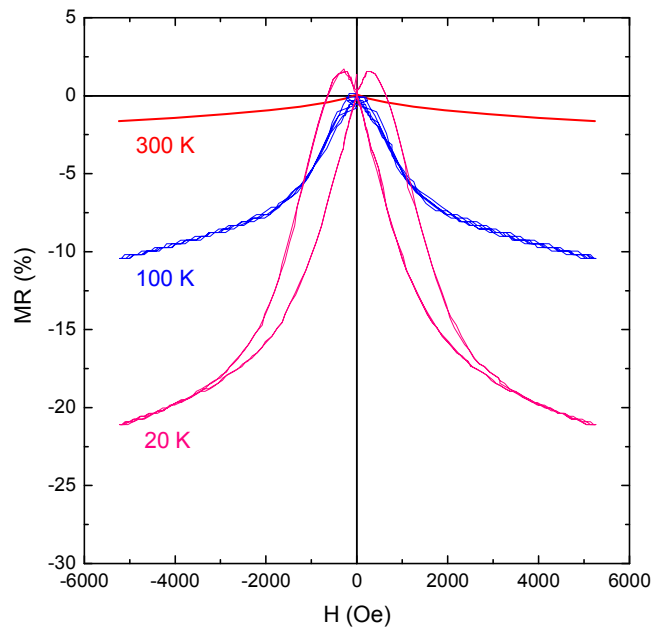


Figure 4.48 Magnetoconductance (MR) of sintered LSMO pellet as a function of an applied magnetic field at different temperatures.

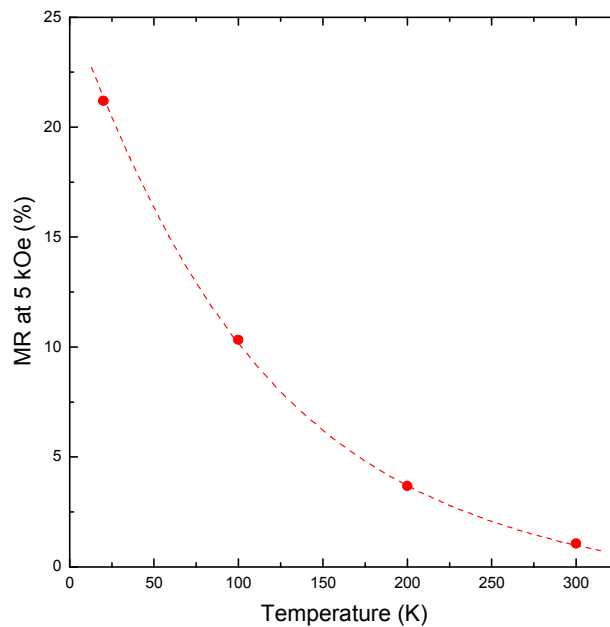


Figure 4.49 Low-field magnetoconductance (MR) of sintered LSMO pellet as a function of temperature.



4.8 Synthesis of $\text{La}_x\text{Ba}_{1-x}\text{MnO}_3$ (LBMO) particles

Similar to the $\text{La}_x\text{Sr}_{1-x}\text{MnO}_3$ (LSMO), $\text{La}_x\text{Ba}_{1-x}\text{MnO}_3$ (LBMO) is another important manganite material that can be used for spintronic device. In comparison with LSMO, the LBMO compounds have been less well studied. It is probably due to the difficulty in substitution of the relatively large Ba^{2+} for La^{3+} ion in the lattice of LaMnO_3 [35]. Recently, submicron-sized LBMO cubes have been successfully synthesized by hydrothermal technique. In this section, we describe the preparation of $\text{La}_x\text{Ba}_{1-x}\text{MnO}_3$ particles where $x = 0.67$ via our hydrothermal condition with cationic surfactant CTAB modification. The physical properties of the LBMO particles are also presented.

Experiment:

The LBMO samples were synthesized with the hydrothermal method similar to those described previously. The chemicals used included LaCl_3 , BaCl_2 , MnCl_2 and KMnO_4 . They were mixed in a stoichiometric proportion. Since the alkalinity played a predominant role in the reaction, aqueous KOH was added to a concentration from 3.2 M – 12 M. Then the precursor obtained was subject to the hydrothermal process in the 11 ml Teflon lined autoclave. The filling ratio was kept at 80%. The hydrothermal process took place at 240 °C for 24 hours. After that, the as-synthesized LBMO particles were cleaned by deionized water and ethanol sequentially in order to remove the excess surfactant and ions. Finally the particles were dried at 70 °C for 1 day and then subject to different characterizations.



Characterization of LBMO particles

The samples were characterized by X-ray diffraction (XRD) with CuK_α radiation. Transmission electron microscope (TEM) was used to image the LBMO particles. Their magnetic properties were studied by measuring the magnetic hysteresis loop as a function of temperature using a vibrating sample magnetometer (VSM).

Results:

LBMO particles were obtained by hydrothermal process with the autoclave temperature being set at 240 °C for 1 day. Various [KOH] were used. The final product was characterized by XRD using diffraction angles of 2-theta between 20° and 80°. The results are shown in Fig 4.50. From this figure, no obvious change in the lattice constant with different [KOH] is observed. The diffraction angle (2-theta) of about 32.45° represents the (110) plane of perovskite $\text{La}_x\text{Ba}_{1-x}\text{MnO}_3$. The lattice constant of the sample derived from d_{110} is 0.552 nm which is in good agreement with standard $\text{La}_{0.67}\text{Ba}_{0.33}\text{MnO}_3$ bulk sample. It suggests that our modified hydrothermal method is applicable to the formation of LBMO materials in similar condition.

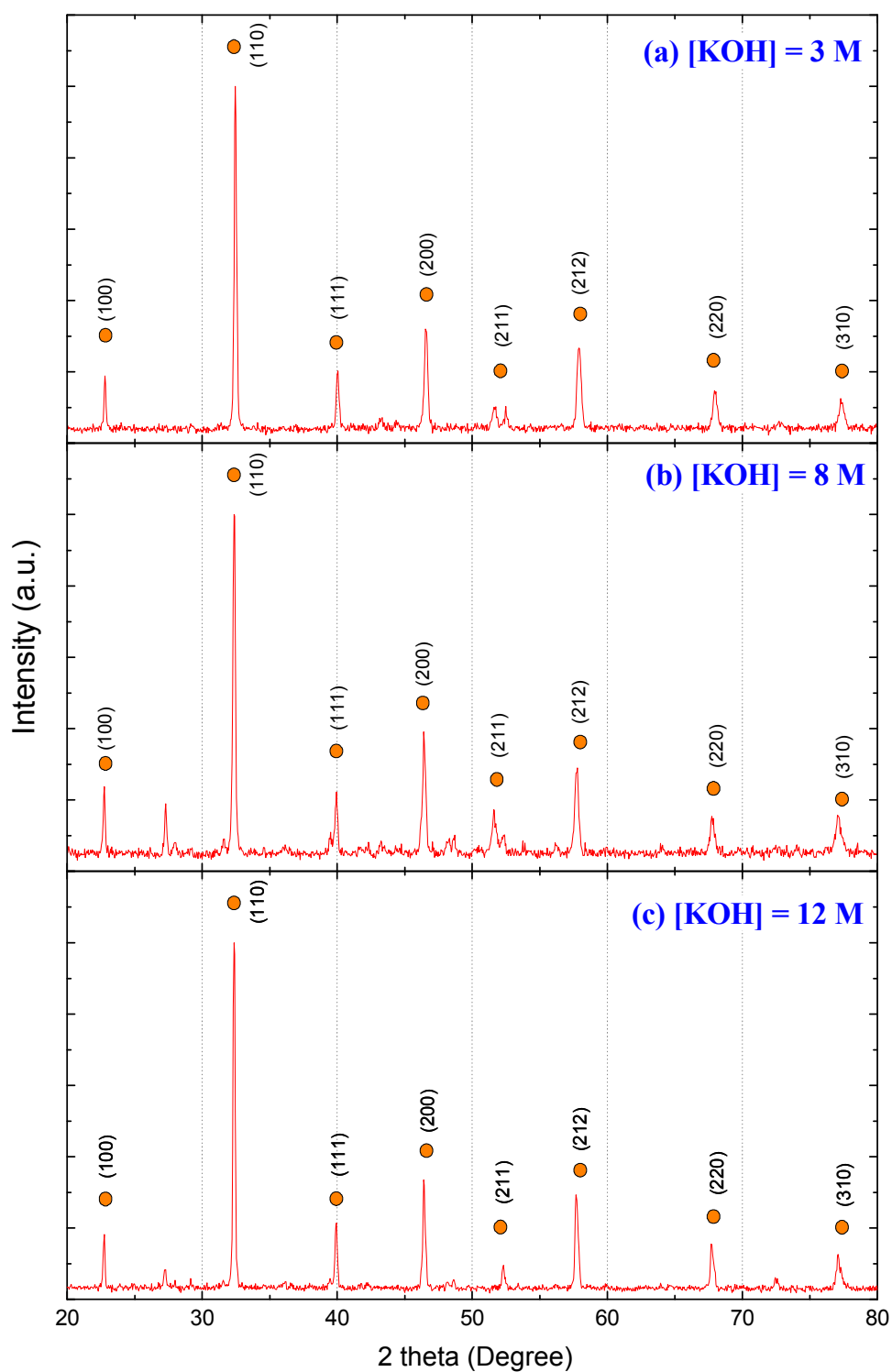


Figure 4.50 XRD patterns of LBM0 samples synthesized at 240 °C at different initial KOH concentration: (a) 3.2 M, (b) 8.0 M and (c) 12.0 M.



The morphologies of the $\text{La}_{0.67}\text{Ba}_{0.33}\text{MnO}_3$ (LBMO) particles obtained under different initial $[\text{KOH}]$ were characterized by TEM. As shown in Fig. 4.51(b), the TEM images of the sample prepared at initial $[\text{KOH}] = 12 \text{ M}$ show that all particles are monodispersed and have a regular cubic shape with clean facets. As shown in Fig. 4.51(a), when the initial $[\text{KOH}]$ of the solution is decreased to 3 M, the cubic shaped particles are replaced by four-horn-shaped particles. Actually, the four-horn-shaped particles under close scrutiny by TEM reveal three dimensional octo-pods.

When the initial $[\text{KOH}]$ is low, the reaction rate becomes slow. The products are three-dimensional octo-pods. It is the results of crystal growth along eight $\langle 111 \rangle$ directions of the cubic lattice of LBMO. When the $[\text{KOH}]$ is higher, all particles show regular cubic shape. Apparently the $\langle 100 \rangle$ growth dominates. So a cube of LBMO enclosed with six $\{100\}$ facets is obtained.

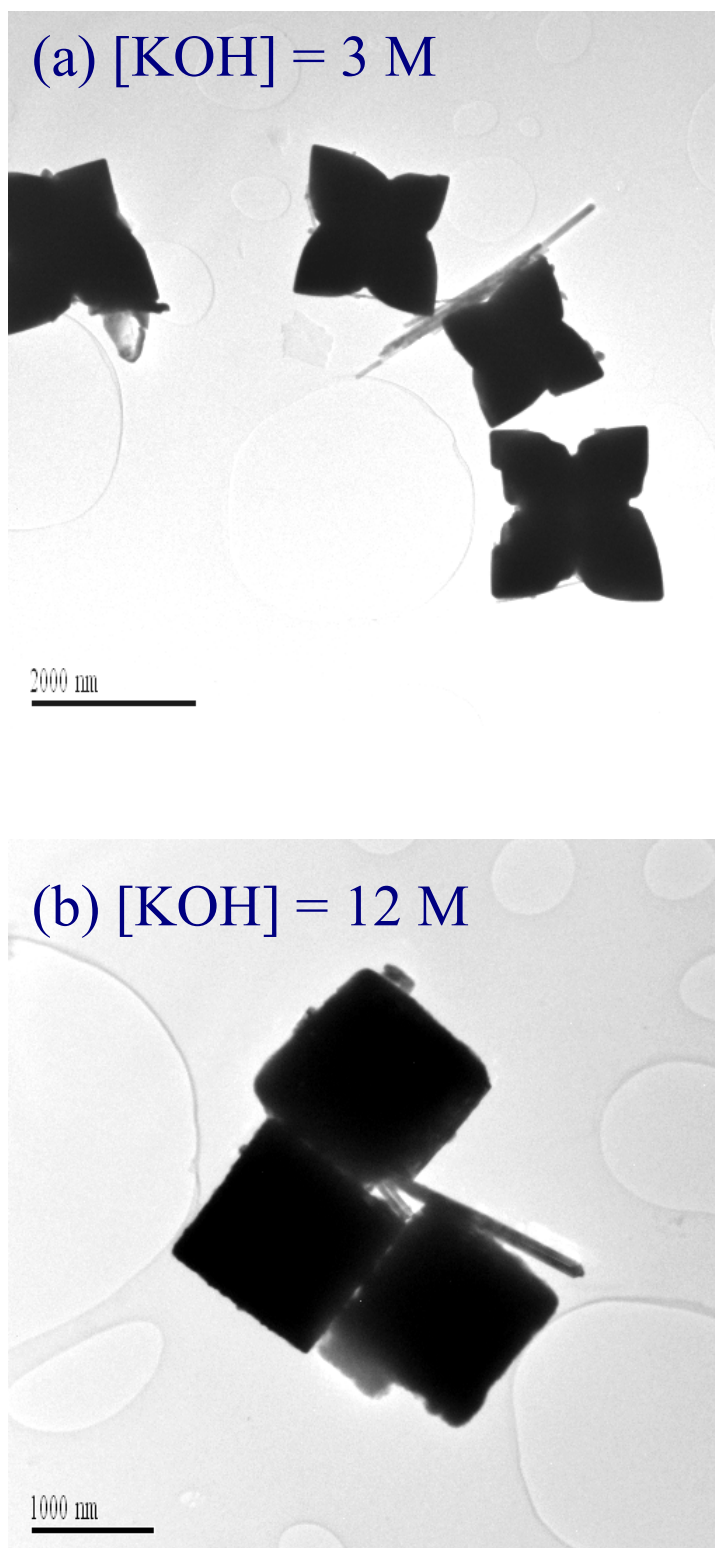


Figure 4.51 TEM images of LBMO particles prepared by cationic surfactant hydrothermal process with (a) $[\text{KOH}] = 3 \text{ M}$ and (b) $[\text{KOH}] = 12 \text{ M}$.

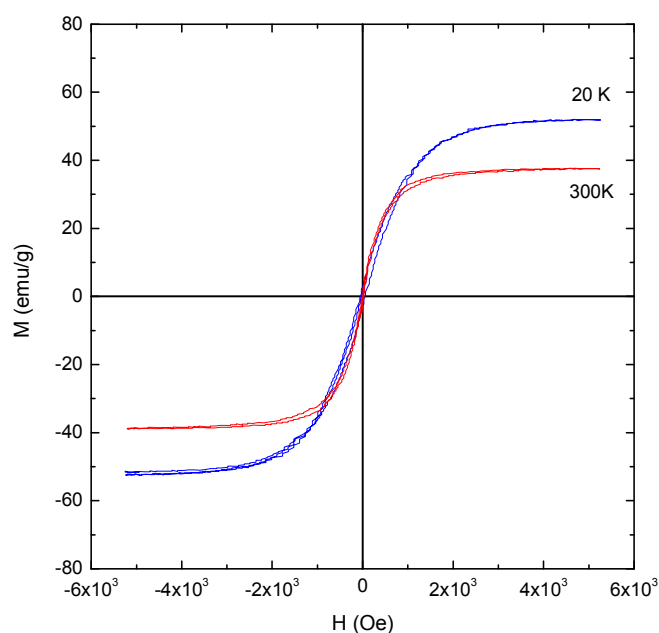


Figure 4.52 Field dependent magnetization curve of the hydrothermal $\text{La}_{0.67}\text{Ba}_{0.33}\text{MnO}_3$ particles at 20 K and 300 K, respectively.

We have measured the temperature and field dependencies of the magnetization of the hydrothermal LBMO particles. The cubic form nanoparticles were prepared by hydrothermal process with initial $[\text{KOH}]$ of 12M. The magnetic measurements were carried out in temperatures from 20 K to 310 K and a field up to ± 5 kOe. Fig. 4.52 presents the hysteresis loops of the sample measured at 20 K and 300 K. Since the LBMO particles are magnetic at 300 K, it implies that their Curie temperature (T_c) is higher than this value. The temperature dependence of magnetization (M) is determined and shown on Fig. 4.53. From this figure, it clearly indicates the decrease of M with increasing temperature. The low temperature M is 60.7 emu/g and the Curie temperature is about 350 K. These values are very close to those reported for bulk LBMO sample.

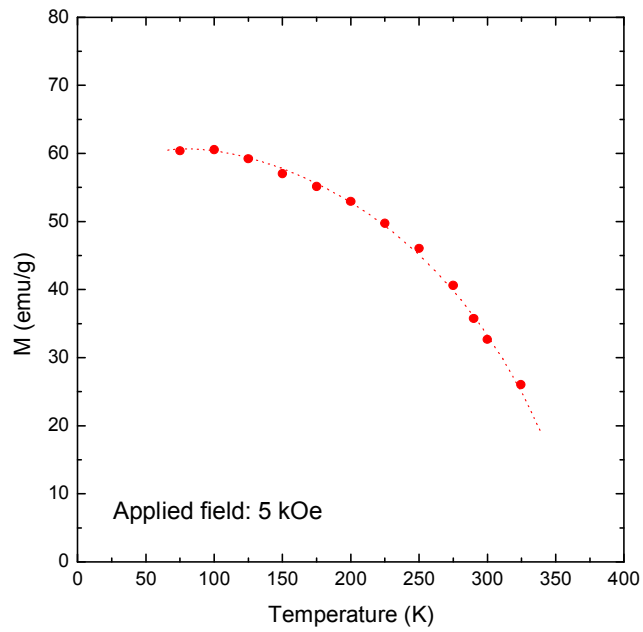


Figure 4.53 Temperature dependence of the magnetization (M) of the hydrothermal LBMO particles.

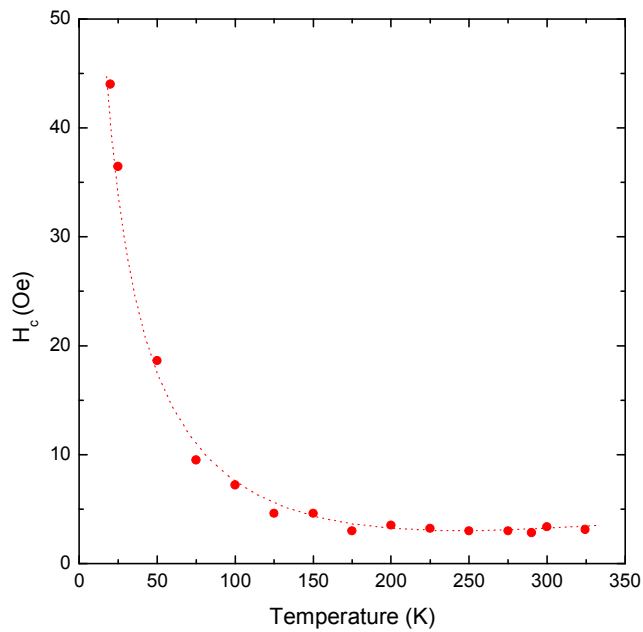


Figure 4.54 Temperature dependence of the coercive field (H_c) of the hydrothermal LBMO particles.

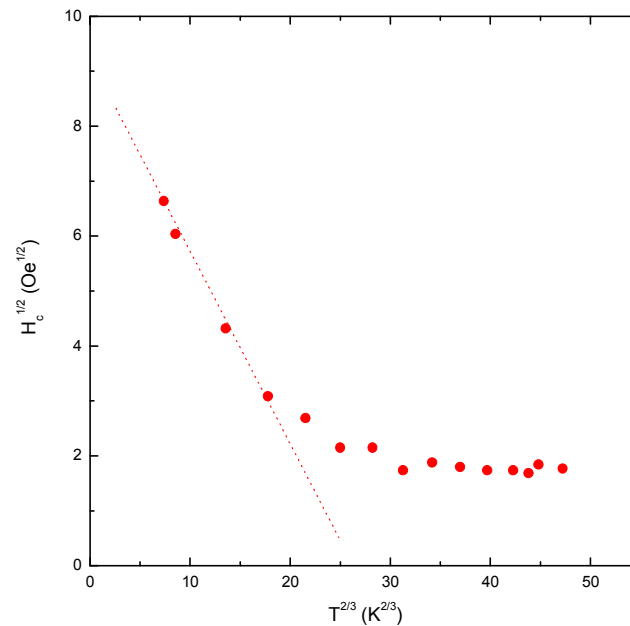


Figure 4.55 A graph of $H_c^{1/2}$ against $T^{2/3}$ of the hydrothermal LBMO particles.

In Fig. 4.54, the coercive field seems to decrease very rapidly when the temperature is increased. Square root of coercive field ($H_c^{1/2}$) as function of the $T^{2/3}$ is shown in Fig. 4.55. The curve clearly shows a linear relation between $H_c^{1/2}$ and $T^{2/3}$ at the low temperature region. It denotes that a strong domain wall pinning nature of the ferromagnetic LBMO polycrystals occurs at low temperature. The strong pinning suggests the defects in the sample may have a dimension comparable to the domain wall width. Usually, the planar defect acts either as a trap or barrier to wall motion. The planar defects are the most effective for pinning centers because the whole wall finds itself with a different energy when it encompasses the defect.

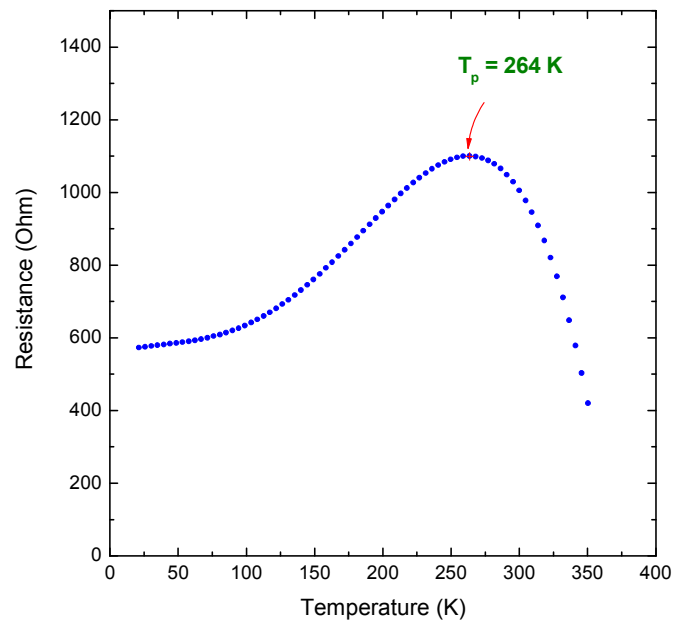


Figure 4.56 The temperature dependence of resistivity of LBMO pellet.

The electrical transport behavior in the LBMO sample was experimentally studied by measuring the resistivity as a function of temperature by means of a standard four-point probe method without the applied magnetic field. The experiment was carried out with an applied current of 10 mA in the temperature range of 20 K – 320 K. The 4 mm diameter pellet composed of 2 μm cubic LBMO powder, was made by compression and low temperature sintering (800 $^{\circ}\text{C}$) for 10 hours. Fig. 4.56 presents the temperature dependent resistivity of LBMO sample in the absence of magnetic field. From this figure, it is found that a maximum resistance is located at 264 K, which is the metal-insulator transition temperature (T_p). This T_p is smaller than the reported bulk value of 320 K. The shifting of T_p towards lower temperature could be due to the loss of long range ferromagnetic order in the sample.

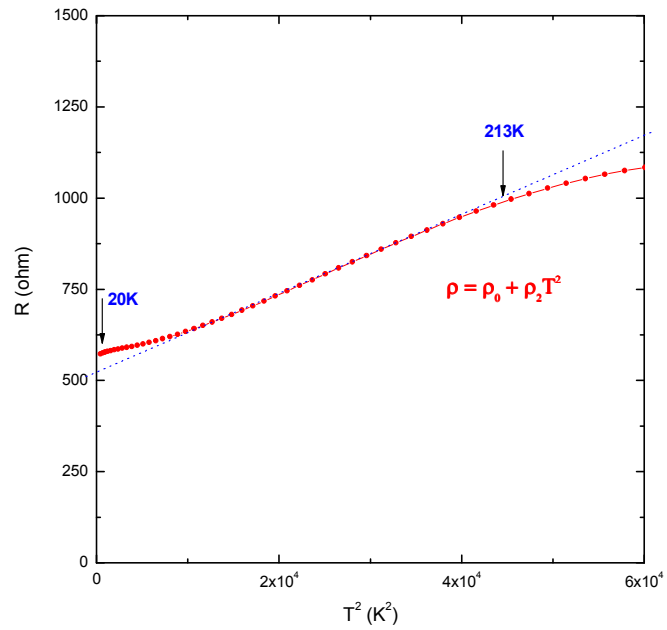


Figure 4.57 A graph of R against T^2 for the sintered LBMO sample

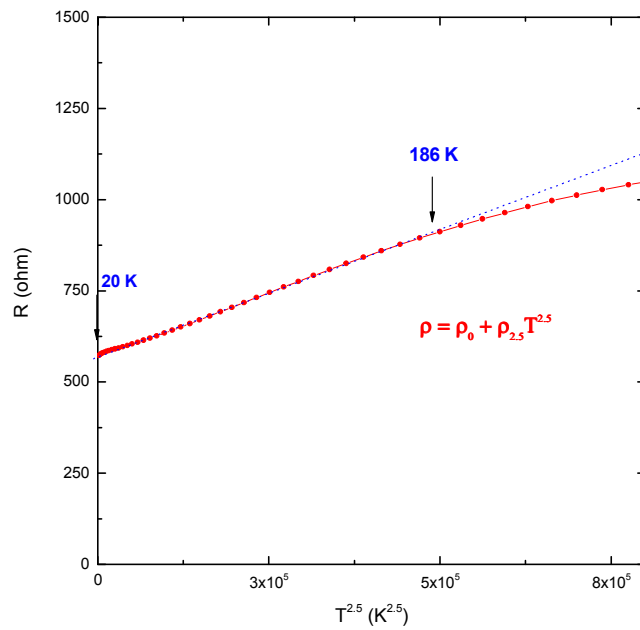


Figure 4.58 A graph of R against $T^{2.5}$ for the sintered LBMO sample



In order to understand the mechanism of electrical conductivity of the LBMO sample at low temperature, the following equations are used:

$$\rho = \rho_o + \rho_2 T^2 \quad \dots \quad (1)$$

$$\rho = \rho_o + \rho_{2.5} T^{2.5} \quad \dots \quad (2)$$

where the temperature independent part ρ_o is the resistivity due to grain boundary, domain and the other temperature independent scattering mechanism. $\rho_2 T^2$ term represents the electrical resistivity due to the electron-phonon scattering process. $\rho_{2.5} T^{2.5}$ term represents the electrical resistivity due to the electron-magnon scattering process.

In Fig 4.57 and Fig 4.58, the plots show the data of resistivity for the LBMO sample fitted to the above two equations. We find that the resistivity data for the sample best fit the equation (2) in the temperature range from 20 K to 186 K. Therefore, the possible mechanism of such low temperature electrical resistivity may be described as follows. In a compact sample of LBMO, the grain-boundary contribution in the resistivity is very large. Below the metal-insulator transition temperature (T_p), spins within a domain are parallel aligned and electron-magnon scattering dominates in this region. Even though the spins within each domain get aligned, the domains themselves are not aligned. Hence the electron-magnon scattering process continues to the lowest temperature. Therefore the LBMO sample is at ferromagnetic phase at low temperature.



On the other hand, the electronic transport properties of manganites at the high temperature regime can be described by the small polarons hopping model. The equation for this model is given by:

$$\rho = \rho_{\alpha} T \exp\left(\frac{E_p}{k_B T}\right)$$

where E_p is the activation energy and ρ_{α} is the residual resistivity.

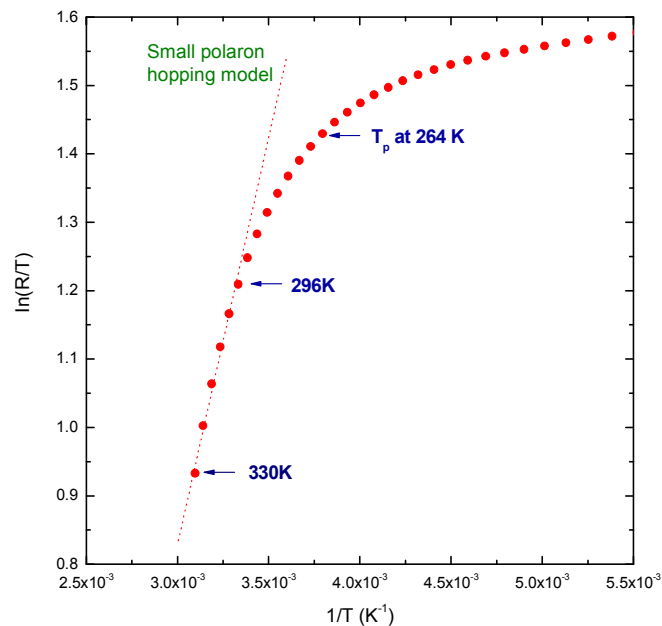


Figure 4.59 A graph of $\ln(R/T)$ against $1/T$ for LBMO sample.

In Fig.4.59 shows a linear relation of $\ln(\rho/T)$ against $1/T$ in the temperature range of 296 K – 330 K. The conduction of LBMO polycrystalline pellets is therefore agreed with the small polaron hopping model. This E_a is the binding energy associated with dynamic Jahn-Teller polaron between Mn^{3+} and Mn^{4+} in the insulating state.



From the slope of this curve, it indicates the activation energy (E_p) for electron hopping of 89.7 meV. This is significantly smaller than the value of LBMO nano-channel reported by Nagabhushana [36]. As mentioned by Venkataiah [37], the values of activation energy are decreasing with increasing grain size. For a sample with larger grain size, the interconnectivity between grains enhances the possibility of conduction electron to hop to the neighboring sites hence reduce the value of hopping energy.



4.9 Summary

The cationic surfactant assisted hydrothermal synthesis has been developed to produce high quality, mono-dispersed $\text{La}_x\text{Sr}_{1-x}\text{MnO}_3$ (LSMO) and $\text{La}_x\text{Ba}_{1-x}\text{MnO}_3$ (LBMO) particles. This method has accelerated the solid state reaction, reducing the conventional formation temperature from 1400 °C in solid state reaction to only 240 °C. Therefore this route saves both time and energy to obtain a high quality mixed oxide crystalline particles. The shape and the particle size are remarkably controlled through the use of precursors, surfactant concentration, aging temperature and also the concentration of mineralizer. The crystal structure, size and size distributions of as-synthesized LSMO nanocrystals have been fully characterized by XRD and TEM.

The success of size-controlled synthesis of LSMO nanoparticles demonstrates that the thermal behavior of precursors is a key reaction parameter for the synthesis of complex multiple-metal oxides nanocrystals. The size and shape dependent magnetic and electrical properties are discussed. The magnetization and coercive field show low magnetic values owing to the presence of a nonmagnetic layer which reduces interparticle interaction, although some agglomerates cannot be discarded. A comparison of the magnetic properties possessed by different shape LSMO nanoparticles offers rich insight on the fundamental of nanomagnetism. Addressing the interesting and important fundamental issues raised by these size and shape dependent studies surely promises further advancement in the understanding and application of magnetism in the nanometer regime.



CHAPTER 5

Synthesis and characterization of nano manganites particles with core shell architecture

5.1 Introduction

Nanoparticles have helped opening up new avenues in nanoscience and nanotechnology. However, early efforts were largely confined to produce them in uniform sizes. But now with the emerging new synthesis techniques, it is possible to synthesize them not only in uniform sizes but also in desired shapes such as rods, tubes, cubes, tetrapod and sheet, and even core-shell structures [1].

In contrast to the traditional nano-materials preparation methods, recent approaches begin to explore the surface modification pathways in synthesis and processing. Because of the enhance stability against aggregation, such surface engineering can overcome the weakness of traditional approaches in controlling size, shape and surface properties. The research on nanocrystals with core-shell architecture based on surface modification has been intensified in the last few years [2]. Core-shell particles constitute a special class of nano-composite materials. They consist of concentric particles, in which particles of one material are coated with a thin layer of another material using specialized technique.



Generally, core-shell particles are highly functional materials with tailored properties, which are quite different from those either of the core or of the shell materials. Indeed, the core-shell structured nanocrystals can, on one hand, provide many desirable properties for practical applications, and on the other, serve effective routes to understanding the fundamental issues in nanoscience. It is well known that the phenomenal increase of the surface to volume ratio in nanoparticles renders the surface phenomena to predominate factors that determine the nanomaterials properties. Nanocrystals with core-shell architecture may be a good system to address such surface effects. Given a specific core, it is feasible to systematically investigate the surface effect upon the intrinsic properties of core part by a precise selection and controlled introduction of a shell part, either organic or inorganic.

Nevertheless, the fabrication of nanomaterials with core-shell architecture can also be an effective mean to understand, optimize and enhance the material's optical, electric, magnetic, catalytic, structural and surface properties in a reliable and predictable manner. It is invaluable in both basic science and a broad range of technical applications. To date, a number of nanocrystals with core-shell architecture have been synthesized and reported [3].



Recently, various bi-magnetic nanocrystals with core-shell architecture have been successfully made by different methods [4]. By deliberately forming a passivating oxide layer, core-shell structured nanoparticles of iron-iron oxides [5] or cobalt-cobalt oxide [6] have been prepared by evaporation deposition technique. Similarly, the reduction of metal salts with NaBH_4 in reverse micelle followed by surface oxidation in air has also been used to form magnetic core-shell structured nanoparticles [7]. However, based on these synthetic methods, the control of shell thickness and sequential variation of chemical compositions of the shell have met with limited successful only.

Basically, proximity between a ferromagnetic (FM) and antiferromagnetic (AFM) material leads to interesting effects that result from the structural modification and competition of different magnetic orderings at the interface between them. In particular, the exchange coupling at a FM/AFM interface may induce unidirectional anisotropy in the FM below the Néel temperature of the AFM, causing a shift in the hysteresis loop, a phenomenon known as exchange bias [8]. In recent years, the study of exchange bias in nanoparticles and nanostructures has gained intense interest. It has been shown that the control of the core-shell interactions of the exchange coupling between the particle surface and the embedding matrix can increase the superparamagnetic limit for use in magnetic recording. Several experiments on different nanoparticle systems with oxidized shells have been studied.

Moreover, recent studies on magnetic properties of nanostructured materials have mainly focused on the chemical composition, size and shape. The understanding of the magnetic properties of core-shell structured nanoparticles is, however, of fundamental interest. The studies of core-shell structures have recently been demonstrated a rational approach to overcoming certain technical issues such as magnetic phase transition of FePt nanocrystals in high-density data storage and the improvement of energy product in permanent magnetic [9].

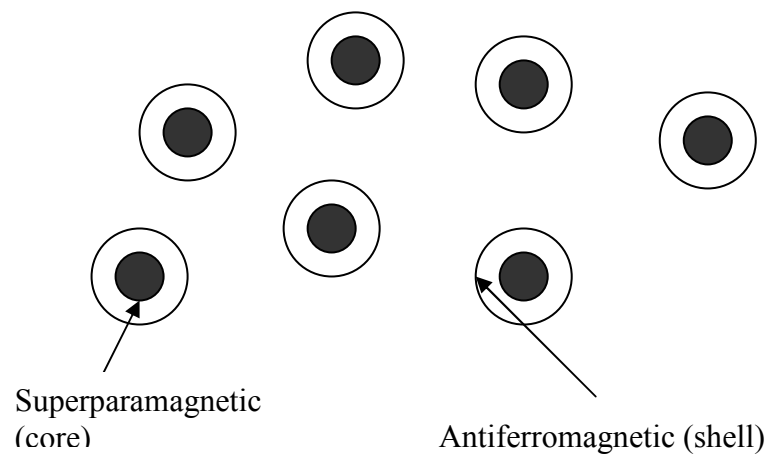


Figure 5.1 Schematic diagram of core shell architecture.

It is well known that the perovskite manganite is a typical strong correlated electron material and therefore consists of both ferromagnetic (FM) phase such as $\text{La}_{0.67}\text{Sr}_{0.33}\text{MnO}_3$ (LSMO) [10] and antiferromagnetic (AFM) [11] phase such as LaMnO_3 (LMO) in the family. Although both LaMnO_3 and $\text{La}_x\text{Sr}_{1-x}\text{MnO}_3$ have identical electronic configuration, the two compounds own a noticeable difference in their magnetic and electrical properties. LMO compound has a Neél temperature (T_N) of 141 K. A schematics of the magnetic arrangement found in these two manganites are presented in Fig. 5.2(a) and 5.2(b). As a result, perovskite manganite can be an ideal experimental system for addressing fundamental issues such as interfacial exchange coupling and surface effect upon magnetic properties through the fabrication of bi-magnetic nanoparticles with core-shell architecture.

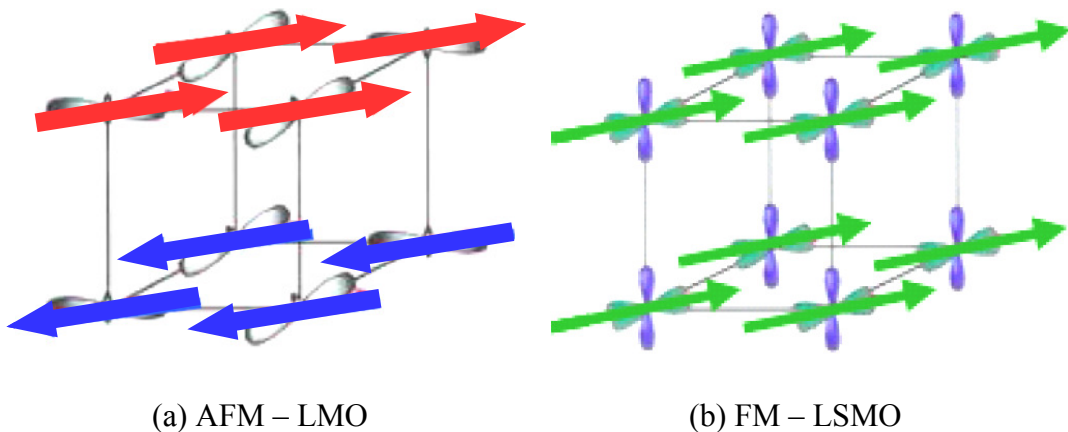


Figure 5.2 Magnetic ordering for the Mn ion in the perovskite lattice of (a) antiferromagnetic LaMnO_3 and (b) ferromagnetic $\text{La}_x\text{Sr}_{1-x}\text{MnO}_3$.



Moreover, due to the similar crystal structure and nearly equal lattice constants, the lattice mismatch among different composition of perovskite manganites is almost negligible. Therefore, it is feasible to create various epitaxial overcoatings on the core materials, instead of the polycrystalline shell normally formed and observed in other studies.

In this Chapter, the synthesis and magnetic properties of bi-magnetic perovskite manganites core-shell structured nanoparticles are presented. Specifically, the effects of the shell layer with the magnetic properties are discussed.

5.1.1 Magnetic coupling interaction

Antiferromagnetic (AFM) materials represent a very interesting class of systems since the uncompensated exchange couplings of the surface spins leads to significant magnetic moment per particles even through the spins in the core are antiferromagnetic ordered. This can produce a ferromagnetic (FM)/antiferromagnetic (AFM) interface. Due to a bias produced by exchange coupling to the AF spins, the so-called exchange bias phenomenon [12], it results a shifted hysteresis loop of the ferromagnetic surface spins as shown in Fig 5.3. Exchange coupling between ferromagnetic (FM) and antiferromagnetic (AFM) materials was discovered in Co/CoO fine particles in 1957. The desirable properties for an exchange bias material are its high Néel temperature (T_N) and large magnetocrystalline anisotropy (K).

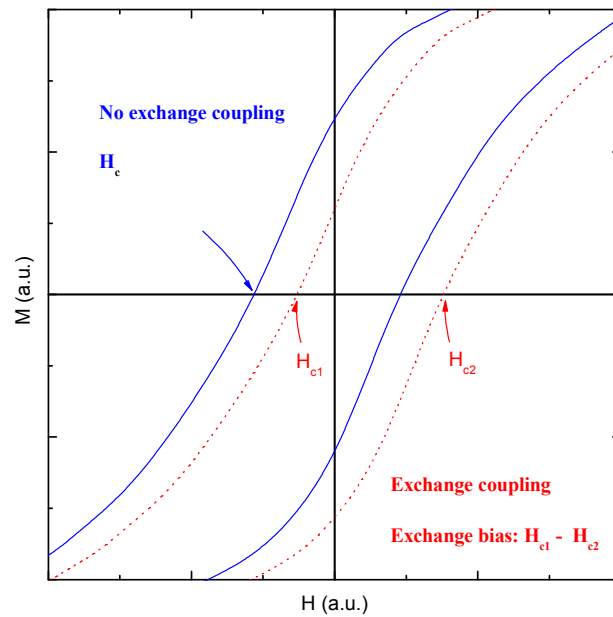


Figure 5.3 Hysteresis loops for the material (a) with and (b) without magnetic coupling.

From the viewpoint of application, exchange bias is used to stabilize the magnetization of soft ferromagnetic layers in reading head based on the anisotropic magnetoresistance effect in the data-storage industry. Without this stabilization, the magnetic domain state of the head can be unpredictable, leading to the reliability problems.



5.1.2 Epitaxial approach

“Epitaxy” always appeared in semiconducting industry, it refers to the ordered crystalline growth on a single crystalline substrate [13]. Hydrothermal process provides an alternative way to utilizes aqueous chemical reactions to form heteroepitaxial thin layer. This method eliminates the problems encountered with high temperature processing as well as the need for ultrahigh vacuum equipment in physical vapor deposition technique.

As a consequence, hydrothermal process has a strong potential for synthesizing new materials with surface properties tailored to specific applications. An example of this possibility is the coating of nanoparticles and porous substrate in heterogeneous catalysis. The impact of hydrothermal epitaxy techniques in industrial technology is large. The desirable features mentioned in previous paragraph have great potential of bringing to the field of inorganic materials processing the same versatility and ease that typifies organic synthesis in chemistry and bio-chemistry.

Indeed, one of the chief difficulties of epitaxial growth by chemical reaction is the control of the supersaturation to avoid spontaneous nucleation. This also means that the driving force for layer formation is too high, making the process highly inefficient since most of the precursor goes to making powder instead of the shell layer formation. Also, the concentration of mineralizer and the process temperature must be carefully chosen such that the complex formed is just stable enough to exist in high concentration but not to condense into stable solid phases.



The stability and processibility of core-shell nanoparticles has not yet been perfected. Two critical issues for maintaining the size distribution of nanocrystals during the epitaxial growth of shell materials include:

- (1) the elimination of the homogeneous nucleation of the shell materials,
- (2) homogeneous monolayer growth of shell precursors onto all core nanocrystals in solution, yielding shell layers with nearly the same thickness around each core nanocrystals.

Colloidal epitaxy provides a mean to direct growth of colloidal crystals. Under the influence of gravity, colloids settle at the bottom of the container, forming close packed crystalline domains. By using a corrugated wall where the pattern of holes equals a well chosen crystal plane, a colloidal crystal can be grown epitaxially.



5.2 Experimental details

5.2.1 Preparation of $\text{La}_{0.67}\text{Sr}_{0.33}\text{MnO}_3$ (LSMO) nanoparticles

In order to fabricate the monodispersed $\text{La}_{0.67}\text{Sr}_{0.33}\text{MnO}_3$ (LSMO) core-particles, the hydrothermal synthesis method, which was mentioned in the Chapter 4, was used. Typically, an aqueous solution of MnCl_2 was prepared by dissolving $\text{MnCl}_2 \cdot 4\text{H}_2\text{O}$ and 0.2 g cationic surfactant CTAB in 40 ml deionized water at 70 °C. Then, the KMnO_4 aqueous solutions were added dropwise into the MnCl_2 solution under vigorous stirring for 2 hours at room temperature. SrCl_2 and LaCl_3 solution were prepared and added into the mixture. To maintain the alkalinity of the solution, KOH was added directly to form the final precursor solution. After the mixture has undergone an aging process at room temperature for 1 day, 9 ml of the precursor is taken to the hydrothermal process. Details of LSMO-precursor preparation are listed in Table 5.1

The synthesis was performed in an 11 mL Teflon-lined stainless steel autoclave with filling ratio of about 80 %. The reaction mixture was placed in the autoclaves and heated at 240 °C under the autogenous pressure for 24 hours. It was then allowed to cool to room temperature naturally. Black colored particles were obtained. These solid residues were subsequently washed several times with ethanol and deionized water. The final sample was then dried in an air-oven at 80 °C for 1 day.



5.2.2 Hydrothermal process for LaMnO_3 (LMO) shell layer on LSMO particles

The shell layer of LMO can be grown on LSMO core by repeating the forgoing hydrothermal process once again. The LMO precursor solution was made by dissolving stoichiometric LaCl_2 , MnCl_2 and KMnO_4 in an aqueous solution. The as-prepared LSMO particles were treated by CTAB surfactant and then mixed with the resultant precursor solution. Details of LMO-precursor preparation are listed in Table 5.1.

The solution was made strongly alkaline by saturating it with KOH. It was then loaded into an 11 ml hydrothermal cell. The filling ratio was kept at 80 %. The reaction was initiated by heating the cell to 240 °C under autogenous pressure for 24 hours. After the hydrothermal cell was cooled, the supernatant liquid was discarded and the remaining product was washed with deionized water through a 0.22 μm nylon membrane filter and then dried in oven at 70 °C for 1 day.

**Table 5.1 Summary of chemicals and processing conditions for preparing core-shell architecture.**

Core			
Chemicals	Mass used (g)	Concentration (M)	Molar ratio
LaCl ₃ · 7H ₂ O	0.82	3.34 x 10 ⁻³	0.67
SrCl ₂ · 6H ₂ O	0.44	1.65 x 10 ⁻³	0.33
MnCl ₂ · 4H ₂ O	0.67	3.38 x 10 ⁻³	0.67
KMnO ₄	0.26	1.65 x 10 ⁻³	0.33
CTAB	0.2	5.48 x 10 ⁻⁴	0.10
Hydrothermal condition (1st stage)			
Processing temperature	240 °C	[KOH]	5.0 M
Processing time	24 hours	Filling ratio	80 %
Shell			
Chemicals	Mass used (g)	Concentration (M)	Molar ratio
LaCl ₃ · 7H ₂ O	0.130	6 x 10 ⁻³	1.0
SrCl ₂ · 6H ₂ O	---	---	---
MnCl ₂ · 4H ₂ O	0.067	4 x 10 ⁻³	0.67
KMnO ₄	0.027	2 x 10 ⁻³	0.33
CTAB	0.002	3 x 10 ⁻⁵	5 x 10 ⁻³
LSMO (core particle)	0.5	1.6 x 10 ⁻³	0.27
Hydrothermal condition (2nd stage)			
Processing temperature	240 °C	[KOH]	5.0 M
Processing time	24 hours	Filling ratio	80 %



5.2.3 Characterization of core-shell particles

In order to examine the crystal structure of the sample, a Bruker D8 Advance X-ray diffractometer (CuK_α radiation) at a scanning rate of 3° per minutes spanning 2-theta from 20° to 80° was used. The XRD diffraction patterns were then compared with standard value for the same composition. Micrographs of the samples were taken with a transmission electron microscopy images (TEM) in order to determine the particles size and morphology.

Magnetic measurements were performed using a vibrating sample magnetometer (VSM). In order to take the measurement, samples were prepared by just pressing the as-synthesized particles into a small Teflon holder. Field dependent magnetization curves were measured from 20 K to 310 K.



5.3 Results and discussion:

5.3.1 Structural characterization

By purposely selecting a ferromagnetic (FM) phase (LSMO) and an antiferromagnetic (AFM) phase from the same perovskite manganites, core-shell structured bi-magnetic nanocrystals of LSMO/LMO have been synthesized via a seed-mediated growth hydrothermal process.

The hydrothermal reaction produced a well dispersed black colloidal solution. After the cleaning and drying process, highly crystalline black particles were obtained. Structural characterization of the as-synthesized LSMO nanoparticles and LSMO/LMO core-shell particles were studied by XRD. Fig. 5.2 (a) and 5.2 (b) show the 2-theta scan of these two samples. From this figures, the reflection peaks of the LSMO particles for both samples are indexed as pseudo-cubic structure. The lattice parameters of d_{110} of these two samples are found to be the same value of 0.55 nm, which is in agreement of standard perovskite LSMO sample. Also, it can be seen that the samples are single phase compound and have no difference between them. Although we cannot use these XRD patterns to qualify the presence of a shell layer, the absence of impurity phases suggests the formation of a single perovskite phase from the precursor solution in such a hydrothermal condition.

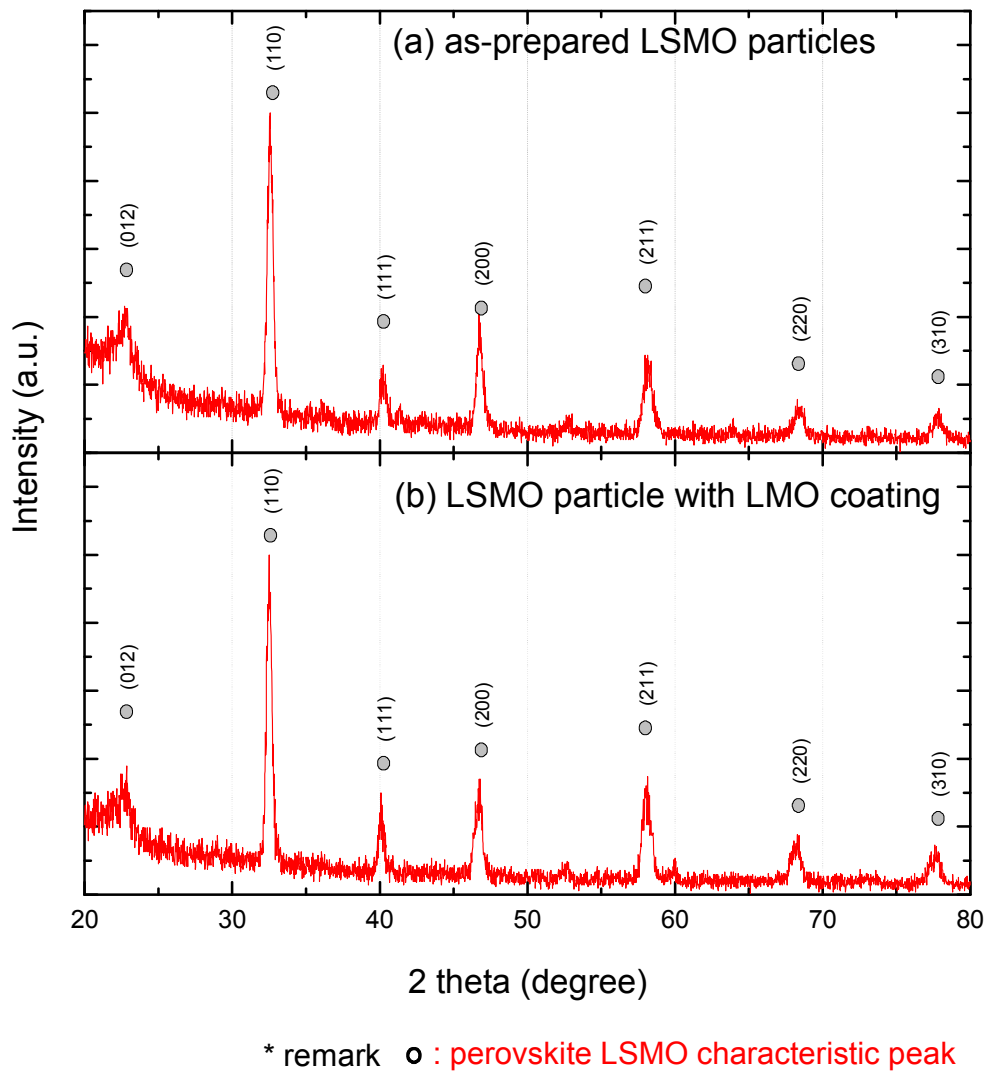


Figure 5.4 XRD patterns of (a) as-prepared LSMO particles and (b) LMO/LSMO particles with core-shell architecture.



In order to confirm the presence of core-shell structure in the as-prepared sample and to determine their dimensions, we have used transmission electron microscopy (TEM) for the purpose. Fig 5.4 (a) and 5.4 (b) show the morphology of the LSMO particles after the first stage of hydrothermal process. The isolated particle has a typical size of 80 – 100 nm. Most as-synthesized particles suffer from serious agglomeration. By adjusting an appropriate molar ratio of seeds to the amount of precursors in the second stage of hydrothermal process, a 5 nm uniform thick shell layer is seen to coat on the surface of the core particle. The apparently uniform shell layers suggest a homogeneous layered growth of material from the shell-precursor under the current hydrothermal condition. Moreover, it also clearly shows that coatings are in close contact with the particle surface. This image thus confirms the formation of core-shell structured nanoparticles where the inner LSMO core is coated uniformly with a thin layer of LMO.

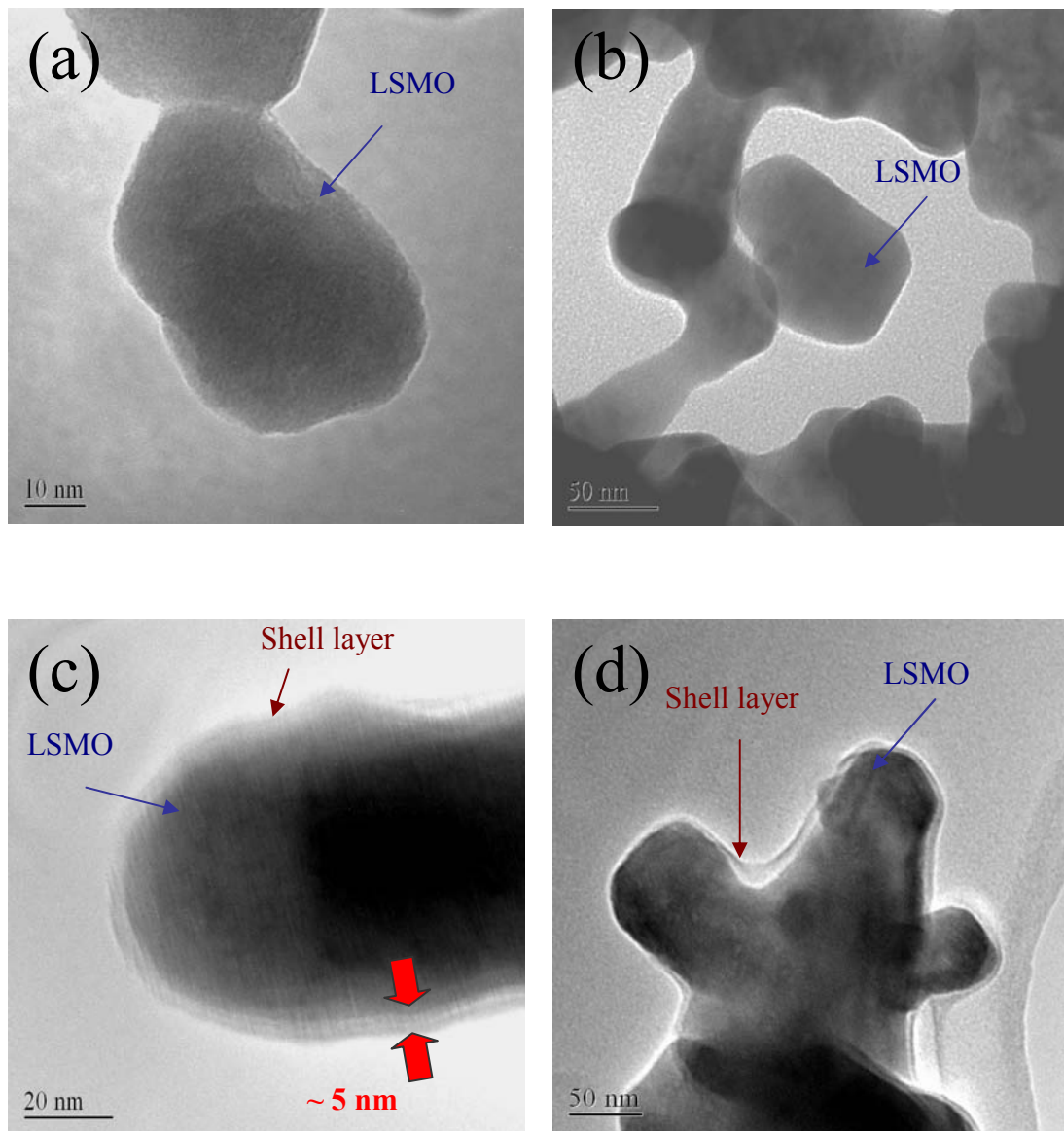


Figure 5.5 Typical TEM images showing the morphology of LSMO core particle (a-b) without LMO shell layer and (c-d) with LMO shell layer.



5.3.2 Magnetic characterization

To examine the exchange effect arising from the presence of the LMO phase, the magnetic hysteresis loops of LMO-coated LSMO particle assemblies were measured at temperatures from 20 K to 300 K by our VSM system. Firstly the dependency of magnetization (M) for the LSMO nanoparticles with and without core-shell structured was determined. The temperature dependent magnetization curves are shown in Fig 5.6. Although we cannot take this measurement at higher temperature, the shape of the M - T curves for these two samples implies that the Curie temperature (T_c) is substantially decreased by the additional coating on LSMO particle surface. Another effect is that the M of shell-coated LSMO has substantial enhancement also. The sharp FM-PM transition in LSMO/LMO sample indicates that the spin disorder has been improved. It is recognized that the magnetization in the manganite is very sensitive to the stoichiometry, atomic defects oxygen content, and the Mn^{3+} and Mn^{4+} ratio. The XRD peaks for the LSMO particles are identical as that of the LMO/LSMO particles. The results obtained from the M - T curves indicate that the perovskite phase in the LSMO particle may be still inhomogeneous and contains defects. By extrapolation of the M_s - T curve to the temperature axis, we can obtain an intercept at 291 K which is the T_c of LSMO/LMO sample.

At very low temperature of 20K, the magnetization measurement showed hysteresis loops with a coercive field (H_c) for LSMO nanoparticles and LMO/LSMO core-shells being of 296 Oe and 75 Oe, respectively. It is noted that the pure LSMO nanoparticles and the core particles of the LMO/LSMO core-shells are actually come



from the same batch of LSMO particles. Their magnetic properties should be the same. The second stage hydrothermal process may have some effect on the LSMO core particles, although it is expected to be small.

The large difference in H_c between the pure LSMO nanoparticles and the LMO/LSMO core-shells, therefore clearly shows an unmistakable effect of the shell layer. It is well known that the multidomain manganite particle have much lower coercive field of 100 Oe or less. Fig. 5.7 shows the coercive field dependence on temperature. Apparently the coercive field (H_c) decreases with increase of measuring temperature, dropping from 75 Oe at 20 K to about 0 Oe at 300 K for LMO/LSMO. This may be caused by a contribution of intrinsic temperature dependence of the anisotropy and magnetization, and thermal activation effects. The smaller coercive field of the shell coated particles reflects the stronger interparticle interaction than the sample without coating. Hence, we suggest that the coating of LMO shell layer from the second hydrothermal process improves the magnetic ordering on the particle surface. By comparing the dependence of coercive field with temperature for the two samples, the two sets of data points were fitted to different relations. In Fig 5.7, the curve for pure LSMO particle obviously indicates a non-linear relation and in agreement with $H_c^{1/2} \propto T^{2/3}$. The existence of weak domain wall pinning regime of random inhomogeneities is thus discarded. It suggests that the ferromagnetic switching of the pure LSMO particle is guided by strong domain pinning. On the other hand, a linear relation ($H_c \propto -T$) was obtained for the LNO/LSMO. This suggests that the weak domain wall pinning is dominated.

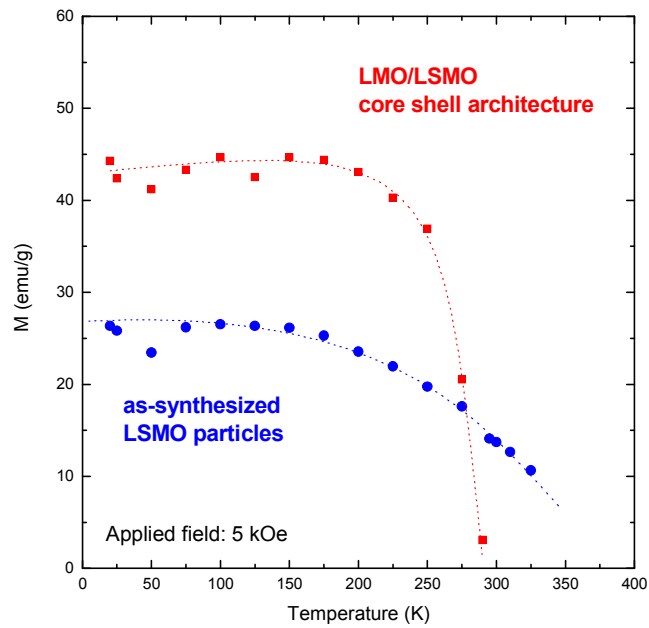


Figure 5.6 Temperature dependence of magnetization of (a) as-synthesized LSMO nanoparticles and (b) LSMO/LMO core-shell particles (Applied field: 5 kOe).

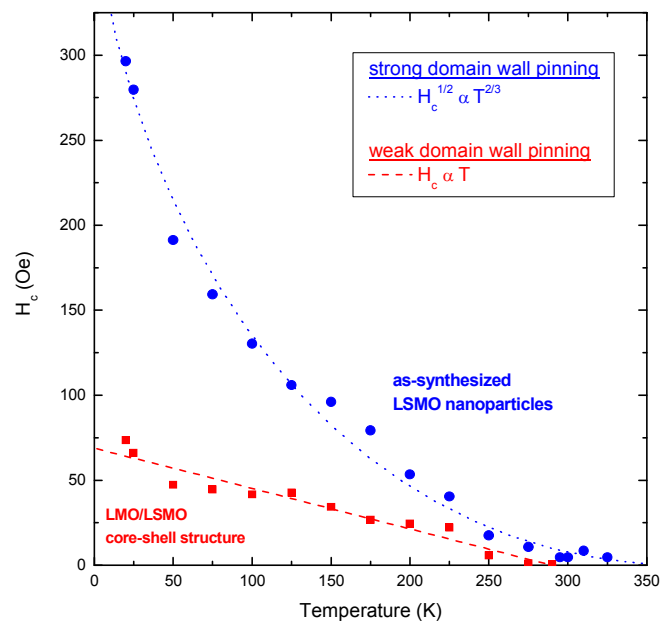


Figure 5.7 Temperature dependence of coercive field of (a) as-synthesized LSMO nanoparticles and (b) LSMO/LMO core-shell particles.

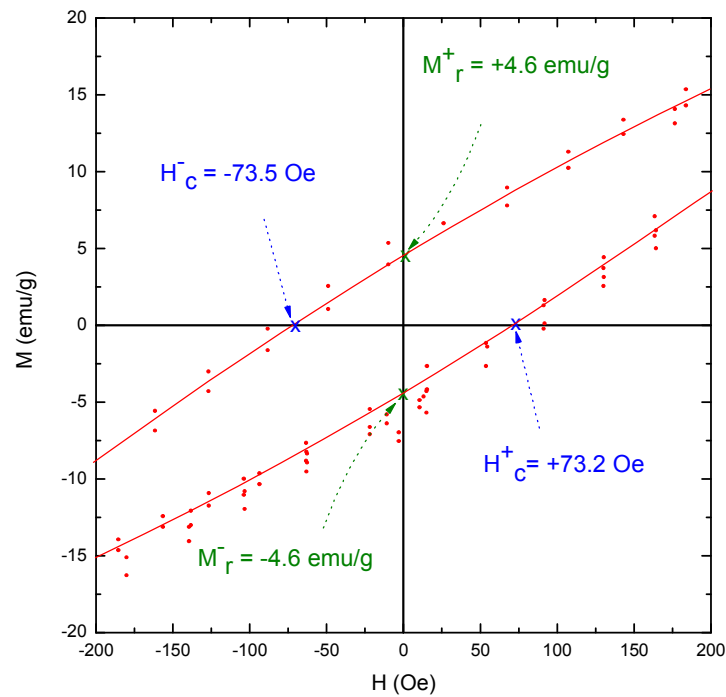


Figure 5.8 Hysteresis loop of LMO/LSMO core-shell architecture at 20K. (ZFC)

The LMO/LSMO sample was cooled down to low temperature without any magnetic field (ZFC). At sample temperature of 20 K, a symmetric hysteresis loop is observed with a remanence of 4.6 emu/g and a coercivity of 75 Oe. These are signs of ferromagnetic nature of the nanoparticle at low temperature. We also note that the exchange bias (H_c^+ and H_c^-) in the present system is symmetric about the zero field axis. No observable exchange bias through the contact of LSMO (FM) to LMO (AFM) was detected. Since the exchange bias can only be detected from field cooled sample, more studies are needed to clarify and to improve this exchange bias coupling.



5.4 Summary

LMO/LSMO core-shell architecture has been synthesized by a two-stage hydrothermal process. To ensure the complete dispersion of as-prepared LSMO particles in the shell-precursor, cationic surfactant CTAB has been used to modify the particle surface. After the second stage hydrothermal process, structural and magnetic characterizations have been performed. The XRD patterns are not able to confirm the formation of LaMnO_3 since LSMO and LMO possess similar crystal structure. The core-shell structure, nevertheless, has been confirmed by TEM analysis. A 4~5 nm thick layer have been detected on the LSMO surface. The characterizations on the nanoparticles further show some significant modification of the magnetic properties after the second stage hydrothermal process, i.e. a substantially increase in magnetization, a large reduction of H_c at low temperature and lower Curie temperature for the core-shell structure. We suggest the additional treatment of the particles improves the magnetic ordering on the surface.

According to our analysis, this core-shell structure gives rise to an additional term in magnetic interaction. This additional term, which we call interfacial interaction, describes the interaction between the surface layer LMO and the core LSMO. The unique magnetic properties of core-shell structured nanoparticles clearly demonstrate that the fabrication of core-shell magnetic nanocomposites is an effective approach to precisely customizing material properties for a wide variety of technical applications. Since it is a novel investigation of manganite nanoparticle in this combination, we believe that the present research could serve as a good foundation for many future research works on functionalized oxide nanoengineering.



CHAPTER 6

Dispersion of magnetic nano-manganite in polymer matrix

6.1 Introduction

Nanocomposites are materials that are created by introducing nanoparticles into a macroscopic material matrix. After mixing the nanoparticles into the matrix material, the resulting nanocomposite may exhibit drastically enhanced properties. One common example in the plastic industry is the reinforcing polymers with a second phase of either organic or inorganic materials. Traditionally, polymers have been considered as excellent host matrices for composite materials. Many attractive properties of polymers, such as high corrosive resistance, light weight, high mechanical strength and dielectric tunability can be utilized along with novel properties of additives to make multifunctional materials [1].

Actually, polymer nanocomposites represent a new class of materials that differs from the conventional filled polymers. In this class of materials, nano-scaled inorganic filler are dispersed in the polymer matrix offering tremendous improvement in their properties [2].



Several advanced polymer nanocomposites have been synthesized with a wide variety of inclusions like metal cluster, carbon nanotubes, magnetic nanoparticles and semiconductor particles [3]. These materials also possess the processing and handling advantages of bulk materials. For this reason there is an increasing technological interest in polymers reinforced by nanoparticles. Their potential to provide enhanced mechanical properties as well as many unique, value-added properties such as increased barrier, high thermal and electrical conductivities and enhanced flammability resistance etc. have been actively researched [4].

Also, self assembly of nanoparticles mediated by polymer provides access to stabilized metal and semiconductor nanocomposites as well as allows for the fabrication of new structure nanoscale materials. The support or matrix within which the magnetic nanoclusters are synthesized plays an active role in determining their physical properties in addition to providing a means for particle dispersion. The macroscopic magnetic properties of the nanocomposites derive from the combined action of finite-size effects, strain and interface effects, matrix properties and morphology of the nanostructures. All these parameters can be strategically controlled for the design of artificially structured materials with tailored properties.

Nanocomposites based on magnetic particles-polymer mixtures have been an active area of recent research. They have a wide range of applications in electromagnetic interference shielding (EMI), drug delivery and as contrasting agents in magnetic resonance imaging (MRI) [5].



Magnetic nanocomposites in which magnetic species dispersed within nonmagnetic or magnetic matrices are practically very useful. Magnetic recording, giant magnetoresistance and magnetic refrigeration are some important areas in which magnetic nanocomposites bear relevance. Nanocomposite magnets with both particle/matrix systems being magnetic have received much attention, because they may have high remanence and large energy product, $(BH)_{\max}$ relative to conventional magnetic materials. The effect of the strength of intergrain exchange interaction is important in these materials. It influences the properties of nanocomposite magnets such as coercivity and maximum energy product.

In the case of magnetic manganite, mixing them with other compound, such as nonmagnetic insulating oxide, will dilute the concentration of the ferromagnetic grains or change the structural boundaries between grains, and hence improved MR is expected. In fact, significant enhanced low field MR (LFMR) or room temperature MR has been found in ferromagnetic/insulator type composites, such as LSMO/CeO₂ [6], LCMO/SrTiO₃ [7], LSMO/SiO₂ [8] etc. However, manganite-insulating polymer nanocomposite has not been reported. We believe that our current magnetic nanoparticles/polymer composites can lead to many potential applications.



In this chapter, the synthesis and magnetic studies of the manganite-polymer composites are presented. Here we adopt a simple strategy to synthesize nanocomposites. Manganites nanoparticles produced by hydrothermal process were mixed with water soluble poly(vinyl alcohol) (PVA). The polymers with sufficient number of –OH groups on the backbone and the magnetoresistive LSMO as filler are expected to show interesting morphologies and properties. Specifically, some information regarding the magnetic and electrical properties of nanoscale LSMO nanoparticles are presented. The experimental data of the present investigation are compared with the empirical equation in order to gain better understanding of the conduction mechanism of this material.

6.1.1 Magnetoresistance (MR) of polycrystalline manganite

The magnetoresistance of a polycrystalline manganite material derives from two distinct contributions. One of them is the intrinsic MR and is likely to arise from the suppression of spin fluctuation when the spins are aligned on application of a magnetic field. This MR has the highest value near the ferromagnetic transition temperature and decreases with the sample temperature. It is generally observed among single crystal or bulk manganites. The second type of contribution is an extrinsic MR, generally observed among the polycrystalline samples and attributed to effect of transportation at grain/interface boundaries [9].

6.1.2 Extrinsic effects in polycrystal samples

In samples with multiple grain structures, it has been shown that there exist the so-called tunneling magnetoresistance (TMR) phenomena through the spin valve mechanism. Magnetoresistance of the material with artificially controlled grain/interface boundaries are also studied to realize a low-field magnetoresistivity (LFMR) device through TMR [10].

In manganites, the half metallic behavior due to Double Exchange (DE) interaction is responsible for inducing a large magnetoresistance ratio. Spin polarizations in grains are schematically depicted in Fig. 6.1. In the zero field case, each grain has different spin orientations. Namely, the spins of the half-metallic electrons are different from one grain to another. Due to the nearly perfect polarization nature of itinerant electrons, inter-grain hopping amplitude is suppressed by such random spin polarizations. Under the magnetic field, spin polarization of grains become parallel to the external field. Inter-grain electron hopping becomes larger in this case. For multi-grain system with half-metallic states such spin valve phenomenon becomes prominent and produces MR effect in a low field range. Resistivity in polycrystal samples seem to be dominated by such extrinsic effects.

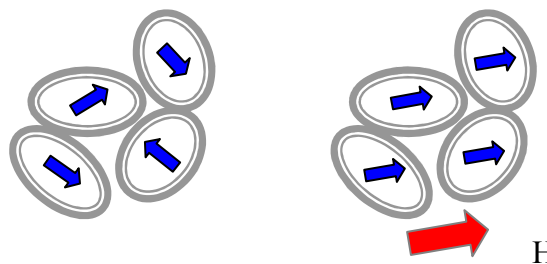


Figure 6.1 Grains of the polycrystalline samples. (a) at zero magnetic field $H = 0$, (b) under magnetic field $H > 0$. Small arrows indicate the orientations of the magnetization for each grain.



6.2 Nanoparticle/ Polymer composite Processing

There are three general ways of dispersing nanoparticles in polymers. The first is direct mixing of the polymer and the nanoparticles either as discrete phases or in solution. The second is in-situ polymerization in the presence of the nanoparticles, and the third is both in-situ formation of the nanoparticles and in-situ polymerization. The latter can result in composites called hybrid nanocomposites because of the intimate mixing of the two phases.

Direct mixing takes the advantage of well established polymer processing techniques. Basically, dispersion of the particle can be achieved primarily by ultrasonic agitation of nanoparticles in a solvent. Nanoparticles tend to agglomerate again after ultrasonic treatment. This re-agglomeration phenomenon depends upon solvent-nanoparticles interaction, chemical treatment given to nanoparticles, presence of dispersing agent or surfactant in solvent and most importantly concentration of particles in solvent.



Indeed, in most nano-composite systems, the crystalline nanoparticles require surface treatment to enable good dispersion into the matrix materials. There are several processes for surface treatment of metal oxide nanoparticles, each designed to provide one or more of the following properties:

- Well dispersed particle in fluid
- Avoid of particles agglomeration
- Compatibility with polymer matrix materials
- Chemical functionalization of the nanoparticle surface with reactive group
- Passivation of the nanoparticle surface chemistry

In some instance, the surface treatment process incorporate functional groups onto the oxide particles.

Some of the limitations of direct-mixing can be overcome if both the polymer and the nanoparticles are dissolved or dispersed in solution. This allows modification of the particle surface without drying, which reduces particle agglomeration. The nanoparticle/polymer solution can then be cast into a solid, or the nanoparticle/polymer can be isolated from the solution by solvent evaporation or precipitation.



In order to improve the miscibility with polymer matrices, one must convert the normally hydrophilic nanoparticles to organophilic, which enables easy intercalation in many engineering polymers. Generally, this can be done by ion-exchange reactions with cationic surfactant, such as CTAB. The role of this alkylammonium cation ($^+NR_4$) is to lower the surface energy of the inorganic host and improve the wetting characteristic with the polymer matrix [11]. It results in larger spacing between the particles. Moreover, the alkylammonium cations could provide functional groups that can react with the polymer matrix or, in some cases, initiate the polymerization of monomers to improve the strength of the interface between the inorganic and polymer matrix [12].



6.2.1 Polymer matrix of Poly(vinyl alcohol) -- PVA

For synthesizing our magnetic-polymer nanocomposite, we have used the poly (vinyl alcohol) (PVA) as the host matrix material. PVA was chosen as the matrix material since it has a lot of attractive properties. For example, PVA owns an excellent film forming ability, high chemical resistance, good transparency, high tensile strength and also high flexibility [13]. Moreover it is a promising candidate for a good polymer dielectric material since it has a high dielectric constant, good surface alignment effect, photosensitivity and good resistance to damage by solvents involved in the fabrication process [14].

Due to such properties, PVA has found wide applications. However, its actual utilization is limited by its affinity to water, which leads to high degree of swelling and even complete solubilization of the resulting products. It is a water soluble polymer extensively used in paper coating, textile sizing, and flexible water soluble packaging film. These sample applications have stimulated interests in improving the mechanical, thermal, and permeability properties of a thin nanocomposite, while ultimately with the hope of retaining the optical clarity of PVA.



PVA have a chemical formula of $(C_2H_3OH)_n$ and structural formula of $\{CH_2CHOH\}_n$. It is widely known that PVA elicits little or no host biological response when implanted in animals. It is a rubbery synthetic polymer of great interest because of its many desirable characteristics specifically for various pharmaceutical and biomedical applications. It has a relatively simple chemical structure with a pendant hydroxyl group. A sketch of PVA chemical structure is shown in Fig. 6.2.

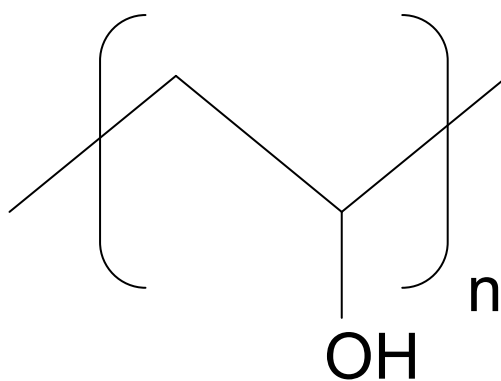


Figure 6.2 Repeating unit of Poly(vinyl alcohol) polymer.



6.2.2 Mixing of LSMO nanoparticles in PVA polymer matrix

LSMO-PVA nanocomposite samples were cast from $\text{La}_x\text{Sr}_{1-x}\text{MnO}_3$ (LSMO)/water dispersions where certain amount of PVA was dissolved. Initially deionized water was used to form a suspension of LSMO nanoparticles. The suspension was first mechanical stirred for one hour and then sonicated for 30 minutes. Low viscosity, fully hydrolyzed PVA was then added to the stirring suspensions. The mixtures were then heated to 70 °C to completely dissolve the PVA. They were sonicated again for 30 minutes and then cast into films and dried in a closed oven at 50 °C for one day. The films were then characterized by magnetization measurement and electrical transport measurements. Procedures for preparing the LSMO/PVA composites were schematically shown in Fig. 6.3.

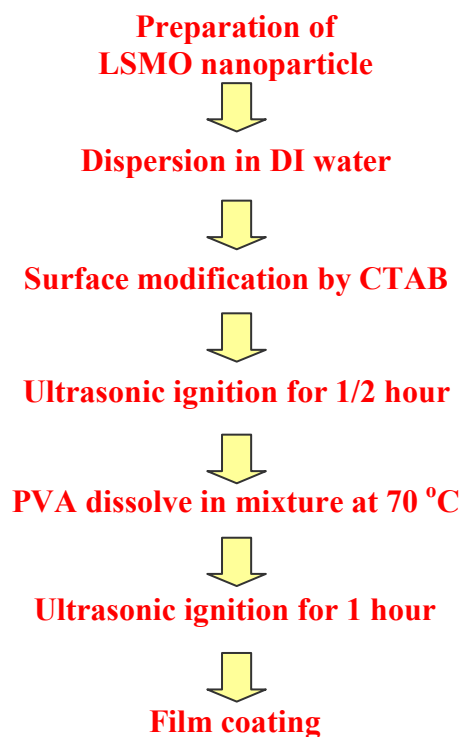


Figure 6.3 Procedures for synthesizing LSMO/PVA magnetic composites.



6.3 Experimental Section

6.3.1 Synthesis of LSMO/ PVA composite

The LSMO-PVA composites were prepared by two steps. It includes preparation of LSMO nanoparticles, dispersion of nanoparticles in polymer solution and polymerization of final composite at elevated temperature.

6.3.1.1 Preparation of LSMO nanoparticles

LSMO nanoparticles were prepared by mixing proper portions of MnCl_2 , KMnO_4 , SrCl_2 and LaCl_3 with KOH and then put into a Teflon lined autoclave for hydrothermal treatment. The detailed synthesis procedures for perovskite nanocrystals have been reported in Chapter 4. The as-prepared particles were cleaned and dried before the next procedures.

6.3.1.2 Formation of polymer composite

PVA powder with molecular weight of 15 000 g was dissolved in deionized water at 60 °C. Ultrasonic agitation was used to disperse the as-prepared LSMO nanoparticles in polymer solution with a help of cationic surfactant CTAB. The weight-ratio of the LSMO nanoparticles: PVA: DI water: CTAB was 5000: 1000: 5000: 1.

6.3.1.3 Formation of LSMO/PVA polymer composite film

The aqueous PVA polymer solution dropped on pre-cleaned glass substrate was dried at 60 °C in an oven for two days. Then the nanocomposite film was detached from the glass substrate.



6.3.2 Characterization of LSMO/PVA composite

6.3.2.1 X-ray powder diffraction

To qualify the crystalline structure of the LSMO nanoparticles, x-ray diffraction patterns were obtained with a Philips x-ray diffractometer using $\text{CuK}\alpha$ radiation with a nickel filter. Bragg equation and Scherrer's equation were used to determine the lattice parameter and the particle sizes, respectively.

6.3.2.2 Transmission electron Microscope (TEM) Analysis

TEM image studies and energy dispersive x-ray spectroscopy (EDX) microanalysis were carried out on the JEOL JEM-2010 operated at 200 kV. The samples for TEM analysis were prepared by dispersed a drop of nanocrystals solution on holey carbon-coated copper grids.

6.3.2.3 Scanning electron microscope (SEM) Analysis

The morphological studies of the LSMO-PVA composite were carried out using a JEOL JSM-6335F field emission SEM. Since the LSMO have been confirmed to be metallic in the previous chapter, no additional metal coating was required.



6.3.2.4 Magnetic Characterization

Both temperature and field dependent magnetization measurements were carried out on a vibrating sample magnetometer (VSM) with a magnetic field up to 5 kOe and temperature ranging from 20K to 300 K. All samples for field dependent hysteresis measurements were prepared by compressing the manganite-polymer composite into the small Teflon holder.

6.3.2.5 Electrical transport properties

The RT measurement and MR measurement were performed on a small piece of sample using standard two-point method. A compressed helium cryostat with sample temperature varied from 350 K down to 20 K and a magnetic field ranging from 0 Oe to ± 5 kOe were used.

6.4 Results and Discussion

6.4.1 Structural characterization

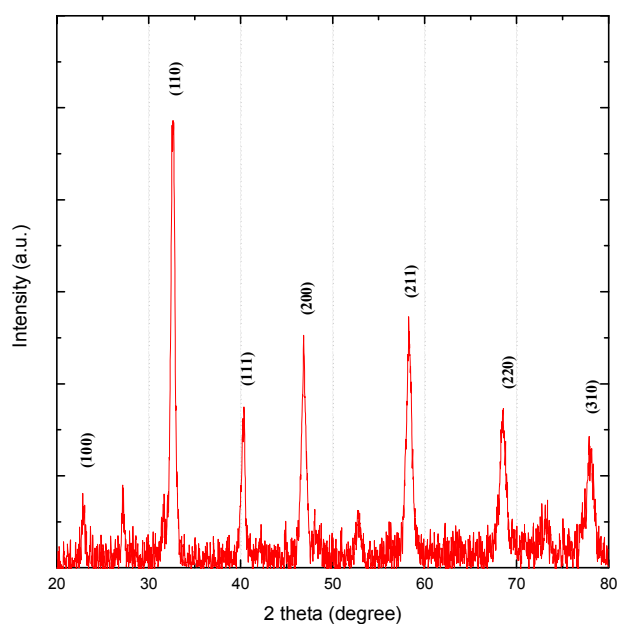


Figure 6.4 XRD pattern of as-synthesized LSMO particles.

Fig. 6.4 shows the x-ray diffraction 2-theta scan of as-prepared $\text{La}_{0.67}\text{Sr}_{0.33}\text{MnO}_3$ (LSMO) nanoparticles. The diffraction peaks are well indexed to LSMO pseudo-cubic structure. The absence of extra lines in the diffraction patterns assures phase purity. The lattice parameter of $d_{(110)}$ is calculated as 0.548 nm, which is in agreement with reported value. The broad characteristic of the XRD peaks reveals the nanocrystalline nature of the hydrothermal products. The average particle size is estimated from full width at half-maximum (FWHM) of the diffraction peak (110) of the particles using Scherrer's equation. In the present work, the crystallite size of the manganites is around 40 nm.



TEM images

A TEM image of the as-synthesized LSMO particle is shown in Fig. 6.5. It is clear that the size of most particles is in the range of ~ 40 nm. Particles size determined from TEM images agrees with the XRD measurements except for some agglomerated particles. These agglomerates can increase the magnetic interaction between particles, and therefore may influence the magnetic properties of the composite. The electron diffraction pattern (SAD) taken from the particles is shown in Fig 6.5b. It exhibits strong discrete diffraction spots aligned on the Debye cones. As determined from SAD, it is a cubic structure with a d_{110} lattice constant of 0.55 nm. The above XRD and high resolution TEM data confirm that the $\text{La}_{0.67}\text{Sr}_{0.33}\text{MnO}_3$ (LSMO) nanoparticles are indeed of typical perovskite structure. These LSMO nanoparticles thus prepared are suitable to mix with PVA to form the magnetic nanocomposite.

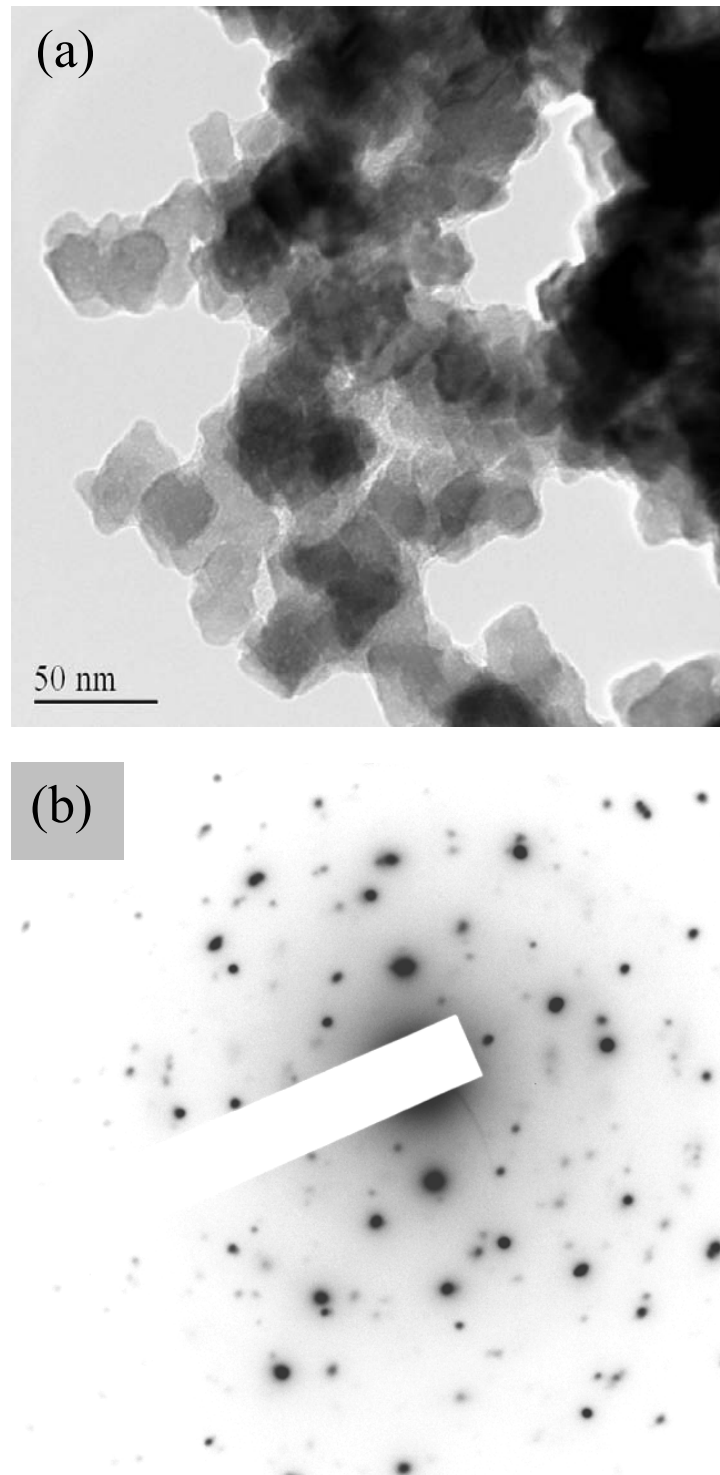


Figure 6.5 (a) TEM image and (b) electron diffraction of as-synthesized LSMO nanoparticles.



SEM images

When studying a nanocomposite system, it is very important to examine and characterize the distribution/dispersion of the particles in the polymer matrix. The SEM micrograph of our nanocomposite sample shows the manganite particles bonded to the polymeric chains of PVA. Fig. 6.6 shows that the LSMO nanoparticles are fairly uniformly dispersed in the PVA matrix. As can be judged from the micrograph, only few LSMO particles are seen to locate on the surface.

One the other hand, it is well know that the volume fraction of additives in polymer matrix is a key parameter to its physical properties, such as electrical conduction, thermal conduction, elasticity, etc. One typical example is the conducting carbon black/polymer composite, abrupt conductivity increase when the percolation threshold is reach at a critical volume fraction. However, we have not determined the volume fraction of our sample because of the too small quantity of LSMO nanoparticles and PVA. For better investigation of this magnetic field dependent conducting material, the correlation between the volume fraction and physical properties should be further explored..

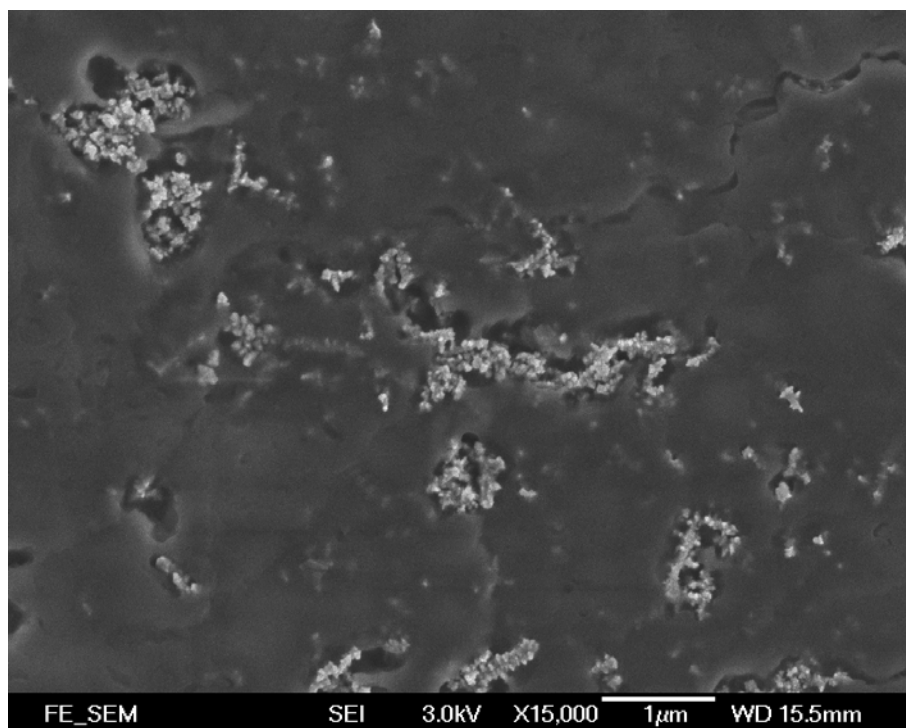
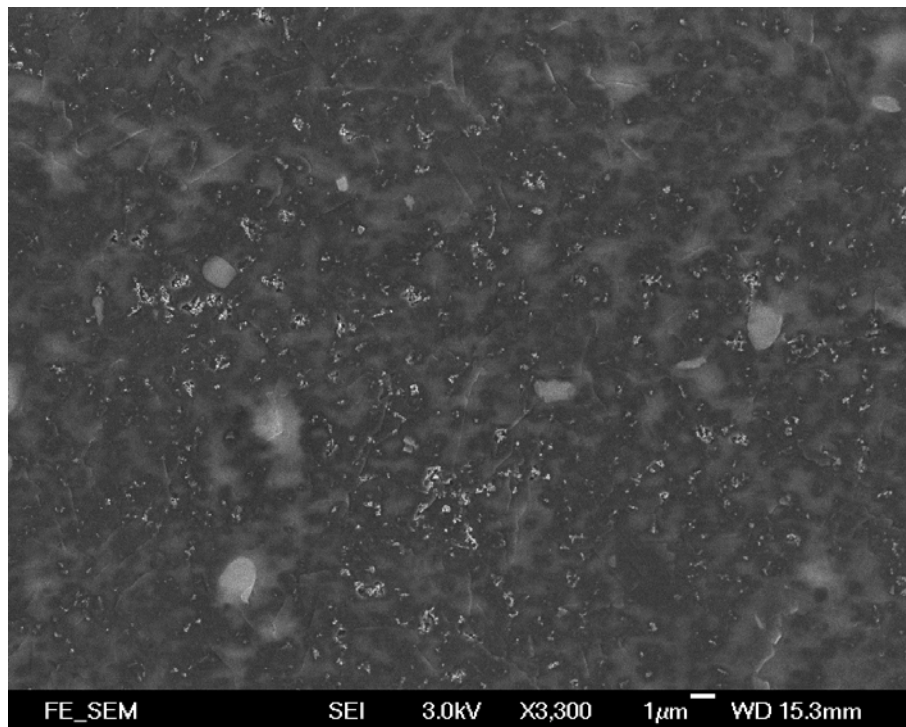


Figure 6.6 SEM images of the LSMO nanoparticles inside the PVA matrix. The bright dots are LSMO nanoparticles and the ridges are associated with the polymer surface.



6.4.2 Magnetization properties

To study the magnetic properties of the LSMO/PVA nanocomposite, magnetization measurements were performed as a function of temperature and applied magnetic field. During the measurement, a small piece of LSMO/PVA nanocomposite was mounted on the hand-made Teflon holder of the VSM.

Fig 6.8 shows the magnetization M curves of the sample measured at different temperatures. At 290 K, the M_s of the composite is 41 emu/g. This is smaller than that (80 emu/g) of the LSMO bulk sample. It may be due to the small particle size and high surface disordering of manganite. No magnetic hysteresis is observed at 290 K whereas a clear hysteresis loop with a large coercivity of 138 Oe is obtained at 20 K. This indicates that the LSMO nanoparticles are superparamagnetic at room temperature. Clearly the superparamagnetic blocking temperature is below room temperature. Although our cryostat only enables us to achieve 300K sample temperature, the well defined magnetization can verify that the Curie temperature (T_c) of this nanocomposite is higher than 300 K.

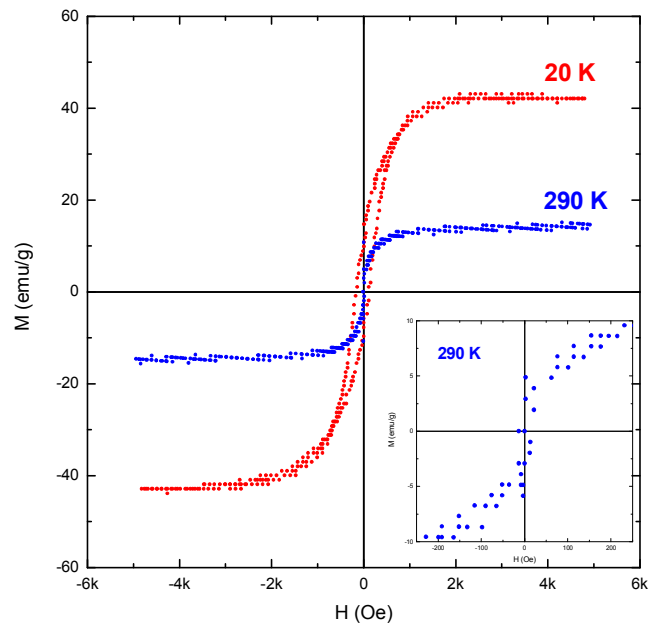


Figure 6.7 Magnetic hysteresis loop for LSMO/PVA nanocomposite prepared by cationic surfactant assisted hydrothermal method at 20 K and 300 K, respectively.

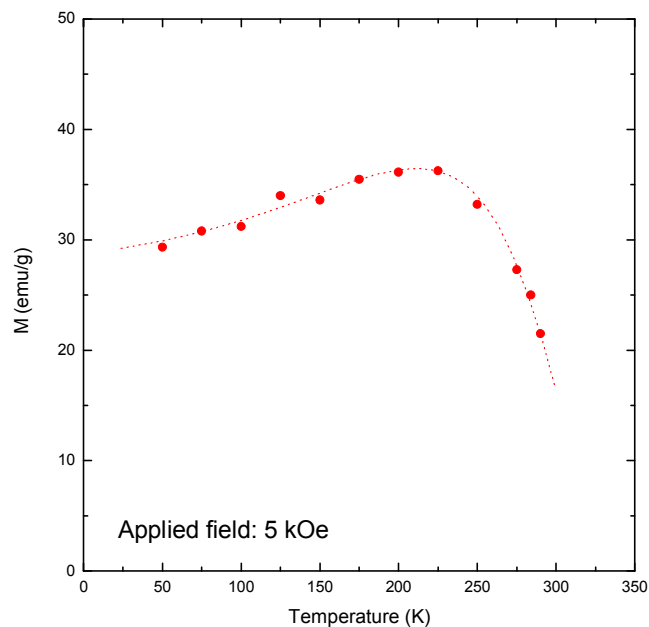


Figure 6.8 Magnetization of LSMO/PVA nanocomposite as a function of temperature. (Applied field: 5 kOe)



It is known that for magnetic nanoparticle system the coercive field increases with decreasing temperature. This increase in the coercive field is due to the lower thermal activation energy of spins at lower temperature. The variation of the coercivity with temperature for our LSMO/PVA nanocomposites is shown in Fig. 6.9. Indeed, the coercive field is seen to decrease with increasing temperature, dropping from 145 Oe at 20 K to about 0 Oe at 300 K. Also, we find that the H_c of the sample is linear proportional to T at temperature below 250K. This suggests that the magnetic properties of as-synthesized LSMO/PVA composite are guided by weak domain wall pinning. This profile of LSMO/PVA clearly indicates a sudden drop of coercivity at near T_B . It differs from the gradually decrease seen in synthesized LSMO particles in Fig 4.9. Apparently this unusual characteristic is directly related to the PVA matrix and will be an interesting topic for further studies.

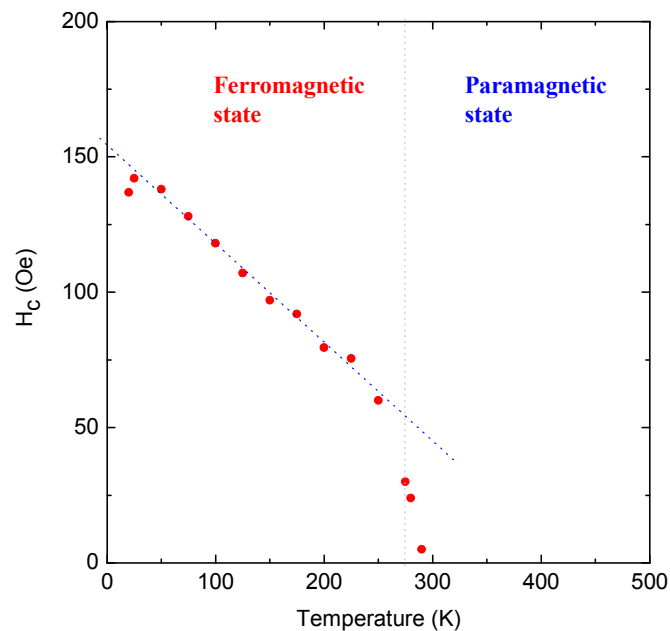


Figure 6.9 Temperature dependence of coercive field of as-synthesized LSMO/PVA nanocomposites.



6.4.3 Electrical transport properties

In order to measure the electrical conduction properties, two silver paste electrodes were coated on the surface of the LSMO/PVA composite. The dimension of the test section was kept at 0.2 mm (thick) x 2 mm (width) x 0.5 mm (length) in order to calculate the resistivity from the measured resistance value.

Fig 6.10 shows the temperature dependence of the resistivity of the LSMO/PVA composite without applied magnetic field. The resistivity-temperature (R-T) profiles in the range from 20 K to 325 K are presented in various plots [Fig. 6.11 and 6.12]. In general, the composites display semiconducting behavior. The room temperature resistivity is found to be 324 Ω cm, which is much larger than those of pure LSMO samples.

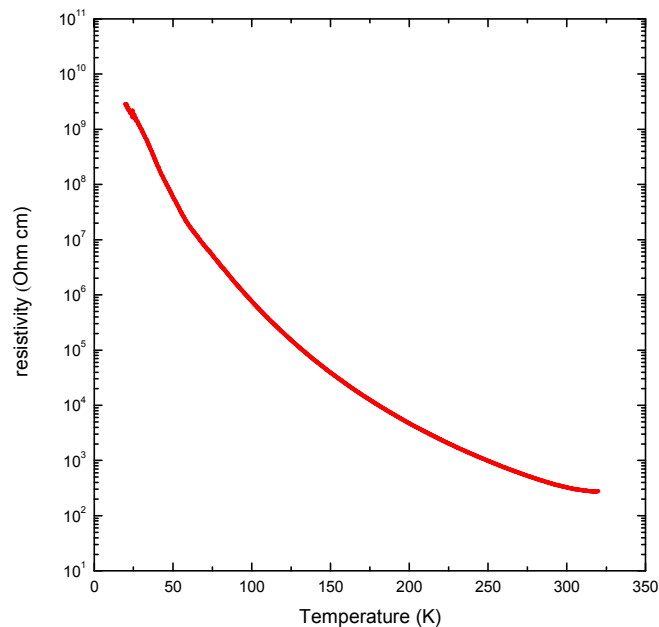


Figure 6.10 Temperature dependence of resistance of the LSMO-PVA composite.



Moreover, no characteristic abrupt change was found from the R-T curves. For this reason the contribution from the metal-insulating transition is negligible. The observed R-T profile, however, may originate from a number of contributions including the grain boundary induced effect. Since the grain boundary is similar to amorphous state, the magnetic configuration on the grain surface is more chaotic than in the core. Thus the insulating regions appear near the grain boundaries. Indeed a manganite with small particle size and large number of boundaries formed from the polymer isolation is of a ferromagnetic/insulator/ferromagnetic tunneling junction structure. Therefore the sample behaves as an insulator in the temperature range from 20 to 325 K.

As mentioned before, three typical models are used to describe the conduction mechanism of the paramagnetic insulator. These models are proposed in terms of conventional thermal activation (TA), small polaron hopping (SPH) and variable range hopping (VRH), respectively. Each predicts a different temperature dependence of resistivity. In Fig 6.11 and 6.12, the comparison of these two fitting results exhibits that the variable range hopping model well describes transport behavior of the nanocomposite in the temperature range of 95 K – 325 K. Therefore, the resistivity of the sample follows the Mott's equation which is given by:

$$\rho = \rho_o \exp\left(\frac{T_o}{T}\right)^{1/4}$$

Therefore the electrical conduction of the composite is dominated by the electron hopping process between the localized states in LSMO nanoparticles.

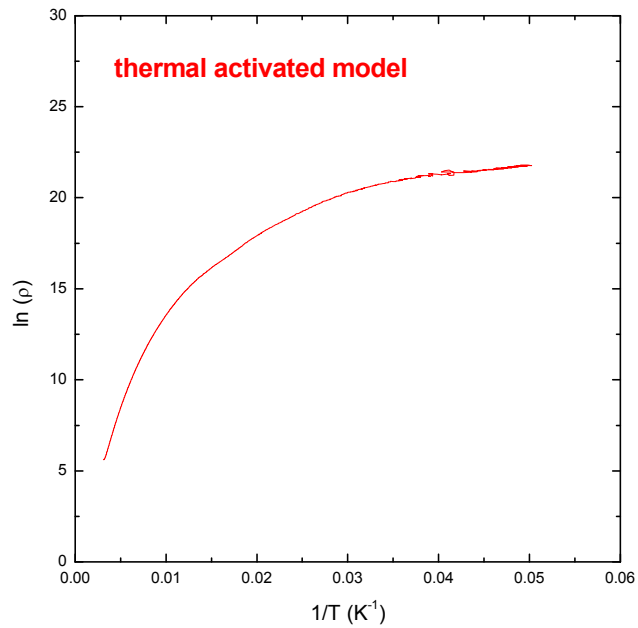


Figure 6.11 A graph of $\ln(\rho)$ against $1/T$.

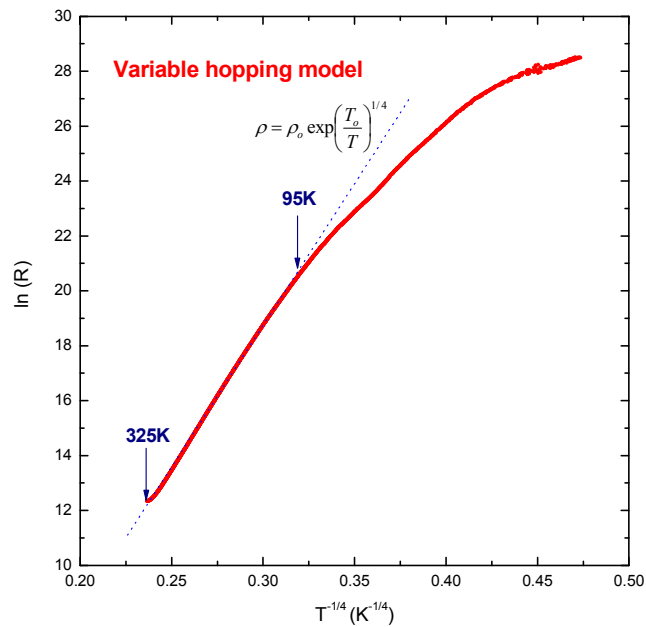


Figure 6.12 A graph of $\ln(\rho)$ versus $1/T^4$.



6.4.4 Magnetoresistance properties

The magnetoresistance measurement was performed on the sample with dimension of 0.2 mm (thickness) x 2 mm (width) x 0.5 mm (length). Electrodes for the two-point probe method measurement were made by brushing silver paste on the high resistive sample. The MR ratio is defined by:

$$MR = \frac{R_H - R_{0Oe}}{R_{0Oe}} \times 100\%$$

where R_H and R_{0Oe} correspond to electrical resistance at an external field of H and 0 Oe, respectively.

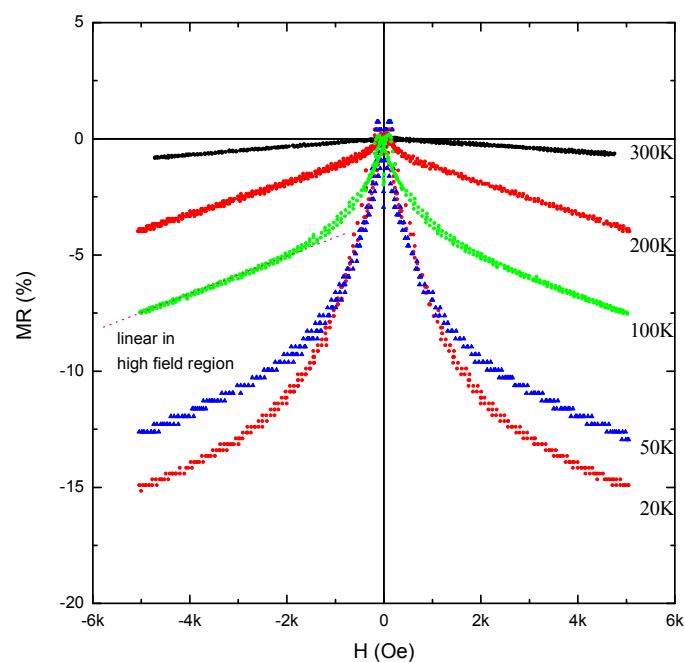


Figure 6.13 Magnetoresistance ratio of LSMO-PVA composite at different temperatures.



Fig. 6.13 shows the field dependence of magnetoresistance (MR(H)) of the LSMO-PVA composite at different temperatures. The magnetic field range used is ± 5 kOe. It is found that the magnetoresistance curve is less linear in low field and becomes more linear when the external field is increased. Also, the double peaks in MR(H) are obvious for the sample measured at 20 K. It is commonly known that such double peaks correspond to a large coercive field. These features can be explained as follows. Within low field range, the response is highly nonlinear and associated with the ferromagnetic domain relaxation. The structure of the grain domain in long-range order is parallel to the applied field, and the long range magnetic order is increased by increasing the external applied field leading to a linear relationship of MR-H.

When the applied field is higher, a roughly linear MR occurs. This is primarily attributed to the spin-related electron scattering at grain boundaries. Also, an obvious feature of the LSMO-PVA composite is that the MR sensitivity which defined by $S = \left| \frac{\partial MR}{\partial H} \right|$, remains nearly constant of 0.08 at 100 K. This measured value is much higher than the 0.03 of the conventional bulk LSMO with the same composition [15].

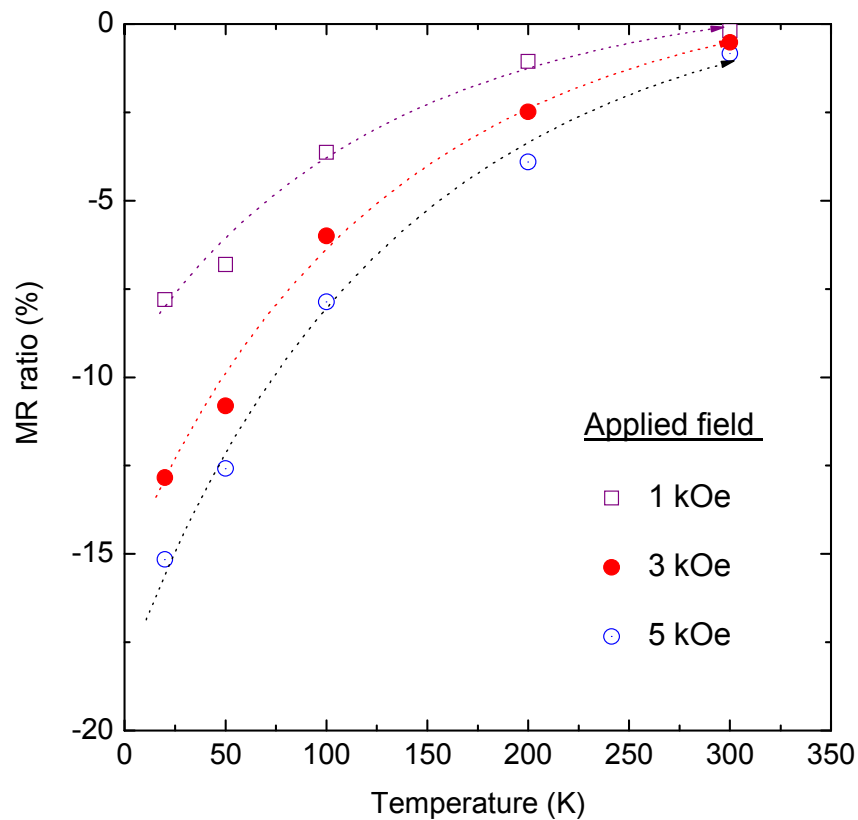


Figure 6.14 Temperature dependence of MR ratio for the LSMO/PVA composite under different applied fields.

Magnetoresistance against temperature is plotted in Fig. 6.14. The figure clearly shows a large LFMR of the composite material as a function of temperature. The high sensitive of magnetic field suggests that it can be use in spin-device. As mentioned before, the SEM images have revealed that the LSMO particles appear to link up in the PVA matrix. However, the insulating PVA can still create non-conducting layers separating individual LSMO grains. Thus it is reasonable to believe that the spin polarized electron may tunnel through the polymer matrix between the LSMO grains, making contributions to the low field magnetoresistance.



6.5 Summary

LSMO magnetic nanoparticles have been successfully embedded into PVA polymer matrix. About 40 nm sized $\text{La}_{0.67}\text{Sr}_{0.33}\text{MnO}_3$ (LSMO) particles have been synthesized by cationic surfactant assisted hydrothermal method. The as-prepared LSMO nanoparticles have been ultrasonic-mixed with insulating PVA polymer in order to form a magnetic polymer nanocomposite. Structural, magnetic and electrical properties have been examined. For our investigation, a novel low temperature templating strategy was introduced for the synthesis of these magnetic nanocomposites. No thermal cycling steps are required. This makes it particularly attractive for integration into the fabrication of novel magnetic devices.

In the present study, structural characterization indicates that a homogeneously distributed LSMO/PVA composite can be obtained with the help of cationic surfactant (CTAB). The magnetic properties of the composite are nearly the same as the as-synthesized nanoparticles; hence it can maintain a superparamagnetic nature even at room temperature. Electrical conductivity measurement have been carried out, the transport properties are dominated by the variable range hopping model in the temperature range of 95 – 325 K. A large magnetoresistance ratio of 15 % at 20 K has been demonstrated with a small field of 5 kOe. One may conclude that the LSMO nanocomposite is exhibiting extrinsic nature of magnetoresistance and the responsible mechanism is found to be inter-grain spin polarized tunneling (SPT).



Since the artificial insulating grain boundary is formed by introducing an insulating PVA between the LSMO nanoparticles, we believe that the magnetoresistance of the sample can be further enhanced by varying the PVA content. To use other organic insulating polymers instead of PVA may also help to increase the MR.

In this new attempt of sample preparation we have shown that an effective and simple technique is able to prepare manganite-polymer nanocomposite with good dispersion of particles in the matrix. The very same technique could also be used to prepare other kinds of nanocomposite. The present study is promising in terms of applying this synthesis and processing techniques for making multilayer nanostructures with other polymer matrices. The successful fabrication of manganite-polymer composite is only the first step towards utilizing the magneto-organic for devices. The potential for practical use of magnetic nanocomposites is definitely encouraging.



CHAPTER 7

Conclusion

Since the discovery of colossal magnetoresistance in manganites such as $\text{La}_{0.67}\text{Sr}_{0.33}\text{MnO}_3$, practical applications of these new spintronic materials are being intensively explored. In this respect, high quality ceramic powders of good compositional homogeneity, better stoichiometry, fine particles size and sometimes non-agglomerated particles are required for practical purpose.

In this project we have developed a simple cationic surfactant assisted hydrothermal method to synthesize nanoparticles with controllable size. This modified process technique has the advantages of ease of chemical composition control, low temperature operation and uniform nano-sized particle formation. Using this technique, we have produced stoichiometric nanocrystallites of $\text{La}_x\text{Sr}_{1-x}\text{MnO}_3$ (LSMO) and $\text{La}_x\text{Ba}_{1-x}\text{MnO}_3$ (LBMO). High purity and homogeneity can be easily achieved at temperature as low as 220 °C as against 1300 °C needed to synthesize these materials via a standard solid state reaction. Moreover, the studies on magnetic properties of the as-synthesized particles clearly demonstrate the nanomagnetism.

We have systematically studied the effect of various processing conditions, such as concentration of mineralizer, processing temperature, surfactant concentration and aging temperature, on the final particles. The particle size, size distribution, morphology and crystallinity of the $\text{La}_{0.67}\text{Sr}_{0.33}\text{MnO}_3$ powders were



measured by a host of advanced structural characterization equipment including XRD, EDX, field emission SEM and TEM. Magnetic properties such as the temperature dependent magnetization, coercive field, magnetic anisotropy and magnetic transition temperature have also been measured and analyzed using a VSM. A major portion of the current investigation is to unravel the relations between the structure and the magnetic properties of the LSMO magnetic nanoparticles.

Our results show that the cationic surfactant cetyltrimethylammonium bromide (CTAB) has an obvious effect on the manganite nanoparticle formation. Without the CTAB, the as-formed powder contains a lot of impurities such as the pure $\text{La}(\text{OH})_3$ nanorods. Increase the CTAB content can substantially improve the formation of stoichiometric LSMO particles as well as help to narrow the size distribution of the as-synthesized particles. Lattice fringes in HRTEM images reveal well-crystallized LSMO nanocrystals synthesized by this method. We propose a mechanism of how CTAB micelles work. We have also identified and explained the role of CTAB as a catalyst for initiating the nucleation process and forming the nano-sized manganite particles.

Typical $\text{La}_{0.67}\text{Sr}_{0.33}\text{MnO}_3$ (LSMO) crystallites formed from the surfactant assisted hydrothermal method is in the range of several tens of nanometer. The as-prepared nano-sized LSMO particles are ferromagnetic below the spin freezing temperature (T_f) and normally exhibit superparamagnetism (SPM) at room temperature. No exchange bias has been observed when the sample is in ferromagnetic state; therefore it implies that the nanoparticles are free of any



antiferromagnetic layer. Also, the saturation magnetization (M_s) has been found to decrease with the size of LSMO particle. The large coercive field of the particles (~ 400 Oe) at 20 K can be attributed to the surface induced anisotropy and the domain wall pinning process. Through the magnetometry technique such as ZFC/FC curve measurements, the spin freezing temperature for the 50 nm LSMO particles is 200 K.

In conventional hydrothermal synthesis, temperature should be a crucial factor to modify the homogeneity and morphology of the product. Crystallized and stoichiometric LSMO particles have been produced under a wide range of processing temperature from 210 °C to 250 °C. We have demonstrated that the stoichiometric LSMO particles can be successfully obtained when the processing temperature is higher than 210 °C. Otherwise, $\text{La}(\text{OH})_3$ nanorods coexist with the product. When the processing temperature is in the range of 220 °C to 250 °C, the as-synthesized particle's crystallinity, particle size and particle morphology in our system do not seem to be sensitive to temperature.

From the precursor aging studies, we have found that the particles formation is highly dependent on the initial state of the precursor. Through the treatment of the precursor at different aging temperature for 5 hours duration, different particle size and morphology of LSMO have been obtained. It is noted that the aging temperature is far lower than the hydrothermal temperature of 240 °C. In such a case, we believe that there are no LSMO crystals formed at the aging stage. TEM images reveal that particles are formed in rod-like shape with some dendrites when the precursor has



been aged at 30 °C for 5 hours, but in spherical form when it has been aged at 70 °C. Indeed the formation of crystalline nanoparticles from hydrothermal method can be described by the La Mer Model which states that the size and morphology are affected by the probabilities of crystal nucleation and crystal growth. Evidently, when the aging temperature is increased from 30 °C to 70 °C for 5 hours duration, the dissolution/recrystallization becomes more vigorous. This can facilitate a fast nucleating process and hence formation of large numbers of nuclei, which will subsequently result in submicron-sized rod-shape particles to nano-sized spherical particles. This obvious modification in particle morphology also leads to changes in the magnetic properties of the LSMO particles. A smaller saturation magnetization (M_s) and a higher coercive field (H_c) have been obtained from the tiny spherical LSMO particles. It suggests that the strong effect from the high surface anisotropy and surface magnetic disorder predominate.

It is also found that the initial concentration of mineralizer plays an important role to guide the hydrothermal reaction and crystalline growth. In our experiment, impurities, mainly of $\text{La}(\text{OH})_3$, are observed to co-exist with the LSMO particles when they are prepared at a relative low $[\text{KOH}]$ of 1.5 M to 4.5 M. When the $[\text{KOH}]$ is increased to about 5 M, impurities were completely removed and the pure LSMO is formed. It suggests that the minimum $[\text{KOH}]$ required for the LSMO particle formation via our hydrothermal condition is 5M. On the other hand, TEM observations provide evidence that the initial $[\text{KOH}]$ has a stronger influence on the LSMO morphologies than the processing temperature. Basically when the $[\text{KOH}]$ is 5 M, uniform size spherical LSMO nanoparticles have been obtained. When the



[KOH] is further increase, larger particles with sharp edges and well defined crystal facets could be produced. Therefore, the [KOH] is a critical process parameter that determines the particles crystallinity, size and also the morphology. Hence, selection of a suitable [KOH] value is very important to produce the desired particle from the hydrothermal processing.

In the composition study, particles of $\text{La}_x\text{Sr}_{1-x}\text{MnO}_3$ with x from 0.5 to 0.7 have been synthesized by the hydrothermal process. Through the control of mole ratio of the precursors, high purity nanosized particles have been prepared. XRD pattern and EDX results have confirm the stoichiometry of the as-synthesized particles. Again, through the magnetization measurement, similar superparamagnetic features of the samples have been obtained. The successful tuning of LSMO composition strongly suggests that this chemical method allows the material properties to be easily tailored to the task at hand.

The electrical transport behavior of hydrothermal synthesized $\text{La}_{0.67}\text{Sr}_{0.33}\text{MnO}_3$ particles have been experimentally studied by resistivity-temperature (RT) and magnetoresistivity (MR) measurements. In the RT measurement, the resistivity of LSMO increases substantially as the crystal size decreases. Also, we have found that the sintered sample with initial LSMO crystal sizes of 40 nm and 2000 nm show an insulator-metal (I-M) transition at T_p of 209.6 K and 309.7 K, respectively. But for the LSMO particles as small as 20 nm, no such transition has been determined. It suggests that T_p decreases substantially with particle size. The main reason may due to the insulating nature of the grain



boundaries of the manganites. Therefore, the extrinsic transport mechanism overwhelms the intrinsic one for nano-sized manganites.

In the MR study, the MR-H loop of low temperature sintered LSMO pellet at 20 K shows a butterfly feature at low-field but quite linear at the high fields region. At such temperature, the low field MR of the LSMO pellet at 5 kOe has found to be 22 % and monotonically decreasing with temperature. It suggests that the sample is behaving like a typical granular ferromagnetic metal dispersed in non-magnetic matrix. This butterfly feature has been explained by the spin-polarized tunneling (SPT) mechanism. Since this model states that the low-field MR (LFMR) is strongly dependent on temperature, it follows that the lower the temperature the higher is the MR of the sample.

In the same manner, barium doped manganite nanoparticles have also been synthesized successfully. Large stoichiometric $\text{La}_{0.67}\text{Ba}_{0.33}\text{MnO}_3$ particles of about 2 μm big and without impurities have been obtained. Shape evolutions of LBMO particles from octapod particles to perfect cubes have been synthesized by adjusting the concentration of mineralizer [KOH] of the solution. The possible explanation is that the concentration of mineralizer of the solution affects the crystal growth rate, which helps to shape the final morphology of the as-grown particles.

The low temperature saturation magnetization (M_s) of as-synthesized LBMO particles is 60.7 emu/g and the Curie temperature (T_c) is about 350 K, similar to those reported for bulk samples. The temperature dependent resistivity measurement



of sintered LBMO sample has been carried out by a standard four-point probe method. The sample exhibits metal-insulator (I-M) behavior and this transition occurred at temperature T_p of 264 K. The result reveals good electrical properties of the hydrothermal derived LBMO particles. This result also implies that our hydrothermal process is so flexible that it enables us to produce many other related materials.

Our preliminary studies indicate that the hydrothermal technique can prepare LSMO particles with good magnetic properties. The process is also versatile in morphology and composition controls. For the LSMO nanoparticles to be used in spintronic device, their properties must be well behaved and characterized. Therefore, further research should be focused on understanding more clearly the inter-relationships between the particles size, dispersivity, morphology, possibility of self-assembles, electrical conductivity and magnetic responses. Moreover, the important superparamagnetic properties of these LSMO nanoparticles unambiguously make LSMO a promising candidate for various practical applications in areas such as magnetic fluidity, probes for biomolecules and magnetic guided delivery. To explore more possibility of the application and compatibility, LSMO hybrid composites have also been prepared. They included the LSMO/PVA composite and LMO/LSMO core-shell architecture.

Considerable effort has been devoted to the synthesis and characterization of LMO/LSMO core-shell architectures. Core-shell nanoparticles comprising ferromagnetic $\text{La}_{0.67}\text{Sr}_{0.33}\text{MnO}_3$ (LSMO) core and antiferromagnetic LaMnO_3 (LMO)



shell have been synthesized by a two-stage hydrothermal process. The core-shell structure has been confirmed by TEM analysis. A 4 - 5 nm thick shell layer have been detected on the surface of LSMO nanoparticles. The magnetic characterizations on the nanoparticles show further evidence on the successful fabrication of core-shell structured nanoparticles. The obvious effects of the shell such as enhancement of magnetization and decrease in Curie temperature have been obtained. However, the exchange bias (shift in H_c) which is the seeming feature of magnetic coupling did not appear in our samples. At present we do not have a good explanation. It might be that the magnetic properties of the thin LMO shell layer may differ from a bulk sample.

We have also prepared samples of LSMO nanoparticles dispersed in poly(vinyl alcohol) (PVA) polymer matrix. These composites exhibit superparamagnetism above the blocking temperature. Their magnetic properties are nearly the same as the raw LSMO nano-particles. The temperature dependent magnetoresistivity (MR) has been verified. A large negative magnetoresistance ratio of 15 % at 20 K has been demonstrated. The MR decreases monotonically with increasing temperature at low field of 5 kOe. The hysteresis shown in the MR-curve suggests that the LSMO-PVA nanocomposites exhibit extrinsic transport properties of spin polarization tunneling. As we know, PVA possesses a lot of attractive properties such as high chemical resistance, good optical transparency, high dielectric constant and commendable biocompatibility. The fabrication of such magnetic manganite-polymer nanocomposites therefore represents a rational design approach to alter the magnetic properties for a wide variety of technical applications.



Up to now, some of the physical properties of the magnetic nanoparticles have been measured. However, proper controls of many of these properties remain elusive. Examples are the broad particle size distribution and particle agglomeration. Both of these features alter the magnetic single domain characteristics of the magnetic nanoparticles. One potential way to yield a more uniform particle size distribution over a large volume would be to use the reverse micelles method to limit the growth of individual particle and to avoid the particle agglomeration. To some extent, our work has demonstrated the validity of this approach. For better understanding of these low-dimension magnetic materials, more electrical and magnetic characterization, such as ac magnetic field response, magnetic viscosity and magnetoimpedance measurements, should be performed. For the LSMO based nanocomposites, the surface treatment on the LSMO particles should be further investigated in order to achieve better particle dispersion in the matrix and consequently better magnetic properties.



References

Chapter 1 Introduction

- [1-1] G. Alex, Handbook of modern ferromagnetic materials, (Boston: Kluwer Academic Publishers, C1999). P.1
- [1-2] D. Sellmyer, R. Skomski, Advanced Magnetic Nanostructure, (Springer, 2006), P. 491
- [1-3] Z. L. Wang, Y. Liu, Z. Zhang, Handbook of Nanophase and Nanostructured Materials, Vol. 1 (Tsinghua University Press, 2003)
- [1-4] J. L. Dormann, D. Fiorani, Magnetic Properties of Fine Particles, (Proceedings of the International Workshop on Studies of Magnetic Properties of Fine Particles and their Relevance to Materials Science, 1991) P.3
- [1-5] D. Sellmyer, R. Skomski, Advanced Magnetic Nanostructures, (Springer, 2006) P.13
- [1-6] X. M. Lin, A. C. S. Samia, J. Mag. Mater. Vol. 305, (2006) P.100-109
- [1-7] D. Sellmyer, R. Skomski, Advanced Magnetic Nanostructures, (Springer, 2006) P.40
- [1-8] D. Sellmyer, R. Skomski, Advanced Magnetic Nanostructures, (Springer, 2006) P.185
- [1-9] D. Sellmyer, R. Skomski, Advanced Magnetic Nanostructures, (Springer, 2006) P.295
- [1-10] J. M. Daughton, J. Mag. Mater., Vol.192, (1999) P.334-342
- [1-11] A.M. Tishin, The magnetocaloric effect and its applications, (Bristol: Institute of Physics Pub., 2003) P. 1.
- [1-12] A. Hutten, D. Sudfeld, I. Ennen, G. Reiss, W. Hachmann, U. Heinzmann, K. Wojczykowski, P. Jutzi, W. Saikaly, G. Thomas, J. Biotechnology 112 (2004) 47-63
- [1-13] R. Badescu, D. Condurache, M. Ivanoiu, J. Mag. Mater. 202 (1999) P.197-200



- [1-14] J. R. Christman, Fundamentals of solid state physics, (John Wiley & Sons, Inc., 1988) P. 344
- [1-15] J. R. Christman, Fundamentals of solid state physics, (John Wiley & Sons, Inc., 1988) P. 345
- [1-16] P. Lorrain, D. R. Corson, F. Lorrain, Electromagnetic Fields and Waves, Third Edition (W.H. Freeman and Company, 1996) P.368
- [1-17] K. H. J. Buschow, F. R. De Boer, Physics of magnetism and magnetic materials, (New York: Kluwer, Academic/ Plenum Publishers. 2003), P.59
- [1-18] J. R. Christman, Fundamentals of solid state physics, (John Wiley & Sons, Inc., 1988) P. 352
- [1-19] J. R. Christman, Fundamentals of solid state physics, (John Wiley & Sons, Inc., 1988) P. 361
- [1-20] J. R. Christman, Fundamentals of solid state physics, (John Wiley & Sons, Inc., 1988) P. 362
- [1-21] J. R. Christman, Fundamentals of solid state physics, (John Wiley & Sons, Inc., 1988) P. 373
- [1-22] M. Ghosh, K. Biswas, A. Sundaresan, C. N. R. Rao, J. Mater. Chem., 16 (2006) 106 - 111
- [1-23] J. A. C. Bland, B. Heinrich, Ultrathin magnetic structures (Springer, 2005) P.266
- [1-24] D. Fiorani, Surface Effects in Magnetic Nanoparticles, (Springer, 2005) P.46
- [1-25] J. R. Christman, Fundamentals of solid state physics, (John Wiley & Sons, Inc., 1988) P. 367
- [1-26] Z. L. Wang, Y. Liu, Z. Zhang, Handbook of Nanophase and Nanostructured Materials, Vol. 3 (Tsinghua University Press, 2003) P.215
- [1-27] E. Dagotto, Nanoscale Phase Separation and Colossal Magneto-resistance, (Springer, 2003) P.72
- [1-28] D. Fiorani, Surface Effects in Magnetic Nanoparticles, (Springer, 2005) P.209
- [1-29] D. Sellmyer, R. Skomski, Advanced Magnetic Nanostructures, (Springer, 2006) P.368



- [1-30] Z. L. Wang, Y. Liu, Z. Zhang, Handbook of Nanophase and Nanostructured Materials, Vol. 3 (Tsinghua University Press, 2003) P.217
- [1-31] D. Sellmyer, R. Skomski, Advanced Magnetic Nanostructures, (Springer, 2006) P.52
- [1-32] Z. L. Wang, Y. Liu, Z. Zhang, Handbook of Nanophase and Nanostructured Materials, Vol. 3 (Tsinghua University Press, 2003) P.219
- [1-33] Z. L. Wang, Y. Liu, Z. Zhang, Handbook of Nanophase and Nanostructured Materials, Vol. 3 (Tsinghua University Press, 2003) P.218
- [1-34] J. M. Zuluaga, J. Restrepo, J. M. Lopez, Phys. B, Vol.398 (2007) P.187-190
- [1-35] D. Fiorani, Surface Effects in Magnetic Nanoparticles, (Springer, 2005) P. 114
- [1-36] D. Fiorani, Surface Effects in Magnetic Nanoparticles, (Springer, 2005)
- [1-37] D. Fiorani, Surface Effects in Magnetic Nanoparticles, (Springer, 2005) P.209
- [1-38] P. Zhang, F. Zuo, F. K. Urban III, A. Khabari, P. Griffiths, A. Hosseini-Tehrani, J. Mag. Mater., Vol.255, (2001) P.337-345
- [1-39] S. Roy, I. Dubenko, D. Ederh, N. Ali, J. Appl. Phys., Vol.96, No. 2, (2004) P. 1202-1208
- [1-40] X. M. Lin, A. C. S. Samia, J. Mag. Mater., Vol. 305, (2006) P.100-109
- [1-41] K. D. Sorge, "Magnetic Properties of Nanoparticle System of Fe, Co, Ni, and FePt, Created by Ion Implantation", PhD dissertation (2001), The University of Tennessee.
- [1-42] C. Kittel., Phys. Rev., Vol.70, (1946) P.965
- [1-43] D. Sellmyer, R. Skomski, Advanced Magnetic Nanostructures, (Springer, 2006) P.184
- [1-44] T. Hyeon, A. A. Lee, J. Park, Y. Chung, H. B. Na, J. Am. Chem. Soc, 123 (2001) 12798-12801
- [1-45] M. Zhang, C. Estournes, W. Bietsch, A. H. E. Muller, Adv. Funct. Mater. 14 (2004) P.871



- [1-46] J. H. Kim, J. Kim, K. H. Baek, D. H. Im, C. K. Kim, C. S. Yoon, *Col. Surf. A: Physicochem. Eng. Aspects.*, Vol.301 (2007) P.419-424
- [1-47] Y.Hou, J.Yu, S.Gao, *J. Matter. Chem*, 13 (2003) 1983-1987
- [1-48] E. Dagotto, *Nanoscale Phase Separation and Colossal Magneto-resistance*, (Springer, 2003) P.1-3
- [1-49] T. A. Kaplan, S. D. Mahanti, *Physics of Manganites*, (Kluwer Academic/Plenum Publishers - New York, 1998) P.71
- [1-50] W.D.Yang, Y.H.Chang, S.H.Huang, *J.Eur.Cer Soc.*25 (2005) 3611-3618
- [1-51] G. Popov, S. V. Kalinin, R. A. Alvarez, M. Greenblatt, D. A. Bonnell, *Mat. Res. Soc.Symp.Proc.* Vol. 658
- [1-52] A.P.Rao, D.Lavric, T. K. Nath, C. B. Eorn, L. Wu, F. Tsui, *Appl. Phys. Lett.* 73, (1998) 3294
- [1-53] A. Urushibara, *Phys. Rev.* B51, (1995) 14103
- [1-54] A. M. Haghiri-Gosnet, J.P. Renard, *J.Phys. D: Appl. Phys.* 36 (2003) R127-R150
- [1-55] E. Dagotto, *Nanoscale Phase Separation and Colossal Magneto-resistance*, (Springer, 2003) P.63
- [1-56] A. E. Teplykh, S. G. Bogdanov, E. Z. Valiev, A. N. Pirogov, Y. A. Dorofeev, A. A. Ostroushko, A. E. Udilov, V. A. Kazantzev, *Physica B* 350 (2004) 55-58
- [1-57] W. L. Sin, "Structural and electrical properties of MnO films grown by pulsed laser deposition", Mphil thesis (2004) P.1
- [1-58] S. Roy, I. Dubenko, D. Edorn, N. Ali, *J. App. Phys.*, 96 (2004) 1202-1208
- [1-59] E. Dagotto, *Nanoscale Phase Separation and Colossal Magneto-resistance*, P19, Springer, (2003)
- [1-60] E. L. Nagaev, *Colossal Magnetoresistance and Phase Separation in Magnetic Semiconductors* (Imperial College Press 2002) P. 298
- [1-61] G. Venkataiah, V. Prasad, P. V. Reddy, *J. Alloys and Compounds*, 429(2007) 1-9



- [1-62] A.M. Haghiri-Gosnet, T. Arnal, R. Soulimane, M. Koubaa, J.P. Renard, *Phys. Stat. sol. (a)* 201, No 7 (2004) P 1392-1397
- [1-63] M. Bowen, M. Bibes, A. Barthelemy, J. P. Contour, A. Anane, Y. Lemsitre, A. Fert, *Appl. Phys. Lett.*, Vol. 82, No. 2, (2003) P. 233-235
- [1-64] A.M. Haghiri-Gosnet, T. Arnal, R. Soulimane, M. Koubaa, J.P. Renard, *Phys. Stat. sol. (a)* 201, No 7 (2004) P 1392-1397
- [1-66] J. M. D. Coey, C.L. Chien, *MRS Bulletin*, (2003) P.720
- [1-67] M. Bowen, M. Bibes, A. Barthelemy, J. P. Contour, A. Anane, Y. Lemsitre, A. Fert, *Appl. Phys. Lett.*, Vol. 82, No. 2, (2003) P. 233-235
- [1-68] J. M. D. Coey, C.L. Chien, *MRS Bulletin*, (2003) P.720
- [1-69] H. Kachkachi, D. A. Garanin, *Springer science* (2005) P.75
- [1-70] J. M. D. Coey, C.L. Chien, *MRS Bulletin*, (2003) P.720
- [1-71] S. Roy, I. Dubenko, D. Edorn, N. Ali, *J. App. Phys.*, 96 (2004) 1202-1208
- [1-72] E.S. Vlahov, K. A. Nenkov, T.I. Donchev, A.Y. Spasov, *Vacuum*, Vol.69, (2003) P255-259
- [1-73] R. Mahesh, R. Mahendiran, A. K. Raychaudhuri, C. N. R. Rao, *Appl. Phys. Lett.*, Vol.68, No.16, (1996) P.2291-2293
- [1-74] M. L. Moreira, J. M. Soares, W. M. de Azevedo, A. R. Rodrigues, F. L. A. Machado, J. H. Araujo, *Physica B* 384 (2006) P.51- 53
- [1-75] M. Ziese., *Phys. Rev. B*, 60-2 (1999) R738-741

**Chapter 2 Nanoparticle formation and hydrothermal technique**

- [2-1] R. Kelsall, I. Hamley, M. Geoghegan, *Nanoscale – Science and Technology* (Wiley, 2005) P.19
- [2-2] I. Capek, *Nanocomposite structures and Dispersions*, (Elsevier, 2006) P.19
- [2-3] L. Zhang, *Preparation of multi-component ceramic nanoparticles* (The Ohio State University, 2004) P.5
- [2-4] P. W. Yip, “Pulsed laser deposition of heteroepitaxial ferroelectric thin film capacitor”, Mphil thesis (2001)
- [2-5] K. S. So, “Fabrication and Characterization of ferroelectric field effect transistor”, Mphil thesis (2001)
- [2-6] R. Kelsall, I. Hamley, M. Geoghegan, *Nanoscale – Science and Technology* (Wiley, 2005) P.32
- [2-7] Z. L. Wang, Y. Liu, Z. Zhang, *Handbook of Nanophase and Nanostructured Materials*, Vol.1 (Tsinghau University Press, 2002)
- [2-8] L. Zhang, *Preparation of multi-component ceramic nanoparticles* (The Ohio State University, 2004) P.5
- [2-9] Z. L. Wang, Y. Liu, Z. Zhang, *Handbook of Nanophase and Nanostructured Materials*, Vol.1 (Tsinghau University Press, 2002) P.102
- [2-10] Z. L. Wang, Y. Liu, Z. Zhang, *Handbook of Nanophase and Nanostructured Materials*, Vol.1 (Tsinghau University Press, 2002) P.195
- [2-11] W. D. Yang, Y. H. Chang, S. H. Haung, *J. Euro. Cer. Soc.* 25 (2005) 3611-3618
- [2-12] C. Bernard, G. Dauzet, F. Methieu, B. Durand, E. Puech-Costes, *Mater. Lett.* (2005) 2615 – 2620
- [2-13] R. J. Hunter, *Introduction to Modern Colloid Science* (Oxford Science Publications, 1993) P.16
- [2-14] C. H. Bae, S. H. Nam, S. M. Park, *Appl. Sur. Sci.*, 197-198 (2002) P.628 - 634
- [2-15] A. Gedanken, *Current Science*, Vol. 85, No. 12(2003) P.1720-1722



- [2-16] V. Krivoruchko, T. Konstantinova, A. Mazur, A. Prokhorov, V. Varyukhin, *J. Mag. Mater.* (2005)
- [2-17] K. Byrappa, M. Yoshimura, *Handbook of Hydrothermal Technology*, (Noyes Publications / William Andrew Publishing, LLC, 2001) P.182
- [2-18] V.K. LaMer, R. Dineger, *J. Am. Chem. Soc.* 72 (1950) P.4847
- [2-19] Y. Waseda, A. Muramatsu, *Morphology Control of Materials and Nanoparticles* (Springer, 2004) P.29
- [2-20] Y. Waseda, A. Muramatsu, *Morphology Control of Materials and Nanoparticles* (Springer, 2004) P.31
- [2-21] E. G. Gurvich, *Metallonosyne osadki Mirovogo okeana* (English), (Springer, 2006) P.1-5
- [2-22] K. Byrappa, M. Yoshimura, *Handbook of Hydrothermal Technology*, (Noyes Publications / William Andrew Publishing, LLC, 2001) P.11
- [2-23] L. Zhang, *Preparation of multi-component ceramic nanoparticles* (The Ohio State University, 2004) P.5
- [2-24] S. Somiya, R. Roy, *Bull. Mater. Sci.*, Vol. 23, No. 6 (2000) P. 453-460
- [2-25] L. Zhang, *Preparation of multi-component ceramic nanoparticles* (The Ohio State University, 2004) P.5
- [2-26] K. Byrappa, M. Yoshimura, *Handbook of Hydrothermal Technology*, (Noyes Publications / William Andrew Publishing, LLC, 2001) P.10
- [2-27] K. Byrappa, M. Yoshimura, *Handbook of Hydrothermal Technology*, (Noyes Publications / William Andrew Publishing, LLC, 2001) P.232
- [2-28] K. Byrappa, M. Yoshimura, *Handbook of Hydrothermal Technology*, (Noyes Publications / William Andrew Publishing, LLC, 2001) P.93-94
- [2-29] DuPont, *Fluoropolymer Composition – Typical properties*, 2008
- [2-30] K. Byrappa, M. Yoshimura, *Handbook of Hydrothermal Technology*, (Noyes Publications / William Andrew Publishing, LLC, 2001) P.180
- [2-31] K. Byrappa, M. Yoshimura, *Handbook of Hydrothermal Technology*, (Noyes Publications / William Andrew Publishing, LLC, 2001) P.461
- [2-32] Y. J. Wang, S. H. Zhang, K. Wei, N. Zhao, J. D. Chen, X. D. Wang, *Mater. Lett.* 60 (2006) 1484 – 1487



- [2-33] K. Byrappa, M. Yoshimura, Handbook of Hydrothermal Technology, (Noyes Publications / William Andrew Publishing, LLC, 2001) P.766
- [2-34] A.G. Leyva, P. Stoliar, M. Rosenbusch, V. Lorenzo, P. Levy, C. Albonetti, M. Cavallini, F. Biscarini, H. E. Troiani, J. Curiale, R. D. Sanchez, J. Sol. State Chem. 177 (2004) 3949 - 3953
- [2-35] J. Goodwin, Colloids and Interfaces with Surfactants and Polymers (John Wiley & Sons Ltd, 2004) P.20
- [2-36] R. J. Hunter, Introduction to Modern Colloid Science (Oxford Science Publications, 1993) P.17
- [2-37] H. H. Paradies, S. F. Clancy, The Rigaku Journal, Vol. 17, No.2 (2000) P.25
- [2-38] J. Goodwin, Colloids and Interfaces with Surfactants and Polymers (John Wiley & Sons Ltd, 2004) P.20
- [2-39] C. J. Brinker, Y. Lu, A. Sellinger, Adv. Mater. Vol.11, No.7 (1999) P.580
- [2-40] J. Goodwin, Colloids and Interfaces with Surfactants and Polymers (John Wiley & Sons Ltd, 2004) P.21
- [2-41] C. Bernard, G. Dauzet, F. Mathieu, B. Durand, E. Puech-Costes, Mater. Lett. 59 (2005) 2615-2620
- [2-42] D. Zhu, H. Zhu, Y. Zhang, Appl. Phys. Lett, 80, No.9 (2002) 1634-1636
- [2-43] J. J. Urban, L. Ouyang, M. H. Jo, D. S. Wang, H. Park, Nano. Lett., Vol. 4 No. 8 (2004) P.1547-1550
- [2-44] S. A. Mirji, Y. B. Kholam, S. B. Deshpande, H.S.Potdar, R.N.Bathe, S.R.Sainkar, S.K.Date, Mater. Lett., 58 (2004) 837

**Chapter 3 Characterization method**

- [3-1] R. Kelsall, I. Hamley, M. Geoghegan, *Nanoscale – Science and Technology* (Wiley, 2005) P.19
- [3-2] D. B. Williams, C. B. Carter, *Transmission Electron Microscopy* (Kluwer Academic/ Plenum Publishers, 1996)
- [3-3] Y. Waseda, A. Muramatsu, *Morphology Control of Materials and Nanoparticles* (Springer, 2004) P.100
- [3-4] Y. Waseda, A. Muramatsu, *Morphology Control of Materials and Nanoparticles* (Springer, 2004) P.101
- [3-5] D. B. Williams, C. B. Carter, *Transmission Electron Microscopy* (Kluwer Academic/ Plenum Publishers, 1996)
- [3-6] Y. Waseda, A. Muramatsu, *Morphology Control of Materials and Nanoparticles* (Springer, 2004) P.154
- [3-7] C. Y. Lam, “Semiconducting properties of oxide thin films prepared by pulsed laser deposition”, Mphil thesis (2005)
- [3-8] B. D. Cullity., *Elements of X-ray Diffraction*, 2nd ed.; (Addison-Wiley Publishing Company: Reading, 1978.)
- [3-9] J. L. Dormann, D. Fiorani, *Magnetic Properties of Fine Particles* (Proceedings of the international Workshop on Studies of Magnetic Properties of Fine Particles and their Relevance to Materials Science, 1991) P. 166
- [3-10] Y. L. Hou, J. F. Yu, S. Gao, *J. Mater. Chem.*, 13 (2003) 1983-1987
- [3-11] B. D. Cullity, *Introduction to Magnetic Materials*, (Addison-Wesley, Reading, M.A. 1984) P. 279
- [3-12] J. W. Ekin, *Experimental Techniques for Low-Temperature Measurements*, (Oxford University Press, 2006) P.274-276

**Chapter 4 Synthesis of magnetic manganite nanoparticles**

- [4-1] D. Sellmyer, R. Skomski, *Advanced Magnetic Nanostructure*, (Springer, 2006), P. 4
- [4-2] S. Sun, C. B. Murray, *J. Appl. Phys.*, Vol. 85, No. 8 (1999), P. 4325-4330
- [4-3] T. Chatterji, *Colossal Magnetoresistive Manganites* (Kluwer Academic Publishers, 2004) P.11
- [4-4] S. Roy, I. Dubenko, D. D. Edoth, N. Ali, *J. Appl. Phys.*, Vol. 96, No. 2, (2004) P. 1202-1208
- [4-5] M. Bowen, M. Bibes, A. Barthelemy, J. P. Contour, A. Anane, Y. Lemaitre, A. Fert, *Appl. Phys. Lett.*, Vol. 82, No. 2, (2003) P. 233-235
- [4-6] A. M. Haghiri-Gosnet, J. P. Renard, *Appl. Phys. Lett.*, Vol. 36, (2003) R-127-150
- [4-7] E. Dagotto, *Nanoscale Phase Separation and Colossal Magneto-Resistance*, (Springer, 2003) P.35
- [4-8] H. Kachkachi, D. A. Garanin, *Springer Science* (2005) P.75
- [4-9] J. Spooren, R. I. Walton, F. Millange, *J. Mater. Chem.*, Vol. 15, (2005) P.1542-1551
- [4-10] K. Byrappa, M. Yoshimura, *Handbook of Hydrothermal Technology*, (Noyes Publications / William Andrew Publishing, LLC, 2001) P.161
- [4-11] J.J.Urban, L. Ouyang, M. H. Jo, D. S. Wang, H. K. Park, *Nano Lett*, Vol. 4, No.8, (2004) P.1547 -1550
- [4-12] R.N. Bathe., S.R. Sainkar, S. K. Date, *Mater. Lett.*, Vol. 58, (2004) P.837
- [4-13] N.V. Cuuraev, I.P. Sergeeva, V.D. Sobolev, H.J. Jacobasch, P. Weidenhammer, F.J. Schmitt, *Colloids Surface A*, Vol 164 (2000) P.121-129
- [4-14] Y. Waseda, A. Muramatsu, *Morphology Control of Materials and Nanoparticles* (Springer, 2004) P.159
- [4-15] J.J.Urban, L. Ouyang, M. H. Jo, D. S. Wang, H. K. Park, *Nano Lett*, Vol. 4, No.8, (2004) P.1547 -1550



- [4-16] S. Roy, I. Dubenko, D. D. Edoth, N. Ali, *J. Appl. Phys.*, Vol. 96 (2004) P.1202-1208
- [4-17] H.L.J, Hyunchul Sohn, *J. Mag. Mater.* 167(1997) 200-208
- [4-18] V. Sreeja, P. A. Joy, *Mater. Research Bulletin*, Vol.42, (2006) P.1570-1576
- [4-19] P. Gaunt, *Phi. Mag. B*, 48. 3 (1983) 261
- [4-20] L.B.Steren, M. Sirena, J. Guimpel, *Phys. Rev. B*, 65 (2002) 09443
- [4-21] P.Zhang, F.Zuo, F.K.Urban III, A. Khabari, P.Griffiths, A. H-Tehrani, *J. Mag. Mater.* 225 (2001) 337-34
- [4-22] H.L.Ju, Y.S.Nam, J.E.Lee, H.S.Shin, *J. Mag. Mater.* 219(2000) 1-8
- [4-23] V. Sreeja, P. A. Joy, *Mater. Res. Bull.* 42, 8 (2007) P1570
- [4-24] M. L. Moreira, J. M. Soares, W. M. de Azevedo, A. R. Rodrigues, F. L. A. Machado, J. H. Araujo, *Physica B* 384 (2006) P.51- 53
- [4-25] A. Adamski, P. Jakubus, Z. Sojka, *Nukleonika – Proceeding* 51 (2006) S27-S33
- [4-26] X.Y. Chen, X. Wang, Z.H. Wang, X.G. Yang, Y.T. Qian, *Cryst. Growth. Des.* 5 (2005) 347
- [4-27] A. Datta, S. Gorai, D. Ganguli, S. Chaudhuri, *Mater. Chem. Phys.* 102 (2007) 195
- [4-28] E. Dagotto, *Nanoscale Phase Separation and Colossal Magneto-Resistance*, (Springer, 2003) P.36
- [4-29] R.W. Li, H. Xiong, J. R. Sun, Q. A. Li, Z. H. Wang, J. Zhang, B.G. Shen, *J. Phys.: Condens. Matter* 13 (2001) 141-148
- [4-30] B.M. Nagabhushana, G.T.Chandrappa, P.R.S. Chakradhar, K.P.Ramesh, C. Shivakumara, *Solid State Comm.* 136 (2005) 427-432
- [4-31] A. Benerjee, S. Pal, B. K. Chaudhuri, *J. Chem. Phys.* 115 (2001) 155
- [4-32] G. Venkataiah, V. Prasad, P. Venugopal Reddy, *J. Alloys Comp.* 429 (2007) 1-9



- [4-33] D. Garcia, B. Alascio, D. G. Lamas, D. Niebieskikwiat, A. Caneiro, R. D. Sanchez, E. D. Cabanillas, *J. Phys. Chem. Solids*. Vol. 66, (2005) P.1687-1694
- [4-34] M. Bowen, M. Bibes, A. Barthelemy, J. P. Contour, A. Anane, Y. Lemaitre, A. Fert, *Appl. Phys. Lett.*, Vol. 82, No. 2, (2003) P. 233-235
- [4-35] B.M. Nagabhushana, R.P. Sreekanth Chakradhar, K. P. Ramesh, V. Prasad, C. Shivakumara, G. T. Chandrappa, *J. Alloys. Comp.* (2006)
- [4-36] B.M Nagabhushana, R.P. Sreekanth Chakradhar, K. P. Ramesh, V. Prasad, C. Shivakumara, G. T. Chandrappa, *J. Alloys Compd* (2006) in Press
- [4-37] G. Venkataiah, D. C. Krishna, M. Vithal, S. S. Rao, S.V. Bhat, V. Prasad, S.V. Cubramanyam, P. Venugopal Reddy, *Physica B*, 357 (2004) 370 – 379



Chapter 5 Synthesis and characterization of nano manganites particles with core shell architecture

- [5-1] Y. Waseda, A. Muramatsu, Morphology Control of Materials and Nanoparticles (Springer, 2004) P.34
- [5-2] S. C. Zhang, X. G. Li, Powder Tech. , Vol.141, (2004) P.75-79
- [5-3] Y. H. Zhu, H. Da, X. L. Yang, Y. Hu, Colloids and Surfaces. Eng Aspects, 231 (2003) P123-129
- [5-4] I. Capek, Nanocomposite Structures and Dispersions, (Elsevier, 2006) P.178
- [5-5] Y. Qiang, J. Antony, A. Sharma, J. Nutting, D. Sikes, D. Meyer, J. Nano. Research (2005)
- [5-6] E.S. Mushailov, B. V. Vasiliev, J. Mag. Mater., Vol. 279 (2004) P.235-240
- [5-7] B. B. Nayak, S. Vitta, A.K. Nigam, D. Bahadur, Thin Solid Films, Vol. 505, (2006) P.109 -112
- [5-8] O. Iglesias, X. Battle, A. Labarta, J. Mag. Mater, 316 (2007) 140-142
- [5-9] U. Kawald, W. Zemke, H. Bach, J. Pelzl, G. A. Saunders, Physica B, Vol. 161 (1989) P.72-74
- [5-10] D. W. Kim, Solid State Communication, 137 (2006) P.545-548
- [5-11] H. Sawada, Y. Morikawa, N. Hamada, K. Terakurn, J. Mag. Mater., 177-181 (1998) P.879-880
- [5-12] J. Nogues, J. Sort, V. Langlais, V. Skumryev, S. Surinach, J. S. Munoz, M. D. Baro, Phys. Reports, Vol. 422 (2005) P65-117
- [5-13] W. L. Sin, "Structural and electrical properties of MnO films grown by pulsed laser deposition", Mphil thesis (2004) P.11

**Chapter 6 Dispersion of magnetic nano-manganite in polymer****matrix**

- [6-1] B. C. Shekar, V. Veeravazhuthi, S. Sakthivel, D. Mangalaraj, S. K. Narayandass, *Thin Solid Films*, 348 (1999) 122-129
- [6-2] P. M. Ajayan, L. S. Schadler, P. V. Braun, *Nanocomposite Science and Technology*, (Wiley-VCH, 2003) P.77
- [6-3] P. M. Ajayan, L. S. Schadler, P. V. Braun, *Nanocomposite Science and Technology*, (Wiley-VCH, 2003) P.80
- [6-4] A. Elgafy, K. Lafdi, *Carbon*, Vol. 44 (2006) P.1682-1689
- [6-5] Mack MG, Balzer JO, Straub R, *Radiology*, Vol. 44, (2002) P.222-239
- [6-6] L. Balcells, A. E. Carrillo, B. Martinez, J. Fontcuberta, *Appl. Phys. Lett.* Vol. 74, No. 26, (1999) P.4014
- [6-7] H. Kumigashira, R. Hashimoto, A. Chikamatsu, M. Oshima, H. Wadati, A. Fujimori, M. Lippmaa, M. Kawasaki, H. Koinuma, *J. Mag. Mater.*, Vol 310 (2007) 1997-1999
- [6-8] Y. H. Huang, S. Wang, F. Luo, S. Jiang, C. H. Yan, *Chem. Phys. Lett.*, Vol. 362, (2002) P.114-118
- [6-9] D. L. Zhu, Q. Q. Shu, W. J. Liu, X. C. Ma, P. J. Cao, S. M. Bhagat, S.E. Lofland, I. O. Troyanchuk, *Mater. Chem. Phys.*, Vol. 103, (2007) P.437-440
- [6-10] F. C. Zhang, W. Z. Gong, C. Cai, B. Xu, X. G. Qiu, R. Vanfleet, L. Chow, B. R. Zhao, *Solid State Communications*, Vol.131 (2004) P.271-274
- [6-11] D. Lee, K. Char, *Langmuir*, Vol.18 (2002) P6445-6448
- [6-12] T. M. Wu, C. Y. Wu, *Polymer Degradation and Stability*, Vol. 91 (2006) P.2198-2204
- [6-13] K. E. Strawhecker, E. Manias, *Chem. Mater.*, Vol. 12, (2000) P.2943-2349
- [6-14] C. M. Hassan, N. A. Peppas, Vol. 153 (2000) P. 37
- [6-15] R. W. Li, H. Xiong, J. R. Sun, Q. A. Li, Z. H. Wang, J. Zhang, B. G. Shen, *J. Phys.: Condens. Matter* 13 (2001) 141-148